Research Dissertation

Protein Biophysics in Hollow-Core Photonic Crystal Fibres

Label-Free Monitoring of Biomolecules in Optofluidic Waveguides

Jan Heck

Christ's College

July 2023

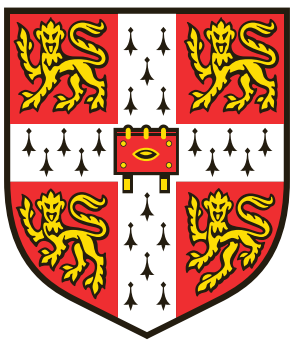

This thesis is submitted for the degree of Doctor of Philosophy

Declaration

This thesis is the result of my own work and includes nothing which is the outcome of work done in collaboration except as declared in the Preface and specified in the text. I further state that no substantial part of my thesis has already been submitted, or, is being concurrently submitted for any such degree, diploma or other qualification at the University of Cambridge or any other University or similar institution except as declared in the Preface and specified in the text. It does not exceed the prescribed word limit for the relevant Degree Committee

Jan Heck
20th July 2023
Revised 12th September 2023

Contact the Author

I've benefited greatly in my own work from reading many PhD dissertations, and I humbly hope this present writing can do the same for those who come across it. The author warmly invites correspondence of any kind, feedback and questions at:

jan-heck.net/phd

Abstract

Protein Biophysics in Hollow-Core Photonic Crystal Fibres
Label-Free Monitoring of Biomolecules in Optofluidic Waveguides

Jan Heck

Proteins are the central building blocks of life, and experimental methods for their study are fundamental to deepening our understanding of biology and the life sciences. When studying protein interactions, we seek new experimental methods that can detect and monitor proteins in solution, at small volumes and low concentrations. Of particular interest are optical methods that leave the system undisturbed and allow for in-situ measurements over a span of time. Indirect optical detection, using fluorescent stains or genetically-incorporated fluorophores as proxies, has enabled these aims in many applications. However, these labels have been shown to alter protein behaviour, such as the protein–protein interactions that determine their aggregation mechanisms.

In this PhD dissertation, we study the use of hollow-core photonic crystal fibre (HC-PCF), a class of optofluidic waveguides, to optically detect and monitor proteins in microfluidic environments without labels. Within this waveguiding microfluidic fibre geometry, we monitor the label-free optical extinction and fluorescence of different proteins in the ultraviolet spectrum, in native and aggregated forms, and over extended periods of time as they undergo aggregation.

Specifically, we developed and demonstrate here three applications that form the experimental chapters of this dissertation. First, we quantify serum proteins by exciting and collecting their intrinsic protein fluorescence in the deep ultraviolet ($\lambda_{\text{exc}} = 280\,\text{nm}$, $\lambda_{\text{ems}} = 350\,\text{nm}$) within a HC-PCF ($49\,\text{nL}\,\text{cm}^{-1}$) under continuous flow at sub-micromolar concentrations. Second, we adapt and redesign this system to enable long-pathlength ($17\,\text{cm}$), ultraviolet ($365\,\text{nm}$) extinction measurements on protein aggregates. Finally, combining these two techniques into a multiplexed measurement, we demonstrate the ability to monitor the aggregation kinetics of silk protein over several days in both extinction and fluorescence.

Graphical Abstract

Chapter 1
Context
Literature review

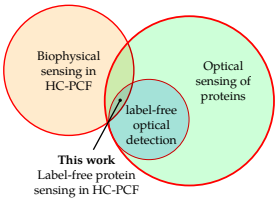

Chapter 2
Concepts
Theory & Background

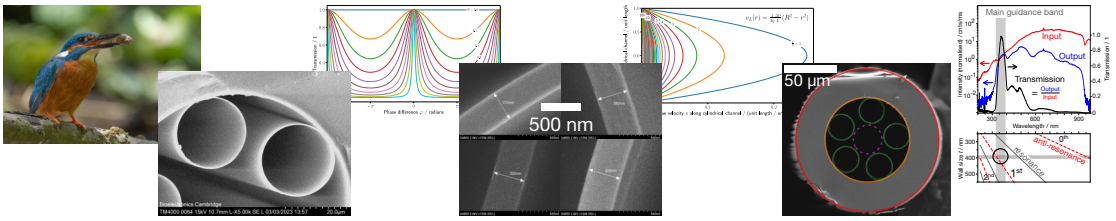

Chapter 3
Fluorescence
Intrinsic fluorescence of proteins in HC-PCF

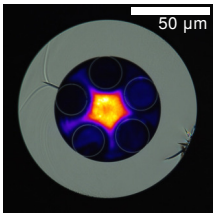

λ = 365 nm
through 17 cm water

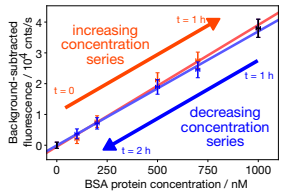

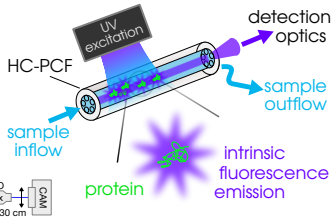

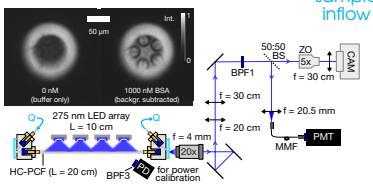

Chapter 4
Extinction
Long-pathlength extinction in HC-PCF

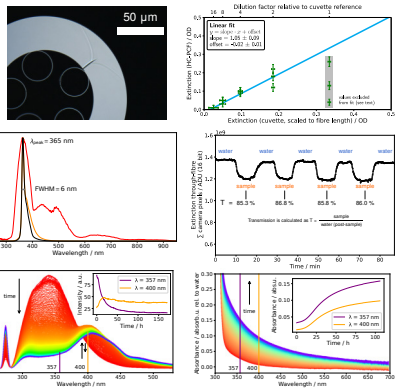

Chapter 5
Low-Volume
Filling HC-PCF with microlitre samples

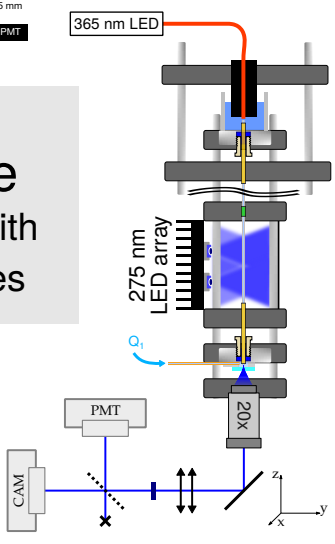

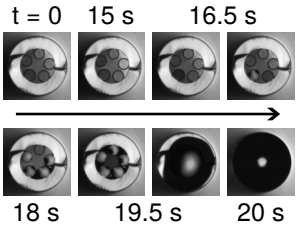

Chapter 6
Aggregation
Protein aggregation monitored in HC-PCF

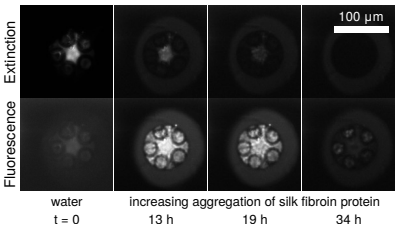

Contents

Pre Preface **14**

Pre.1 Notes for readers . . . 15
Pre.2 Acknowledgements . . . 15
Pre.3 Publications . . . 18
Pre.4 Conference presentations . . . 19
Pre.5 Abbreviated abstracts . . . 20

1 Context **21**

1.1 Motivation . . . 22
1.2 Literature . . . 25
1.2.1 Label-free optical detection of proteins . . . 25
1.2.2 HC-PCF for biophysical sensing . . . 42
1.2.3 Label-free detection of proteins in HC-PCF . . . 49
1.2.4 Summary . . . 55
1.3 Practical considerations . . . 56

2 Concepts in Optofluidics **57**

2.1 Optical waveguides . . . 58
2.1.1 Light propagation through media . . . 58
2.1.2 Photonic crystal fibres . . . 62
2.1.3 ARROW model simulation . . . 67
2.1.4 Modes in HC-PCF . . . 68
2.1.5 Comparison to other photonic crystal fibre geometries . . . 71
2.1.6 Manufacturing of HC-PCF . . . 73
2.2 Microfluidics . . . 76
2.2.1 General theory . . . 76
2.2.2 Theory of microfluidic flows and the Reynolds number . . . 77
2.2.3 Laminar flow profile . . . 78
2.2.4 Hydrodynamic resistance . . . 78
2.3 Molecular mass transport . . . 80
2.3.1 Diffusion theory . . . 80
2.3.2 Diffusion simulation . . . 81
2.4 Materials and Methods . . . 86
2.4.1 HC-PCF geometry . . . 86
2.4.2 HC-PCF preparation . . . 86

2.4.3 Transmission properties 91

3 Label-free Intrinsic Protein Fluorescence 95
3.1 Motivation 96
3.2 Experimental Method 97
3.2.1 Experimental setup 97
3.2.2 Characterisation of excitation light 102
3.3 Results 107
3.3.1 Spectral comparison 107
3.3.2 Key experiment: Label-free quantification of intrinsic protein fluorescence in HC-PCF under flow 109
3.4 Discussion and outlook 113
3.4.1 Summary of findings 113
3.4.2 Possible improvements 113

4 Label-free Ultraviolet Extinction on Protein Aggregates 116
4.1 Motivation 117
4.2 Experimental Method 118
4.2.1 Characterisation measurements 118
4.2.2 Experimental setup 123
4.2.3 Sample preparation 127
4.3 Results 133
4.3.1 Gold nanoparticles 134
4.3.2 Key experiment: Label-free quantification of silk fibril aggregates via extinction in HC-PCF under flow 139
4.4 Discussion and outlook 141
4.4.1 Summary of findings 141
4.4.2 Possible improvements 141

5 Capillary Action Infiltration for Minimal Sample Volume 144
5.1 Motivation 145
5.1.1 Note about availability 145
5.2 Experimental method 146
5.3 Results 148
5.4 Discussion and outlook 151

6 Towards Monitoring of Protein Aggregation In-Situ **152**
6.1 Motivation . . . 153
6.2 Experimental Method . . . 153
6.2.1 Silk fibroin protein . . . 154
6.2.2 Experimental setup . . . 156
6.2.3 Data collection . . . 162
6.3 Results . . . 164
6.3.1 Key experiment: Label-free monitoring of protein aggregation via multimodal sensing in HC-PCF under flow . . . 164
6.4 Discussion and outlook . . . 169
6.4.1 Summary of findings . . . 170
6.4.2 Possible improvements . . . 170

7 Conclusion and outlook **172**
7.1 Summary of results . . . 173
7.2 Outlook . . . 174
7.3 Closing statement . . . 177

SI Supplementary Information **178**
SI.1 Construction drawings . . . 179
SI.2 Silk aggregates measurement data . . . 183
SI.3 State machine algorithm to separate multiplexed measurement data . . . 185
SI.4 Flows from thermal volume expansion . . . 187
SI.5 Microfluidic device fabrication protocol . . . 189
SI.6 Other approaches to light guidance through water . . . 190
SI.6.1 Water jets . . . 190
SI.6.2 Mirror-coated capillaries . . . 191
SI.6.3 Total internal reflection by coating . . . 192
SI.7 Derivation of hydrodynamic resistance . . . 192

Ref References **199**

List of Figures

1.1 Venn diagram outlining the scope and structure of the literature review, identifying the position of this dissertation 25

1.2 The effect of labels on protein aggregation studied by Saar *et al.* . . . 27

1.3 Chemical structure of tryptophan 36

1.5 Absorbance and fluorescence spectra of the intrinsically fluorescent amino acids 37

1.6 HC-PCFs for optical tracking of Brownian motion by Förster *et al.* . . 44

1.7 Deformation of red blood cells in HC-PCF by Unterkofler *et al.* 46

1.8 UV absorption spectroscopy on drug molecules in HC-PCF by Nissen *et al.* 48

1.9 Measurement of proteins inside HC-PCF using transmission spectroscopy by Giovanardi *et al.* 51

2.1 Examples of photonic crystal structures used to produce PCFs, with their resulting light guidance properties 63

2.2 Photonic crystals producing structural colouration, appearing in nature both inorganic (a) and biological (b, c) in origin 64

2.3 The Fabry – Pérot etalon 66

2.4 Geometry of the HC-PCF used in this project 68

2.5 Fabry – Pérot resonance and antiresonance wavelengths as a function of the HC-PCF strut thickness 69

2.6 Mode simulations for the HC-PCF used in this dissertation 70

2.7 Higher-order modes observed in a water-filled HC-PCF 71

2.8 Basic steps for manufacturing photonic crystal fibres 74

2.9 Illustration of Poiseuille flow 79

2.10 Simulation of a single BSA molecule freely diffusing inside a HC-PCF core 83

2.11 Diffusion simulation of proteins inside a HC-PCF, with autocorrelation fit 84

2.12 Optical micrographs of a cleaved fibre facet 87

2.13 SEM image of a cleaved HC-PCF facet 88

2.14 SEM close-up of two HC-PCF cladding capillaries 88

2.15 SEM image of a knife-cut fibre facet, resulting in a rough, non-planar facet 89

2.16 Confocal microscopy z-scan of a cleaved HC-PCF 90

2.17 Comparing the theoretical and measured transmission spectrum of the HC-PCF 91

2.18 Fundamental mode image in a plain glass capillary 94

3.1 Concept drawing for using HC-PCF for the continuous-flow label-free detection of proteins under ultraviolet light side excitation 96

3.2 Experimental setup 98

3.3 Photograph of the experimental setup's HC-PCF section 99

3.4 Optofluidic interconnect design and realisation 103

3.5 Comparison of 280 nm and 275 nm fluorescence excitation wavelengths in a cuvette for intrinsic fluorescence of BSA protein 105

3.6 Spectrum of the 275 nm LEDs used to excite intrinsic protein fluorescence106

3.7 Line scan of the irradiation profile at the HC-PCF plane 106

3.8 Ray optics diagram for the effect of cylindrical lensing on the HC-PCF 108

3.9 Spectral comparison of the intrinsic protein fluorescence of BSA measured in cuvette and HC-PCF 109

3.10 Intrinsic protein fluorescence of BSA protein recorded inside a HC-PCF under continuous flow 110

3.11 Label-free quantification of BSA protein under continuous flow inside a HC-PCF using intrinsic protein fluorescence 111

4.1 Characterising the 365 nm LED output power linearity with the modulation signal 119

4.2 Stability testing of the input light source 121

4.3 Choice of light source optimised for HC-PCF transmission 122

4.4 Experimental setup 123

4.5 Photographs of the optical bench and the HC-PCF insert module . . . 124

4.6 Photo of several earlier design prototypes that preceded the final design used in the extinction experiments 125

4.7 Microfluidic production of nanosized silk aggregates 128

4.8 SEM images of the silk fibril aggregates 129

4.9 UV-VIS absorbance spectrum of the silk aggregate solution 130

4.10 Microfluidic compliance testing of the system 131

4.11 Reproducibility testing of the system, showing the extinction measurement procedure repeated four times in sequence 132

4.12 Typical mode image of 365 nm light transmitted through 17 cm of water 134

4.13 Ultraviolet extinction measurement of a 1/200 gold nanoparticle solution in HC-PCF 135

4.14 Complete signal trace of the gold nanoparticle dilution series measured in HC-PCF 136

4.15 Quantification of gold nanoparticles inside a HC-PCF using long-pathlength ultraviolet extinction measurement under continuous flow . 137

4.16 Long-term test of the system 138

4.17 Quantification of silk fibril aggregates inside a HC-PCF using long-pathlength ultraviolet extinction measurement under continuous flow . 139

4.18 Post-experiment brightfield microscopy of a HC-PCF used with silk fibrils140

5.1 Measuring filling speed and uniformity by timelapse microscopy 147

5.2 Infiltrating the HC-PCF by capillary action 148

5.3 Water–water control measurement for minimal sample volume extinction measurements through capillary filling 149

5.4 Exchanging a sample filled by capillary action with water as the extinction reference 150

6.1 Experimental setup showing how side-excitation is added to the extinction setup 158

6.2 Multiplexing extinction and fluorescence measurements in HC-PCF . . 159

6.3 Fluorimetry of an aggregating silk solution in cuvette 159

6.4 UV-VIS extinction of an aggregating silk solution in cuvette 161

6.5 Silk aggregating in HC-PCF 164

6.6 Silk protein aggregation measured inside a HC-PCF via fluorescence and extinction 166

S-1 Construction drawing of the low dead volume, high compliance optofluidic interconnect 179

S-2 Construction drawing of the optofluidic T butt-coupling interconnect . 180

S-3 Construction drawing of an alternative version of a low dead volume optofluidic interconnect 181

S-4 Absorption spectrum of BSA (10 µM) measured in cuvette compared to the excitation LED spectrum (normalised) 182

S-5 The first of the triplicate undiluted solution of silk aggregates being measured in HC-PCF 184

S-6 Categorising plain PMT data into different categories for multiplexed measurements 185

S-7 A harmonically perturbed circle overlaid on our fibre channel geometry 196

List of Tables

1.1 Fluorescence properties of aromatic amino acids 36

2.1 Refractive indices of some common materials or material classes 59

2.2 Primary advantages of AR-HCFs compared to other HC-PCFs 72

SI.1 Experimental data for the silk aggregates 183

Für meine Eltern und Großeltern,

ohne die all dies
– und so vieles mehr –
nie möglich gewesen wäre.

„Das Gericht will nichts von dir. Es nimmt dich auf, wenn du kommst, und es entläßt dich, wenn du gehst." – Franz Kafka, *Der Prozess*, 1925

Pre | Preface

This preface contains relevant notes and background information for readers of this PhD dissertation.

Pre.1 Notes for readers 15
Pre.2 Acknowledgements 15
Pre.3 Publications 18
Pre.4 Conference presentations 19
Pre.5 Abbreviated abstracts 20

Pre.1 Notes for readers

I hope this dissertation will be useful to you, the reader. These are some general points about this document.

Reuse of figures in other works

I am more than happy to provide source files for any figures or other elements of this dissertation to be reproduced in other works, most likely under a CC-BY license. Similarly, to the extent I am permitted to do so, feel free to ask me for preprints of works that are non-accessible due to the academic publishing system.

Reuse of code

Equally, I am happy to provide relevant source code for any of the figures or simulations in this dissertation under a free software license, most likely under the GPL. Contact me at jan-heck.net/phd.

Use of 'we'

As a stylistic choice, I prefer and often adopt the use of 'we' in the main text. This is to include the reader and promote a dialectical approach, similar to the narrative writing style of textbooks. It also reflects the common writing style of co-authored academic papers. This does not imply that the work was done by anyone other than myself, as declared in the front matter and spelled out explicitly throughout this dissertation.

Margin titles

Margin titles throughout the text reproduce the high-level argument structure of the text. They are not meant to replace section titles, but rather to allow for quick visual panning across the text. They should relay the semantic structure of the text and make it quicker to skip through the narrative and find a particular point in the text. For the same reason, section titles are offset to be present in the left margin.

Pre.2 Acknowledgements

I can only begin by thanking my supervisors, Dr. Tijmen Euser and Prof. Tuomas Knowles, for guiding me throughout the work I am putting to the page today. The breadth and quality of research I could be part of, and the people I met in their labs, are both a testament to the thriving research environments they create.

First, to my family, who know what they are to me: I lack words to express my gratitude for everything you have done for me, so that I can live the life that I do.

And to Mayuko: with your invaluable kindness and support you have enriched my every day all this time. 一生に感謝します。

I've been blessed in my friends, and I share so many happy memories with you all. Of those that will always occupy a special place in my thoughts when I

think of my time in Cambridge: Julian, you've been a fantastic friend for so many years. Stay how you are. You have truly enriched my life. Loren, our journeys continue to cross after we met in the Royal Holloway library in my first month of undergraduate, where you left me toppling over with a stack of Physics books on my arms, and I still remember seeing you again on my first day in Cambridge. Where will be next? Alex and Michael, you will stay my fellow DD生s for life, thank you for the great times we had in Cambridge when you came to visit. And finally, to Ms. Weber – who I know since my childhood years in Baden-Baden but now had to find out that she had been to a Cambridge Mayball some fifty years ago, long before I ever set foot in this memorable city –, thank you for all the wonders of fine culture you have introduced me to over the years.

I thank the entire Optofluidics group (past and present!) that were around to witness my failures and successes in the laboratory: Ermanno, Omid, Philipp, Takashi, Ralf, Alex, Megan, Matthew, Ivan, Stephen, Jonathan, Henry, Ashleigh, Ahmad, and all future OFers: Remember, fibres have two ends.

I thank all members of the Knowles group, especially those I had the pleasure of working with more closely: Zenon, Raphaël, Georg, Quentin, Oliver, Magdalena, Sid, Challa, Joe, Jack, Akhila, Matthias, and everyone else who I had the pleasure of discussing science with.

I thank everyone of the Nanophotonics group, where I had many insightful discussions and a great time in the Yorkshire Dales. I want to particularly thank Dean for his invaluable mentorship in my choice of postdoc fellowships, and Giovanni for his invaluable presence maintaining the labs.

To those who, like myself, hold permanent residency in the Maxwell Centre; in particular Filip and Mohammed: thank you for your company during all the overnight and weekend experiments.

To the 2018 cohort of the Sensor CDT: I fondly remember our shared MRes year. Thank you for being a fantastic start into this journey towards the PhD.

I also want express my gratitude to all administrative, support and teaching staff of the University. I especially want to thank Kevin Mott for his excellent support and training he provides through the Cavendish student workshop – spaces like this are being closed or made inaccessible to students all around, and I am very glad to have had the opportunity to practise and learn machining in your workshop –; the undergraduate Part IB lab technicians that I had the pleasure of working with during my undergraduate laboratory supervision; and

– making it all possible behind the scenes – the administrative staff of the Sensor CDT, Kapitza Hub, Knowles group, and the Physics and Chemistry departments.

My college, Christ's, has provided me with all of what makes Cambridge special, and I thank the Porters, the Kitchen, Buttery, and Tutorial staff, the Gardeners (tending the Fellows' Garden into a beautiful hidden marvel of Cambridge), the MCR, and the Master and Fellows that I had the pleasure to meet, for treasuring this wonderful, welcoming place.

In the same way, the countless encounters in Cambridge of the people I lived with, shared a formal dinner with, or even just met in passing: you've enriched my time there thousandfold. Thank you Patrick, David, and Hettie for my time in your home.

I couldn't have even started this PhD if it hadn't been for many great teachers. Before my arrival in Cambridge, for supporting me in venturing astray from science (only for a little while!) towards the humanities, and taking me to Japan, I thank Prof. Murata and Prof. Oberländer. Few things have changed my trajectory in life as much as this opportunity.

At my undergraduate alma mater, Royal Holloway College, I want to particularly thank Dr. Kauer and Prof. Cowan for their mentorship. The final projects I could do with them shaped my desire to do independent research.

Looking further back, that I even began to set out on this journey of academic learning is in no small part to my school teachers. In particular, I wouldn't have followed the path I went on without the passion for science and curious inquiry that was kindled in me by Hr. Bruker, Hr. Buchheister, Fr. Huber, Hr. Resch, Hr. Simeon, and Fr. Warnecke from my high school, together with Fr. Schneider from my elementary school.

I shall finish the list here, knowing that attempting to complete it would be futile. Suffice it to say: from the chance encounters with people in Cambridge that give life its colour, all the way to the global and anonymous sea of people that wrote my software, built my hardware, and shared their knowledge on which I thrive: Thank you.

Pre.3 Publications

For reference, publications relating to the time of my PhD (at the time of writing) are given below.

Jan R Heck et al. 'Label-Free Monitoring of Proteins in Optofluidic Hollow-Core Photonic Crystal Fibres'. In: *Methods and Applications in Fluorescence* 10.4 (1st Oct. 2022), p. 045008. ISSN: 2050-6120. DOI: 10.1088/2050-6120/ac9113

This publication describes the work primarily covered in Chapter 3.

Jan R. Heck et al. 'Label-Free Detection of Proteins with Optofluidic Hollow-Core Photonic Crystal Fibre Sensors'. In: *SPIE Future Sensing Technologies 2023*. SPIE Future Sensing Technologies. Ed. by Osamu Matoba, Christopher R. Valenta and Joseph A. Shaw. Yokohama, Japan: SPIE, 22nd May 2023, p. 12. ISBN: 978-1-5106-5722-9. DOI: 10.1117/12.2643905

Published in the proceedings of the SPIE Future Sensing Technologies 2023 conference held in Japan. This publication is based on the talk presented there, which showed and put into context work presented throughout this dissertation.

Jan R. Heck et al. (*in preparation*)

The results of Chapter 4 and Chapter 6 are being prepared for publication.

The publication below falls into the time of my PhD studies, but does not form a part of the core body of work presented in this dissertation.

Vasileios Tsoutsouras et al. 'The Laplace Microarchitecture for Tracking Data Uncertainty'. In: *IEEE Micro* 42.4 (1st July 2022), pp. 78–86. ISSN: 0272-1732, 1937-4143. DOI: 10.1109/MM.2022.3166067

This work resulted from a research project during my research assistant position in the group of Prof. Phillip Stanley-Marbell in the Department of Electrical Engineering.

Further publications currently in preparation resulting from research carried out during the PhD, but not covered in this dissertation, are not listed here.

Pre.4 Conference presentations

The work of this dissertation was presented at different conferences, the most relevant of which are listed below in chronological order.

- At the Cavendish Graduate Student Conference 2021 (UK), I presented a poster for which I received the Best Poster prize. (*link*)

- At the 17$^{\text{th}}$ Conference on Methods and Applications in Fluorescence 2022 (Sweden), I presented a poster. (*link*)

- At the Sensors Day 2022 (UK), I presented a talk for which I was awarded the Best Talk prize. (*link*)

- At the Centre for Physical Biology Annual Meeting 2022 (UK), I presented a poster. (*link*)

- At the 2022 Launch Symposium for the Precision Health Initiative (UK), I presented a poster. (*link*)

- At SPIE Future Sensing Technologies 2023 (Japan), I presented a talk. I received a SPIE student award to support my travel, and the presentation's contents are covered in a resulting proceedings paper.[2] (*link*)

Pre.5 Abbreviated abstracts

To understand the findings resulting from any extended investigation, be it scientific or otherwise, I feel there is great value in the exercise of distilling one's thoughts down to fewer and fewer words, retaining their essential core at each step. An attempt at this is as follows.

One page

As included earlier in the front matter.

One paragraph

With new techniques based on photonic waveguides that provide guidance along a microfluidic channel, we can collect and guide light in extended microfluidic geometries. This allows us to increase the light–matter interaction in our experiments, which becomes a way of increasing the sensitivity of optical detection, while still using only microscopic amounts of sample. We describe and explore these techniques, how they operate, and how we built them. Specifically, we review the relevant literature and explain the physical principles that underlie these optofluidic waveguides, before demonstrating their use in the detection of proteins. We do so without the use of added contrast-enhancing fluorescent labels. These label-free methods are increasingly sought after, as the labels have been shown to change how proteins behave.

One sentence

Optofluidic waveguides combine photonic and microfluidic technologies to open up new ways of studying proteins, doing so without the need for contrast-enhancing labels that potentially disturb their behaviour.

One line

Light, when guided inside liquid, can help us look at proteins in new ways.

Three words

Light, Liquid, Life.

1 | Context

We begin by setting out the context from which this dissertation and its research emerge: the motivation behind it, the relevant literature, as well as practical considerations surrounding the PhD. Thereby, together with the next chapter covering background and theory, this chapter lays the groundwork for the later experimental chapters.

1.1 Motivation 22
1.2 Literature 25
1.2.1 Label-free optical detection of proteins 25
1.2.2 HC-PCF for biophysical sensing 42
1.2.3 Label-free detection of proteins in HC-PCF 49
1.2.4 Summary 55
1.3 Practical considerations 56

1.1 Motivation

Seeing is believing

Optical measurements are, quite commonly, the preferred means of elucidating physical phenomena. From the microscope[4] to the telescope,[5] newly-discovered optical techniques have not only sharpened our observations, but unlocked entirely new worlds to be discovered.

Proteins are life

As the building blocks from which all known life is made, proteins attract an accordingly large amount of research devoted to finding new methods for scientific measurements to be performed on them, both historic[6] and current.[7]

Studying proteins ex-situ

Among these methods are techniques originating from all disciplines of physics and beyond. Historically, some of the earliest achievements in understanding what proteins are made of and what they look like (their composition and structure) came from mass spectroscopy analysis[8][9] and X-ray crystallography.[10][11] These and other analytical techniques have been and continue to be crucial in understanding proteins on the atomic level. However, as ex-situ techniques, they are inherently incompatible with studying proteins undisturbed and in their native state, which is only possible in liquid environments.

In-situ optical and microfluidic measurements

Then, to study proteins in liquid and under native, possibly even living conditions, optical methods become a preferred choice and form one of the backbones of today's biological science.[6][12][13][14] Optical detection generally does not affect the system under study significantly, given the irradiation power and deposited dose is limited, as is typically achievable. Furthermore, for any detection method, its usefulness increases with our ability to integrate the measurement setup into other systems.[15] In the case of proteins, the systems that we use to efficiently contain and manipulate dissolved proteins are increasingly microfluidic ones, making integration with microfluidic systems and operation on microfluidic volumes a key requirement.[16]

Why the optical detection of proteins is challenging

Proteins, however, remain challenging to observe optically for several reasons. First, they are small, typically smaller than 10 nm. Second, they have low refractive index contrast ($\mathrm{d}n/\mathrm{d}c = (1.899 \pm 0.003) \times 10^{-4}\,\mathrm{L\,g^{-1}}$ for the human proteome[17]). Both of these facts combine to give proteins a small scattering cross section, making them nearly transparent in aqueous solutions. In standard light microscopy, they appear invisible unless present in high concentration. When measuring a protein solution in bulk, the commonly used techniques to quantify optical extinction within cuvettes (UV-VIS spectrometers) require a large (millilitre-scale) volume of sample to yield a sufficiently long optical path-

length and in turn a strong enough signal. However, protein measurements often happen at both low concentration and low volume, such that their optical detection remains challenging.

Fluorescent labels

To overcome these limitations, fluorescent detection with labels is arguably the gold standard of protein science, and its impact on the field can hardly be overstated.[12][18] The advent of highly optimised fluorophore labels that can be added as stains or dyes, yet even more so the advent of the green fluorescent protein beginning some three decades ago[19] that spawned many engineered derivatives[12] have unlocked a level of specificity and sensitivity that was not possible before. Where the proteins to be studied are synthesised artificially, these fluorophores can be genetically incorporated, making the label an integral part of the protein under study.

Label-free methods

These approaches, in turn, bring new challenges. Recent literature has shown that the addition of fluorophores alters protein behaviour.[20][21][22] Specifically, studies show that labels bind to positions that are important in different protein aggregation or misfolding pathways, leading to steric hindrance.[23][24][25] Despite the great sensitivities and specificities afforded by labelling, this has lead to increased interest in using label-free methods for the study of protein-protein interactions.

Intrinsic fluorescence

One possibility to perform label-free measurements is to use the fact that proteins can contain natural fluorophores. Of these, the most significant one is the amino acid tryptophan.[26] With an abundance in the human proteome of ca. 1%,[27] most proteins (which are typically hundreds of amino acids in length) are likely to contain at least one tryptophan and hence can be detected by their intrinsic fluorescence. On the other hand, intrinsic fluorescence (unlike the purposely engineered highly-optimised labels) has a low quantum yield and is easily quenched. The excitation wavelength of tryptophan (280 nm) is in the deep ultraviolet, where many (especially polymer-based) materials exhibit background fluorescence. Even regular (non-quartz) glass effectively blocks these wavelengths, complicating experimental design.

Extinction

Similarly, techniques commonly used in larger volumes such as UV-VIS extinction measurements do not necessarily translate easily to microfluidic sizes. Since extinction-based measurements scale with optical pathlength, measurements across a microfluidic channel will have pathlengths on the order of 10 µm, and hence signals, of $1000\times$ less than standard cuvettes at 1 cm. If measurements are instead done along the channel instead of across it, a plain microfluidic chan-

nel will not guide light and therefore incur losses that scale with length. This counteracts the attempted increase in signal by extending the pathlength, besides adding engineering constraints of providing perpendicular optical access at both ends of the channel.

The need for new methods

These challenges of translating macroscopic techniques to microfluidic ones, detecting proteins label-free at both low volumes and concentrations, form a demand for new approaches. Furthermore, no single technique will be suitable for all experiments. Instead, many different techniques are required, and in particular there is a need for those that are versatile and easily combined to become an integrated sensing platform.

Hollow-Core Photonic Crystal Fibres

Hollow-Core Photonic Crystal Fibres (HC-PCFs) are a candidate for this. As optofluidic waveguides, HC-PCFs collect and confine light in microfluidic channels by microstructured sub-wavelength features surrounding a hollow core. The HC-PCF as used in this dissertation forms antiresonantly-guiding $30\,\mu m$ microfluidic channels, which we use in lengths of over ten centimetres, an aspect ratio of more than 1000. Through the low-loss guidance of HC-PCFs, which unifies the light-guiding and liquid-flowing channels to be the same region of space (an inherently optofluidic system), high light–matter interaction can be achieved. Offering the potential to enable higher sensitivities and new detection mechanisms, HC-PCF are being explored as new sensing platforms in a variety of research fields. This dissertation and its research aim to explore and apply HC-PCFs for developing new measurement techniques in biophysics, and in particular to the label-free detection of proteins in microfluidic systems.

Dissertation outline

The structure of this dissertation is as follows. In the remainder of this chapter, we expand on these thoughts and review key literature with a view towards the label-free, optical detection of proteins within HC-PCF. Next, Chapter 2 is devoted to the theoretical underpinnings and experimental methods of our work, before the following four chapters detail different experimental studies conducted during this PhD. There, we develop and demonstrate the experimental use of HC-PCF in the ultraviolet for the collection of intrinsic protein fluorescence (Chapter 3) or the measurement of optical extinction of nanosized protein aggregates (Chapter 4), a technique that we show to be adaptable to minimal requirements of sample volume (Chapter 5). Finally, we demonstrate a combined application of these techniques by monitoring the aggregation of a silk protein solution over several days in both extinction and fluorescence (Chapter 6).

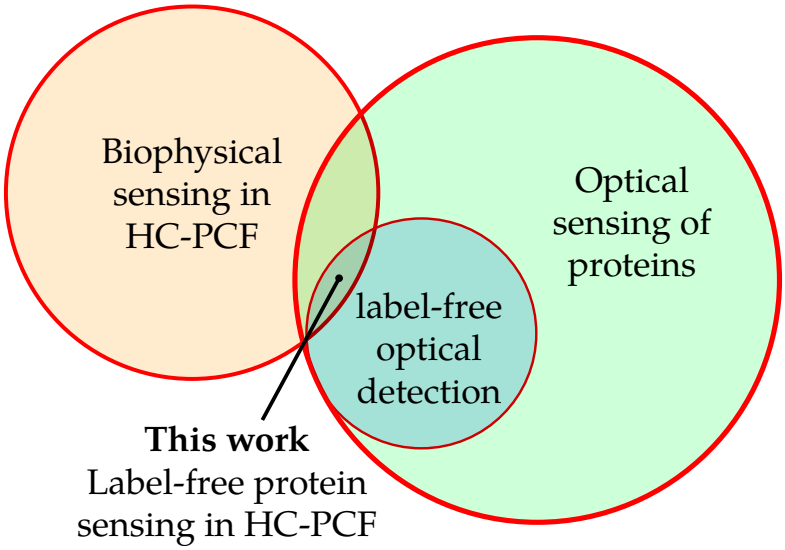

Fig. 1.1 Venn diagram outlining the scope and structure of the literature review, identifying the position of this dissertation. Sizes are qualitative. (*Fig. first referenced on p. 25*)

1.2 Literature

Outline of literature review

To give context to our work, we now review the literature systematically as laid out in Fig. 1.1. We begin by reviewing methods for the label-free optical detection of proteins, followed by HC-PCF for optical sensing with applications in biophysics. These two topics then meet, which narrows down the scope to the label-free optical detection of proteins in HC-PCF, which is the topic of this present dissertation.

1.2.1 Label-free optical detection of proteins

The interaction of light with biological macromolecules, and proteins in particular, can shed light on a number of physical properties.[28][29] Optical measurements are able to probe proteins in a native environment, i.e. freely suspended in liquid, which in turn allows the study of the dynamic, stateful nature of proteins.[30] The light–matter interaction interrogates their internal conformation in addition to their molecular orientation. In this part, we consider the label-free detection of proteins, first outside of HC-PCF (which will be treated later in Section 1.2.3). We do, however, review the literature with a view to how amenable the methods are to be performed within a HC-PCF geometry.

Scope of review

In this section, we include works that use *all-optical* methods for the *label-free* detection of *proteins* in *liquids*. In other words, we explicitly exclude from this the use of optical methods adjunct to a non-optical measurement (e.g. optical methods to read out another sensor, or to photo-activate molecules for a different measurement[31]), methods that use fluorescently labelled proteins or otherwise require them to interact with another object (e.g. SERS), and any methods that do not operate under standard room temperature and pressure inside a water or buffer solution.

Motivation for label-free protein detection methods

Labels: why not?

Labels have significant advantages in terms of sensitivity and specificity over label-free methods, which we discuss and quantify later in this chapter. If labels are of generally better optical brightness and contrast, the need for label-free methods must be motivated by the shortcomings of these labels. It is therefore prudent to first ask what these shortcomings are. Three key reasons can be identified why one might not use labels: because of their potentially complex interactions with the system under study; to avoid the added system complexity incurred by the labelling process (e.g. genetic engineering); and to keep the proteins unmodified since the environment requires it (e.g. detection in-vivo).

Protein aggregation

Of the systems where labels interfere with protein behaviour, we focus on protein-protein interactions in the form of aggregation. Aggregation is the process of proteins forming larger complexes that are more energetically favourable. We focus on the aspects relevant to motivate label-free methods, but note that the mechanisms, detection, and (possibly pharmacological) control of aggregates is an active research field.[32] For the case of silk protein, as used in our own aggregation experiments, these mechanisms are discussed in more detail in Chapter 6 where these experiments are carried out.

In general, the primary motivation for detecting low concentrations of aggregation-prone proteins is to allow their aggregation kinetics to be monitored from earlier stages of nucleation.[33][34][35] In turn, this can yield new insights into what triggers these initial events that set off aggregation, or accelerate its progress significantly.

Effect of labels on aggregation

The dominant mechanism by which labels interfere with aggregation is steric hindrance.[23][24] When a label is present at (covalently attached or electrostatically bound to) a site that contributes to the protein's aggregation kinetics, a

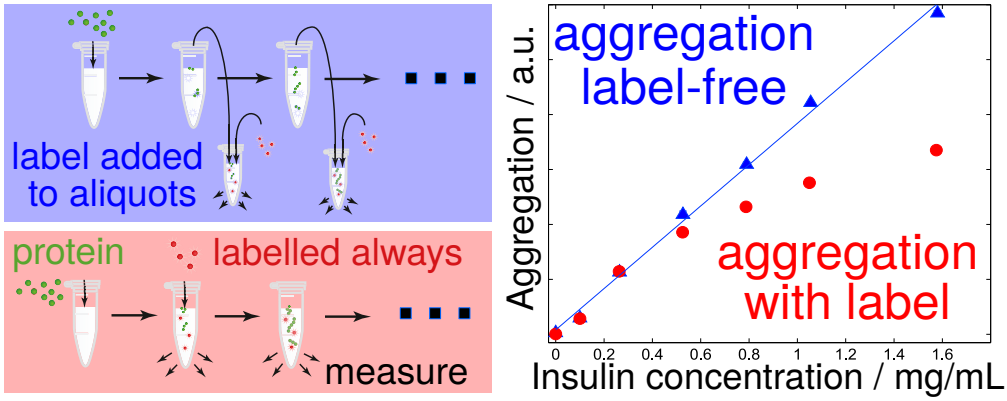

Fig. 1.2 The effect of labels on protein aggregation studied by Saar *et al.*[20] The method schematically shown on the left side was performed in an automated fashion in microfluidic chips, leading to the results on the right. The authors measured the aggregation state of insulin protein using an aggregation-indicating fluorophore label. The label is added either to an aliquot just prior to each measurement (blue), or at the start of the entire aggregation experiment (red). The difference shows that labels interfere with aggregation kinetics. Figure compiled and adapted from [20]. (*Fig. first referenced on p. 27*)

difference in aggregation between labelled and label-free proteins can occur. This effect has been shown to exist for a range of relevant labels.[25]

To quantify this influence of labels on aggregation, Saar *et al.* performed the following experiment (Fig. 1.2).[20] Insulin was aggregated in basic conditions at pH 2, with 5 % of the protein added as pre-aggregated and fragmented (by sonication) fibrils to act as seeds for the aggregation process. Accelerating the kinetics in this way, the aggregation took place over 10 h. During this time, aliquots were taken from the protein solution, and aggregation measurements performed either manually every few hours, or continually using their automated microfluidic chip.

The aggregation measurements were performed using thioflavin-T (ThT), a commonly used fluorescent probe to measure aggregation state. ThT binds to β-sheets, the relative abundance of which are an indicator for the presence of fibrils, i.e. aggregation.[36][37] When this dye was added at the beginning of the aggregation experiment, the measurement was referred to as *in-situ*; when the dye was added just prior to each measurement, it was *ex-situ*.

The ex-situ measurements were performed both manually, taking individual aliquots at different timepoints (approximately every hour), and with a microfluidic chip. The chip was designed such that the aggregating mixture was brought into

co-laminar flow with the dye solution, and allowed to mix by diffusion before a fluorescence reading was obtained downstream of the dye–protein junction.

Comparing these two kinds of measurements, the aggregation (i.e. the ThT fluorescence) was seen to increase less quickly with the in-situ measurements compared to the ex-situ measurements. Hence, the authors conclude an effect of the labels on the aggregation process.

Connection to disease pathology

Protein aggregation forms the physical basis of several clinical disorders, such as Alzheimer's disease and Parkinson's.[38][39] Proteins are found to have states of lower free energy when forming aggregate pseudo-crystalline structures known as amyloid fibrils.[33] The formation of these fibrils, known as fibrillogenesis,[40] follows an interdependent multiple-stage one-side-leaning equilibrium process. Under carefully controlled laboratory conditions, the individual steps of nucleation, seeding, growth and multiplication can be modelled independently to understand their relative contributions to the aggregation kinetics,[41] while in-vivo many factors such as active regulatory systems complicate the kinetics that determine the speed of aggregation.[42]

Then, in a laboratory-setting aggregation experiment, the simplest model of aggregation is as follows. First, some initial nucleation occurs to create seeds. Then, a cycle begins of repeat multiplication (aggregates fragmenting into smaller pieces) and growth (aggregates growing by the addition of monomers or oligomers).[41] This leads to a competition in mechanism, where the overall replication rate is the product of growth and multiplication rates. This forms a self-catalytic process with kinetics more complex than those seen in common chemical reactions.[43]

Aggregation changing fluorescence

Protein aggregation causes changes in the fluorescence signature of the proteins, as discussed in more detail later. While there are examples of amyloids developing visible fluorescence during aggregation,[44] these are unsuitable to track the early stages of protein aggregation kinetics dominated by mono- and oligomers. Generally, the fluorescence signature will change both in intensity and spectral signature, possibly developing new fluorescence peaks as aggregation progresses.

Summary

Despite continued research on protein misfolding and aggregation, there remain many questions unanswered on both a theoretical and experimental level.[34] The many different molecular mechanisms[35] that play a role in protein–protein interactions require a correspondingly wide range of different experimental approaches to cross-validate results. Increasingly, machine learning approaches[45] are used to tackle the large sample space of protein conforma-

tional states, but these approaches nonetheless require large amounts of ground truth training data to reach their stated goals, only adding to the motivation for high-throughput experimental methods.

Non-fluorescence label-free optical methods

We now review a range of label-free methods commonly used in bulk, with a discussion on how each of them would translate to a microfluidic HC-PCF environment.

UV-VIS extinction

When we hold up an object against the light to look at its colour, we are performing an extinction measurement. Extinction is the combination of absorbance and scattering. Scattering is in the $r \ll \lambda$ Rayleigh scattering regime for proteins ($\sim 5\,\text{nm} \ll 280$ to $400\,\text{nm}$), and hence the scattering cross section scales as λ^{-4}. In the context of label-free protein sensing, the absorbance at 280 nm, if present, will generally dominate over this scattering component (we refer to our experimental data of later chapters, for example Fig. 6.4). Measuring the absorbance at 280 nm is a widely used standard assay for protein concentration due to its simplicity.[46] Nonetheless, there can be reasons to prefer using wavelengths other than 280 nm.

First, the strong absorptivity at 280 nm can be a disadvantage when the absorbance (the product of absorptivity and pathlength) is high enough to leave the transmitted light beneath the noise floor of the experiment, i.e. when the dynamic range of the measurement setup becomes exhausted. If concentrations, as is typically the case, must be chosen according to some biophysical process of interest (and cannot be diluted to reach ideal optical density), this is likely to be the case (as in Fig. 6.4). Using wavelengths that have lower extinction can then actually lead to more sensitive measurements with a higher dynamic range.

Second, as discussed in detail later, the intrinsically fluorescent amino acid tryptophan is a sensitive indicator of its local environment, esp. hydrophobicity. While this has many experimental uses, having a scattering-dominated measurement can be less affected by these changes. If this is the case, this opens up the possibility of using a non-tryptophan wavelength measurement an in-situ reference for the tryptophan fluorescence. This forms the motivation behind developing the experimental techniques of Chapter 4, in turn leading up to allow this reference to be used for the experiments of Chapter 6.

... in HC-PCF

We refer to review articles for the wide range of measurements in HC-PCF that are outside the label-free protein sensing scope of this section.[47][48][49][50][51]

To the best of my knowledge, no label-free extinction-based measurement on proteins in HC-PCF is currently published in the literature. We present our own experimental data in Chapters 4 and 6.

A related but different approach is transmission spectroscopy on proteins in HC-PCF, where proteins adsorb onto the HC-PCF surfaces and change their geometry and hence guidance (transmission) characteristics. Extinction and transmission spectroscopy share the same experimental measurement, but are based on a different sensing principle (Section 1.2.3).

Raman spectroscopy

Raman spectroscopy is a widely used spectroscopic technique, in particular when combined with engineered Raman-enhancing structures, known as surface-enhanced Raman spectroscopy (SERS).[52] Non-SERS, direct Raman scattering is typically weak, whereas SERS can boost signals over many orders of magnitude, making the technique sensitive and versatile in application, albeit reproducibility remains a concern.[53]

For the sensing of biomolecules, a wide range of SERS substrates has been developed to reach enhancement factors exceeding 10^9.[54] Differently-fabricated gold nanoparticles can serve as the Raman equivalent of labels, giving specificity through their different Raman-spectroscopic signatures. These remain distinguishable even in complex local environments, such as within living organisms.[55] Sensing a range of proteins with Raman is possible in the same way.[56]

... in HC-PCF

HC-PCFs have several favourable characteristics that make them useful for Raman spectroscopy. Since HC-PCFs guide light with little overlap of the surrounding glass, the silica Raman background signal is strongly suppressed (in our work, we use the same advantage, where ultraviolet-excited background fluorescence is suppressed). Our group has recently shown this application for monitoring of battery electrolyte chemistry, where the all-optical measurement has the key advantage of leaving the battery's electrochemistry undisturbed, allowing for in-operando studies.[57] Furthermore, strong light–matter interaction gives rise to higher signals. Applied to the sensing of the antibiotic moxifloxacin, Yan *et al.* show that a HC-PCF had a 20 times higher sensitivity compared to a non-fibre measurement, giving a limit of detection of 1.7 μM.[58] The HC-PCF in this work was partially collapsed by fusion splicing to selectively infiltrate only the core. This leaves the cladding holes air-filled, which produces a step-index fibre of broadband guidance.

If using SERS, the substrate that enables the enhancement in Raman scattering can become an integral part of the HC-PCF, for example by functionalising its

inner surfaces. Xia *et al.* have shown HC-PCFs to reach over 5000-fold enhancement over planar geometries in comparable SERS measurements.[59] While SERS enhances the effectiveness of Raman spectroscopy across many orders of magnitude, it requires proteins to be close to a surface (either a channel wall or a co-suspended nanoparticle). This carries many of the same concerns that labels have when altering protein behaviour, a point which will be further discussed in Section 1.2.3.

Circular dichroism

Chirality, i.e. a non-mirror-symmetry on the molecular level, is commonly found to exist in proteins. As polypeptides, they are particularly likely to exhibit chirality through one of their two main elements, the α-helix, which generally forms right-hand spirals.[60] When such a chiral molecule interacts with light, the interaction cross section depends strongly on the polarisation of the light relative to the molecular orientation. On the ensemble (bulk) scale, this can be analysed by polarisation spectroscopy.[61][62] In the most common form, circularly-polarised light is used, and the resulting measurement is known as a circular dichroism (CD) spectrum. The use of circular dichroism for protein characterisation is a sufficiently established technique for there to be compiled reference databases to compare against.[63] While UV light circular dichroism remains the most popular form, the underlying principle translates to other parts of the electromagnetic spectrum, where different molecular energy scales can be probed.[64] In addition to direct absorbance circular dichroism, the technique can also be applied to the fluorescence emitted when excited by polarised light,[65] which can be combined with intrinsic fluorescence measurements of proteins.[66]

... in HC-PCF

Circular dichroism is being explored in HC-PCF, both in kagome-type HC-PCF[67] or by creating specialised fibres through twisted drawing[68][69] or nested antiresonant elements[70] that prevent cross-coupling between guided polarisations. The use of circular dichroism for this dissertation was not explored further as we did not have access to a polarised ultraviolet light source (or one bright enough to polarise its output by rejecting all but one polarisation); and the polarisation-maintaining nature of our particular HC-PCF is expected to be poor due to modal mixing.

Photon correlation spectroscopy: PCS, DLS, FCS

Photon correlation spectroscopy (PCS) is a common technique to determine the size distribution of particles in solution.[71][72][73] The technique is based on autocorrelation, where the self-similarity of the signal over time can be related to the particles' diffusive movement over time.

The correlation being analysed is generally either from a scattering signal, where the technique is known as dynamic light scattering (DLS); or from fluorescence intensity fluctuations, known as fluorescence correlation spectroscopy (FCS). The underlying concept and numerical analysis remain substantially the same, but the physical measurement being recorded differs between the two.

... in HC-PCF

An application of FCS using a HC-PCF is shown by Ghenuche *et al.*[74] In their work, the HC-PCF remains air-filled and serves to deliver and collect light, with a polystyrene bead at its tip used to focus light into a sample solution reservoir. Since the sensing does not take place within the HC-PCF, their approach differs somewhat from the one described above, but remains a valuable demonstration of the concept using HC-PCFs.

Simulation of PCS in HC-PCF

To study and evaluate the suitability of performing FCS on proteins inside HC-PCF, a diffusion simulation for our experimental conditions was written. It simulates and plots the diffusion of particles, tracks the change in signal over time, finds the autocorrelation, and finally fits the measured signal to an exponential decay. The discussion of this simulation work is deferred to the following chapter covering molecular transport in HC-PCF, Section 2.3.2.

Single molecule approaches

For label-free optical measurements of proteins, single molecule microscopy forms a large and varied field. While a full review is beyond the scope of this work, we will review some recent developments and consider the different meanings of 'detection sensitivity' in this context as they relate to our own research.

iSCAT

The first optical label-free single molecule observation of a protein in solution was achieved by the creation of a technique known as iSCAT (interferometric scattering microscopy)[75] on the motor protein myosin 5a.[76] The technique uses the backreflection from a coverslip, which in standard (darkfield) microscopy is a source of background noise, as a carrier wave onto which the light scattered from particles is superimposed by interference. As long as this background remains static (which can be achieved post-experiment through averaging at the cost of temporal resolution), the scaling of the iSCAT interference term ($\sim \sigma_{\mathrm{bkg}} \cdot \sigma_{\mathrm{s}}$) is more favourable at lower sizes than direct scatter ($\sim \sigma_{\mathrm{s}}^2$).[77]

iSCAT for smaller proteins

iSCAT has since been applied to the label-free imaging detection of cancer marker proteins[78] and integrated with other techniques[79] Recent improvements in the technique have allowed quantitative calibration of the interferometric contrast, which can be correlated to the proteins' masses. Young *et al.*

experimentally validate this technique, known as interferometric scattering mass spectroscopy. They demonstrate a linear relationship between contrast and protein size down to streptavidin-biotin complexes (ca. 55 kDa), with a mass error of below 10%, and in the single-digit range for larger proteins.[80] This technique relies on the specific refractive index of proteins being nearly constant (cf. Section 1.2.3), which makes the scattering signal scale linearly with its size (number of peptides).[80]

Non-imaging iSCAT

While iSCAT is generally known as an imaging label-free microscopy technique, its principle can be adapted to non-imaging measurements. For example, performing interferometric backscatter analysis downstream on an electrophoresis microfluidic chip to inject and separate protein mixtures, Wang *et al.* show a label-free detection of 7.5 μM bovine serum albumin protein, and estimate the resulting limit of detection as 240 nM for a SNR of 3σ.[81]

What makes detection 'sensitive'?

Single molecule label-free microscopy is, in some sense, the ultimate level of sensitivity that can be achieved. However, all measurement approaches come with different trade-offs. In the case of highly-sensitive single molecule measurements, data is only obtained from a small fraction of the sample under study.

For example, in the approaches described below, the detection volume is within a few wavelengths of a surface (typically a microscope coverslip) and within the lateral field of view of a $100\times$ objective-based microscope. Even for small microfluidic volumes (say, a channel of 50 μm height), this detection volume will be less than 1% of the sample volume for the ideal case where the lateral extension of the field of view matches the microfluidic channel length without edge effects, i.e. the whole channel is observed at once (estimating as $\lambda \sim 500\,\mathrm{nm} / d \sim 50\,\mu\mathrm{m} = 0.01$). If the measurement can be done continuously, diffusion will increase the fraction of molecules that have crossed the detection volume and are potentially observed, but the fact that only a tiny fraction is observed at any given time remains unchanged. Conversely, if the system is operated with the sample flowing past in a microfluidic channel, most of the sample will remain unobserved.

The right tool for the right experiment

For many experiments, these points notwithstanding, single molecule measurements remain an invaluable experimental tool in biophysics, such as for performing time-resolved studies of proteins as they bind to an antibody, change in conformation or undergo protein-protein interactions. Generally speaking, single molecule approaches are ideal for in-depth mechanistic insights from a

single part, but less so for quantifying the concentration of a solution as a whole, as we do in this work.

Finally, we note that (trivially) single molecule experiments are inherently single molecule sensitive, and consequently a large body of work concerns itself with optimal surface and sample preparation strategies to avoid even minute contamination on a molecular level and improve reproducibility.[82] Trace contamination can persist even after application of aggressive cleaning techniques.[83]

Long-term observations

Even if the above limitation of only observing a small fraction of the sample is acceptable, there is another consideration regarding extended investigations over time. At the nanometre lengthscale defined by proteins, Brownian motion is unavoidable when working in a near-room-temperature liquid.[84] When a laser beam is focussed down, the focal volume will capture a part of the sample volume (without exact boundaries). Except for very short measurements, proteins will diffuse in and out of the focal volume. If the detector being used supports fast acquisitions, the exposure time can be reduced to limit the proteins diffusive motion to within the field of view. However, the amount of light captured during an exposure is inversely proportional to the exposure time. This, in turn, requires increased illumination (if possible) to retain the same amount of signal. Increased irradiation must be balanced with the risk of phototoxicity and photothermal heating. Finally, the most commonly used single molecule technique is fluorescence microscopy, which is further limited in useful brightness by photobleaching of the fluorophores, known as the 'photon budget'.[85]

... by counteracting diffusion

One solution would be to trap proteins in place.[86][87] This allows the same proteins to be imaged repeatedly, revealing time dynamics. However, trapping proteins conflicts with the goal of performing measurements on proteins natively in solution. Where trapping is achieved by geometrical confinement, surface interactions become dominant; where trapping is achieved by forces, for example in optical tweezers enhanced by nanoapertures,[88][89] using tether-beads,[90] or driven by active feedback,[91][92] native-state protein-protein interactions are generally altered from their native behaviour, requiring extra consideration when studying such phenomena.

... by constricted flow

If the flow is constricted to a volume smaller than the detection volume at some point, then all sample passing through this point can be detected over time, even if the sample volume on either side of the constriction is much larger. This is the principle behind Coulter counters.[93][94] On much smaller size scales, nanopore-based sensing uses constrictions on the same lengthscale as biomo-

lecules such as DNA or proteins.[95][96] While nanopores typically operate as a electrical (transconductance) measurements, recent research combines them with plasmonic nanostructures that greatly enhance light–matter interaction strengths, enabling label-free optical measurements in-situ at the nanopore opening.[97]

... by increasing the detection volume

Finally, if the proteins are to remain freely diffusing over long periods of observation time ($2\sqrt{Dt} \ll$ channel size), the detection volume has to be increased to accommodate the entire region explored by the protein via diffusive movement. This is one of the reasons that motivates the use of waveguides in microfluidics, where their long-pathlength guidance increases the detection volume to some large fraction of the sample volume compared to point-focussed imaging. As discussed and simulated in Section 2.3.2, the lengthscale of protein diffusion compared to the length of the irradiated HC-PCF length is negligible. Hence, proteins in the centre of a HC-PCF several centimetres long will stay confined to the irradiated detection volume practically indefinitely, with free diffusion only limited by the diameter of the microfluidic channel.

Intrinsic fluorescence

Fluorescence for protein detection

Fluorescence spectroscopy and microscopy are highly effective methods for the optical detection and study of proteins.[98][99][100] Fluorescent labelling of proteins allows for both high specificity and sensitivity. The fluorophore label is either covalently attached, van-der-Waals bonded, or directly incorporated into the protein by genetic modification, such that the fluorophore is expressed during protein synthesis.[18]

However, as discussed in Section 1.2.1, recent research has shown that fluorescent labelling can significantly alter protein behaviour, such as inhibition of aggregation. This is of particular importance for the study of small proteins, where the relative label size becomes non-negligible and affects their mobility and reactivity.

Origin of intrinsic fluorescence

Many proteins exhibit intrinsic fluorescence (synonymous: autofluorescence) due to their chemical structure.[13] Most commonly, these will be proteins that include one or more of the aromatic residues listed in Table 1.1, with their individual fluorescence characteristics given in Fig. 1.5. For the main fluorophore of this dissertation, the chemical origin of the fluorescence is shown in Fig. 1.3.

While these aromatic acids offer a conveniently 'intrinsically labelled' means of detection, they are naturally-present fluorophores. Unlike the extrinsic artificial labels, they do not benefit from the decades of targeted research and industrial

Amino acid	Absorption characteristics (molar absorptivity ε and λ_{exc})	Fluorescence emission (quantum yield and λ_{ems})
Tryptophan	5600 mol^{-1} cm^{-1} @ 280 nm	0.20 @ 348 nm
Tyrosine	1400 mol^{-1} cm^{-1} @ 274 nm	0.14 @ 303 nm
Phenyl alanine	200 mol^{-1} cm^{-1} @ 257 nm	0.04 @ 282 nm

Tbl. 1.1 Fluorescence properties of aromatic amino acids. Tryptophan is the most widely used source of intrinsic fluorescence due to its comparatively strong fluorescence (the highest product of absorptivity and quantum yield), comparatively large spectral separation of excitation and emission (reduced inner filter effect), and the highest excitation wavelength, where generally brighter light sources are available. Data are from [26]. (*Table first referenced on p. 35*)

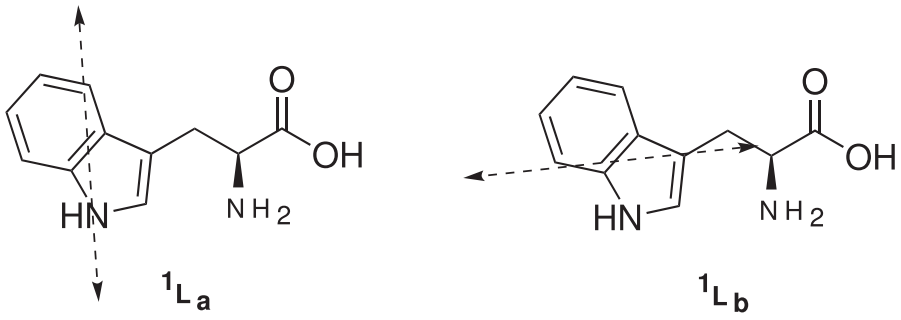

Fig. 1.3 Chemical structure of tryptophan, showing the two electronic absorption transitions involving the aromatic ring system that give it its fluorescence. Adapted from [26]. (*Fig. first referenced on p. 35*)

development to improve their suitability for fluorescence experiments, such as high brightness, resistance to photobleaching, large spectral separation between excitation and emission, convenient wavelengths in the visible range, specific attachment, and others.

Comparing label-free intrinsic fluorescence to extrinsic labels

To understand the magnitude of this difference, we can compare the commonly used commercial fluorescent label atto488 with tryptophan (as a first estimate, as the act of labelling will change the fluorophore's activity). The brightness of a fluorophore can be specified as the product of absorptivity and its emission quantum yield, which taken together give the fraction of light emitted as fluorescence relative to the incoming light (ignoring re-absorption, also known as inner filter effect) at a given concentration and pathlength, as described by the

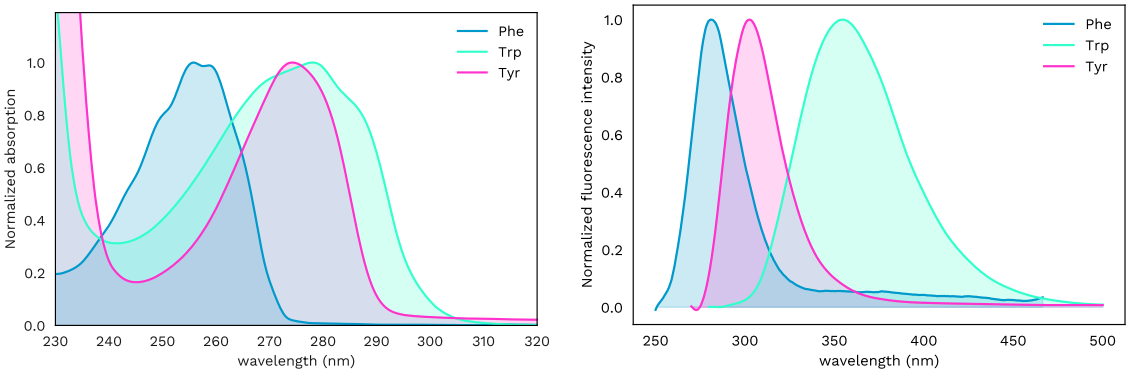

(a) Absorbance spectra (b) Fluorescence spectra

Fig. 1.5 Absorbance and fluorescence spectra of the intrinsically fluorescent amino acids. The values are plotted normalised, but differ significantly in absolute value (tabulated in Table 1.1). Adapted with permission from Labbot (Probation Labs Sweden AB) (*link*).
(*Fig. first referenced on p. 35*)

Beer-Lambert law. The comparison then becomes:

for the **extrinsic label atto488**: ref. [101]

$$900\,000\,\mathrm{mol}^{-1}\,\mathrm{cm}^{-1} \cdot 0.80 = 72\,000\,\mathrm{mol}^{-1}\,\mathrm{cm}^{-1}, \tag{1.2.1}$$

for the **intrinsic fluorophore tryptophan**: ref. [26]

$$5600\,\mathrm{mol}^{-1}\,\mathrm{cm}^{-1} \cdot 0.20 = 1120\,\mathrm{mol}^{-1}\,\mathrm{cm}^{-1}, \tag{1.2.2}$$

making the extrinsic, engineered fluorophore atto488 over fifty times brighter than the intrinsic fluorophore tryptophan. This is a conservative estimate, as atto488 further benefits from the fact that light sources, optics and detectors will all be much more widely available and (cost-)effective at the visible wavelength of atto488 compared to the ultraviolet wavelengths of tryptophan. Furthermore, extrinsic labelling density is under the control of the experimenter, such that the concentration of atto488 relative to the concentration of the target protein can be increased manyfold compared to tryptophan, which occurs naturally at a fixed relative abundance. The achievable extrinsic labelling density is only limited by the protein–label chemistry, with the important caveat that the system under study will be increasingly affected by the labels, as discussed in Section 1.2.1.

From this back-of-the-envelope comparison, it can be concluded that extrinsic labels are at least two orders of magnitude more sensitive than intrinsic labels.

Another advantage of labels is that the experimenter is not limited to using a single type of fluorophore as with intrinsic fluorescence.[102] By attaching different labels, specificity can be achieved at the same time as increasing sensitivity, limited primarily by spectral bandwidth. The number of suitable labels is large and well-characterised, especially for super-resolution imaging,[103] and spectral bandwidth can be increased further by using two-photon excitation.[104] By using DNA as a carrier for the fluorophore label, such as in DNA-PAINT super-resolution imaging, ligand-binding specificity and number of possible targets becomes increasingly large, limited in practice only by synthesis costs and number of washing steps.[105][106]

Scarcity of intrinsic fluorophores

In addition to much lower sensitivities, as naturally occurring fluorophores, the fluorescent aromatic acids in proteins are irregularly distributed(note 1) across the protein's molecular structure in both number and position. Different positions lead to buried or solvent-exposed fluorophores that alter or quench fluorescence.

Notably, the actual number of intrinsically fluorescent proteins in biology is less than one percent when compared on a molar basis.[13] However, this statistic is not representative for the proteins commonly studied in a laboratory context, as the proteins of high scientific or medical interest are typically more complex (large) and therefore likely to contain one of the above aromatic acids.

Tryptophan as the most suitable intrinsic fluorophore

Out of the aromatic acids in Table 1.1, tryptophan-induced intrinsic fluorescence in particular is used to probe conformation. The tryptophan's exposure to the solvent (quenching) and reachability by the excitation light strongly affect fluorescence.[107] This allows information on the location of tryptophan within the protein to be extracted from fluorescence intensity and wavelength shift, thereby revealing the protein's conformational state.[26][108][109] Using a pH far from physiological values (highly basic or acidic) is also seen to increase fluorescence intensity by an order of magnitude,[110] but is of less biological relevance as the proteins are in a denatured state.

Engineering challenges of ultraviolet fluorescence

When using ultraviolet light (280 nm for tryptophan excitation), many materials will exhibit a fluorescence signature even if they are non-fluorescent at higher wavelengths. Polymeric materials in particular show this effect, which includes plastics. In particular, the polydimethylsiloxane (PDMS) polymer in microfluidic chips shows strong fluorescence, posing particular challenges to

note 1 'Irregular' if, for the purposes of optical detection of a given protein, we remain naive as to the biological origins for this distribution. Of course, the question as to where and why aromatic acids exist in a particular protein can be studied to give meaning to this distribution, and is key to a functional understanding of proteins and their molecular dynamics.

intrinsic fluorescence measurements in microfluidic systems produced by soft lithography.

While polymers are especially strong absorbers of ultraviolet light, even regular glasses that are not pure quartz (fused silica) absorb strongly below 300 nm. This makes HC-PCFs particularly well suited to UV applications, as the guided mode has only small overlap with the surrounding silica, leading to significantly reduced light–silica interaction. Furthermore, since the HC-PCF in this dissertation are manufactured entirely from fused silica, whatever light does enter the glass results in relatively low background fluorescence.

Finally, ultraviolet light sources, detectors and optics are generally more expensive and less performant than their visible-wavelength equivalents.

All of the above combine to form engineering challenges in designing suitable experimental setups for intrinsic fluorescence measurements on low volume and concentration protein samples. Different strategies have been employed to overcome these challenges.

Fluorescence microscopy with intrinsic fluorescence

For example, Challa *et al.* were able to achieve a limit of detection of 500 nM for bovine serum albumin (BSA) in a custom-built fluorescence microscope observing PDMS microfluidic chips.[111] The microscope used a 280 nm LED collimated to provide the excitation light, and the resulting intrinsic fluorescence was observed via a dichroic. To enable their detection, two improvements were key. First, they developed and employed custom background-subtraction algorithms that produce a pseudo-static average over time. Second, they added carbon black powder to the PDMS to reduce its fluorescence signature. The latter makes the PDMS polymer much less adhesive to the glass surface (by adding impurities that interfere with the plasma-activated bonding process), which leads to frequent device failures, while also making the handling and inspection of the now opaque microfluidic chips more difficult.

By comparison, at much higher concentrations and in aggregated states (fibrils), 6.9 mM lysozyme was observed label-free using a similar experimental setup but without the need for background subtraction, enabling real-time observation. Aggregation was performed over at least 10 h of incubation at 60 °C in a microdroplet array, which was then imaged directly by a UV microscope.[21]

When the absorbance of a sample does not need to be measured absolutely, but only its relative concentration across a region of space is required, the above approach can be adapted without the need for carbon black or background-subtraction algorithms. Saar *et al.* used this for the label-free detection and

sizing of BSA and lysozyme proteins in a microfluidic chip by combining an electrophoretic separation step with a diffusional sizing element.[112] The fits the diffusion profiles observed by label-free intrinsic fluorescence at different points of the microfluidic channel, corresponding to different amounts of time during which the protein was allowed to diffuse orthogonally to its flow direction. This has the advantage of not requiring an absolute concentration measurement, but only a concentration gradient which can be background-subtracted locally. The measurements were performed at comparatively high concentrations of 100 μM, with the authors assessing that their setup should still perform acceptably at a tenth of this concentration.

Below 280 nm

While tryptophan fluorescence is the most widely used, it is possible to target the other fluorophores of Table 1.1 with added complexity. Using a custom-designed compound objective that integrates the laser delivery, and a fused-silica microfluidic chip, Schulze *et al.* were able to perform intrinsic fluorescence measurements at 266 nm excitation.[113] In this wavelength range, tryptophan fluorescence combines with tyrosine fluorescence due to overlapping emission bands and by FRET coupling (discussed below in Section 1.2.1). Lysozyme was detected label-free at 900 nM.

Visible-wavelength intrinsic fluorescence

Finally, we mention that proteins aggregated into a fibrillar state can develop intrinsic fluorescence at visible wavelengths.[30][44] For example, one study finds that using an excitation of 405 nm, a fluorescence emission centred around 460 nm is observed.[114] These can be investigated for spectroscopy in HC-PCF, but do not benefit from UV guidance specific to our HC-PCF.

Tryptophan methods

As discussed above, tryptophan combines several favourable characteristics to make it the most commonly used intrinsic fluorophore,[13] and quantifying the concentration of proteins using their ultraviolet (mostly tryptophan) extinction and/or fluorescence is a widely used standard laboratory assay.[115] It is also used in the purification of proteins via crystallisation, before labelling can usefully occur.[116]

Enhancing tryptophan fluorescence

Arguably an intermediate between label-free and labelled fluorescence, there exist ways of enhancing the fluorescence of tryptophan. A straightforward way is to denature the protein. This decreases the exposure of tryptophan to the solvent and hence reduces quenching, leading to an increase of fluorescence that can be over an order of magnitude.[110] However, denaturing proteins is unsuitable to study their native-state behaviour.

Metals can enhance the fluorescence of tryptophan,[27] and this method translates to entire proteins.[117] Ray *et al.* show how an aluminium layer beneath a 5 nm silica spacer layer that avoids direct contact can enhance the intrinsic fluorescence of BSA by a factor of 12.[117] Their experiments show an even greater effect on some proteins, which the authors explain as relating to the location of tryptophan within the protein relative to the aluminium surface. This variable enhancement is a result of two counteracting effects: the metal providing non-radiative decay pathways (i.e. quenching) but also electric field enhancement leading to enhanced fluorescence.[118][119]

Whether such methods are suitable for a given experiment depends on whether the proteins are to be studied in the bulk or in proximity to the surface, possibly even covalently or electrostatically bound to it. Furthermore, the question of whether these methods are label-free depends on the information sought from the experiment, and the specific implementation of the enhancement (nanoparticle or subsurface layer). Since the detection mechanism remains based on an intrinsic fluorescence, these methods can be understood as sensitivity enhancement at the cost of added fabrication complexity.

Tryptophan as an indicator of conformation

Besides quantifying changes in protein concentration, tryptophan can also be used to observe changes in protein conformation at a constant concentration. Several standard laboratory protocols exist for performing such experiments.[120] The location of tryptophan within the protein affects the fluorescence emission in strength, spectrum and lifetime.[110] It is through this mechanism that changes in pH lead to significant changes in the intrinsic fluorescence of proteins.[121]

Tracking conformational changes helps to understand protein dynamics and thereby elucidate functional relationships. Akbar *et al.* show that tryptophan fluorescence can be used as an assay inside cells, where a protein conformation change within an organelle membrane is detected by tryptophan fluorescence quenching.[122] The authors use this to observe the toxic action of insecticides on mitochondria.

Fluorescence mechanism

The fluorescence lifetime of tryptophan in solution[123] and within proteins[124] varies according to their environment, and can be understood as a linear superposition of pure-hydrophobic and pure-hydrophilic lifetimes. The excitation–emission mechanism of tryptophan fluorescence in proteins can be modelled based on the electrostatic interactions of the tryptophan with its local environment, and semi-classical molecular dynamics simulations, which then predict the fluorescence wavelength correctly for a range of proteins.[109]

FRET

Förster resonance energy transfer (FRET) plays a role in the fluorescence of tryptophan.[26] When tyrosine and phenylalanine enter an excited state, this can transfer to an excitation of tryptophan through FRET.[117] Hence, while the fluorophore tryptophan is already the brightest of the three kinds found in proteins (Table 1.1), FRET increases its relative contribution to the total intrinsic fluorescence of proteins even further. This again confirms tryptophan as the target fluorophore of choice for intrinsic protein fluorescence measurements, as any excitation of the lower-wavelength tyrosine and phenylalanine residues will still emit significantly via tryptophan fluorescence.

Tryptophan in BSA

As used in the experiments of this dissertation, the common model protein BSA has a sequence length of 583 polypeptides, of which number 134 and 213 are tryptophans.[108][125] Of these, one tryptophan is close to the surface (where it can experience solvent-induced quenching), and the other tryptophan is buried inside the protein in a hydrophobic environment.[108]

1.2.2 HC-PCF for biophysical sensing

Scope of review

In this section, we include works that use HC-PCF for *in-situ*, *liquid* sensing on *biologically-relevant* samples. In other words, we explicitly exclude from this the use of HC-PCF as ex-situ sensors (i.e. the HC-PCF only serves for light collection or delivery and the sample is outside the HC-PCF), for non-liquid samples (e.g. gases), or without a demonstrated application relevant to biophysics. Meanwhile, HC-PCFs for protein sensing are treated separately in the last part of the literature review, Section 1.2.3.

Introduction

HC-PCF theory: next chapter

We briefly note that this literature review focuses on HC-PCFs for sensing. The physical principles underlying their properties, together with a motivating historical discussion, will be covered in the next chapter (Section 2.1).

Why use HC-PCF for optical sensing?

By enabling low-loss light guidance over long pathlengths in water, HC-PCF increase the detection volume to many orders of magnitude more than a point-focussed Gaussian beam would achieve in a standard microscope, while also possibly capturing a much larger fraction of the sample volume for detection.[47] At the same time, compared to non-waveguiding geometries (i.e. light freely traversing homogeneous media), enhanced pathlengths[48] and the efficient collection[49][50] of light in HC-PCF enable higher sensitivities, reaching down to

attomole levels for fluorimetric detection of fluorescein.[51] Finally, mode-based light guidance[126][127] allows for a more well-defined determination of optical interactions and spatially-resolved measurements. By virtue of their low sample volume and in-situ continuous-flow operation, HC-PCF can integrate with a range of microfluidic applications.[128][129]

General overview of HC-PCF applications

HC-PCFs have been applied to problems in different fields.[130][131][132][133][134] To mention a few selected examples that fall outside the scope of this review but cover relevant experimental techniques, HC-PCF have been applied in experiments on photochemistry,[135][136][137] Raman spectroscopy with reduced background,[57][138][139][140] micro-endoscopy,[141] photothermal gas sensing,[142] strongly enhanced fluorescence collection,[47][74][143] mass spectroscopy integration that enabled low-volume rapid screening,[128][129] biomechanical studies on cells,[144] and the delivery[145] or generation[146] of high-power laser light.

HC-PCFs for studying whole biological organisms

Tracking whole organisms

HC-PCFs can be manufactured in a wide variety of designs (detailed in Section 2.1.2), and this includes size scales large enough to accommodate entire biological organisms, especially phages, viruses, and cells.(note 2) As microscopically-visible objects (even if only as point sources below the diffraction limit), these organisms can be imaged optically, making tracking of individual objects possible.

Medium-sized: Phages

To this end, HC-PCFs have been applied by Förster *et al.* as homogeneously-illuminated microchannels.[147] By imaging their contents orthogonally over a long distance (aspect ratio $\gg 1000$), the Brownian motion of λ-phages (ca. 100 nm, ellipsoidal) inside HC-PCF was detected by direct observation of transverse Rayleigh scatter through the glass cladding using a high-speed camera (Fig. 1.6).

The authors argue the case for HC-PCF as acting effectively like light-line illumination, irradiating the field of view evenly and over distances orders of magnitude longer than the diffusion lengthscale of their object under study. The system results in a sample volume of 400 nL and a light intensity of 20 μW μm^{-2}. With their technique applied to $d = 41$ nm gold nanoparticles, they find a 17 % relative error in the diameter by diffusional sizing. Data was acquired by localising and tracking individual particles from a single 10 s, 1000 frame capture. The authors note the need to correct for liquid flows within the HC-PCF, which they

note 2 We leave aside the question of whether phages or viruses constitute independent organisms or inanimate functional matter.

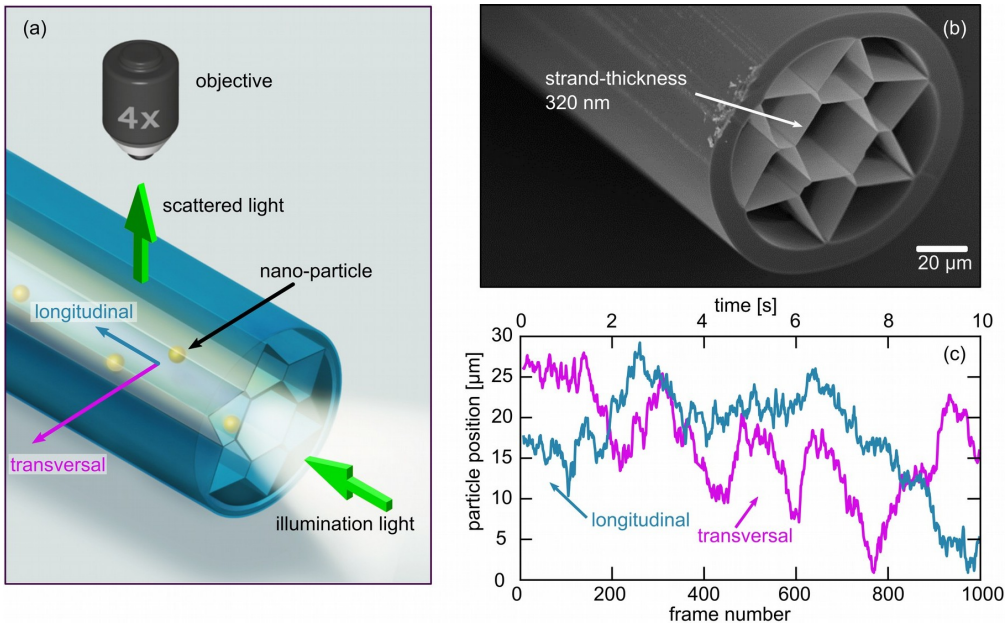

Fig. 1.6 HC-PCFs for optical tracking of Brownian motion by Förster *et al.*[147] Gold nanoparticles ($d = 41\,\text{nm}$) and λ-phages ($d_{\text{head}} = 60\,\text{nm}$, non-spherical) were tracked by observing scattered light through the cladding of a HC-PCF. The resulting trajectories were analysed to yield the particle diffusion dynamics. Figure from [147].
(*Fig. first referenced on p. 43*)

do by subtracting the average motion of all tracked particles, although a more detailed analysis could also take into account the non-uniform flow profile within microfluidic channels.

For tracking of even smaller biological particles such as individual viruses, tapered or nanochannel fibres have been used to observe and track viruses (below 30 nm).[148][149][150] However, these non-HC-PCF geometries use sub-wavelength nanochannels that do not support light guidance, with light transmission inherently leaky. To counteract this, the excitation light is coupled into a much larger total internal reflection fibre core surrounding the nanochannel. Attempts to advance to single-molecule biophysics in waveguides are explored but not yet successful.[151] Tapered fibres suffer from large manufacturing variability, low throughput (usually filled only once by capillary action[149]), and reduced signal transmission as they are leaky waveguides.

Smaller: viruses

As a continuation of the above work, observing even smaller particles inside a optofluidic fibre waveguide was achieved very recently by Wieduwilt *et al.* by translating the approach to a waveguiding geometry.[152] With a custom

antiresonantly-guiding fibre design,[note 3] gold particles down to 9 nm were tracked. They do not apply this technique to biological molecules, which would need to be several times larger to have the same optical cross-section (visibility) as gold nanoparticles of this size.

Larger: Whole cells

On the large end of the lengthscale, entire cells have been observed inside HC-PCF. Building on their earlier work,[153] Khetani *et al.* have used HC-PCF to measure surface-enhanced Raman spectra (SERS) of leukaemia cells mixed with silver nanoparticles.[154] In the spectra, the authors identify a set of broad spectral features with different features, in particular those of lipids and DNA/RNA bases.

While the authors conclude an enhancement factor of 2700 when using the HC-PCF compared to a cuvette, this number was derived from comparing the HC-PCF measurement with nanoparticles to a cuvette measurement without nanoparticles. Hence, the enhancement will be dominated by the SERS enhancement and no immediate conclusion can be drawn as to the advantage of using a HC-PCF for this measurement.

Cell lysates for cancer detection

As a related application, rather than using whole cells, HC-PCF have been applied to cancer detection by screening for target proteins in cell lysates.[155] Padmanabhan *et al.* used a fluorescently labelled sandwich antibody configuration to detect target proteins in cell lysates infiltrated into HC-PCF.[156] Based on tagged antibodies and protein immobilisation, this approach is neither label-free nor does it allow for continuous-flow measurements where the proteins would leave the HC-PCF again, but nonetheless shows the small sample volumes required by HC-PCF (in this work, 50 nL of sample representing 20 pg of protein).

Optical trapping in HC-PCF

Optical tweezers

Optical forces can become significant at microscopic scales, and optical manipulation and trapping has become an established tool in biology in the form of optical tweezers.[86][157][158][159][160] Besides manipulation and trapping, mechanical properties such as the elastic modulus of cells can be probed by stretching them under a known force.[161][162] Amongst the smallest trapped objects in free-

note 3 Elaborated on in Section 2.1.5, the definition of what qualifies as a 'photonic crystal' to have a fibre be named a (HC-)PCF varies across the literature, and with a single capillary providing the guidance in this work, this fibre is arguably not a HC-PCF. Indeed, the authors also do not use the (HC-)PCF terminology, instead denoting their design a 'single antiresonant element fiber'.

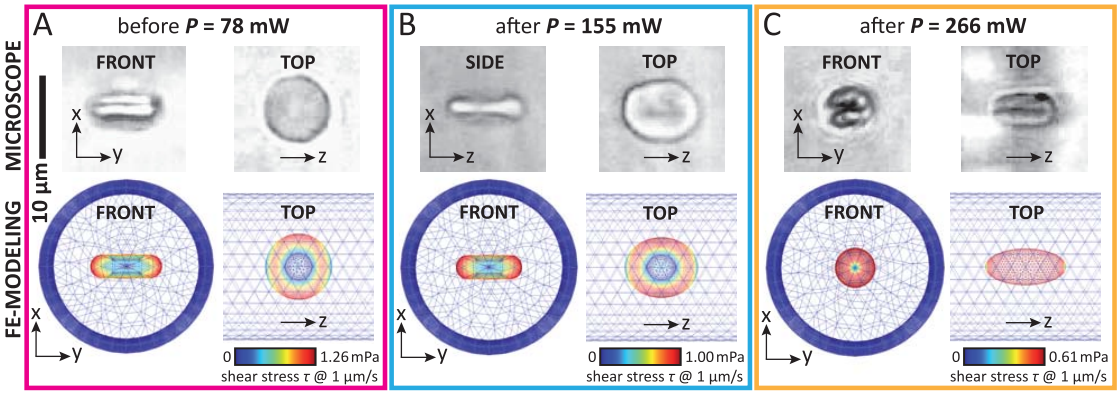

Fig. 1.7 Deformation of red blood cells in HC-PCF by Unterkofler *et al.* A red blood cell is propelled along the HC-PCF, where optical gradient and viscous forces deform it. This was tracked by direct side-imaging (shown here for different powers), and by an optical Doppler measurement to record a change in terminal velocity as the deformed cross-section leads to a change in viscous drag. Figure from [174].
(*Fig. first referenced on p. 46*)

space optical tweezers are viruses with particularly high polarisability due to their molecular structures.[87]

Optical manipulation and sorting

In microfluidic geometries, the concept of optical–viscous force balance is referred to as optical chromatography.[163][164][165] Micrometer-sized polystyrene and silica particles can be separated and sorted,[166][167] or the relative particle concentrations between differently-sized species can be controlled[168][169][170] and separated[171]. Lower particle sizes are accessible by similar techniques in more recent research, reaching down to 100 nm for polystyrene particles (or gold nanoparticles half the size due to their much higher optical cross-section).[172][173]

... within HC-PCF: red blood cells

Within a HC-PCF, optical manipulation can be used for both movement and measurement of microscopic particles. For large enough objects, such as cells, completely optical control and trapping is possible.[126][144][174][175][176]

For example, applying this technique to biomedical measurements, Unterkofler *et al.* showed how red blood cells can be deformed and their force response studied in HC-PCF (Fig. 1.7).[174] They used a bandgap HC-PCF (see Section 2.1.2) at 1064 nm in D_2O (due to its lower absorption compared to plain water). The 7.5 µm red blood cells fill around half the diameter of the 17.5 µm core, before deformation and at coplanar orientation.

A single red blood cell from a dilute solution was moved to the incoupling side HC-PCF core inlet by a standard external optical tweezers microscope, before being propelled through the fibre by the laser beam. The backreflected light from

the red blood cell exits the HC-PCF on the laser incoupling side, where a Doppler measurement is performed to record its velocity.

While a rigid particle would move at constant terminal velocity for a given optical power after a short acceleration phase,[177] the red blood cells change their cross-section as they are deformed by the optical (and, to a lesser extent, thermal) forces. This results in a shift of the equilibrium between viscous drag and photon pressures, leading to a change in terminal velocity. This, in turn, was tracked by the above-mentioned Doppler measurement, giving an experimental indicator of deformability (and re-orientation).

After demonstrations by Guck *et al.* in 2001,[161] similar cell deformability studies have gathered increased interest as label-free and non-destructive (if the elastic deformability limits of the system under study are understood) microfluidic methods for high-throughput cell-level medical diagnostics.[178][179][180]

Smaller particles and biomolecules

For smaller, microscopic particles in microfluidic environments including HC-PCF, a force balance between optical and viscous forces allows particle sizing.[177][181][182][183][184] If such particles are being actively held inside a HC-PCF, they are still affected by external forces such as temperature or magnetic fields, meaning they can be used for indirect sensing of the environment.[185][186]

However, at the even smaller nanometre lengthscale of biomolecules, none of the above techniques succeed due to low interaction cross-sections. One of several methods for enhancing light–matter interaction can be used to overcome this limitation.[86] For example, nanoapertures show thousand-fold enhancement of field strengths, sufficient to enable optical tweezing.[88] However, for the label-free optical detection of proteins as done in this dissertation, the optical forces involved are negligible.

Ultraviolet absorption spectroscopy

Absorption spectroscopy in HC-PCF

Ultraviolet absorption spectroscopy in HC-PCFs has been used by Nissen *et al.* to detect drug molecules at low micromolar concentrations.[187] Shown in Fig. 1.8, their experiment butt-couples a solid-core multimode delivery fibre to a HC-PCF inside a microfluidic chip. A HC-PCF length of 1 m is used for the absorbance measurement, the output of which is again butt-coupled into a solid-core multimode fibre connected to a spectrometer.

The microfluidic chip used in their experiments to couple the fluidics and optics, i.e. the optofluidic interconnect, was manufactured from two glass plates that were etched and then glued together to form an enclosed channel of 128 µm,

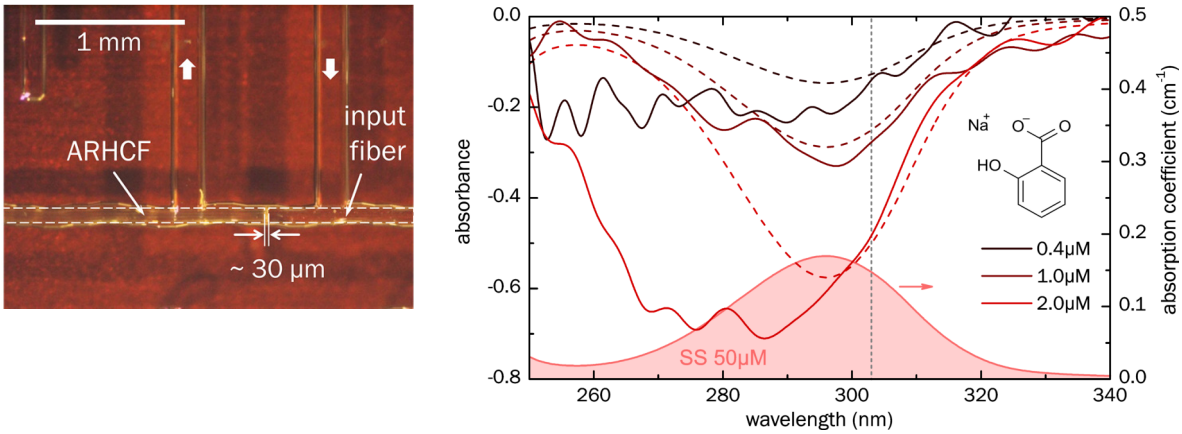

(a) Setup (b) Results

Fig. 1.8 UV absorption spectroscopy on drug molecules in HC-PCF by Nissen *et al.*[187] Using a microfluidic coupling chip, a solid-core fibre is used to deliver UV light to an antiresonant HC-PCF by butt coupling. The transmission through the HC-PCF filled with the drug sodium salicylate, which has an aromatic residue resulting in an absorbance peak in the UV, is shown in simulation (dashed lines) and experiment (solid lines) for different concentrations. Figure from [187]. (*Fig. first referenced on p. 47*)

a few microns larger than the HC-PCF diameter. These channels feature a small undulation to ease fibre movement and alignment when positioning them against the solid-core multimode fibres. Finally, the inlets and outlets to the resulting channels were fabricated by ultrasonic drilling.

The authors measure two drugs, with respective absorption maxima in the UV-C band ($< 280\,\mathrm{nm}$) and the UV-B band (up to 315 nm). For the UV-B band, the authors measure sample sodium salicylate (molar absorptivity of $2450\,\mathrm{M^{-1}\,cm^{-1}}$ at 303 nm), shown in Fig. 1.8. With this extinction measurement, Nissen *et al.* experimentally find a limit of detection of 230 nM, based on a 3σ distance from the blank control.

Discussion of Nissen *et al.* transmission spectroscopy data

The UV absorption spectroscopy setup utilised by Nissen *et al.* uses solid-core multimode fibres at either end of the HC-PCF for in- and outcoupling of light. As these move (on the lengthscale of λ), light coupling conditions will change, resulting in a change of signal. In their results, experimental (solid) and simulated (dashed) results disagree increasingly at shorter wavelengths, with an approximately periodic modulation appearing on the data. If incoupling and outcoupling conditions were held perfectly unmoving, any spectral artefacts resulting from imperfect incoupling can be subtracted by referencing to a blank

control, but the mechanical rigidity needed to fix light coupling conditions is difficult to achieve in practice.

This apparent beating pattern in the data could originate as the interference between two modes, i.e. from significant coupling into higher-order modes. Similar effects are commonly seen in our experiments when the optical setup is misaligned. Modes that couple more strongly to the silica cladding will show increased absorbance. This is especially true at shorter wavelengths ($< 300\,\mathrm{nm}$), where silica (and impurities) absorb strongly, potentially explaining the increased absorbance seen in the data. Finally, for the setup used by Nissen *et al.*, the optical alignment is provided entirely by the etched-channel optofluidic chip. Since there are no manual degrees of freedom that could be used for fine translational or angular alignment, such a setup relies on highly coplanar cleaves and tight tolerances in channel and fibre diameter.

1.2.3 Label-free detection of proteins in HC-PCF

Scope of review

In this section, we include works that demonstrate the label-free, all-optical detection of proteins in HC-PCF. However, as discussed below, the term label-free carries different meanings. We also note that the form factor and biological inertness of HC-PCFs (and fibres in general) allow them to be embedded minimally-invasive into live organisms, which can enable in-vivo sensing.[188] These in-vivo applications, most commonly for medical diagnostics on the tissue level, are arguably sensing proteins. However, this is not considered as a biophysical application in the context of this review (laboratory experiments on protein solutions).

Refractive index sensing of proteins and surface adhesion

One possibility of detecting label-free proteins is by their effect on the refractive index of the liquid they are dissolved in.[189][190][191] We have already discussed interferometric scattering approaches in Section 1.2.1, which study single molecules by the interference of light scattered by the proteins with back-reflected light from a static surface. In bulk, the change in refractive index of the solution can be measured directly.

However, proteins have a generally low refractive index contrast, i.e. the refractive index of a solution of proteins in some solvent will not be substantially different from that of the solvent alone.[192][193] A study by Zhaol *et al.* investigates a variety of proteins and individual residues, finding a mean refractive index

change with varying concentration of $\mathrm{d}n/\mathrm{d}c = (1.899 \pm 0.003) \times 10^{-4}\,\mathrm{L\,g^{-1}}$ for the human proteome.[17] To put this into our measurement context, consider the nanomolar concentrations typically of interest in biophysical studies, and bovine serum albumin (BSA) as a common model protein with molecular weight of $M_{\mathrm{BSA}} = 66.5\,\mathrm{kDa}$. Each change of 1 nM of BSA would therefore require a refractive index measurement precision of $\mathrm{d}n/\mathrm{d}c \cdot (M_{\mathrm{BSA}} \cdot 1\,\mathrm{nM}) \approx 10^{-8}$. This precision is at the edge of what available techniques can achieve.[194] Furthermore, at this level, even small temperature variations and other environmental differences have to be corrected for, adding experimental complexity and limitations.

Many highly sensitive[195][196] refractometric measurements are based on surface adsorption of the analyte, such as surface plasmon resonance (SPR) sensors.[191][197] PCFs for performing measurements based on SPR have been developed by coating the fibre with metals (esp. gold) on the inside[198] or outside.[199] SPR sensors have also been based on planar photonic crystal slabs,[189][200] and femtosecond laser-machined solid-core fibres have been used to perform in-liquid Mach-Zehnder interferometry.[201] However, even these advanced refractometric measurements do not reach the sensitivities described above.

Transmission spectroscopy in HC-PCF

Instead of measuring the refractive index change of the dilute solution directly, HC-PCFs enable an indirect way of performing this measurement. The surface-binding of proteins to the core walls changes the transmission properties of the HC-PCF, with the magnitude of this effect governed by the proteins' refractive index. A uniform film on the HC-PCF walls can be understood as increasing the effective strut thickness, shifting the transmission properties of the HC-PCF.

Based on the resonance condition (discussed fully in Section 2.1.2), which has as its parameter the cladding strut thickness d,

$$\lambda_{\mathrm{res},m} = \frac{4d}{2m}\sqrt{n_{\mathrm{silica}}^2 - n_{\mathrm{core}}^2}\,, \qquad m \in \mathbb{N}, \tag{1.2.3}$$

when a biofilm forms on the struts, it changes the effective thickness to be

$$d \to d_{\mathrm{silica}} + d_{\mathrm{biofilm}} \cdot \frac{n_{\mathrm{biofilm}}}{n_{\mathrm{silica}}}. \tag{1.2.4}$$

The resulting change in the transmission spectrum of the HC-PCF can then be related back to the thickness of the adsorbed protein layer, typically by tracking transmission minima or maxima over time as proteins adsorb onto the surface.

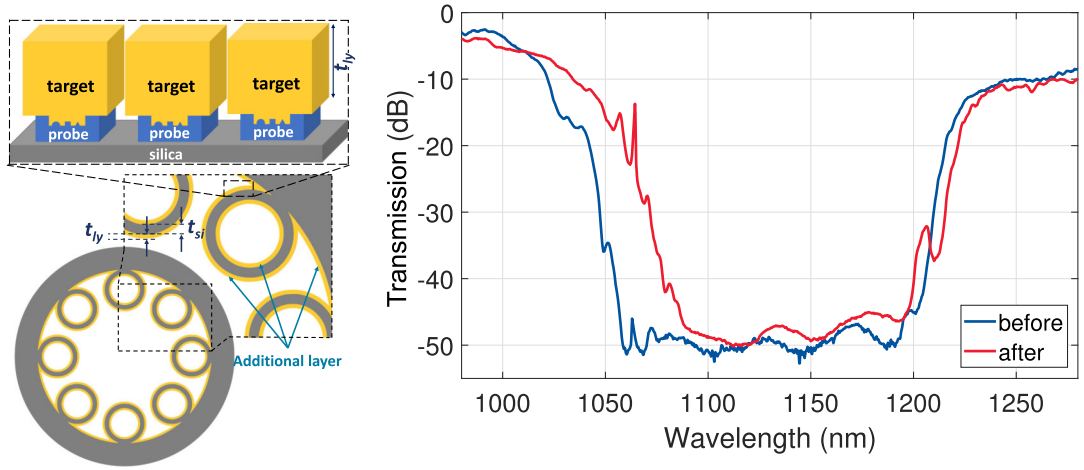

(a) Surface-functionalised HC-PCF with biotin (probe) to bind streptavidin (target)

(b) Transmission spectroscopy tracking the shift of a HC-PCF loss band before and after streptavidin infiltration and formation of an adsorbed film

Fig. 1.9 Measurement of proteins inside HC-PCF using transmission spectroscopy by Giovanardi *et al.* As the proteins bind to the functionalised wall surfaces, the thickness of the HC-PCF cladding changes. These features define its waveguiding characteristics, and the change in effective thickness can be quantified by transmission spectroscopy. Adapted from [206] © 2019 IEEE. (*Fig. first referenced on p. 51*)

Surface functionalisation

Functionalisation of the core of HC-PCF can be used to increase specificity,[202][203][204][205] similar to how many biosensors (e.g. quartz crystal microbalances) can be used with and without functionalisation. However, this approach conflicts with the goal of label-free detection, adds to the complexity of fibre preparation, and will cross-contaminate samples if used multiple times.

Irreversible surface binding

Based on functionalising the surface of HC-PCFs, Giovanardi *et al.* simulate and experimentally demonstrate this effect using the biotin–streptavidin system (Fig. 1.9).[206][207] With one of the strongest known non-covalent bonds in biology, this pairing can give high surface coverage and consequently thick adsorbed protein layers, with the authors measuring films as thick as 30 nm. The functionalisation required multiple incubation–rinsing steps. For the protein measurement, streptavidin solution was passed through the HC-PCF for 2 h at an unspecified concentration.

Reversible surface binding

Since this binding is (practically) irreversible, the sensor has a limited lifetime, which ends with complete coverage of the binding sites by the target protein. For non-functionalised surfaces, strategies exist to repeatedly remove and subsequently rebuild protein coatings with an alkaline (pH 9) solution, and Er-

matov *et al.* demonstrate this approach inside a HC-PCF.[208] By coating their HC-PCF with a mix of tannic acid and BSA protein, up to 30 layers thick, and measuring the change in the HC-PCF's transmission spectrum, they detect the change in number of bilayers formed by the BSA–tannic-acid mixture. The authors explore the use of this method less for the detection of the deposited proteins (and do not specify the concentrations of the protein solutions used), but primarily for creating 'ultrasmooth' (surface roughness 3 nm) coatings that can be removed and re-created as needed.

Pidenko *et al.* detect BSA via transmission spectroscopy in a HC-PCF at a concentration of 1 g L^{-1}, equivalent to 15 μM.[209] They also measure ovalbumin samples and show an effect of pH on the transmission spectrum. As a short conference paper, it does not provide the necessary details to further evaluate these data, as only a single, normalised transmission spectrum at a single concentration is shown. Furthermore, the authors show an electron micrograph of the HC-PCF (an antiresonant negative curvature design with 18 capillaries surrounding the central core), but provide neither a scale bar nor a dimension, such that the sample volume cannot be ascertained.

Advantages and limitations of surface-based sensing

Common to both functionalised and non-functionalised methods is the requirement to have the analyte (target protein) interact with a surface. Consequently, biophysical analysis of the results is limited to surface–protein interactions. Proteins in particular can change between folding states based on their local environment and especially through interactions with interfaces.[33][38][39][210] However, for surface-functionalised measurements, a key advantage is the relative simplicity with which specificity can be achieved through antibodies, and this forms a key reason for their use in complex analytes for biosensing. Finally, surface-adsorption removes the possibility to probe properties of proteins in solution that rely on their mobility, such as diffusion measurements from which hydrodynamic radius and ultimately conformation can be established.

Fluorescence sensing

To the best of knowledge of the author, there are currently no journal publications other than the ones resulting from this PhD which show the label-free (i.e. intrinsic) fluorescent sensing of proteins in HC-PCF. There are related applications of protein sensing in HC-PCF where the proteins themselves are not labelled; we discuss an example of this here.

Monro *et al.* used one of their own HC-PCF designs that has its core exposed to the liquid sample solution to detect organic fluorophores and metal ions.[211] These suspended-core fibres are based on evanescent wave coupling of light to analytes that are present within a few wavelengths of the surface in contact with the sample solution.

In early work, the authors note that their approach can be adapted to proteins if they are bound to the surface with antibodies that are fluorescently labelled.[212] In this approach of Monro *et al.*, the proteins themselves would remain unlabelled, and then bind to fluorescently labelled antibodies for sensing to take place. The study characterises the surface functionalisation and fluorescence collection efficiency of the fluorescently labelled antibodies, but leaves the use for protein sensing (where target analyte proteins would be bound to the labelled antibodies, modulating their fluorescence emission) as future work. The labels are CdSe quantum dots, which the research group shows in a related work to be detectable in free solution down to picomolar levels in their experiments.[213]

Protein absorption or scattering measurements

To the best of knowledge of the author, there are currently no journal publications which show label-free absorption or scattering based sensing (i.e. extinction) of proteins in HC-PCF (a manuscript resulting from the research of this PhD is in preparation).

To clarify this point, the studies covered in Section 1.2.3 are extinction based measurements. As such, they will inevitably have absorption and scattering components from the dissolved proteins contributing to the measured extinction. However, these studies explicitly use extinction not to measure the (weak) absorption or scattering of proteins in HC-PCF, but instead to measure the change in HC-PCF transmission, which they then relate back to a protein concentration (on the surface).

Labelled protein detection

Protein detection in (HC-)PCF, with labels

If HC-PCF are able to detect weak label-free intrinsic fluorescence, they can (unsurprisingly) also be employed to detect the much brighter *labelled* protein fluorescence.[214][156] For example, Ruan *et al.* have measured CdTe–ZnS quantum-dot-labelled IgG antibodies in a microstructured fibre that uses only evanescent coupling.[215] The fibre guides light in a central glass core connected to the

jacket with three thin (relative to the wavelength of light, leading to inhibited coupling) glass struts, forming three microfluidic channels around it (sometimes called a 'Mercedes' fibre). These are then infiltrated with sample solution and the shallow ($\sim \lambda$) layer close to the solid core probed evanescently. With this setup, the authors were able to detect fluorescently labelled IgG antibodies in the 50 nM range at a signal-to-noise ratio of 4.

Immobilisation and adsorption

Label-free proteins vs. label-free measurement

In the studies discussed as label-free protein measurements in HC-PCF, in two different ways, proteins were immobilised. The proteins either underwent adsorption to a surface, or binding to a functionalised surface (anchored antibodies). Both approaches are therefore surface-based. It is worth discussing the term 'label-free' in light of these experiments.

In the strict sense of not using fluorophores to label the proteins, these approaches are undoubtedly label-free. In the case of Giovanardi *et al.* performing transmission spectroscopy, no labels were used in the experiment. In Monro *et al.*, the surface-bound antibodies were fluorescently labelled with quantum dots, while the proteins (if their approach were realised experimentally) would remain unlabelled.

Effect on protein behaviour

One of the key motivations for label-free measurements was to enable insights into how labels affect the proteins under study. This information can only be obtained by a label-free control measurement that, to the largest extent possible, leaves the proteins in the same conditions otherwise, i.e. freely diffusing in solution. Surface-adsorbed (partially reversible) proteins, and even more so antibody-bound proteins (effectively irreversible) will change their behaviour compared to freely-diffusing proteins, and hence their contribution to the aggregation process will change or cease entirely. Depending on the questions asked by an experiment, this might limit the applicability of such surface-based approaches.

Adsorption of protein onto silica surfaces

Nonetheless, any sensor will experience protein surface adsorption, even if it does not rely on this surface adsorption as its sensing principle. Surface occupation can be quantified by adsorption to nanoparticles of a known size and number. For example, lysozyme was found to adsorb onto silica surfaces with a density of $1.5\,\mathrm{mg\,m^{-2}}$, at a pH of 7.5.[216] The adsorption varies strongly with concentration at values below ca. $0.2\,\mathrm{g\,L^{-1}}$, but then plateaus to increase only very slowly, remaining nearly constant to within around 10 %. This measurement

was taken without the presence of salt which, if present, can shift the equilibrium towards lower protein adsorption, depending on the pH of the solution.

To perform such measurements online, the end facet of a solid-core fibre prepared with a glass spheroid can be used to measure adsorption changes continuously by the shift of a resonant microcavity, which has been shown for biomolecules.[217] Adsorption onto surfaces follows an equilibrium process, but a large part of the adsorption remains irreversible when changing back to water. For example, in a study of a culture-medium protein mixture in contact with silica, the irreversible component of adsorption was found to be around 60 %.[218]

1.2.4 Summary

This concludes the review of the literature with regards to related studies, with the next chapter discussing the theoretical background and physical principles relevant to our work. As mentioned in the introduction to this chapter, we discussed the label-free optical detection of proteins, then covering HC-PCF for biophysical sensing, and before combining these two fields to narrow down the scope to become the label-free optical detection of proteins within HC-PCF. The relative scarcity of works that fall in this latter category is where this dissertation hopes to contribute to with the experimental work that follows.

1.3 Practical considerations

We finish the Context chapter with brief mention of the circumstances that shaped this PhD, outside the scientific considerations that are the focus of this dissertation.

Availability of light sources

No 280 nm laser available

The original PhD proposal was fundamentally based on a 280 nm ultraviolet laser that had been successfully used in prior experiments. Shortly after the beginning of the PhD, this laser started experiencing lasing failures and power fluctuations. Eventually, the laser would not start, or only lase intermittently. Company service technicians inspected the device remotely, and – while the issue was known to the engineers – no repair was available for this recently out-of-warranty laser. The company also stopped selling this product line entirely around the same time, offering no sub-350 nm lasers in their product lineup since. Anecdotally, at a conference, the present author asked a sales representative about this at the company's booth. After a brief moment of silence, the question was met with a deadpan, 'Yes – We don't sell that one anymore'.

For this PhD, the absence of a suitable high-brightness, good mode quality 280 nm light source meant that the planned PhD project had become impossible in its original form. Considerable time of the PhD was spent devising alternative approaches to fulfil the stated goal of this work, which are now presented in this dissertation.

COVID-19 pandemic

Effects of the COVID-19 pandemic

This PhD work coincided with the time of the COVID-19 pandemic, meaning no or only restricted experimental laboratory work was possible for the time of the pandemic lockdowns and self-quarantine periods. Besides the direct impact on the work of this dissertation, the resulting delays also affected planned collaborative projects, which reflects in the projects attempted and completed.

2 | Concepts in Optofluidics

Optofluidics combines optics and microfluidics. We review the theory and physical principles underpinning our work: how light propagates in waveguides, the hydrodynamics of microfluidic flows within them, and finally how macromolecules such as proteins move through them.

2.1 Optical waveguides . . . 58
2.1.1 Light propagation through media . . . 58
2.1.2 Photonic crystal fibres . . . 62
2.1.3 ARROW model simulation . . . 67
2.1.4 Modes in HC-PCF . . . 68
2.1.5 Comparison to other photonic crystal fibre geometries . . . 71
2.1.6 Manufacturing of HC-PCF . . . 73
2.2 Microfluidics . . . 76
2.2.1 General theory . . . 76
2.2.2 Theory of microfluidic flows and the Reynolds number . . . 77
2.2.3 Laminar flow profile . . . 78
2.2.4 Hydrodynamic resistance . . . 78
2.3 Molecular mass transport . . . 80
2.3.1 Diffusion theory . . . 80
2.3.2 Diffusion simulation . . . 81
2.4 Materials and Methods . . . 86
2.4.1 HC-PCF geometry . . . 86
2.4.2 HC-PCF preparation . . . 86
2.4.3 Transmission properties . . . 91

Contributions *In this chapter, I gratefully acknowledge contributions by Michael Frosz (HC-PCF fabrication SEM images), Tobias Nägele (SEM images), and Ralf Mouthaan (waveguide mode simulations).*

2.1 Optical waveguides

Introduction

In this part, we explain the optical theory and methods that underlie our experiments. Specifically, we discuss the optical properties of hollow-core photonic crystal fibres which exhibit through-liquid light guidance beyond the limits of traditional optical fibres, and a Materials and Methods section that covers concepts common to all HC-PCF-based experiments in the later chapters.

2.1.1 Light propagation through media

'Traditional' optical fibres

In our experiments we use hollow-core photonic crystal fibres to confine and guide light through water. Photonic crystal fibres are optical fibres that use phenomena other than total internal reflection (TIR) to attain their waveguiding properties. It is therefore of interest to begin by revisiting total internal reflection and thereby understand where the limitations that motivate the use of photonic crystal fibres come from.

Total internal reflection guidance

The 'traditional' optical fibre[219] operates via TIR occurring between the fibre core, and the region just outside the core, known as the cladding. Both materials are typically silica, but can be doped with other elements (e.g. GeO_2) to vary their optical properties, namely their refractive index.[220] A core (having refractive index n_{core}) inside a cladding (n_{cladding}) will support TIR and guide light given that

$$n_{\text{core}} > n_{\text{cladding}} \quad \text{(necessary condition for TIR)}. \tag{2.1.1}$$

Then, all light at angles shallower than the critical angle,

$$\theta_{\text{crit}} = \arcsin\left(\frac{n_{\text{cladding}}}{n_{\text{core}}}\right), \tag{2.1.2}$$

is prevented from leaving the core by TIR, i.e. the light is guided. The arrangement of two concentric, continuous silica regions of different refractive indices is known as a *step-index* fibre.[221] The critical angle defines the acceptance cone (a solid angle) of light that is guided through the fibre. For light that is guided, the loss through the fibre is governed by material absorption, as well as the smoothness of the core–cladding interface that leads to Rayleigh scattering. Fibres which use only a single base material (typically silica) benefit from all interfaces being inherently lattice-matched, except for defects introduced by the dopants.

Material	Refractive index	Comment
Air	1.000	Generally true for gases
Fluoropolymers	1.31 ... 1.29	Low-n formulations of amorphous fluoropolymers[222]
Water	1.33	
Ethanol	1.36	
PDMS polymer	1.4	Polydimethylsiloxane, used in microfluidic chips[223]
Glass (various types)	around 1.5	Up to about 1.8 for specialised optical glasses[224, Tbl. 26.1]
Diamond	2.4	

Tbl. 2.1 Refractive indices of some common materials or material classes. While, for example, the optical industry has produced a large array of glasses with varying n for different applications, there are very few solid materials that are less optically dense than water. All values are approximate around visible wavelengths and standard temperature and pressure. (*Table first referenced on p. 59*)

Limitations of TIR for waveguides

As seen above, light guidance by TIR fundamentally requires the light-guiding medium to be more optically dense than its surroundings. In practice, this severely limits the choice of materials available for the construction of liquid-filled, i.e. optofluidic waveguides. While it is feasible to find practical material combinations (cf. Table 2.1) that confine light in a solid and optically dense material (doped glass) surrounded by another solid but optically less dense material (undoped glass), the same is not true for a liquid within a solid. Only specialised PTFE-derived polymers have refractive indices below that of water, but even then only by a narrow margin of less than 3 %. PTFE-based waveguides are typically constructed by internally coating glass capillaries, and are found in applications of channel diameters larger than 250 µm.[222] Hence, for channel sizes typical in microfluidics (50 µm and below), water-filled total internal reflection fibres remain impractical.(note 1)

note 1 For a suitably general notion of 'fibre', a stream of water could be understood as a realisation of a total internal reflection optical fibre. Water jets have been explored as waveguides, where a thin stream of water flows vertically downwards through air, resulting in water being surrounded by the optically much less dense air. However, most of the convenient engineering properties

Propagation of light through waveguides

Description of electric field in waveguides

Consider now the guidance of light through a general waveguide. Light, as an electromagnetic wave, is described by a wavevector $\vec{k}$, governing the spatial oscillation period of its (by convention) electric field component,

$$\vec{E} = \vec{E}_0 \, \mathrm{e}^{-i\vec{k} \cdot \vec{r}} \,, \tag{2.1.3}$$

where the symbols have their usual meanings.[225][226] It follows that when propagating in the vicinity of interfaces (discontinuities in refractive index), boundary conditions apply and impose certain conditions on $\vec{k}$, giving rise to distinct solutions which correspond to propagation along a waveguide. We introduce the interpretation of these solutions in the context of optical fibres (recommended literature: [131][132][144][227][228]) but more general treatments exist ([229][230][231][232][233]).

Constant of propagation β

Now consider any point in space within a fibre core. $\vec{k}$ can be decomposed into a component $k_{\parallel}(z)$ along the fibre axis, and a radial (i.e. transverse) component $k_{\perp}(\vec{r})$. For a fibre invariant along its axis (and of sufficient length $\gg \lambda$), symmetry dictates that $k_{\parallel}(z)$ is constant everywhere. This *constant of propagation* $\beta := k_{\parallel}$ forms an invariant in the description of waveguides.

More accurately, β as used here applies to perfect (lossless, non-absorbing) waveguides. If absorption were to be included, β would become a complex number indicating loss,[234] similar to how the refractive index n can be generalised to be a complex number to include material absorption.

Geometrical optics picture

In geometrical optics, each possible propagation path for a ray through the fibre corresponds to a given β. For TIR guidance, β can be understood as governing bound or refracting rays.[232] In step-index TIR fibres, $\beta > n_{\text{cladding}}\, k_0$ gives the cut-off for propagation in the cladding, and hence only light with $\beta < n_{\text{cladding}}\, k_0$ is guided in the core.[235]

Waveguide modes

In an electrodynamic description of waveguiding, each β corresponds to a *mode* supported by the fibre. A mode is supported in the waveguide if it can satisfy the existing boundary conditions, namely at the core–cladding interface. These supported modes are then understood as electromagnetic standing waves with $k_{\perp}$ quantised in the transverse direction, and $k_{\parallel}$ as a wave propagating along the fibre. The solutions to Maxwell equations for a fully rotationally-symmetric geometry

that make optical fibres successful are lost in such an arrangement. See Section SI.6 for more discussion.

are given by Bessel functions.[234] Ultimately, for arbitrary fibre geometries, the mode shape generally cannot be solved analytically.

Origin of losses in capillaries

Losses in waveguides

Consider the origin of losses in plain capillaries, where $n_{\text{core}} < n_{\text{cladding}}$ and hence no TIR guidance. Clearly, even without TIR, the light does not pass from the core through the glass as though the glass were nonexistent. Instead, light moves along the capillary with losses due to repeated partial (non-total) reflections. The amount of reflection from the glass back into the core with each such reflection, and hence the loss, will depend on the refractive index difference of the interface for a given angle of incidence θ_{i}. This is quantified by the *Fresnel equations*, with the reflection coefficient (in terms of power) given by[229]

$$R_{\text{s|p}} = \left(\frac{n_i \cos(\theta_{\text{i}}) \mp n_t \cos(\theta_{\text{t}})}{n_i \cos(\theta_{\text{i}}) \pm n_t \cos(\theta_{\text{t}})} \right)^2 \tag{2.1.4}$$

for s and p polarised light. The i, t subscripts refer to incoming and transmitted angles relative to the interface normal.Using Snell's law and trigonometric relations to eliminate θ_{t} yields an expression for the incoming angle θ_{i} only,

Reflection coefficient

$$R_{\text{s|p}} = \left(\frac{n_i \cos(\theta_{\text{i}}) \mp n_t \sqrt{1 - (\frac{n_i}{n_t} \sin(\theta_{\text{i}}))^2}}{n_i \cos(\theta_{\text{i}}) \pm n_t \sqrt{1 - (\frac{n_i}{n_t} \sin(\theta_{\text{i}}))^2}} \right)^2 . \tag{2.1.5}$$

The fraction of light reflected back into the core is light that remains in the core; in other words, it is guided. Thus, large R will lead to less loss through the waveguide.(note 2) Note that the condition for TIR guidance (Eq. (2.1.2): $\theta_{\text{crit}} = \arcsin(n_{\text{t}} / n_{\text{i}})$) follows from this equation by setting the root's radicand to 0, giving $R = 1$.

note 2 More accurately, this will reduce guidance loss, which is one component of transmission loss. Other losses due to material absorption inside the core are mostly desirable for our application, as they correspond to light–matter interaction with the sample under study. Contrast this to solid core step-index fibres, where light is guided by TIR, and losses are almost solely by (undesirable) material absorption or scattering, especially from defects and impurities.[132]

Propagation and attenuation constants

A derivation from Maxwell's equations for a capillary of bore radius a leads to propagation constant β_{nm} and attenuation constant α_{nm} given by

$$\beta_{nm} = \frac{2\pi}{\lambda}\left(1 - \frac{1}{2}\left(\frac{u_{nm}\lambda}{2\pi a}\right)^2\right), \tag{2.1.6}$$

$$\alpha_{nm} = \left(\frac{u_{nm}}{2\pi}\right)^2 \frac{\lambda^2}{a^3}\frac{\nu^2+1}{2\sqrt{\nu^2-1}}, \tag{2.1.7}$$

where u_{nm} is the m^{th} zero of the n^{th} Bessel function J_n, and $\nu = n_{\text{cladding}}/n_{\text{core}}$ is the refractive index ratio of the fibre material to the liquid in its core.[130][233] The length over which a mode decays to $1/e$ of its initial intensity is $1/\alpha_{nm} \propto a^3/\lambda^2$, making losses of capillaries increase rapidly with diminishing size, by the third power of their inner diameter.

2.1.2 Photonic crystal fibres

Beyond TIR guidance

Given this fundamental limit for TIR-guiding channels and high losses in small capillaries, what principle do hollow-core photonic crystal fibres use to achieve waveguiding in microfluidic geometries?

A *photonic crystal* is a spatially-periodic structure where the refractive index varies with position. For such periodic arrangements, the propagation of photons underlies additional boundary conditions compared to isotropic media. The concept of photonic crystals was coined in analogy to electronic crystals when first discussed in 1987.[236][237] Fig. 2.1 shows several examples of photonic crystal structures that have been used to produce PCFs which confine and thereby guide light in different ways.[148] Notably, many living creatures use photonic crystals to produce their structural colouration (Fig. 2.2).

Types of HC-PCF

There are two distinct but related classes of photonic crystals that are used to form waveguiding optical fibres: *photonic bandgap fibres* (PBGFs) and *antiresonant hollow-core fibres* (AR-HCFs).[184] The fibres used in this dissertation are of the latter type.

Historical outline of HC-PCF

Historically, the first PCFs were photonic bandgap fibres, proposed in 1995 based on simulations which showed that the refractive index difference between silica and air would be sufficient to manufacture them.[246][247] Successful realisation was reported one year later with a PBGF that consisted of air holes in a hexagonal lattice, with light guided in the central solid-core defect.[248] Soon, the

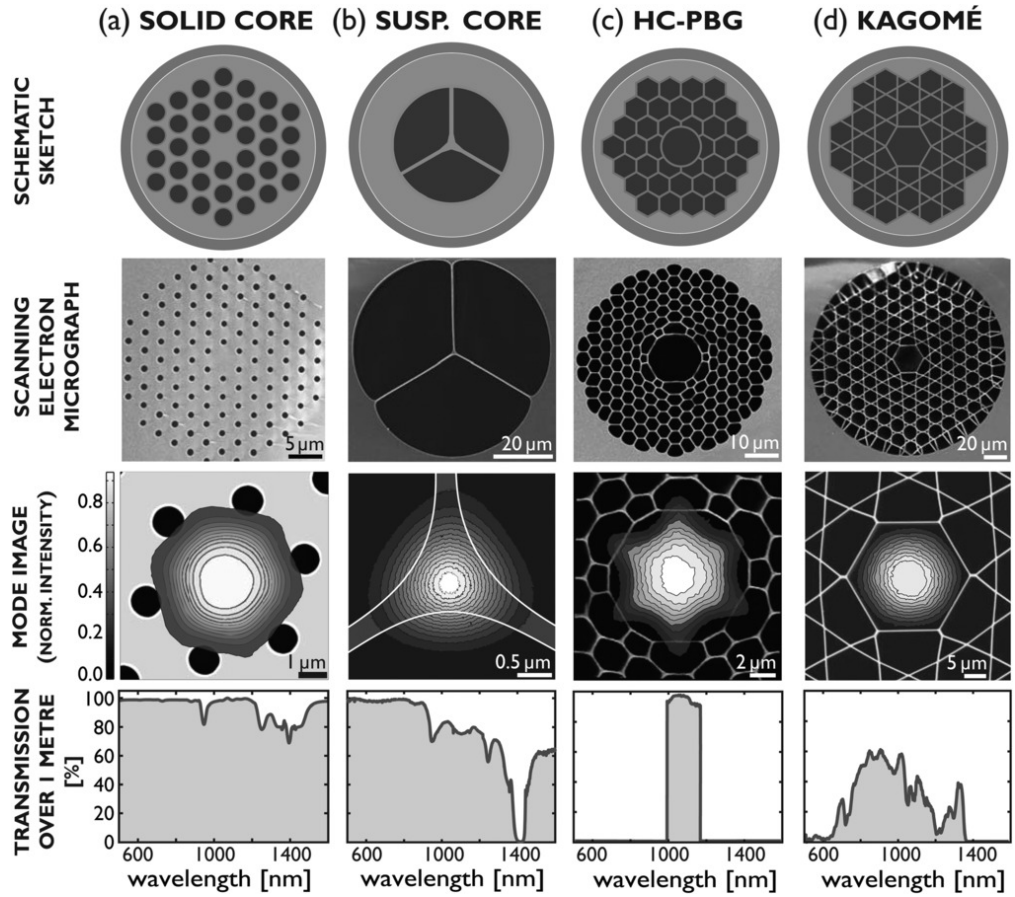

Fig. 2.1 Examples of photonic crystal structures used to produce PCFs, with their resulting light guidance properties. Their working principle varies: a) and b) are by (modified) total internal reflection; c) is by establishing a photonic bandgap in the area around the core, preventing light from leaving the core; and d) is by antiresonance and inhibited coupling[238] between core and cladding. Adapted from [130]. (*Fig. first referenced on p. 62*)

first guidance in a hollow core was reported in 1999, fundamentally based on the same principles, but advancing fabrication to higher air-filling fractions.[249]

Photonic bandgaps

Light guidance in PBG fibres is explained through the existence of bandgaps in their photonic density of states, which prevent light from entering certain regions (propagation modes). There exists a direct analogy to bandgaps in electronic semiconductors, and similarly a density of states plot can be used to identify guided wavelengths. However, the semiconductor analogy does have its limitations related to the differences between photons and electrons (e.g. conservation of charge and their nature as fermions or bosons).[250][251][252]

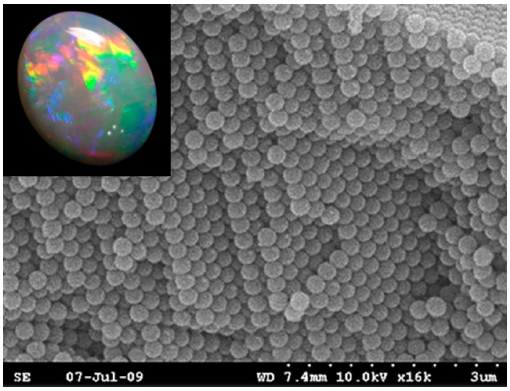

(a) Opal

(b) Kingfisher feathers

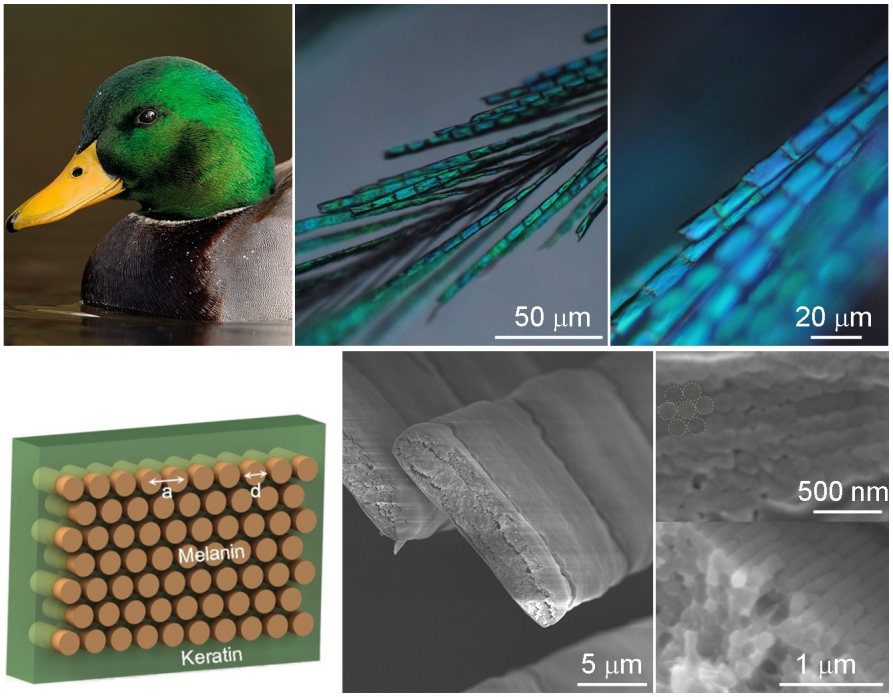

(c) Duck feathers

Fig. 2.2 Photonic crystals producing structural colouration, appearing in nature both inorganic (a) and biological (b, c) in origin.[239][240] Opals are closely-packed colloidal silica particles.[241][242] The iridescent blue colouration of bird feathers generally stems from photonic crystals. The kingfisher combines diffuse orange pigmentation and iridescent blue photonic crystal nanostructures to produce its striking camouflage colouration.[243][244][245] (a, c) adapted from [242, 243]. (b) Image credit Robert Heck. (*Fig. first referenced on p. 62*)

PBGFs have a narrow transmission spectrum (Fig. 2.1), necessitating a close link between fibre design and a given target application. Furthermore, their intricate photonic crystal structure, commonly made of sub-micron glass web structures, complicates fabrication and increases their surface-to-volume ratio such that they exhibit high hydrodynamic resistance and act as porous filters, accumulating particulates on their end facets. These properties have to be considered for integration with microfluidics.

Antiresonant hollow-core fibres

Antiresonant HCFs

The HC-PCFs in our experiment, known as *antiresonant hollow-core fibres* (AR-HCFs), do not employ photonic bandgaps. Instead, they rely for their light guidance on a combination of principles, most importantly *antiresonant reflection* and *inhibited coupling*. Despite exhibiting higher losses than PBGFs, their simpler geometry results in a number of advantages for our experiments. These advantages motivating their use over other geometries is discussed in more detail in Section 2.1.5.

The idea underlying AR-HCFs can be understood by drawing a comparison to *antireflective coatings* on lenses. These reduce reflections by thin-film interference, where reflected and transmitted light undergo destructive and constructive interference, respectively.[253] AR-HCFs use the inverse principle to reduce the intensity of light transmitted out of the core relative to that reflected back into it, confining the light to the core.

Antiresonant guidance mechanism

Consider an optical cavity, such as the space between the optical flats of a Fabry – Pérot etalon (Fig. 2.3), or the core of our fibre surrounded by the cladding capillaries.[254] We say that antiresonant reflection confines the light to the cavity when the geometry and wavelength are such that light destructively interferes when it would otherwise be transmitted to the outside, and constructively interferes when it is reflected back into the cavity. Vice-versa, in the resonant case, light is confined inside the struts, where material absorption causes high loss.

(Anti-) Resonant wavelengths

While AR-HCF are broadband-guiding, they exhibit the lowest losses at antiresonance wavelengths[255]

$$\lambda_{\text{a-res},m} = \frac{4d}{2m+1}\sqrt{n_{\text{silica}}^2 - n_{\text{core}}^2}\,, \qquad m \in \mathbb{Z}_0^+, \tag{2.1.8}$$

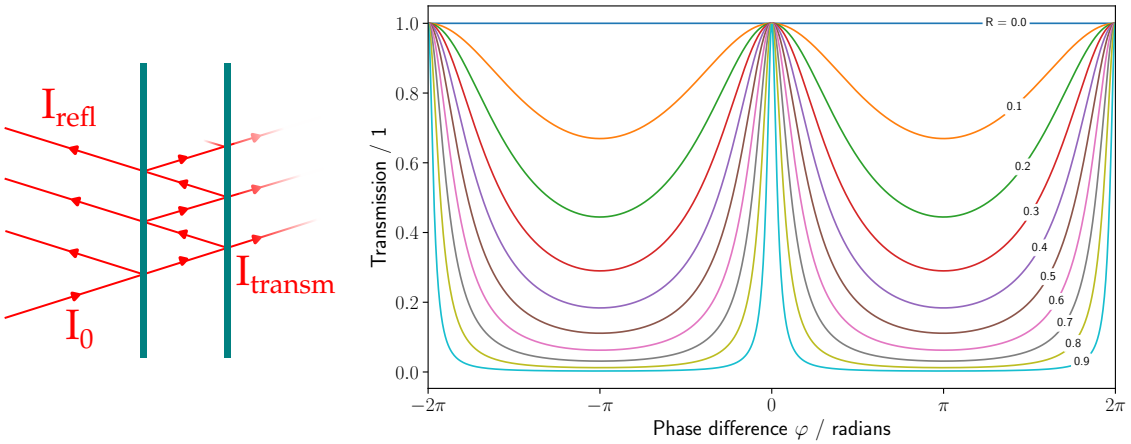

(a) Fabry – Pérot etalon formed by optical flats

(b) Transmittance through a Fabry – Pérot etalon as a function of phase difference φ parametrised by different reflectances R of the optical flats.

Fig. 2.3 The Fabry – Pérot etalon. The transmission and reflectance through two coplanar optical flats varies with optical path difference (phase shift). When this phase shifts is an even multiple of π, transmission is maximal, with the sharpness of the resonance peaks being defined by the reflectance R of the optical flats. (*Fig. first referenced on p. 65*)

while loss peaks occur at the resonance wavelengths

$$\lambda_{\text{res},m} = \frac{4d}{2m}\sqrt{n_{\text{silica}}^2 - n_{\text{core}}^2}\,, \qquad m \in \mathbb{N}, \tag{2.1.9}$$

which are functions of the cladding strut thickness d. These relations can be derived from imposing constructive interference on the reflected or transmitted rays in Fig. 2.3, respectively. Note that Eqs. (2.1.8) and (2.1.9) differ in the domain of m.

Evaluating Eq. (2.1.8) for the HC-PCF in this dissertation ($d \approx 320..390\,\text{nm}$, taking $d \approx 380\,\text{nm}$ as the modal value) filled with water yields the lowest-loss operating wavelengths at

$$\lambda_{\text{a-res},m} = \{1054,\ 351,\ 211,\ 151,\ ...\}\,\text{nm} \tag{2.1.10}$$

when using an averaged refractive index (a first estimate which will be refined below). Crucially, our operating wavelength of 350 nm lies close to a transmission maximum (antiresonance condition) at 351 nm. We will explore this with a full ARROW model simulation in Section 2.1.3 below.

Inhibited coupling

In addition to the antiresonant guidance mechanism of AR-HCFs, there is another necessary property, *inhibited coupling*, without which the low loss guidance of AR-HCFs could not be achieved.

Sub-wavelength features confine light

As the science of fibre drawing progressed (see Section 2.1.6), the smallest features within the fibres (the struts) approached λ in size. Since a guided mode has a mode area on the order of several λ, these small struts do not support modes themselves. When a core is connected to the surrounding solid silica only by thin struts, light is prevented from leaving the core by inhibited coupling. In Fig. 2.1 the suspended core fibre guides light by inhibited coupling to the solid silica surrounding it.

Historical origin of AR-HCFs

All PCFs require some form of inhibited coupling, as otherwise modes would enter the silica cladding. The importance of this effect was studied especially in connection to *kagome* fibres. Found by serendipity in a photonic bandgap fibre drawing,[144] the kagome guidance mechanism was at first unclear,[130] [144][256][257] when it was discovered that small changes in the strut thickness had a significant effect on their transmission properties irrespective of their exact photonic crystal structure.[258] The explanation was found in antiresonant reflection, prompting research into AR-HCF geometries.[259][260]

2.1.3 ARROW model simulation

ARROW model

In general, Eqs. (2.1.8) and (2.1.9) can be understood as a family of curves parametrised by m. The strut thickness d is targeted to a specific value during fabrication, defining the HC-PCF's transmission spectrum. In practice, it underlies manufacturing tolerance and thus spans a range of values. Electron micrographs of the HC-PCF from which these strut thickness values were taken is shown in Fig. 2.4.

Eqs. (2.1.8) and (2.1.9) are simple to evaluate if the refractive indices are assumed constant, i.e. independent of wavelength. This is how the numbers in Eq. (2.1.10) were arrived at as a first estimate. However, in general, the refractive index being dependent on wavelength ($n \to n(\lambda)$) means the equations need to be solved recursively, where the result for λ with some initial guess for n is fed back into $n(\lambda)$ to arrive at the next iterative solution.

Simulating the ARROW model for our HC-PCF

The wavelength-dependent refractive index data of fused silica was acquired from a material database.[261] A program was written to perform a one-pass recursive solution of λ. The results are shown in Fig. 2.5. In this figure, the grey

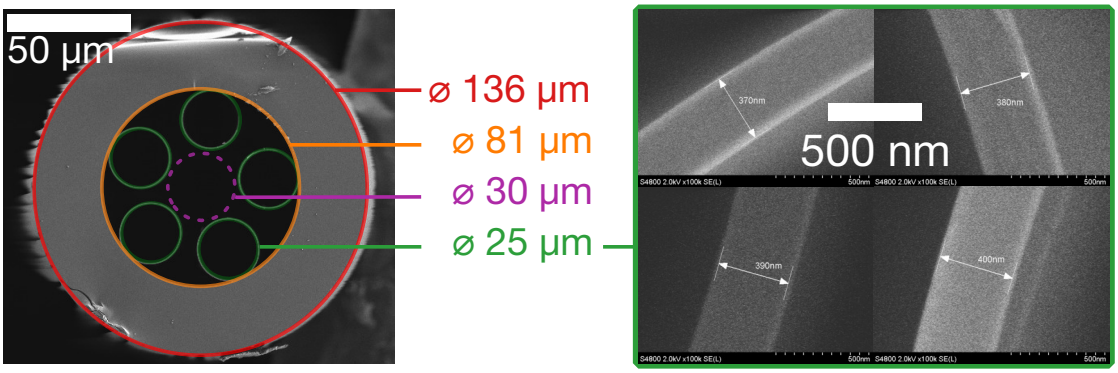

Fig. 2.4 Geometry of the HC-PCF used in this project. **Left:** HC-PCF with overlaid geometry, identifying the jacket outer diameter, jacket inner diameter, and the hollow core surrounded by the cladding capillaries. **Right:** Higher magnifications of the cladding capillaries responsible for the waveguiding properties of the HC-PCF. SEM images provided by Michael Frosz during fibre fabrication at the Max-Planck Institute for the Science of Light, Erlangen.
(*Fig. first referenced on p. 67*)

band indicates the range of cladding strut thicknesses of the HC-PCF used in this present work, as found from electron microscopy images (Fig. 2.4). The range of values comes about from tolerances of the production process, and will vary along the length of a draw (spool) of HC-PCF, as well as surface roughness variations on shorter lengthscales.

Fig. 2.5 shows that higher orders of (anti-)resonances fall closer together, as is expected by Eqs. (2.1.8) and (2.1.9), which corresponds to the classical model of harmonics of standing waves across a fixed length. The fact that antiresonances (high transmission) and resonances (low transmission) lie closer together for higher orders explains why the zeroth order has the strongest transmission peak when measured experimentally in Section 2.4.3.

2.1.4 Modes in HC-PCF

The waveguide propagation theory discussed in Section 2.1.1 also applies to HC-PCF. However, the arrangement of cladding capillaries (or more generally, photonic crystal microstructure) that dictates their modal guidance properties is typically too complex a geometry to be solved by basic analytical methods.

Numerical solutions to HC-PCF modes

Our group's previous PhD student Ralf Mouthaan has worked on simulating modes in HC-PCF using a finite difference frequency domain model.[262] These

Antiresonant simulation printout

Simulation completed for: HC-PCF used in this dissertation, filled with water
Antiresonances (- - -) and resonances (—) of order m for a given wall thickness
The wall thickness tolerance for this fibre is indicated by the grey band

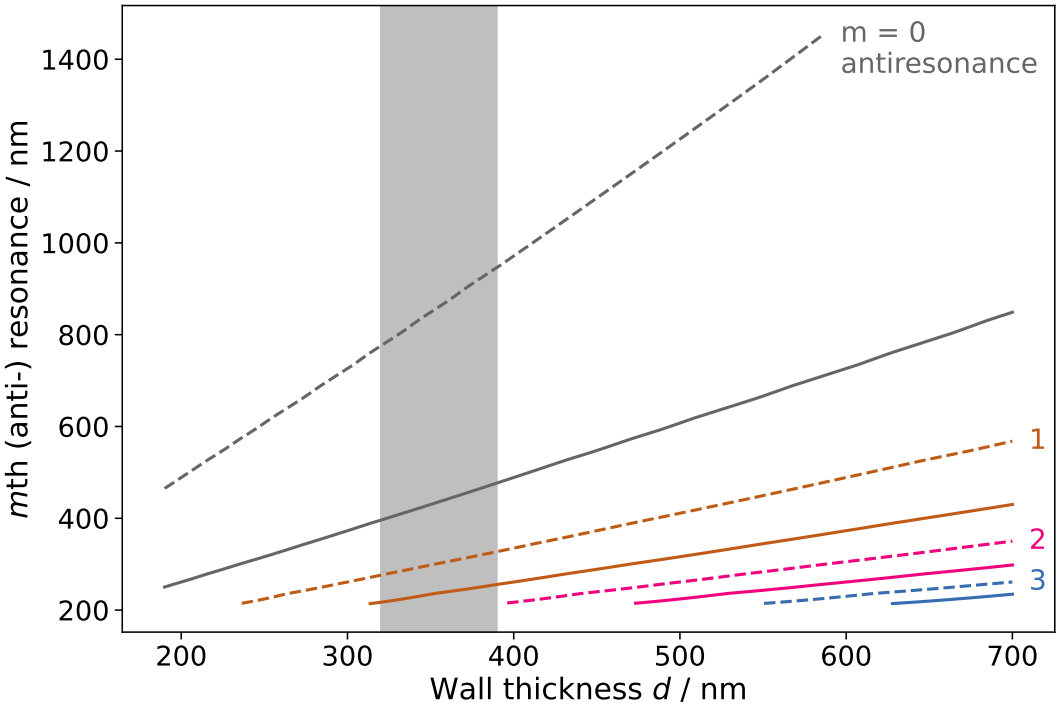

Fig. 2.5 Fabry – Pérot resonance and antiresonance wavelengths as a function of the HC-PCF strut thickness, found by recursively solving Eqs. (2.1.8) and (2.1.9) to second order. Maximum guidance occurs when the antiresonance confines the light in the core. Conversely, guidance is minimal at a resonance. The vertical grey band indicates the range of strut thicknesses in the HC-PCF of this dissertation. Wavelength and material-dependent refractive index data retrieved from [261]. *(Fig. first referenced on p. 67)*

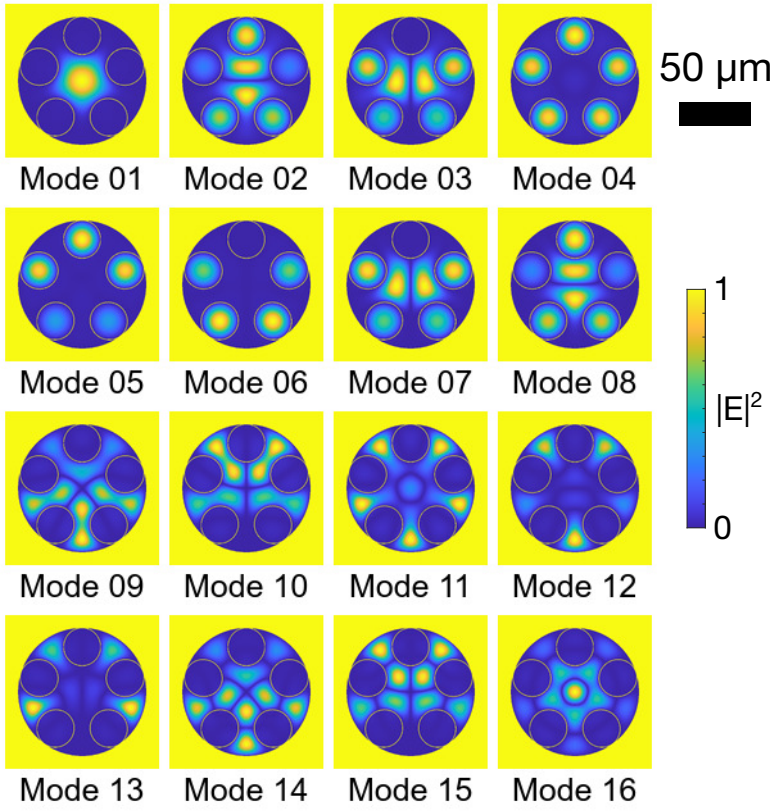

Fig. 2.6 Mode simulations for the HC-PCF used in this dissertation. Yellow represents fused silica geometry, whereas dark blue is the solvent (water). Simulations performed by Ralf Mouthaan using a finite difference frequency domain model.[262] (*Fig. first referenced on p. 70*)

simulations, based on the HC-PCF geometry used in this dissertation, were also used in our co-authored publication [1], and are shown in Fig. 2.6.

Mode profiles observed matched to theory

Throughout this dissertation, these modes appear in our experiments. Core guidance is generally seen to be dominantly in the fundamental mode (Mode 01 in Fig. 2.6), with other higher-order modes (Mode 02 and higher) present as superpositions, creating a more uniform top-hat-like mode profile. We also see modes extending to the interstitial spaces between capillaries (Modes 09 – 15) when the incoupling conditions, i.e. the optical alignment matching the incoming light's wavefront to the HC-PCF's core mode(s), are suboptimal. These are caused by the antiresonant properties of the capillaries still being fulfilled for the space in-between two adjacent capillaries, just like in-between opposite capillaries with the core in the middle, which is the fibre's intended waveguide operation.

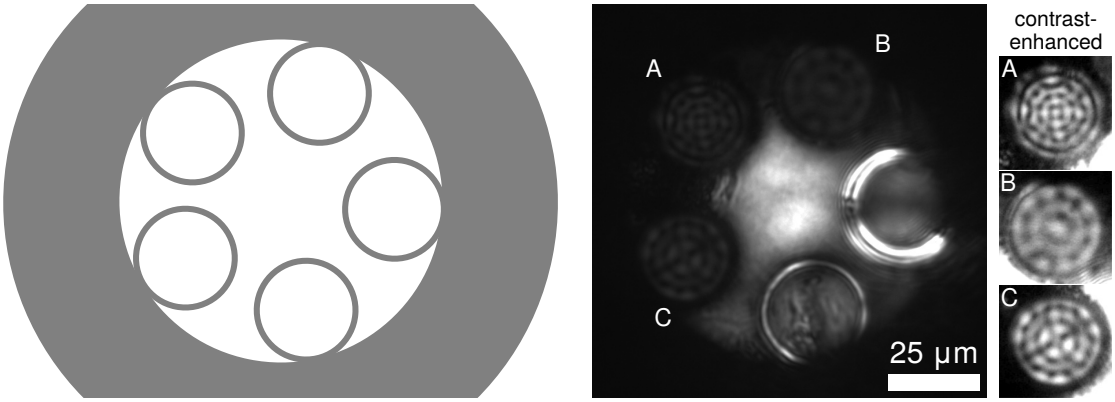

Fig. 2.7 Higher-order modes observed in a water-filled HC-PCF. To excite these higher-order modes, light was coupled-in off-axis, which also results in the direct coupling into the glass of the brightly lit-up capillaries. The capillaries labelled A, B, and C exhibit a range of higher-order modes, which are shown in contrast-enhanced versions on the right. For comparison, the HC-PCF geometry (same scale and rotational alignment) is reproduced on the left, with the white area being filled with water. (*Fig. first referenced on p. 71*)

While experiments aimed at exciting waveguide modes and using them for sensing were not the focus of this dissertation, they were still commonly encountered during alignment. Fig. 2.7 shows how superpositions of many different higher-order modes can be excited experimentally by mere off-axis incoupling. However, which modes are excited is generally not reproducible and very sensitive to small movements.

2.1.5 Comparison to other photonic crystal fibre geometries

HC-PCF terminology

The literature knows several pieces of related terminology concerning HC-PCF, and no single consistent usage has emerged so far.[227] We briefly discuss some of the most common terms here to serve the reader as a guide for literature search.

The antiresonant hollow-core fibres (AR-HCFs) used in this work and shown in Fig. 2.4 could also be referred to as *negative curvature fibres* (referring to the convex features protruding into the core, such as the circular capillaries seen in Fig. 2.4 – in contrast to some other HC-PCFs, e.g. kagome[263] fibres that have hexagonal (and hence flat) core walls, which nonetheless employ antiresonant reflection as one of their guidance mechanisms); or as *tube lattice fibres* (which describes specifically our fibre's photonic crystal arrangement, which are synonymously also termed *revolver fibre* for their appearance). *Microstructured optical fibre* (MOF)

1. High overlap between fluid flow and light guidance (i.e. the cladding bypasses a smaller amount of sample)
2. Less risk of blockage, due to no sub-micron cladding holes, and much fewer cladding channels
3. For the same reason, quick infiltration of the cladding and hence faster time-to-measurement after sample loading
4. Easier to manufacture compared to most other HC-PCF types that have more complex cladding structures

Tbl. 2.2 Primary advantages of AR-HCFs compared to other HC-PCFs for our experiments that motivate their use. Specifically, the comparison is to the other HC-PCF realisations seen in Fig. 2.1, but also applies to other optofluidic architectures.
(*Table first referenced on p. 72*)

is an alternative and more general term to PCF, with some authors limiting the term PCF to photonic bandgap fibres. In planar geometries, possibly in combination with microfluidic chips, the term ARROW (antiresonant reflecting optical waveguide) is used for waveguides based on the antiresonant guidance mechanism, and sometimes also applied to AR-HCFs.[264][265] In this dissertation, I adopt the most general definition of photonic crystal fibres as containing any regular periodic arrangement (a crystal, in the solid state sense) of refractive index differences.

Advantages of AR-HCFs

While kagome fibres were employed in many applications,[130][144] their strut web structure makes them difficult to manufacture; bypasses a large fraction of the infiltrated liquid through non-illuminated regions; and is liable to blockages from impurities. More recently, the introduction of negative curvature geometries enabled a realisation of AR-HCFs[266][267] with a much simpler photonic crystal geometry compared to kagome. Resulting AR-HCFs (especially lattice-tube fibre geometries) show improved manufacturability due to simpler geometries, [258] combined with fewer thin struts and small-diameter holes that can lead to blockages when impure samples (or samples strongly adhering to the walls) are infiltrated. When compared to PBGFs, AR-HCFs can reach wavelength regimes where no suitable photonic bandgap guidance could be found, such as in the UV or mid-infrared.[268][269] Table 2.2 summarises the reasons why AR-HCFs are the preferred choice for our experiments.

Other types of antiresonant fibres

Bragg fibres, also known as *annular core fibres*, are made from concentric rings of different refractive index and also work on the principle of antiresonant reflection. First proposed in 1978,[270] they were first realised in 2004.[271] Several studies propose and numerically or theoretically evaluate possible designs,[272][273][274][275] with possible applications in surface-functionalised biosensing[276] or integrated fluorescence excitation and emission filtering.[277] However, the difficulties in manufacture arising from multi-layer heterogeneous materials to form the concentric refractive index profile makes fabrication for different target wavelengths more challenging.[278][279][280]

Bragg fibres are not be confused with fibre Bragg gratings, where the Bragg mirror is formed along the fibre axis by creating periodic variations of refractive index along some part of the fibre's length, often by post-processing.[281] Fibre Bragg gratings are generally used for sensing the change of some environmental measurand along the fibre, such as strain or temperature, and not for in-fibre measurements.[282]

2.1.6 Manufacturing of HC-PCF

How HC-PCFs are made

PCFs are made with a top-down manufacturing approach, where a macroscopic version is assembled and then successively scaled down by melting the glass (typically high-purity silica, possibly doped to alter its refractive index) and pulling it in a fibre drawing tower at close to 2000 °C (Fig. 2.8).[220] The first PCFs to be realised already used this basic approach, known as *stack-and-draw*, to produce a solid-core fibre with a hexagonally symmetric photonic crystal arrangement of air holes.[248]

Fibre manufacture begins with a *preform*, which is hand-assembled from high-purity silica capillaries or solid rods.[285][269] Through successive re-drawing, the geometry is scaled down to microscopic dimension. Fibre drawing is a continuous and highly scaleable process, easily producing kilometres of fibre per day.[220] While HC-PCF manufacture is in its early stages of becoming a commodity, it benefits heavily from the established body of knowledge and process technology from telecommunication fibre.[283]

Pressurised drawing

Application of tension and air pressure differentials between fibre sections allow further fine-tuning. An essential piece of physics governing the scaling-down during the drawing process is surface tension acting to drive geometry into an equilibrium.[286] The tendency for surface tension to close air gaps (and

(a) The preform, a hand-assembled capillary stack (for kagome fibre). [283]

(b) The cane, a millimetre-sized intermediary to be re-drawn. [283]

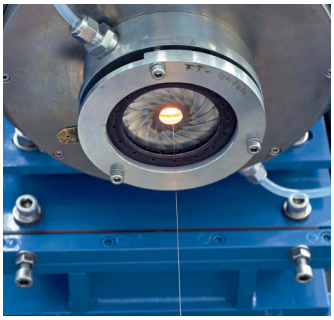

(c) HC-PCF leaving the furnace, ready to be coated. [284]

Fig. 2.8 Basic steps for manufacturing photonic crystal fibres. In a fibre drawing tower, a *preform* is heated until it becomes viscous. As it lengths by stretching, it simultaneously narrows in the transverse plane. The resulting scaled-down *cane* then undergoes the same procedure again, until the fibre geometry is scaled down by a factor of around 10^{-3} to reach microscopic (sub-millimetre) dimensions. Figure from [283, 284]. (*Fig. first referenced on p. 73*)

therefore reduce the surface area of the glass) can be balanced with an applied over-pressure of air within the fibre cane.

Surface capillary waves limiting surface roughness

Surface capillary waves form the ultimate limit to surface roughness even in the absence of any material defects.[287] Heated to its liquid state, the viscously-flowing silica exhibits phenomena that are familiar from liquid streams. Take, say, a thin stream of water running from the tap. As the volume flow is successively lowered, just before the transition from a steady stream to individual droplets occurs, the phenomenon of surface capillary waves is easy to observe. The stream thins and thickens periodically, with the bulges eventually separating and forming droplets. The same happens during the fibre drawing process, except that these periodic variations are frozen into the material as it cools down and solidifies. As the fibre being drawn cools down, temperature-dependent viscosity changes become significant, which adds to the complexity of this phenomenon. Model calculations show loss contributions of this phenomenon to be on the order of 30 dB km^{-1} for hollow-core photonic bandgap fibres,[288][289] and about an order of magnitude less for solid-core versions.[290] AR-HCFs are more sensitive to strut thickness variations, hence their guidance properties are expected to be affected even more by this effect.

Future developments

(HC-)PCFs are still a relatively young technology, and new generations such as the AR-HCFs we use continue to appear. Future developments include multi-

hollow-core fibres that would enable simultaneous dual polarisation analysis,[291] and conjoined-tube AR-HCFs with improved transmission properties by adding another surface to the Fabry – Pérot etalon.[292]

2.2 Microfluidics

Moving on from the optical theory, we cover next the fluidics in the microscopic regime. The largest channel size of our HC-PCF is 30 μm in diameter, putting it firmly into the field of microfluidics.

2.2.1 General theory

Fluid mechanics

Inert fluids behave according to Newtonian mechanics, whose laws are therefore sufficient to describe its behaviour. As with classical mechanics, while an ab-initio simulation of every particle (molecule) in the system is conceptually simple to state mathematically, the number of objects required to reach any useful precision quickly becomes infeasible. Fluid mechanics is the theory concerned with a reformulation of classical mechanics in terms of continuum mechanics using vector calculus, such that solutions to such problems become accessible, either numerically or analytically.

Fluidic laws of motion

The forces acting on a fluid volume element at any point can be categorised into forces proportional to volume (e.g. gravity), pressure gradient forces, and friction.[293] In this Newtonian picture of fluid motion, the net force on any fluid volume element gives its acceleration

$$\vec{a} = \frac{\mathrm{D}\vec{v}}{\mathrm{D}t} = \frac{\partial \vec{v}}{\partial t} + (\vec{v}\cdot\nabla)\vec{v}, \tag{2.2.1}$$

Navier-Stokes equation

where $\vec{v} = \vec{v}(t,\vec{x})$ is the velocity field, and $\frac{\mathrm{D}}{\mathrm{D}t}$ is the material derivative, taking into account the fact that the infinitesimal fluid element itself is moving.[294] The corresponding equation is known as the Navier-Stokes equation, which we write as (adapted from [295])

$$\rho\frac{\mathrm{D}\vec{v}}{\mathrm{D}t} = \sum(\text{all forces}), \tag{2.2.2}$$

$$\rho\left(\frac{\partial}{\partial t} + (\vec{v}\cdot\nabla)\right)\vec{v} = \eta\nabla^2\vec{v} - \nabla p + \vec{F}, \tag{2.2.3}$$

where η is the dynamic viscosity, $p = p(t,\vec{x})$ the pressure field, and $\vec{F} = \vec{F}(t,\vec{x})$ any external forces that might be present. It acts as the fluid-mechanical reformulation of Newton's second law.

2.2.2 Theory of microfluidic flows and the Reynolds number

As noted above, it is, in general, not feasible for Eq. (2.2.3) to be solved directly. Nonetheless, in the microfluidic regime, a powerful theory exists and enables understanding beyond simulation results.[296]

Reynolds number

While there is no single definition of where the boundary between microscopic and macroscopic flows is to be drawn, one key feature of microfluidic flows is that they are of low *Reynolds number*, exhibiting laminar and not turbulent flow throughout. The Reynolds number Re is a measure of the ratio between inertial and viscous forces, i.e. inertial effects dominate at low Re. It is given by

$$\mathrm{Re} = \frac{vd}{\eta}, \tag{2.2.4}$$

where v is the flow speed (take, say, a flow of one fibre traversal per second, $17\,\mathrm{cm\,s^{-1}}$), d is a characteristic lengthscale (take the diameter of our fibre core, $d \sim 30\,\mu\mathrm{m}$), and η is the kinematic viscosity of the fluid ($\eta = 1.00 \times 10^{-6}\,\mathrm{m^2/s}$ for water[297, Tbl. B.2]). Given these conditions, $\mathrm{Re} \sim 5$, which is much less than 2100, an empirical cutoff typically chosen[297] to distinguish turbulent and laminar flow regimes. Hence, throughout our system, inertial forces are negligible; there is laminar flow without turbulence; and consequently the fluid can be assumed to conform immediately to the geometry and forces it is exposed to.

Stokes (frictionless) flow

The fluid-mechanical regime that neglects inertial forces is known as *Stokes flow*.[295] Inertial forces correspond to the left-hand side of Eq. (2.2.3),[294] such that our governing equation becomes

$$\vec{0} = \eta\nabla^2\vec{v} - \nabla p + \vec{F}, \tag{2.2.5}$$

leaving only a balance of viscous, pressure and external forces, respectively. Connecting this equation to our experiments, we generally apply a pressure gradient with a syringe, and external forces are negligible (we discuss future applications based on external forces in the conclusions of Chapter 7). The viscous force, however, is generally a fixed property of the particles under study. We reflect this by rearranging the equation one more time, such that our experimental control amounts to varying the right-hand side of our final equation:

$$\eta\nabla^2\vec{v} = \nabla p - \vec{F}_{\mathrm{ext}}. \tag{2.2.6}$$

2.2.3 Laminar flow profile

The equation above can be solved analytically for certain combinations of geometry and boundary conditions. Take a cylindrical channel as an illustrative example. Given no external forces, we can argue from the infinite rotational symmetry that all $\partial/\partial\theta$ terms must vanish. Furthermore, steady-state conditions in an established flow enforce that $\partial\vec{v}/\partial z \equiv \vec{0}$, but not similarly for p. This enables us to perform separation of variables,

$$\nabla p(z) = \text{const.} = \eta\nabla^2\vec{v}(r,\theta). \tag{2.2.7}$$

Translational invariance means that the pressure gradient must be linear across the channel length L, and so the constant is determined to be $\Delta p/L$, giving rise to a Poisson equation (a Laplace equation with non-zero constant),

$$\nabla^2\,\vec{v}(x,y) = \frac{1}{\eta}\frac{\Delta p}{L}. \tag{2.2.8}$$

Flow velocity profile

The velocity field that solves the Poisson equation under no-slip boundary conditions is known as Poiseuille flow (Fig. 2.9), with a smooth, parabolic velocity distribution,[298][299]

$$v(r) = \frac{1}{4\eta}\,\frac{\Delta p}{L}\,\left(R^2 - r^2\right). \tag{2.2.9}$$

Beneficial optofluidic relationship between flow and mode profile

For our experiments, this means that the flow will be strongest at the centre of the fibre core, although the effect is weak since the aspect ratio of length L to core size $2r$ is large (see Fig. 2.9). Nonetheless, the fact that the fundamental mode in HC-PCFs concentrates the light power density (and hence light–matter interaction) to the same area where the analyte is exchanged most quickly, i.e. at the centre, is the ideal case for continuous-flow analysis.

2.2.4 Hydrodynamic resistance

In the microfluidic regime, the dynamic resistance presented by a channel is due to friction with the channel walls (as opposed to macroscopic flows which experience an additional friction from turbulence). Applied pressure will command a flow inversely proportional to the hydrodynamic resistance.

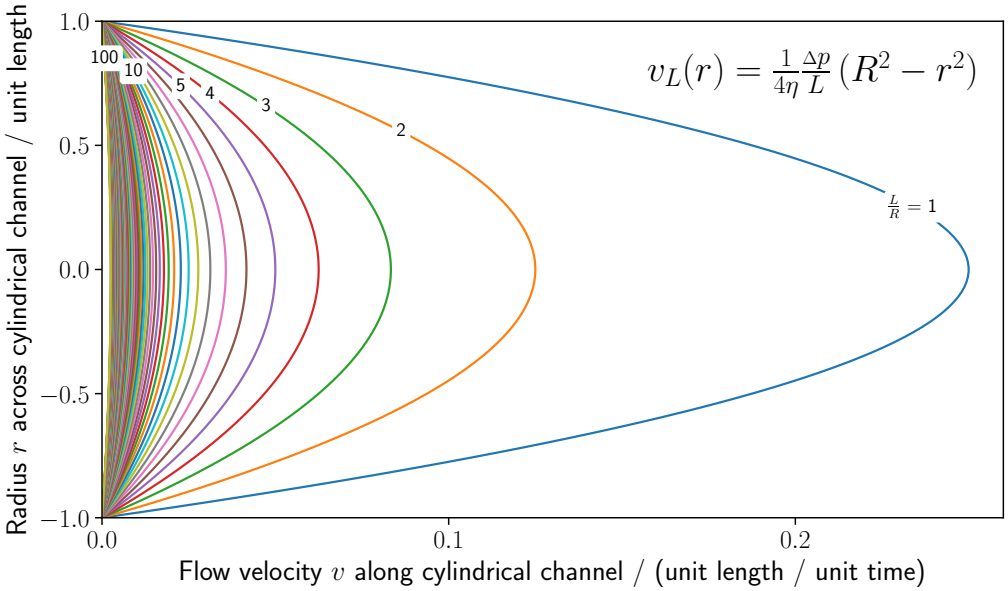

Fig. 2.9 Illustration of Poiseuille flow. This parabolic flow velocity profile is typical of pressure-driven flows, where the no-slip boundary condition requires the liquid to be stationary at the wall. As the channel aspect ratio L/R approaches infinity, the flow becomes relatively more uniform, such that in microfluidics it can be considered as a plug flow. In our HC-PCF, $L/R > 1000$.) (*Fig. first referenced on p. 78*)

Derivation of hydrodynamic resistance

Despite the HC-PCFs in our experiment posing a complex cross-section to the flow, a combination of dimensional analysis and perturbation theory allows a purely analytical derivation of the resulting hydrodynamic resistance. Due to its length, this derivation is presented in the supplementary information, in Section SI.7. Quoting the key result, the ratio of flow through the core relative to flow bypassing it through the capillaries is 0.55, i.e. slightly more than half the flow through the HC-PCF goes through the core.

2.3 Molecular mass transport

Any particle or molecule within the fibre will experience diffusion and convection. Understanding their relative contributions gives insight into the experimental environment we create by using HC-PCF.

Macromolecules in motion

2.3.1 Diffusion theory

As seen above, microfluidic flows such as those present in our experiments are well within the laminar flow regime, meaning turbulent effects do not complicate their analysis. However, instead diffusion becomes significant. To understand the relative strength of diffusion and convection, the dimensionless *Peclet number* Pe characterises this by their timescales,[144][300][301]

Peclet number

$$\mathrm{Pe} = \frac{\tau_{\mathrm{diff}}}{\tau_{\mathrm{conv}}} = \frac{l^2/D}{l/v} = \frac{lv}{D}, \tag{2.3.1}$$

where l is a characteristic lengthscale and v the fluid velocity. HC-PCFs are inherently designed to combine long pathlengths with microfluidic channels, giving aspect ratios of $2r/L \sim 100\,\mu\mathrm{m}/10\,\mathrm{cm} \sim \mathcal{O}(10^{-3})$ or more. It is therefore required to consider the transverse and axial directions separately.

In the transverse plane, no flow is present and mass transport is purely diffusive ($\mathrm{Pe}_\perp = 0$). Axially, we can find the flow at which diffusion and convection reach the same timescale,

Diffusion transversely and axially

$$\mathrm{Pe}_\parallel \stackrel{!}{=} 1, \tag{2.3.2}$$

which evaluates to sub-pL min^{-1} flow rates for BSA protein. For flow rates significantly below or above this number, the limit of pure diffusion or convection can be assumed. In practice, this number is so small that if any axial flow is present, convective mass transport will dominate over diffusive mass transport by orders of magnitude. In fact, even small temperature variations can drive flows by thermal volume expansion that are orders of magnitude larger than the diffusion component to mass transport (calculated in the supplementary, Section SI.4).

Consider now an individual particle in a dilute liquid. Its Brownian motion is modelled as a random walk, such that we can make statements only about

Mean-squared distance (MSD)

average values.[302] A particle moving within a medium for a time t traverses a mean-squared distance

$$\mathrm{MSD} = \left\langle \left| \vec{x}^2 \right| \right\rangle = 2 \cdot \mathrm{dim} \cdot D\,t, \tag{2.3.3}$$

where D is its diffusion constant, and dim is the dimensionality of the problem (since the movement in each Cartesian direction is independent, the MSD is a geometric mean).

Timescale of diffusion against a boundary

To illustrate, we will consider the example of a BSA protein diffusing radially. This is of interest to understand over what timescales such a particle initially located at centre of the fibre core will move around before it touches one of the fibre walls at $r_{\mathrm{core}} \approx 15\,\mu\mathrm{m}$. The diffusion constant is tabulated as $D_{\mathrm{BSA}} = 59\,\mu\mathrm{m}^2\,\mathrm{s}^{-1}$ (20 °C, water).[125] Over the course of 1 s, the root mean square displacement in two dimensions will be

$$\sqrt{\mathrm{MSD}} = 2\sqrt{Dt} \approx 15\,\mu\mathrm{m}. \tag{2.3.4}$$

Hence, we can expect such particles to come into contact with the fibre walls when left undisturbed for several seconds.

2.3.2 Diffusion simulation

Simulation of one protein molecule

To further understand and visualise the movement of proteins within our system, a diffusion simulation was written. It performs a random walk of fixed distance movement in all three spatial dimensions at every timestep, such that the movement speed is (statistically) given by the empirical diffusion constant. The results are shown in Fig. 2.10, and the chosen simulation parameters can be seen in the simulation terminal printout below.

```
Beginning simulation
Time step is 1 µ s
Distance step is 11nm
Particle type: m=66463Da, r_h=3.5nm, D=59 µ m^2/s
Simulation progress ■■■■■■■■■■■■■■■■■■■■■■■■■■■■■■■■■■■■■■■■ 100%
Finished after reaching maximum number of iterations: 2e+06
Simulation time elapsed: 2.0s
Wall time elapsed (simulation finished): 8.991859s
Simulation speed = simulation time / wall time = 0.22
```

```
Number of surface adhesion events: 1740
Evaluating optical intensity throughout the fibre...
Plotting diffusion particle trail...
 (downsampled by a factor of 2000 for clearer visuals)
Saving .py
Saving .npz arrays
Saving .pdf
Script finished. Wall time elapsed (final output): 15.523609s
```

In brief, the simulation started off a particle at the centre ($x = y = 0$, $z = L/2$), and for each timestep, moved the particle along a fixed distance step in a random direction for each axis independently. The distance step was calculated from the specified hydrodynamic radius and mobility. After each iteration, the light intensity at the particle's position is evaluated and recorded as the expected signal (which in experiments would be scatter, absorbance or fluorescence, which all depend linearly on the light intensity for single-photon processes). The light intensity profile was a normalised Gaussian scaled to a third of the wall radius. Finally, if a particle movement were to transport the particle beyond the fibre walls, it is instead kept stationary for a fixed configurable length (set to ten timesteps), and then moved away in both x and y by a distance step. The surface adhesion part of the simulation is considered to be a simple model of reversible adhesion and does not consider specific surface interactions.

From the simulation, it can be seen that a protein such as BSA has a high mobility relative to the HC-PCF core size ($30\,\mu\mathrm{m}$), but insignificant on these timescales relative to the HC-PCF length ($10\,\mathrm{cm}$).

Simulation of an ensemble of protein molecules

After having simulated the diffusion of a single BSA molecule in Fig. 2.10, the simulation was expanded to cover many particles with a view to being able to perform photon correlation spectroscopy (see Section 1.2.1). The results are shown in Fig. 2.11.

The diffusion simulation code was unaltered for each particle, but repeated for many particles ($n = 100$). The light intensity profile changed to a second order Bessel function, representing an LP11 mode. To explore what a feasible system to be explored experimentally might be, a large particle (protein) of $r_\mathrm{h} = 100\,\mathrm{nm}$ was chosen. The number of iterations (simulated time) was reduced to compensate for the large number of particles simulated. To limit the number of points visualised, the number of points displayed (but not simulated) was downsampled to a maximum of 100 per particle. The resulting simulation covers

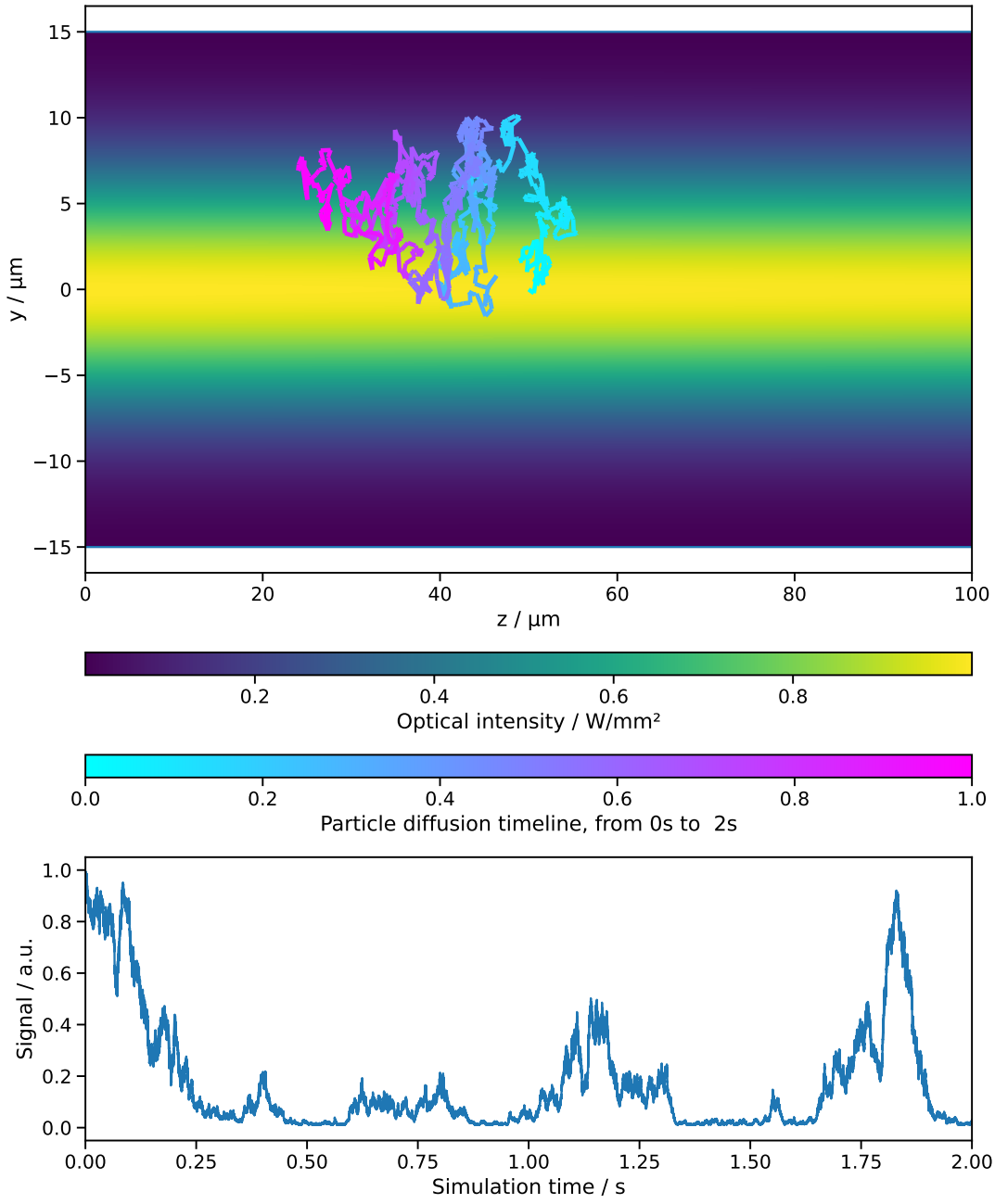

Fig. 2.10 Simulation of a single BSA molecule freely diffusing inside a HC-PCF core. The RMS displacement is $\sqrt{\mathrm{MSD}} = 8\,\mu\mathrm{m\,s}^{-1}$ per axis. To visually simplify the multidimensional data, only movement along y is shown, and the diffusion trail is downsampled to $1/2000^{\mathrm{th}}$.

(*Fig. first referenced on p. 81*)

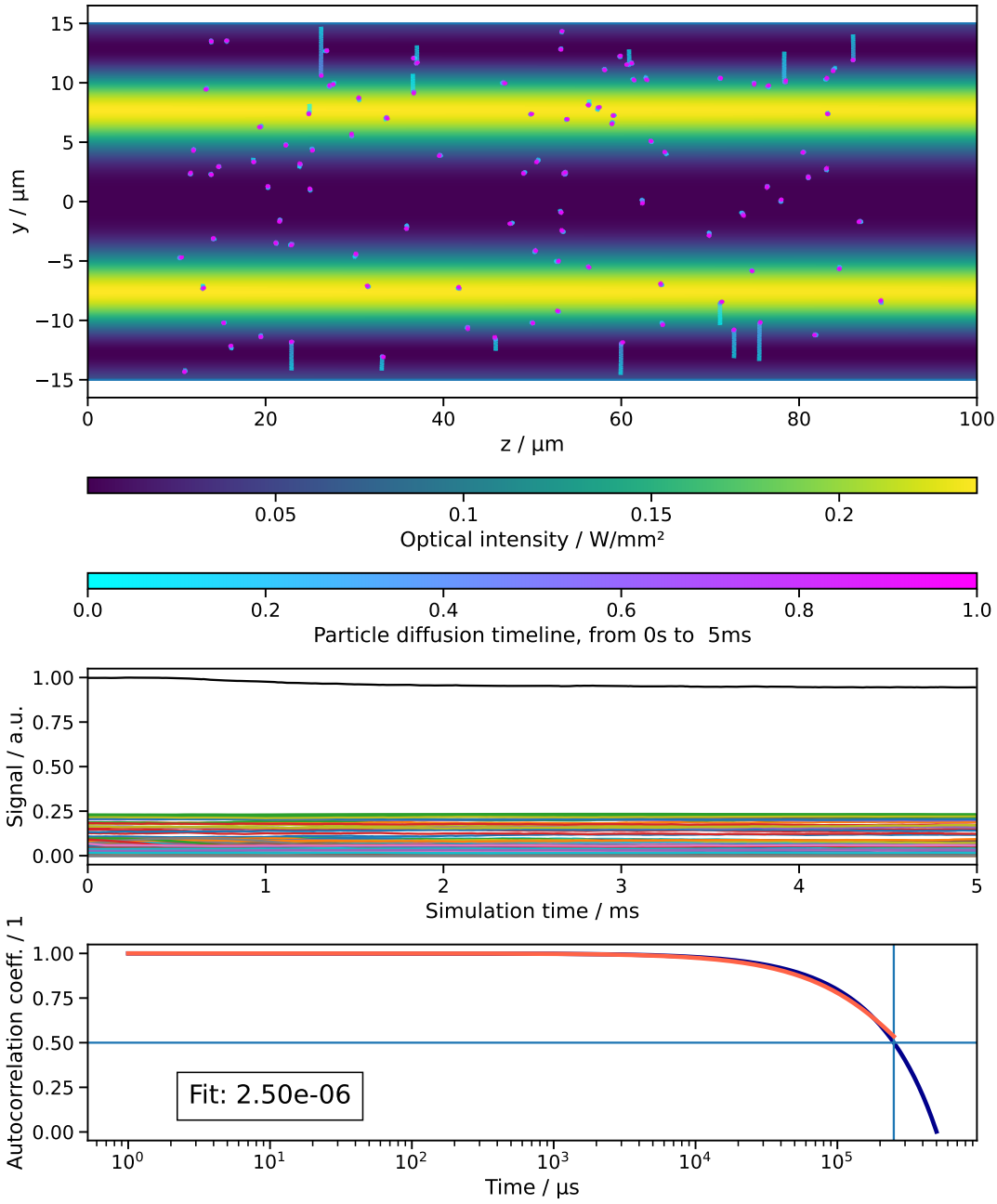

Fig. 2.11 Diffusion simulation of proteins inside a HC-PCF, with autocorrelation fit. The HC-PCF modal intensity profile was chosen to approximate an LP11 mode. As proteins diffuse through the fibre core, they experience different light intensity, which results in a change in signal. By measuring the signal autocorrelation over time, their diffusion behaviour can be studied.

(*Fig. first referenced on p. 82*)

five milliseconds of simulated time at 10 ns timesteps, which was chosen to correspond to the highest time resolution (pulse width) that the available PMT supported.

As the particles move through the varying light intensity, the resulting signal varies over time, and this variation is analysed with an autocorrelation. A commonly employed measure of the diffusion timescale is when the autocorrelation reaches half its initial value, which is indicated in the plot. If this system could be realised experimentally, this value could be used to identify changes in mobility and characterised with known samples.

Experimental aspect of PCS in HC-PCF

Experimentally, the main challenges are the weak scattering and/or fluorescence signals at dilute concentrations, and the simultaneously fast measurement times required that prevent larger integration times. Meanwhile, concentrations have to be kept dilute enough to be able to separate individual photon arrival events. A major challenge is to correct for systematic offsets (transmission losses, changes in light coupling, etc.) across sample changes.

Autocorrelation signal simulation

The simulation was written primarily as a learning exercise and to explore the idea. Ultimately, this work had to be paused after simulations and initial experiments due to a lack of time. It remains a promising avenue for future work to be implemented with the lessons learned since (discussed further in the Conclusions chapter). While not used directly in the remainder of this dissertation other than for building intuition, it is presented here nonetheless in its current form for others to build on this idea.

State of simulation

We note that the simulation has known shortcomings that were not corrected, as they would not change the results qualitatively. Most relevant are two points. First, if proteins meet the HC-PCF wall, they are 'unstuck' by simply moving them a short, random distance away. This is the cause of the unnaturally straight trajectories of some proteins. Second, light transmission is not modelled, i.e. photons can only scatter once in the simulation and are then losslessly transmitted. Finally, the problem is 'embarrassingly parallel' and could be accelerated orders of magnitude by re-implementation.

2.4 Materials and Methods

Concluding this background chapter, we characterise the HC-PCF and discuss methods surrounding its use. More specific materials and methods are discussed where used in the later chapters.

2.4.1 HC-PCF geometry

Imaging

In Fig. 2.12, we show a range of magnifications of the HC-PCF in brightfield light microscopy. The microstructured geometry, including the size of the sub-wavelength capillaries defining its waveguiding properties, has been shown before in Fig. 2.4, provided by Michael Frosz.

Additionally, further micrographs (Figs. 2.13 to 2.15) were taken with a Hitachi TM4000Plus tabletop-sized SEM, with kind assistance and training provided by Tobias Nägele of the Bioelectronics group.

2.4.2 HC-PCF preparation

Stripping the polymer coating

To prepare a length of fibre for experiments, the HC-PCF was first cut to the desired length plus an overhang of approximately 1 cm on each end. The HC-PCF was then scraped with a fresh scalpel on all sides to remove the polymer coating, consisting of UV-cured resin added during the fabrication process to improve the HC-PCF's mechanical properties (similar to how commercial fibres are packaged into multi-layer plastic jackets that avoid sharp bends). Since this polymer material is absorbent and fluorescent in the UV, it has to be removed for our experiments.

Cleaving the HC-PCF

Next, the HC-PCF is cleaved to the desired length. Since our HC-PCF is made from fused silica glass, it cannot be cut in an ordinary way. With a hardness on the Mohs scale of 7, the only (common) materials harder than quartz (and therefore able to scratch it) are, in increasing order, topaz, corundum (known as sapphire or ruby depending on inclusions), and diamond.

In Fig. 2.15, a HC-PCF was cut with razor blade, and imaged with SEM. The action of such a blade, when applied to the much harder silica fibre, does not result in cutting (i.e. incremental material separation), but rather crushing and shattering. This leaves end facet of the HC-PCF both ragged and uneven.

A HC-PCF with such a facet will perform poorly. First, the shattered pieces of glass are likely to embed themselves into the HC-PCF, later being released

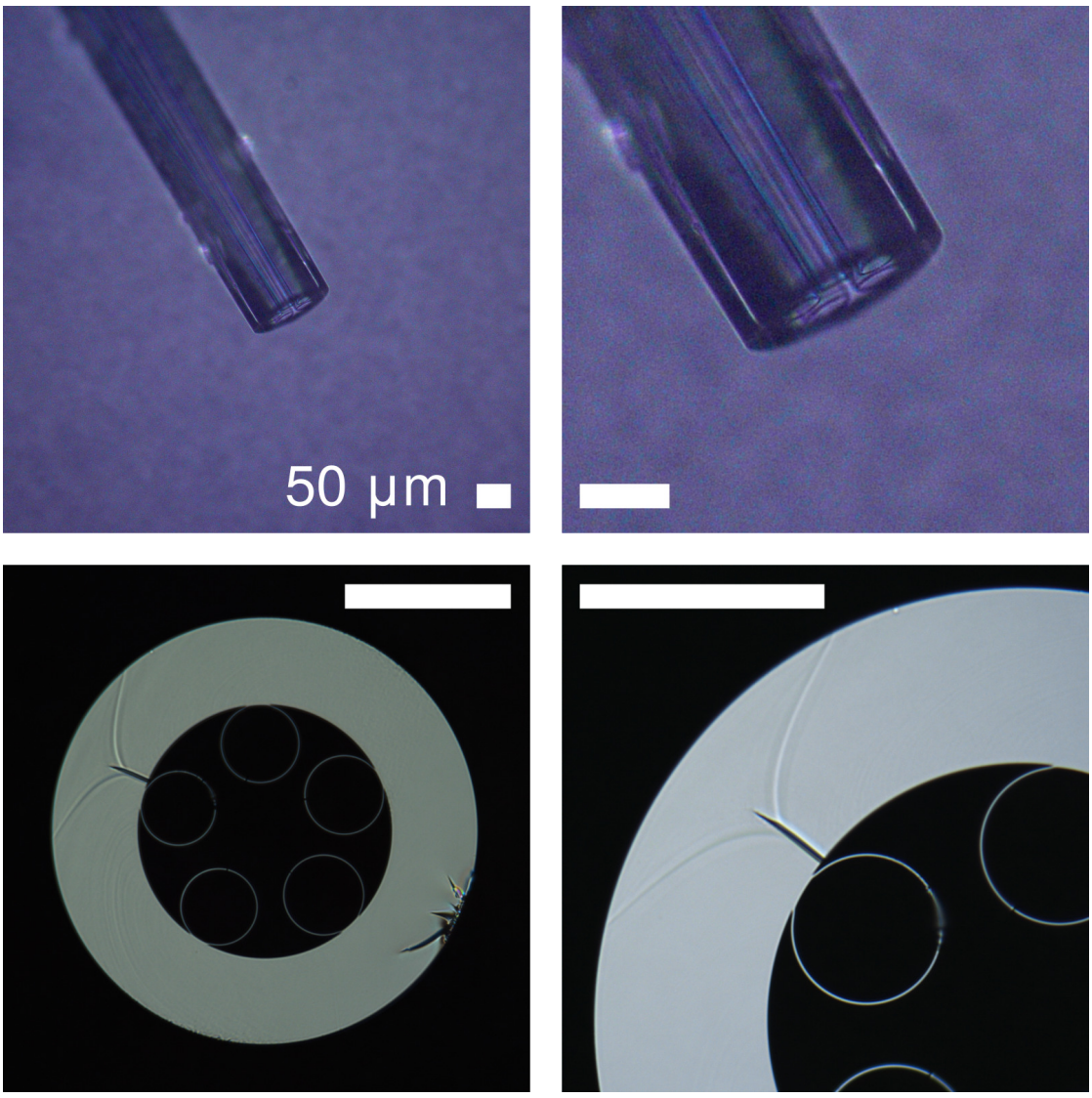

Fig. 2.12 Optical micrographs of a cleaved fibre facet. **Top:** side view and digital close-up. **Bottom:** Two different magnifications of the cleaved fibre facet. Note the symmetry of the fracture resulting from two shockwaves propagating in opposite directions and meeting again on the opposing side. (*Fig. first referenced on p. 86*)

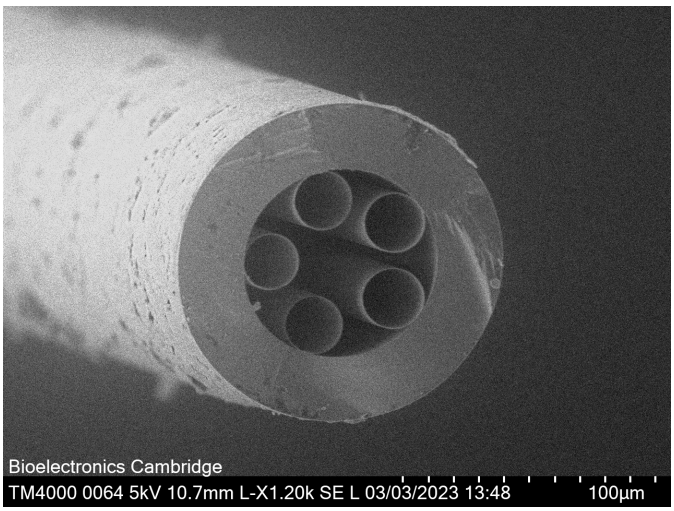

Fig. 2.13 SEM image of a cleaved HC-PCF facet. The cleave gives a smooth, planar surface for optical coupling. The comparatively clean cleaved fibre facet contrasts with the outer surface, which was scraped with a knife blade to remove the polymer coating added during fabrication. See also Fig. 2.14. (*Fig. first referenced on p. 88*)

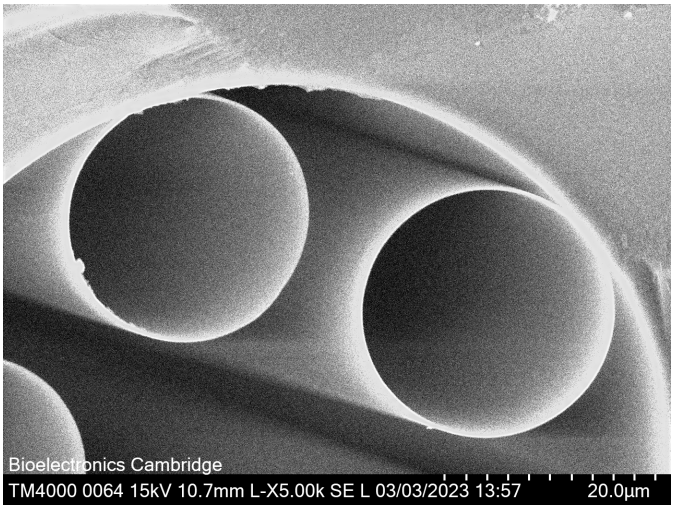

Fig. 2.14 SEM close-up of two HC-PCF cladding capillaries, corresponding to a higher magnification of Fig. 2.13. With a wall thickness of ca. 380 nm, these capillaries provide the antiresonant guidance properties of the HC-PCF (simulation: Fig. 2.5, experimental confirmation: Fig. 2.17). At this tabletop SEM's highest magnification and acceleration voltage, the glass thickness is still somewhat below the resolution limit. Note the charge build-up (bright regions) resulting from the insulating fused silica imaged with a high-vacuum mode. (*Fig. first referenced on p. 88*)

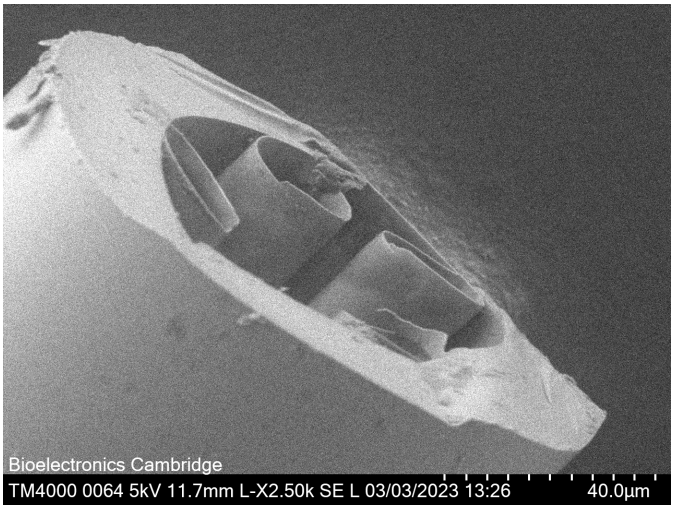

Fig. 2.15 SEM image of a knife-cut fibre facet, resulting in a rough, non-planar facet. Correspondingly, the outcoupled light will not form a well-defined mode, nor exit on-axis. Conversely, when used for incoupling light, efficiency would be low.

(*Fig. first referenced on p. 86*)

and causing blockages or scattering centres. Second, the out- or incoupling from this facet will be of low efficiency, as matching a mode to a complicated, rapidly changing surface is impossible without considerable technical effort (arbitrary wavefront shaping). When outcoupling from this facet, the light leaving this facet will exit off-axis and in ill-defined modes, reducing imaging quality and leading to inferior light collection ability.

Cleaving procedure

To cleave the HC-PCF, a handheld fibre cleaver (Fujikura CT-30) was typically used, or a handheld ruby-bladed pencil. Holding the fibre still, ideally under mild tension, a scratch is made with the blade. The fibre is then forced to fracture at this point by bending. The handheld fibre cleaver automates this process with a retractable blade that comes up against the HC-PCF held taut in rubber grippers. As inspected with a light microscope, this procedure leads to well-cleaved fibre facets with a success rate of around four out of five times.

Cleave quality analysis with confocal microscopy

To characterise the cleave quality, in addition to the SEM images presented above, confocal microscopy was used to analyse the planarity of a cleaved fibre facet. Shown with three images in Fig. 2.16, a z-scan (along the axis of the fibre, held vertically) in 500 nm steps was performed. In each image, the back-reflection of the microscope's illumination source is seen at a different position of the HC-PCF. Correlating the position of this back-reflection to the movement in z allows the tilt angle of the fibre facet plane relative to the microscope xy plane

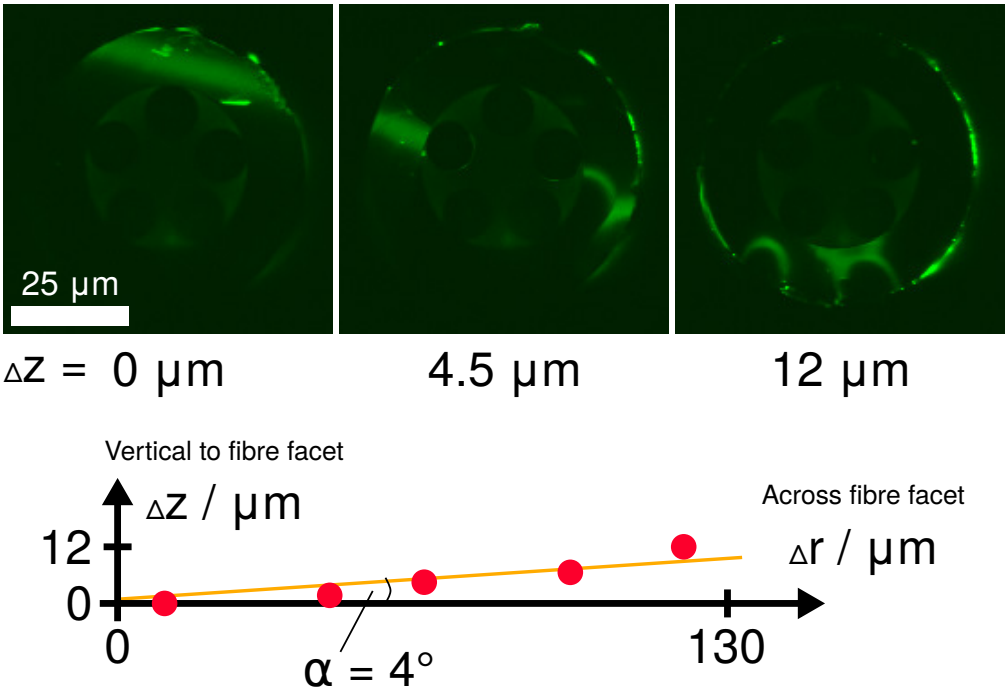

Fig. 2.16 Confocal microscopy z-scan of a cleaved HC-PCF. A back-reflection of the (epi-)confocal illumination is seen moving across the fibre facet as the z-axis is scanned. From the movement of this reflection, the angle between the microscope reference plane and the fibre facet plane for this cleave is calculated to be $\alpha = 4°$.
(*Fig. first referenced on p. 89*)

to be found, which was $\alpha = 4°$ for this particular cleave. The final data point at $\Delta z = 12\,\mu\text{m}$ is significantly above the others, suggesting a rough feature left behind by the cleave near the edge, which is also visible in the confocal image as two adjacent bumps.

Criterion for cleave quality

Because transport and mounting the HC-PCF to the confocal microscope rigidly enough to allow stable imaging is likely to introduce contamination (the HC-PCF was glued with UV-curing adhesive in the confocal images), as well as taking time for setup and imaging, confocal microscopy was only performed as a point of interest. In the experiments of this dissertation, the HC-PCF was inspected with a light microscope for obvious cleaving defects, namely: that there were no detached capillaries; that all of the facet were simultaneously in the field of view of a 20x objective, confirming that there is no strong tilt; that torch light on the opposite end of the HC-PCF was transmitted through the core and no scattering centres were visible along the fibre (which would indicate cracks); and

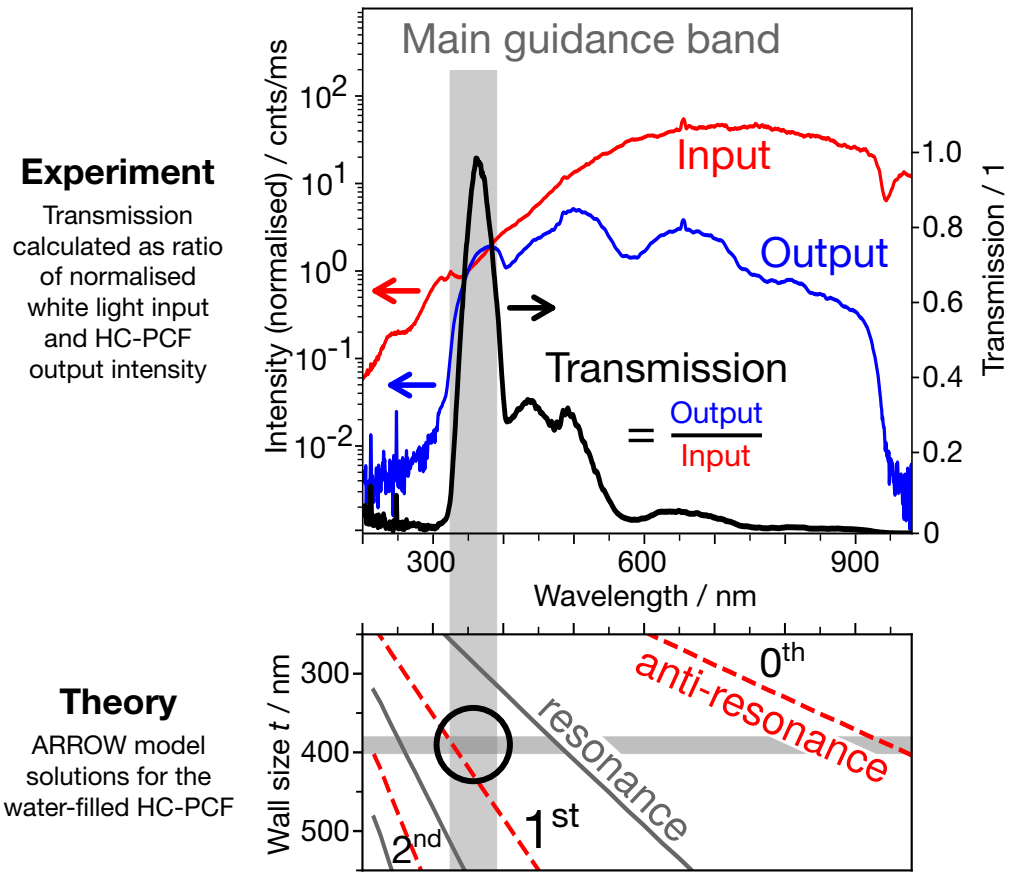

Fig. 2.17 Comparing the theoretical and measured transmission spectrum of the HC-PCF. The main guidance band corresponds to that used for the intrinsic protein fluorescence used in the experiments of Chapters 3 and 6, confirming the suitability of this HC-PCF for our application. (*Fig. first referenced on p. 91*)

that no obvious contamination was present. If this was confirmed, the HC-PCF was mounted in the actual experiment to evaluate its waveguiding performance.

2.4.3 Transmission properties

The HC-PCF's guidance properties were simulated numerically based on the ARROW theory in Section 2.1.3. We now confirm them experimentally, with a side-by-side comparison of the transmission measurement and the simulated theoretical transmission shown in Fig. 2.17.

Experimental setup

The transmission measurement was performed as follows. The light of a broadband halogen-deuterium light source (OceanOptics DH-2000) was butt-coupled to a water-filled HC-PCF of 25 cm length using a UV-grade multimode fibre. A water droplet was present to give a homogeneous interface between the two.

The output of the HC-PCF was first imaged to allow alignment (using a setup similar to the one described in Fig. 3.2), and then coupled to a spectrometer (OceanOptics QE6500) using another multimode fibre of the same type.

Confirmation of guidance at 350 nm

As a confirmation of its design for the intended application of collecting intrinsic protein fluorescence peaked at 350 nm, the HC-PCF indeed exhibits maximum transmission close to this wavelength, at 362 nm. At 350 nm, the transmission is still 80 % of the maximum. At higher wavelengths up to ca. 500 nm, the transmission shows a broad shoulder with around 30 % of peak transmission, after which it drops to below 10 % from 550 nm and up.

Absence of 0^{th} antiresonance

The measured output of the HC-PCF drops rapidly above 900 nm, which is surprising given that this is its zeroth antiresonance, where maximal transmission would be expected. However, there are several reasons that can explain this discrepancy and would suggest this could be a feature of the experimental setup rather than the HC-PCF itself. Of these, the multimode fibre used to couple the HC-PCF output to the spectrometer in particular can explain this effect.

This multimode fibre, transmitting through a solid glass core, suffers from material losses that increase roughly exponentially from a local minima at 650 nm towards shorter wavelengths (manufacturer data (link)). It is a high-OH type multimode fibre, designed for UV applications. By comparison, the equivalent low-OH fibre is one to two orders of magnitude more lossy at 350 nm, making measurement at this wavelength difficult. Hence, the high-OH version was preferred to confirm the HC-PCF's guidance properties at its target wavelength of 350 nm. Conversely, this means the high-OH multimode fibre performs worse at higher wavelengths; specifically, its loss from 850 nm to 950 nm increases by two orders of magnitude.

No broadband alignment

Finally, while the above effect dominates the losses, a further reason the guidance is lower than expected at higher wavelengths is the fact that the HC-PCF was aligned by imaging for the best achievable mode at 350 nm. The lenses used, being single-element UV-grade lenses, have comparatively high chromatic aberrations, meaning alignment far away from the target wavelength of 350 nm is expected to be poor. If maximum guidance at this wavelength range were of interest, the optical setup would need to be re-designed with added complexity to achieve broadband coupling.

Cutback measurement

The gold standard for testing the performance of a waveguiding fibre is to perform a cutback measurement.[292] It was attempted to perform such a mea-

surement in our setup (specifically, in the design iteration used in Chapter 4). Several difficulties were encountered, detailed below.

Crucially, the idea of a cutback measurement is to shorten the outcoupling side of the HC-PCF by a known length without changing the incoupling side; measuring the transmitted light; and then repeating this procedure several times to plot the loss per unit length. In this way, the loss per unit length can be found independently of the incoupling efficiency (which will be a non-zero offset in the loss graph), as incoupling efficiency is prone to variation based on cleave quality and the light source itself.

In our setup, knowing that the HC-PCF is sensitive to bending loss, much design work was done to fix the HC-PCF in place rigidly and straight (described in Section 4.2.2), such that physical access to the HC-PCF for performing the cutback was significantly restricted. Furthermore, the experiments used a short length (ten centimetre) to begin with, compared to how cutback experiments are performed (metres). Nonetheless, a cutback experiment was attempted, but it was not possible to cleave the fibre in place without disturbing the alignment. If such a measurement were desired, it should be performed in a purpose-built setup with sufficient access to the HC-PCF for in-place cleaving.

Comparison to non-waveguiding capillary

Why not a capillary?

As a result, it was decided to not sink further time and resources into optimising this characterisation measurement. Nonetheless, to answer a question often raised during conference discussions, it is of interest to compare our HC-PCF (a microstructured glass capillary) with an ordinary glass capillary (non-structured) as a reference point for the advantage of a waveguiding geometry over a plain microfluidic channel. A direct comparison of the HC-PCF to a simple capillary in the setup used in Chapter 6 was performed. As the closest available match to the HC-PCF's size, a 50 µm inner diameter, outer diameter 130 µm capillary was used. The best achieved mode out of a triplicate experiment is shown in Fig. 2.18.

Taking into account that the LED power modulation was set to its maximum setting, the light transmitted through this capillary was within a few percent of that typically achieved in our HC-PCF in the same setting. However, capillary waveguide losses scale as r^{-3} (Section 2.1.1), and taking this scaling into account, the 60 % larger capillary scaled down to the same size would guide only $(30\,\mu\text{m} / 50\,\mu\text{m})^3 = 0.22$ times as well.

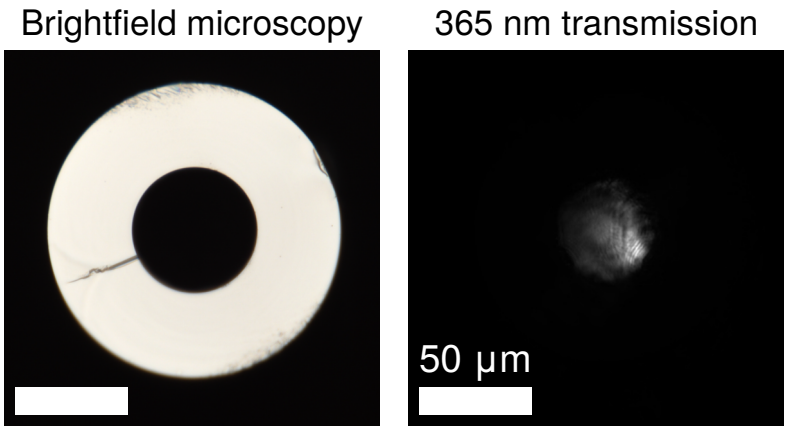

Fig. 2.18 Fundamental mode image in a plain glass capillary. Asymmetry of the mode is attributed to an imperfect cleave, which was the best achieved out of several tries. See text for details.
(*Fig. first referenced on p. 93*)

This single measurement does not represent a thorough characterisation, and a like-for-like quantitative comparison would require further work (the current setup was optimised for HC-PCF experiments). Nonetheless, the result is generally in agreement with the expected better optical performance of a waveguide compared to a plain microfluidic channel.

3 | Label-free Intrinsic Protein Fluorescence

Using the ability of a hollow-core photonic crystal fibre to collect and guide light over an extended region irradiated with ultraviolet light, a system quantifying protein solutions label-free is implemented. We show how such a system can operate as part of a microfluidic circuit, flowing continuously over several hours.

3.1 Motivation 96
3.2 Experimental Method 97
3.2.1 Experimental setup 97
3.2.2 Characterisation of excitation light 102
3.3 Results 107
3.3.1 Spectral comparison 107
3.3.2 Key experiment: Label-free quantification of intrinsic protein fluorescence in HC-PCF under flow 109
3.4 Discussion and outlook 113
3.4.1 Summary of findings 113
3.4.2 Possible improvements 113

Contributions *This chapter corresponds to the publication Heck et al., Label-free monitoring of proteins in optofluidic hollow-core photonic crystal fibres.*[1] *I designed and built the experimental setup, performed the experiments and data analysis, and wrote the first complete draft of the publication. Ermanno Miele provided advice on experiments throughout the project. Ralf Mouthaan carried out the waveguide mode simulations. Michael Frosz supplied the HC-PCF used in this dissertation. Tijmen Euser and Tuomas Knowles supervised this work and provided guidance and advice throughout.*

Jan R Heck et al. 'Label-Free Monitoring of Proteins in Optofluidic Hollow-Core Photonic Crystal Fibres'. In: *Methods and Applications in Fluorescence* 10.4 (1st Oct. 2022), p. 045008. ISSN: 2050-6120. DOI: 10.1088/2050-6120/ac9113

3.1 Motivation

Why develop such a system?

Following the general motivation presented in Chapter 1, we want to study proteins label-free at low volumes. For such a microfluidic system to achieve high throughput, continuous flow operation is essential. Having the detection in such a system occur label-free under continuous flow has two advantages. First, it avoids the possible effects of labels on the system under study, as discussed in Section 1.2.1. Second, if the proteins do not need to be labelled, they can pass through the system unaltered for downstream collection or further measurements, and the lack of a labelling step simplifies in-circuit integration with other systems.

Aims

Translating these conditions into requirements, we want a label-free and in-situ, continuous flow method of measuring proteins at microfluidic volumes. Here, we investigate HC-PCF for this purpose. Exciting the proteins' intrinsic fluorescence around 280 nm as they flow past a 10 cm detection region, we use the fluorescence emission to quantify the protein's concentration as we change samples over one order of magnitude. The system operates in continuous flow over several hours.

Concept

In Fig. 3.1, we conceptually sketch the operating principle for such a HC-PCF-based system.

The HC-PCF serves as a microfluidic channel which is irradiated from the side with ultraviolet light. This light excites the intrinsic fluorescence of proteins

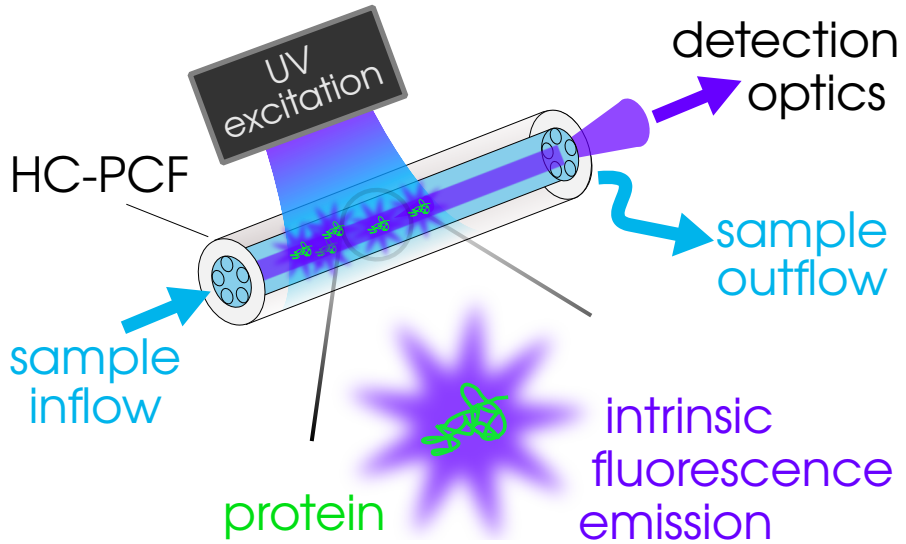

Fig. 3.1 Concept drawing for using HC-PCF for the continuous-flow label-free detection of proteins under ultraviolet light side excitation.
(*Fig. first referenced on p. 96*)

flowing through it. As an optofluidic waveguide, the HC-PCF collects and guides this fluorescence. The HC-PCF thereby acts as an extended detection volume, integrating the signal over many centimetres, such that when the end facet of the HC-PCF is imaged and analysed as in a standard fluorescence microscope, this imaged, outcoupled light has been collected from an orders of magnitude larger volume than the focal volume of the objective itself. This is the key principle by which HC-PCFs increase detection sensitivity, in addition to their other favourable characteristics stemming from having a waveguiding microfluidic geometry.

3.2 Experimental Method

Context within the PhD

In the timeline of the PhD, the work of this chapter represents the first major completed piece of research. It was preceded by much explorative and preparatory research, as well as learning of experimental skills in the laboratory, which find their way into this dissertation only indirectly. In part, this long lead-up to the first piece of published research was precipitated by the absence of a 280 nm laser (cf. Section 1.3), which required new approaches to be found, evaluated, and characterised, before the one described below was settled on.

3.2.1 Experimental setup

The setup, as an optofluidic experiment, consists of optical and (micro-)fluidic parts, together with methods of data acquisition and analysis. An experimental setup diagram is shown in Fig. 3.2, with an illustrative photograph in Fig. 3.3. We first describe the main system components, before discussing various aspects in more detail.

Optical setup

Overview

The optical train consists of the HC-PCF, embedded into optofluidic interconnect cells on both sides to allow liquid infiltration while retaining optical access through fused silica windows (described in detail in Section 3.2.1). Through a set of UV-compatible optics and bandpass filters, this fluorescence is then imaged by a camera (CAM), and the light intensity analysed by a photomultiplier tube (PMT).

HC-PCF

We refer to Section 2.4 for details about the HC-PCF itself. Its ends are held and sealed into the optofluidic interconnect cells on either side by threading it into

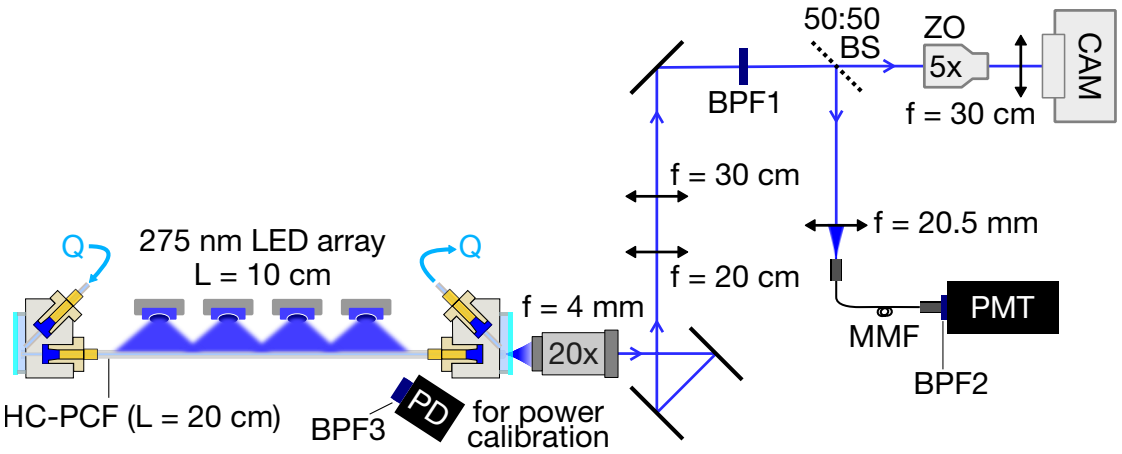

Fig. 3.2 Experimental setup, described in detail in the text. In brief, a protein solution flows (Q) through a HC-PCF while being irradiated by ultraviolet light ($\lambda_{exc} = 275\,nm$), causing the emission of intrinsic fluorescence ($\lambda_{ems} = 350\,nm$). This fluorescence light is collected and guided by the HC-PCF, where it can be imaged at the fibre end facet (20x objective and several lenses), band-filtered (BPF1,2), and analysed with a camera (CAM) and photomultiplier tube (PMT).
(*Fig. first referenced on p. 97*)

short (3 cm) sections of PEEK (an inert polymer) tubing, which are fastened into the stainless steel cells by by screw fittings tightening a conical ferrule seal. The HC-PCF was inserted until it was within less than a millimetre of the fused silica window, such that the working distance of the objective is sufficient to focus on the fibre end facet through the 1 mm thick window.

Imaging optics

Optics in the UV are generally of lesser performance, and higher cost, than equivalent ones in the visible wavelength range. Since the dopants used to lower the melting point and adjust refractive indices in commonly-used optical glass (e.g. borosilicate, such as BK7) absorb strongly in the ultraviolet, the performance of regular lenses drops rapidly below the visible (400 nm). For example, transmission through 1 cm of BK7 is below 30 % at 300 nm, dropping rapidly for shorter wavelengths (the manufacturer does not specify transmission for even shorter wavelengths).[261] More importantly, even if the longer wavelength fluorescence light might be transmitted sufficiently well, any residual excitation light will be absorbed strongly and partially re-emitted as fluorescence at wavelengths similar to intrinsic protein fluorescence. This leads to additional background noise, which can quickly reach levels comparable to the intrinsic protein fluorescence signal. Hence, all optical components are made of fused silica substrate. Where available, lenses had an anti-reflective coating for the UV wavelength band.

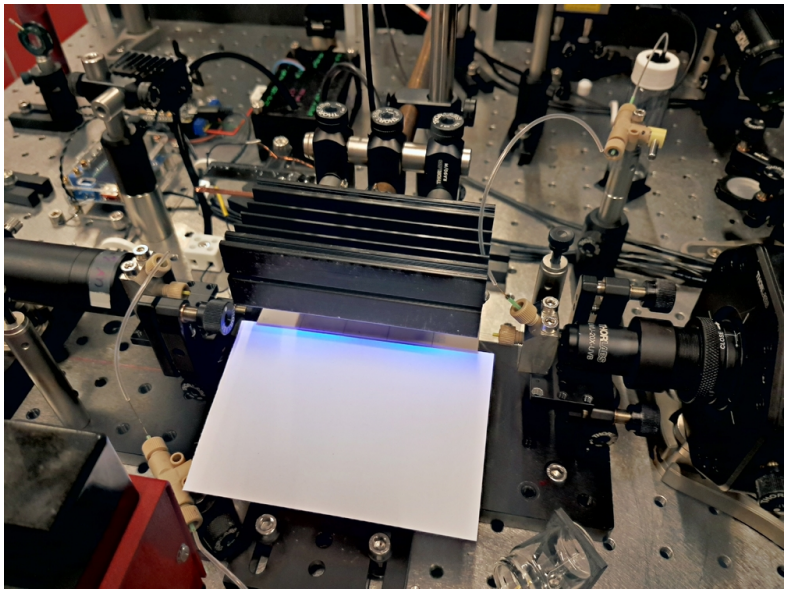

Fig. 3.3 Photograph of the experimental setup's HC-PCF section, where intrinsic protein fluorescence is excited within the HC-PCF. The 275 nm LEDs are mounted on the underside of the black heatsink in the middle. A piece of paper has been added to visualise the UV light through the paper's visible blue fluorescence. On the left and right, the optofluidic interconnects are mounted on pitch–roll stages, which in turn sit on a position-indexed removable breadboard to transport the assembly for fibre preparation. The right side of the HC-PCF is imaged by an UV objective (see Fig. 3.2).
(*Fig. first referenced on p. 97*)

We refer to [1] for a detailed component list of the optics and equipment part numbers. In brief, one end facet of the HC-PCF is imaged by a 20x imaging objective and passes through a set of discrete single-element lenses that form a beam-expanding $2f$ telescope. The collimated beam is then bandpass-filtered and distributed by a 50:50 beamsplitter to both a camera and a photomultiplier tube, detailed below. The optical beampath from HC-PCF to PMT is designed such that the $\sim 30\,\mu\text{m}$ HC-PCF core is imaged onto the $50\,\mu\text{m}$ multimode fibre (MMF) via the $M = 30\,\text{cm}/20\,\text{cm} = 1.5$ magnification of the $2f$ telescope. The camera has a variable-focus 5x beam expander in addition to this magnification. The telescope also serves to give a focal plane where spatial filtering by an aperture is possible, which was useful during optical alignment but not used during the experiments described here.

Bandpass filters

Before being distributed to the camera and PMT by the beamsplitter, the light travels through the $(357 \pm 22)\,\text{nm}$ bandpass filter BPF1 to select the fluorescen-

ce light. The suitability of this bandpass filter for the target intrinsic protein fluorescence spectrum is quantified and discussed below in Section 3.2.2. The filter was placed into infinity space of the optical beam path, as required to avoid angle-dependent spectral shifts in the bandpass.

This means the camera sees only the fluorescence light, up to the rejection ratio of the filter (specified as better than OD 4 at 275 nm by the manufacturer (*link*)), as does the PMT. The two measurements therefore correspond to each other.

The PMT has an identical BPF2 in front of it. This was done primarily such that the PMT would not be oversaturated by room lights when uncovered, and because another filter was available and thus increased the rejection ratio at the cost of a small amount of reflection losses.

Power calibration

Positioned next to the HC-PCF, a photodiode (PD in Fig. 3.2) covered with a (280 ± 5) nm bandpass filter (BPF3) continuously measures the excitation power. Nominally, the power setting remains unchanged and the LEDs are only switched off and on when changing samples (to avoid exposure of the experimenter with ultraviolet radiation when removing the light shielding). However, LEDs change in power efficiency (and spectrum) with temperature. Hence, to quantify and correct for this effect, the above photodiode was installed, in addition to pre-heating the LEDs before the first measurement.

In Fig. 3.10, the normalised signal from this photodiode is shown in blue. This signal, corresponding to the irradiation power (as seen through the bandpass filter), is seen to vary by no more than 5 %. While small and close to the noise, the above effect can be seen in the measured fluorescence light, where the output power of the LEDs is temporarily higher when turned on again as they cooled down slightly while turned off and the light shielding opened, allowing ambient air to enter.

The impact of turning the light source on and off was visible at a few percent, but quickly diminished if the light source was already preheated and only switched off briefly. This is in part due to the system being driven by a constant-current power supply. As a first approximation, the power output of an LED is proportional to the current flowing through it (and not its power dissipation), as each electron passing the semiconductor junction's bandgap has a certain probability of causing the emission of a photon. A constant-current source counteracts most of the temperature-driven changes in LED efficiency by increasing the power (via increasing the voltage) to maintain the same current and hence radiant flux. As

a conclusion from these results, in the experiments of later chapters, the power reference was omitted in favour of system simplicity.

Camera

The camera used was a 16 bit sCMOS Photometrics Prime 95B (*link*). It was selected based on availability, its large-area sensor ($(11\,\mu m)^2$ pixels), and relatively high quantum efficiency down to the UV (QE 40 % at 350 nm). The camera exists in a UV version, which would increase sensitivity by around 75 %.

Camera exposure time was chosen to fill the dynamic range available (16 bit). For the experimental data shown in this chapter, the exposure time was 1 s. The light sensitivity of the camera is evaluated quantitatively later in Section 4.2.1.

PMT

The photomultiplier tube (PMT) used to measure the fluorescence light was a Hamamatsu H1068201 (*link*). Its peak sensitivity is at 400 nm, and it retains a sensitivity greater than $2 \times 10^5\,s^{-1}\,pW^{-1}$ at the wavelength of interest, 350 nm. The dark count rate is negligible in our experiments at below $1 \times 10^3\,s^{-1}$. This is confirmed by the signal dropping to close to zero when turning off the excitation light (Fig. 3.10).

The noise floor in our measurements (Fig. 3.10) therefore corresponds to 400 fW, with the lowest concentration measured (100 nM) corresponding to an increase of 75 fW. The probable source of the background (noise floor) is residual fluorescence of optics, and the long-wavelength tail of the excitation light.

Microfluidic setup

In overview, the microfluidic setup consists of a glass syringe driven by a syringe pump, fed through fused silica tubing into the HC-PCF via optofluidic interconnect cells on both ends, and then led into a waste outlet via more tubing.

Materials for microfluidic components

Throughout, all wetted surfaces were either glass, steel or PEEK polymer. The syringe was a glass barrel, PEEK plunger syringe for minimal protein adsorption, and fused silica tubing (typ. 350 µm inner diameter) was preferred over polymer tubing for its stiffness resulting in better hydrodynamic compliance, i.e. more directly transmitting pressure changes.

Optofluidic interconnect cells

The optofluidic interconnect cells (also referred to as pressure cells) were manufactured by the Cavendish Laboratory workshop after a CAD design made by the author, shown in Fig. 3.4. The optofluidic interconnect design was limited by the working distance of the objective. Thicker glass is preferred to reduce bending when liquid pressure is applied, as bending leads to wavefront distortion and focal shifts. The window used was cut to size from a 1 mm thick fused silica microscope slide using a diamond tile cutter, and glued onto the metal cells with

a large contact area, leaving only a small channel for liquid to flow through from tubing to HC-PCF, visible in the last photograph of Fig. 3.4.

Sample exchange procedure

To exchange the sample solution, the syringe was switched for an identical syringe with the new solution. Between the syringe and the HC-PCF, a four-way valve was used to stop the flow during the change of syringes. This valve was also used to pre-flush tubing after a syringe change to counteract air introduced into the system when opening a line.

Protein sample

BSA as a model protein

Bovine serum albumin (BSA) was chosen as the protein for this study. It is a commonly used model protein thanks to its well-characterised nature,[303] which in turn is a result of its ready and inexpensive availability. It is an inert plasma protein that has a long shelf life and can be readily freeze-dried.[125] Its hydrodynamic radius is $r_\mathrm{h} \approx 3.5\,\mathrm{nm}$ at a molecular weight of 66 463 Da, with its shape being ellipsoidal.[304][305] However, in solution it can form complexes, primarily dimers and trimers.[306] The extent of complexation depends strongly on the solvent properties and concentration. The relative abundances in a specific system studied by Young *et al.* were found to be $88.63\%, 9.94\%, 1.18\%$ and 0.25% for the mono-, di-, tri- and tetramer, respectively, using interferometric scattering mass spectrometry (see Section 1.2.1).[80]

Preparation protocol

Protein solutions were freshly prepared on the day of experiment from lyophilised BSA powder dissolved into PBS buffer. A stock solution (few micromolar) was prepared from a measured mass and volume, vortexed for approximately 5 s, and then aliquoted into the desired concentrations.

3.2.2 Characterisation of excitation light

Choice of excitation wavelength

The intrinsic fluorescence for BSA protein has its absorption peak at 280 nm, and the same wavelength would therefore be the expected choice for the excitation light source. However, a slightly different wavelength of 275 nm was used instead. As discussed in Section 1.3, the preferred choice of excitation by an ultraviolet laser was not available. Two different UV LEDs were experimentally evaluated instead (Bolb, S6060-DR250-W275-P100 and Roithner Lasertechnik, UVR280-SA3P), and the choice for the 275 nm ones used in these experiments is explained and experimentally confirmed below.

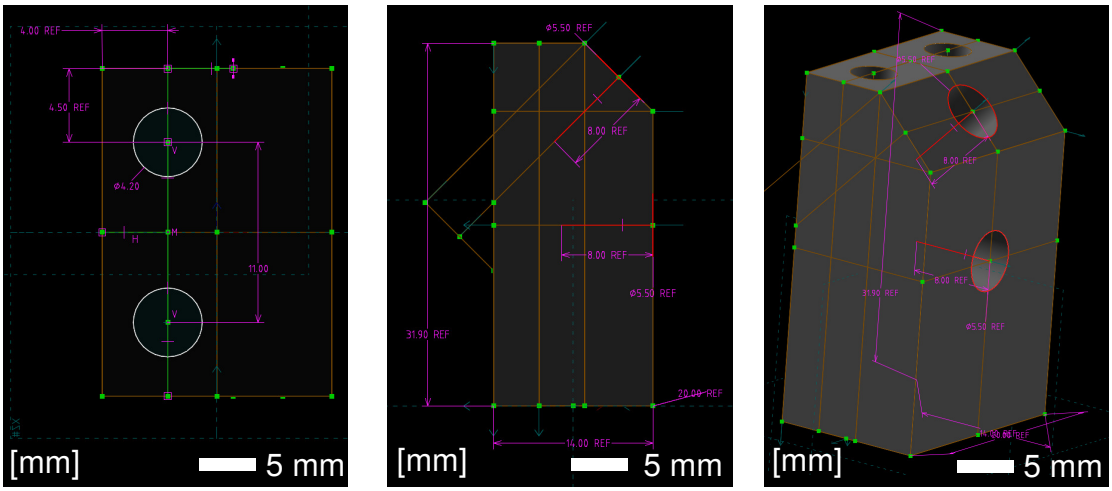

(a) Top view (b) Side view (c) Isometric view

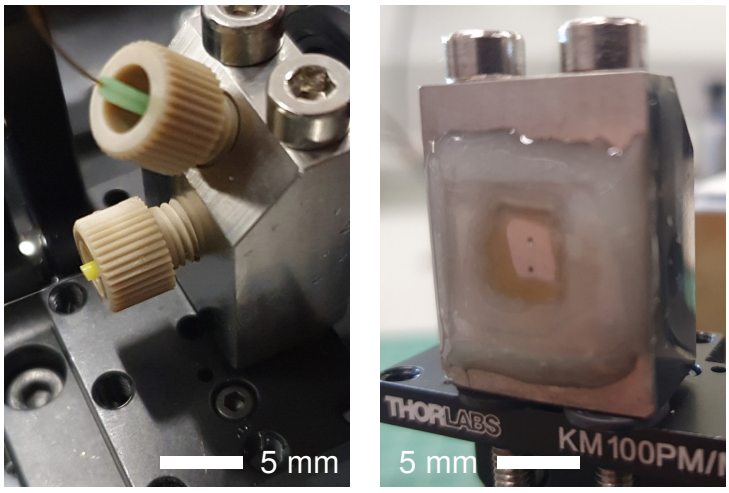

(d) Photograph (e) Photograph

Fig. 3.4 Optofluidic interconnect design and realisation. **Top row:** CAD drawings of the cell showing design and dimensions. **Bottom row:** Photographs of the cell with a HC-PCF (inside the yellow polymer sleeve) connected to fused silica microfluidic tubing (green). The flow from the tubing reaches the HC-PCF through a reservoir formed between the metal and a quartz slide, which also provides optical access. (*Fig. first referenced on p. 101*)

Excitation at 275 nm vs. 280 nm

From a search of suitable LEDs available on the market, it became clear that LEDs at 275 nm were available at much higher irradiance (100 mW) than 280 nm LEDs (10 mW), as well as being sold in more favourable lensing characteristics. The higher power is likely a result of what semiconductor material combinations are commercially mass-produced, and their respective bandgap energies. However, since the intrinsic fluorescence of tryptophan has its excitation peak at 280 nm, the 275 nm LEDs will excite the fluorescence less efficiently. Since emitted fluorescence is the product of incoming optical power with absorptivity and quantum efficiency at that wavelength, the loss of fluorescence emission by using a 5 nm off-peak wavelength was quantified in Fig. 3.5. A UV-VIS absorption measurement alone would have not been sufficient as not all absorption leads to fluorescence with the same quantum yield, and hence measurements were performed in a commercial cuvette fluorimeter instead. The sample was the same BSA protein solution as used in the experiments, at the highest concentration also measured in HC-PCF (1 μM). This concentration results in 10 % transmission through the 1 cm cuvette at 280 nm, avoiding a strong inner filter (re-absorption) effect and reducing stray scattered light.

Relative fluorescence intensity

From Fig. 3.5, the measurements showed that the peak fluorescence emission shifted down by 12 % when using the off-peak excitation wavelength at 275 nm. The peak shift was not significant at the resolution of the instrument. The sharp, narrow peaks on the left of the spectrum correspond to stray excitation light scattered into the detection arm of the instrument.

Using peak values, the 275 nm LEDs are therefore

$$(1 - 12\%) \cdot (100\,\mathrm{mW}/10\,\mathrm{mW}) = 8.8 \tag{3.2.1}$$

times as efficient at producing intrinsic protein fluorescence than the on-peak 280 nm LEDs, and were consequently chosen for the experiments.

Excitation spectrum

The spectrum of the UV LEDs was measured in Fig. 3.6. An UV-compatible multimode fibre (50 μm, 0.22 NA) was placed in the fibre plane facing the LEDs. The multimode fibre was moved far enough away (ca. 5 cm) such that the light intensity was within the spectrometer's dynamic range. This approach was favoured over dimming the LEDs to remain close to experimental conditions (esp. the LED equilibrium temperature), and the LEDs were preheated over at least an hour for the same reason.

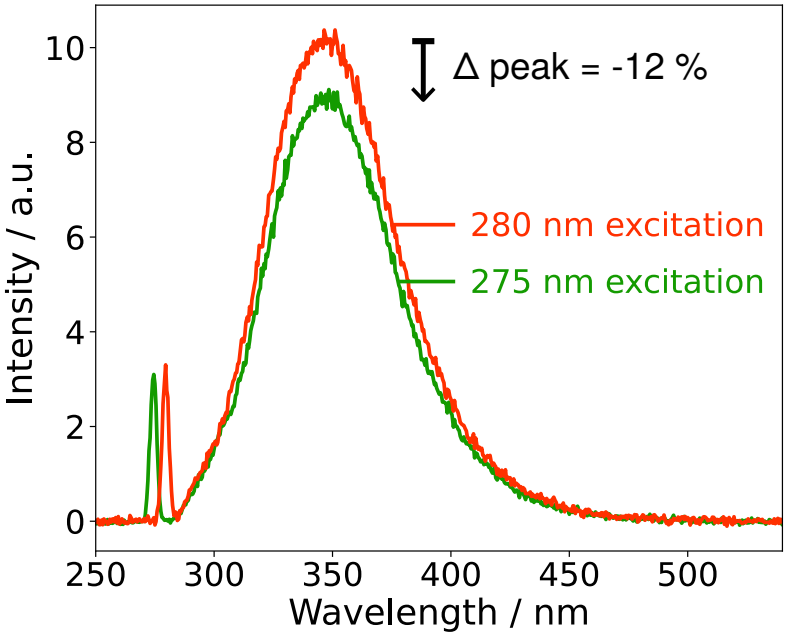

Fig. 3.5 Comparison of 280 nm and 275 nm fluorescence excitation wavelengths in a cuvette for intrinsic fluorescence of BSA protein. This graph confirms the suitability of using 275 nm excitation in our setup, despite the absorption peak being at 280 nm. In particular, much stronger LEDs are available at 275 nm, more than compensating for the weaker fluorescence efficiency.
(*Fig. first referenced on p. 104*)

The LEDs were seen to have a nearly symmetrical emission spectrum around a peak at 274 nm. The FWHM was 11 nm (the manufacturer specifies the FWHM in close agreement at 10 nm, varying with temperature), such that the LEDs have ca. 50 % of their peak intensity at the fluorescence absorption maximum of 280 nm. For more detail, a spectral comparison is given in the supplementary, Fig. S-4.

Excitation spatial homogeneity

After evaluating the spectral properties of the LED, its irradiance power and spatial homogeneity thereof were measured. Again, the measurement was performed in the fibre plane as above. Measurements were taken with a calibrated photodiode power meter of circular 1 cm^2 active detector area. A (280 ± 10) nm bandpass filter was mounted on top. This setup is the same as the one used for power reference measurements (Section 3.2.1), but placed in the position of the fibre instead of adjacent to it. The detector is moved in small increments and measurements taken at each position, giving a z-axis line scan. The resulting irradiation profile is shown in Fig. 3.7.

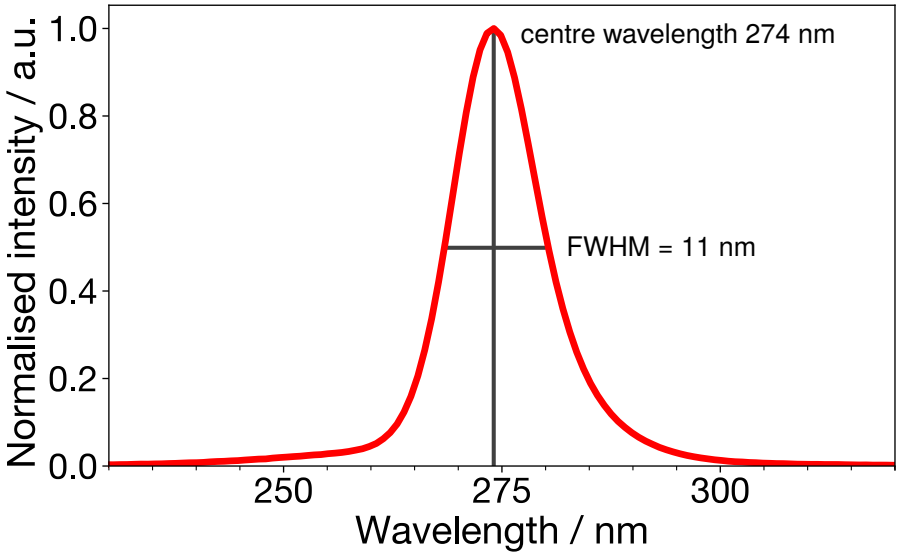

Fig. 3.6 Spectrum of the 275 nm LEDs used to excite intrinsic protein fluorescence. Since the spectrum will vary with temperature, the LEDs were preheated to equilibrium temperature before measurement.
(*Fig. first referenced on p. 104*)

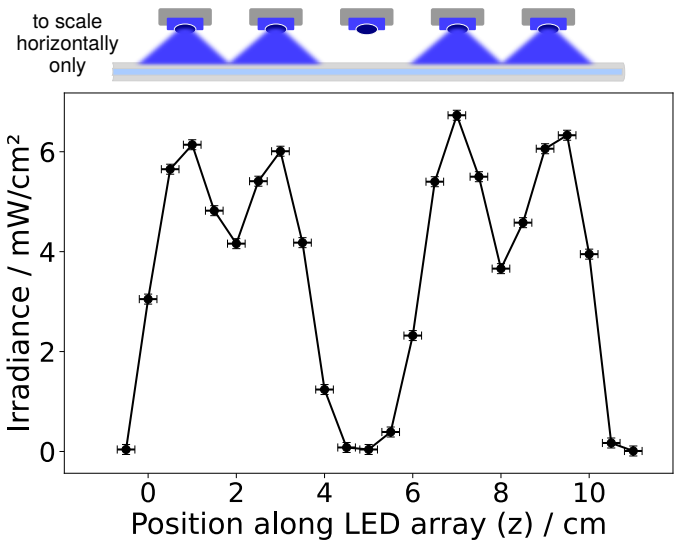

Fig. 3.7 Line scan of the irradiation profile at the HC-PCF plane to assess the absolute irradiance impinging on the HC-PCF, as well as the spatial irradiance profile. A calibrated photodiode power meter with a (280 ± 10) nm bandpass filter was moved in increments along the z-axis where the HC-PCF is situated during the experiments. The central LED is inactive (see text). (*Fig. first referenced on p. 105*)

The LEDs are placed with their heatsinks flush against each other, creating a string of five LEDs with emitters spaced 2 cm apart. Note that the middle LED was not active either here or in any other experiments, making it a ■■□■■ pattern, creating a dip in the irradiance profile at the centre. This was for two practical reason: the available power supply could only supply enough current per each of its two outputs for up to two LEDs in series, such that adding the middle LED would have required using two power supplies. This would have made synchronised on/off switching more complex. Furthermore, the current arrangement allowed easy switching between proximate and distal side irradiation to check for inconsistency, and was intended to be used for cross-referencing of the signal. For example, by alternating the two sides, larger fluorescent objects flowing through the HC-PCF could be identified by the time taken for them to traverse a certain distance. However, these capabilities were not implemented for lack of time.

Lensing

We note that the HC-PCF, as a microstructured cylindrical piece of glass, also acts as a lens. A geometrical optics ray diagram explaining this effect is shown in Fig. 3.8. Since the LED excitation light was of wide angle and not focussed, a study of the effect of HC-PCF rotation on the experiments is expected but was not explored further, as the effects of alignment and rotation cannot be isolated from each other. For experiments that rely on side observation (cf. Section 1.2.2), this effect would need to be taken into consideration.

3.3 Results

Two measurements form the key results of this experimental investigation: a spectral comparison of intrinsic protein fluorescence measured in HC-PCF, and a dilution series to test the system performance in terms of linearity and hysteresis for detecting proteins via their intrinsic fluorescence.

3.3.1 Spectral comparison

First, the fluorescence measured in the HC-PCF was compared to a reference large-volume cuvette measurement. The results are shown in Fig. 3.9.

Motivation for this experiment

The question asked in this experiment was if the intrinsic fluorescence would be significantly altered spectrally in the HC-PCF compared to the bulk cuvette. For example, a hypothesis would be that surface adsorption in the high surface-

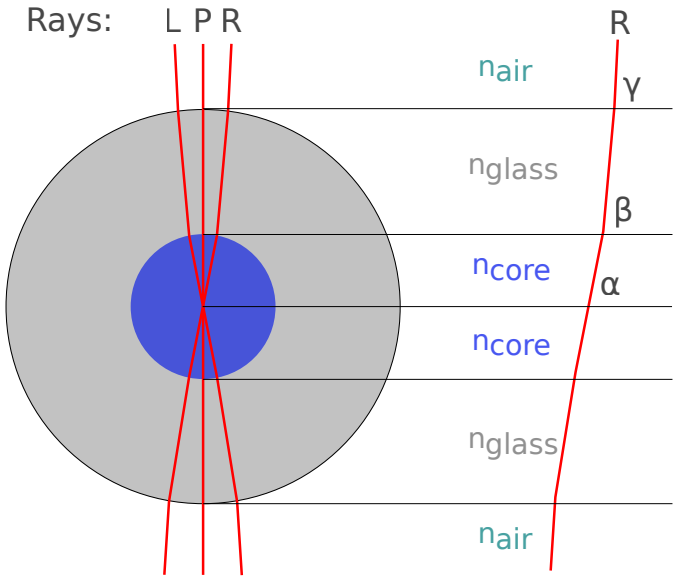

Fig. 3.8 Ray optics diagram for the effect of cylindrical lensing on the HC-PCF, at the outer surface air–glass interface and the inner glass–solvent interface. Assuming a water-filled core (i.e. $n_{\text{core}} < n_{\text{glass}}$), light is concentrated into the fibre relative to if the lensing effect were absent. Note that the cladding capillaries are not considered, and would cause aberrations and scatter if the light were not to pass entirely in-between two capillaries. Drawing not to scale.
(*Fig. first referenced on p. 107*)

area-to-volume HC-PCF geometry might have significant effects on the intrinsic protein fluorescence spectrum.

To compare the free-space cuvette measurement with the waveguiding HC-PCF measurement, both measurements were scaled to the same peak height, and the cuvette data was normalised by the HC-PCF transmission spectrum (Fig. 2.17). The uncorrected spectra are published open-access in the supplementary information of [1].

The cuvette measurement was already described in Section 3.2.2. The HC-PCF measurement was performed as described in the experimental setup above, except that the PMT was replaced by a spectrometer (OceanOptics QE6500), and the bandpass filter was removed. Since the spectrometer is significantly less sensitive than the PMT, a relatively high concentration of 10 µM and long integration time of 5 s was used. The use of multimode fibre coupling allowed this adjustment to take place without significantly disturbing the alignment of the setup.

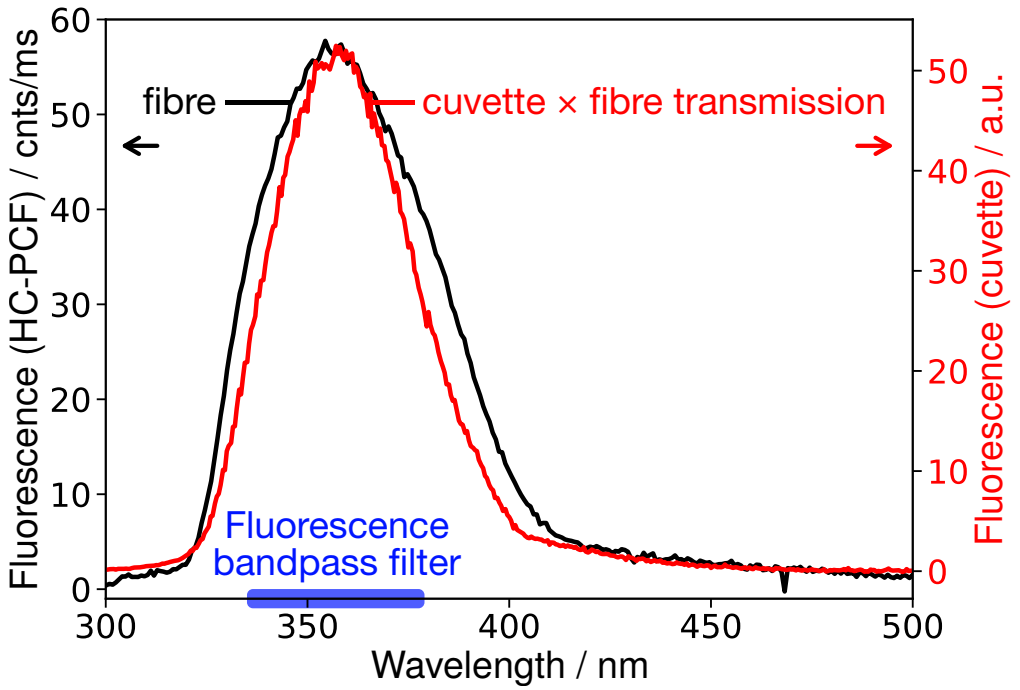

Fig. 3.9 Spectral comparison of the intrinsic protein fluorescence of BSA measured in cuvette and HC-PCF. To compare the free-space cuvette to the waveguiding HC-PCF, the cuvette data has been normalised using the HC-PCF's transmission spectrum.

(*Fig. first referenced on p. 107*)

Results

As seen in Fig. 3.9, the HC-PCF (fibre) spectrum matches that of the cuvette closely. The deviation of the two measurements takes the form of the cuvette spectrum being slightly more narrow, with the FWHM of the cuvette spectrum being 80 % of the HC-PCF spectrum. A peak shift, if present, is within the measurement uncertainty.

From these measurements, we conclude that apart from the HC-PCF's transmission spectrum (as characterised separately in Fig. 2.17), the intrinsic protein fluorescence is of very similar spectral shape as in bulk measurements.

3.3.2 Key experiment: Label-free quantification of intrinsic protein fluorescence in HC-PCF under flow

Motivation for this experiment

As the key experiment to evaluate the stated research aims of this chapter, namely the continuous flow detection of proteins by their label-free intrinsic fluorescence inside HC-PCF, the following experiment was performed.

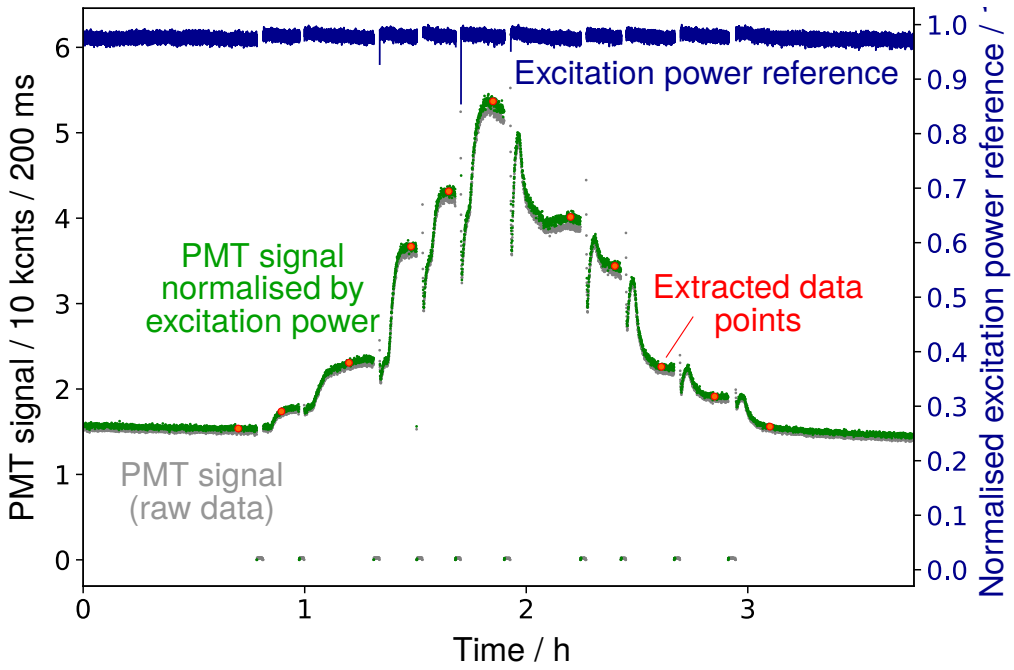

Fig. 3.10 Intrinsic protein fluorescence of BSA protein recorded inside a HC-PCF under continuous flow by a bandpass-filtered PMT. As detailed in the text, different concentrations of protein were measured in increasing and then decreasing order, and the PMT signal (grey) was normalised by the excitation power (blue), yielding the green curve. Data extracted at the red points are used in the next figure to discuss these results. (*Fig. first referenced on p. 100*)

Experimental procedure

Over a total of ca. four hours, the HC-PCF was under continuous flow with different sample solutions, and the fluorescence resulting from ultraviolet excitation measured as described above. The sample solutions were changed sequentially, beginning with an hour of buffer flowing through the system, followed by a dilution series of different concentrations of BSA over two hours, before ending with another hour of buffer flowing. The concentration series was chosen to increase to a maximum of 1 µM and decreases back down to 0 nM to understand possible hysteresis effects; the concentration steps used were, in order: 0, 100, 200, 500, 700, 1000, 700, 500, 200, 100 and 0 nM. The resulting trace of the PMT signal is shown in Fig. 3.10.

Discussion of PMT trace

As discussed above, the raw PMT signal (grey data points) representing the measured fluorescence was referenced to the excitation power (normalised, in blue), resulting in the excitation power corrected PMT signal (green). Where this signal abruptly drops to zero, the excitation was turned off to allow a change of the sample syringe. After restoring the flow and turning the excitation light back

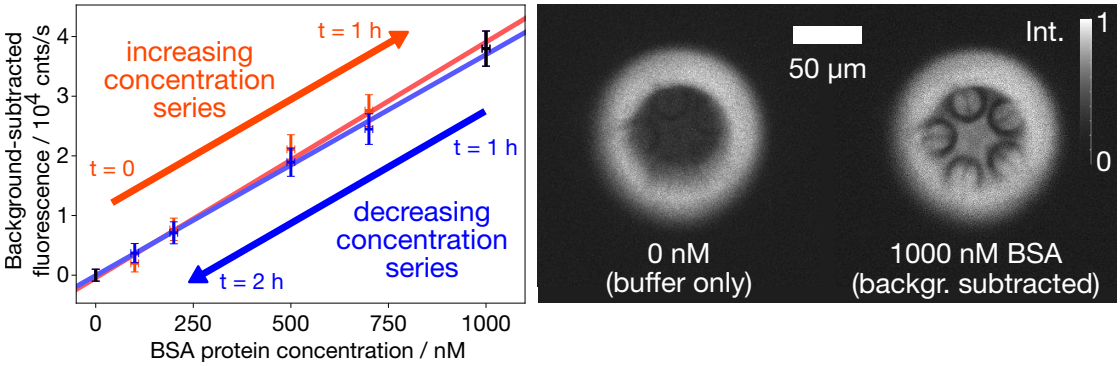

Fig. 3.11 Label-free quantification of BSA protein under continuous flow inside a HC-PCF using intrinsic protein fluorescence. Over two hours, the system shows good linearity (average $R^2 = 0.996$) and small hysteresis (fit of increasing and decreasing slopes differ by 7 %). The filtered fluorescence images are discussed in the text. (*Fig. first referenced on p. 111*)

on, the system requires some time to reach equilibrium, both because the liquid infiltration takes some time, as well as the pressure buildup changing alignment back to the original (optimised) state. The sample change procedure consisted of manually changing syringes in a syringe pump, and the initial pressure applied to the system was not well controlled, explaining the difference in time taken to reach equilibrium (plateau) again after a sample change. These shortcomings motivate the flow characterisation experiments of the next chapter.

Taking readings

In particular, the resulting variability in flow conditions made the time taken to reach a steady state signal change (at which point a reading of the fluorescence signal was taken), with the chosen time points indicated in Fig. 3.10. The steady state was determined during the experiment as five minutes of no observed variation in the PMT reading beyond the signal noise, but since this procedure was not automated, it was still liable to experimenter error. If an automated sample change mechanism were implemented, this would greatly reduce variation in the time taken to reach steady state, and a moving average over the past few minutes could be used to establish whether the signal has stabilised.

Dilution series

The linearity and hysteresis of the HC-PCF measurement were quantified by plotting the data points from the above experiment, indicated in Fig. 3.10, as a function of concentration. The data were split in two, corresponding to the increasing and decreasing halves of the dilution series, to evaluate possible hysteresis between the two. The results are shown in Fig. 3.11.

Results

The linearity of the fits was found to be $R^2 = 0.994$ for the increasing series, $R^2 = 0.997$ for the decreasing series, or an average of $R^2 = 0.996$ for both.

Hysteresis was small, with the difference in the linear fit slopes being 7 %. This suggests that adsorption onto the core walls was either highly reversible, does not strongly affect the measurement, or was simply weak. In any of these cases, as the experiment showed, the system can perform as intended over extended periods of time (hours).

Reproducibility has therefore been shown for the intensity–concentration relationship within a continuously-operated setup without re-calibration (i.e. without re-adjusting the subtracted background reading). If the experiment were set up again with a fresh HC-PCF, or otherwise altered significantly between runs, re-calibration would be required in the form of a background reading before measurements are taken, adding a factor of variability across experiments.

Limit of detection

Different definitions of the limit of detection exist, and we adopt the standard definition of

$$\mathrm{LoD} = \frac{3.3\sigma(\text{from intercept of linear fit})}{\text{slope of linear fit}}, \tag{3.3.1}$$

resulting in a limit of detection of 22 nM in the present system.

Fluorescence imaging

The fluorescence-filtered images show that the intrinsic protein fluorescence is guided not only in the central core, but also in the side capillaries. This is explained by the fact that the guidance mechanism of this HC-PCF is defined by the thickness of the capillary walls, and consequently, the guidance criterion is fulfilled not only in the core surrounded on all sides by the capillaries, but also *within* the capillaries themselves.

LP11 modes in capillaries

Interestingly, the capillaries show a LP11 mode guidance, which is seen to be always aligned such that the axis of symmetry (i.e. the line of minimal intensity in the LP11 mode) points towards the centre of the HC-PCF. Since the cylindrical capillaries are rotationally symmetric, one might assume there to be no preferred direction in this system. However, we explain this effect by the coupling of the modes inside the capillaries to the surrounding jacket least strongly when the LP11 mode is aligned as shown; hence, LP11 modes oriented differently are coupled more strongly to the jacket, causing the light to be coupled into the much larger jacket, where it can leak away.

3.4 Discussion and outlook

This concludes the first experimental chapter. We finish by summarising the findings and possible improvements to the system.

3.4.1 Summary of findings

Summary

We have shown that it is possible to use HC-PCF in a continuous flow microfluidic circuit to quantify the concentration of BSA protein label-free, using the intrinsic tryptophan fluorescence of the BSA. An emphasis was put on showing that the system could operate long-term, with measurements performed continuously over hours. Despite this long operation, the system showed a sensing performance of good linearity and low hysteresis. Measurements of the label-free protein solution was shown over an order of magnitude of concentration.

3.4.2 Possible improvements

There are many possible improvements that could be made to the system, and we discuss a selection of them that were considered here.

Beamsplitter

A 50:50 beamsplitter was used in the experiments, as it gave the most flexibility for different experiments. To optimise the system, a motorised flip mirror could be implemented. Synchronised with the PMT and camera exposures, it could alternate these two measurements, trading a 2x improvement in signal for 2x decrease in achievable temporal resolution, as well as increased system complexity.

Using both ends of the HC-PCF

Currently, one end of the HC-PCF (the left end in Fig. 3.2) remains unused during the experimental data acquisition. When exciting from the side, fluorescence light is emitted isotropically (because the fluorescence lifetime is longer than the rotational diffusion timescale), and either side or both could be chosen for collecting outcoupled light. The favoured choice is to use the liquid outflow side, as this is the low pressure side with less strain on the window which causes wavefront distortion.

If light emerging from both ends of the HC-PCF were captured, a signal increase by a factor of two could be expected, or a factor of four if the beamsplitter was omitted, too. There are several reasons this was not pursued in our experiments.

In practice, the 'unused' end of the HC-PCF was used during initial alignment prior to measurements. The intrinsic fluorescence was too weak to see by eye even

when imaged with a piece of paper or fluorescent card. Hence, either a visible light handheld laser pointer, or an ultraviolet torch were held against this window to give sufficient brightness for aligning the optical beam path. Coupling light into the HC-PCF modes like this without fine alignment was not reproducible (as expected), but light transmitted through the solid-glass cladding was sufficient to perform initial alignment and imaging. This made leaving one end of the HC-PCF free desirable.

If both sides were to be used, as the simplest approach on paper, the entire setup could be mirrored on both ends of the HC-PCF. This would be prohibitively expensive and double the size requirements of the experiment.

The most practical solution would be to move the PMT to the left end of the HC-PCF. The PMT's sensor area is large enough to capture the outcoupled light without any optics, allowing it to be simply positioned flush against the window. This would make the beamsplitter and PMT beam path unnecessary, increasing signal by another factor of two for a fourfold signal increase in total.

Another approach would be to back-reflect the outcoupled light back into the HC-PCF with either an objective and a flat mirror, or a shaped mirror corresponding to the NA of the fibre. Since there are losses associated with each step, the gain would be below a factor of two in this case.

All of the above approaches (excluding mirroring the entire setup) have the disadvantage that the camera and PMT signals would not come from the same optical beam. If unexpected features appear on the PMT trace, correlating them to an image of the HC-PCF mode and facet (e.g. blockages or aggregates) becomes impossible. Seeing is believing, and as a new system being explored, having corresponding images and PMT signals was the major motivation for not optimising the system in this direction.

Spatially resolved detection

The current system was, approximately, imaging the HC-PCF core onto the multimode fibre feeding into the PMT. As seen in the camera images (Fig. 3.11), the fluorescence light is guided also in the capillaries and the cladding. When this experiment was designed, to evaluate the HC-PCF's intended use as an optofluidic waveguide, imaging the core was preferred over imaging the entire HC-PCF. This was done in anticipation of mode-based sensing, such as by autocorrelation (Section 2.3.2). If this research had been aimed at reaching the lowest possible limit of detection – instead of the current approach targeted at understanding the system without optimising for maximum performance – all fluorescence

light should be collected irrespectively of whether it is guided in the HC-PCF, or non-specifically transmitted through the glass.

Position of data points

The data points taken from Fig. 3.10 to produce the calibration plot in Fig. 3.11 were taken after the flow and therefore signal had stabilised after each sample change. This point was determined during the experiment by observing the signal change and taking a reading when the signal had been stable for some time (approximately 5 min). This procedure is liable to human error and experimenter bias. As the system is studied and understood more closely, a more objective criterion should be established. For example, during the experiment, a moving average and moving standard deviation could be computed and after some pre-defined threshold for stability has been reached, a reading would be taken.

Microfluidic sample exchange

In connection to the previous point, one of the most promising ways of improving the system would be to implement a way of switching between sample syringes without deadtime or introduction of air. Whenever a sample was exchanged, the pressurised system (i.e. under flow) began to relax, and the resulting step changes in pressure could disturb alignment. The new syringe was not necessarily at the same pressure, leading to further step changes in pressure. Finally, introduction of air when connecting a new syringe was reduced greatly by using the four-way valve to pre-flush tubing, but could not be entirely eliminated. Taken together, all these issues associated with syringe changes were the least controlled aspect of the experiments, and their (partial) remediation remained one of the most time demanding challenges throughout the PhD.

Summary

Ultimately, the system as described in this chapter showed many opportunities to be expanded into a versatile sensing platform for different use cases. Nonetheless, the decision was made to forego incremental improvements in favour of prioritising a system-wide re-design. This takes the experience gained into account, and was done with a personal focus on learning further new experimental techniques along the way.

4 | Label-free Ultraviolet Extinction on Protein Aggregates

Moving from *side-excitation* of fluorophores in the previous chapter, this chapter explores *through-fibre-excitation* extinction measurements. These are complementary approaches, and we will show their multiplexed combination in Chapter 6. In this chapter, to realise continuous flow optofluidic coupling, a new optofluidic interconnect is designed and built. We characterise the setup and its microfluidic behaviour by measuring the extinction of inorganic nanoparticle solutions, before using the setup to quantify the concentration of aggregated fibrils made from silk fibroin protein.

4.1 Motivation . . . 117
4.2 Experimental Method . . . 118
4.2.1 Characterisation measurements . . . 118
4.2.2 Experimental setup . . . 123
4.2.3 Sample preparation . . . 127
4.3 Results . . . 133
4.3.1 Gold nanoparticles . . . 134
4.3.2 Key experiment: Label-free quantification of silk fibril aggregates via extinction in HC-PCF under flow . . . 139
4.4 Discussion and outlook . . . 141
4.4.1 Summary of findings . . . 141
4.4.2 Possible improvements . . . 141

Contributions *This chapter corresponds to a publication currently in preparation. Zenon Toprakcioglu supplied the silk fibroin protein stock, and helped with training and assistance for the microfluidic aggregation and SEM imaging. Michael Frosz supplied the HC-PCF used in this dissertation. Tijmen Euser and Tuomas Knowles supervised this work and provided guidance and advice throughout.*

4.1 Motivation

Extinction benefits from long pathlengths

HC-PCFs are waveguides, and while side excitation as in the previous chapter is often used in the literature, the by far dominant type of experiment is to couple in light at one end of the fibre, and measure the light emerging at the distal end. By observing the difference between these two, caused by the strong light–matter interaction over an extended pathlength, sensitive measurements of low-concentration analytes can take place.

Extinction probes different sample properties

This approach, i.e. performing extinction measurements similar to those commonly done in cuvettes, probes different aspects of the sample proteins. In particular, if the extinction contains a significant contribution from scattering, the measurement is sensitive to size ($\propto r^{-6}$). Furthermore, a common response when presenting our research in the first chapter was whether this work could also be adapted to non-fluorescent samples.

We note that the term extinction carries different meanings depending on context. In our work, it refers simply to the light not transmitted $(1 - T)$, and we use the term absorbance synonymously. Sometimes, an explicit distinction is made between the two, with absorbance being from photon absorption (with or without radiative emission, in particular as fluorescence), while extinction would include both this component as well as non-absorptive losses such as scattering or guidance losses. In our work, when we refer to extinction or absorbance, the measurand is light received at the detector after it has passed through the HC-PCF containing the sample or reference.

Adding extinction to fluorescence measurements

Taking these ideas into consideration, it was decided to study if an extinction-based measurement could be added to the fluorescence-based setup, and therefore two different qualities of a sample could be analysed in-situ. As is very generally the case in the experimental sciences, measuring several parameters at once and correlating them leads to new insights, often by enabling the effects of several entangled effects to be separated through ratiometric measurements.

Consequently, an extinction-based measurement was designed, built and characterised, and the results are shown in this chapter. In addition to allowing the measurements in this chapter to be carried out, it was also built with a view towards enabling the multiplexed fluorescence and extinction measurements that form the final experimental chapter on protein aggregation (Chapter 6).

4.2 Experimental Method

Resulting ultimately in the version presented below, over several months, the setup saw various improvements and re-designs compared to the previous chapter. To understand the impact of these changes, several characterisation measurements were performed. The most relevant of these are presented here.

4.2.1 Characterisation measurements

LED modulation linearity

First, the relationship of the 365 nm LED to be used for excitation was characterised to verify linear output power relative to the input modulation signal. A signal generator was used to produce a stairstep modulation signal from zero to 5 V, which is the LED's full scale modulation input. The results are shown in Fig. 4.1.

LED modulation to output power linearity

The LED output power was seen to be proportional to the setpoint (modulation input) to within better than 2 % for all but the maximum power level. At this point, the LED (and LED driver) operate near their maximum power, and this is assumed to explain the non-linearity. Furthermore, for the highest power settings, the output power is seen to decrease slightly ($< 1\,\%$) with time, explained as a temperature increase due to waste heat, reducing the LED's efficiency. At the highest power settings, the driver has less headroom to counteract this with more current.

For the HC-PCF experiments, these findings led to three experimental decisions. First, we did not operate the LED in the high power range. This was not needed as the detector (camera, PMT or spectrometer) were saturated in their dynamic range well before the LED was at its maximum power.

Second, due to the good ($< 2\,\%$ in the worst case) proportionality between modulation and output power, the relationship was considered to be insignificant to warrant referencing with an external detector as done in the previous chapter.

Finally, the LED was preheated for at least an hour before an experiment at a medium power level, and then set to the desired power level for at least thirty minutes before a measurement.

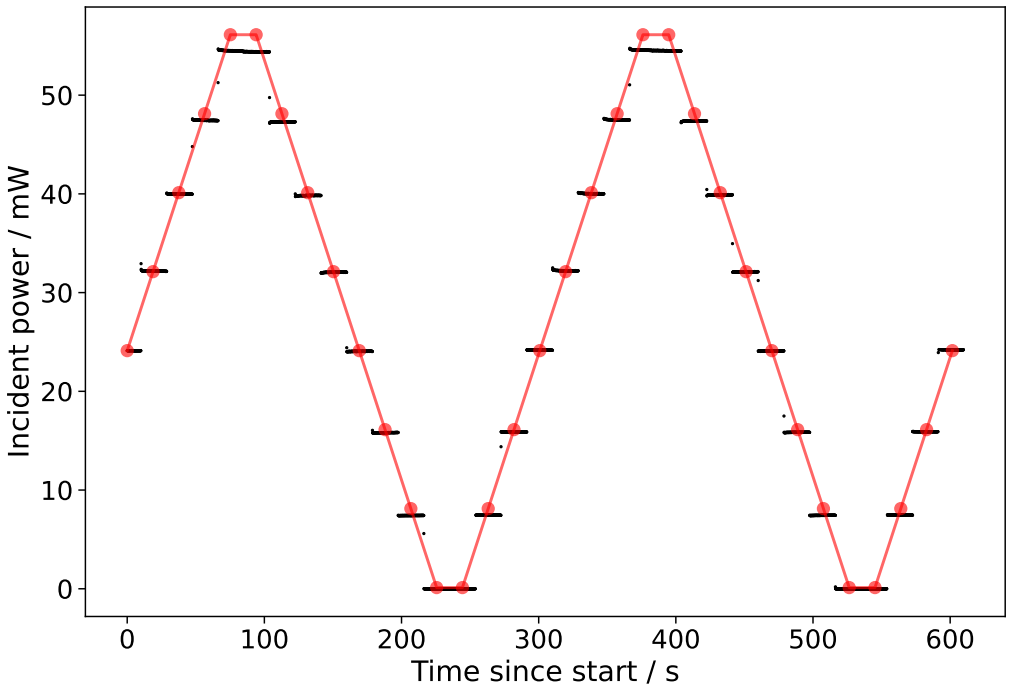

Fig. 4.1 Characterising the 365 nm LED output power linearity with the modulation signal. The modulation input (red) agrees to within a few percent with the LED output power as measured by a calibrated photodiode (black), except at the highest power levels where the LED power becomes sublinear. This is likely an effect of the LED being driven close to its maximum; hence, this region was avoided in the HC-PCF experiments. Plot points downsampled 10×.
(*Fig. first referenced on p. 118*)

Using the camera for intensity measurements

Can the camera replace the PMT?

One of the key changes to the previous chapter is that, unlike the weak intrinsic protein fluorescence, the LED light used for the extinction measurements can easily be made strong enough to oversaturate either the camera (or any other sensor used in the experiments, which are generally less sensitive). While for the weak intrinsic fluorescence a PMT was favoured over the camera for its superior sensitivity, for the extinction measurements in this chapter, the sensitivity of the sensor is of lesser importance compared to its resolution (dynamic range). It was therefore assumed that the experimental setup could be simplified by using only the camera, which would give flexibility for future experiments by post-processing the spatially-resolved camera images, e.g. to select only the core light, or to measure the light profile and compare near-surface measurements with those done far away from any surfaces.

What is needed

This will only be possible if the camera's pixel readings are linear to incoming light intensity. Besides the manufacturer explicitly guaranteeing the linearity of this camera, its CMOS technology is substantially the same as the photodiode used for light power measurements, i.e. they rely on the same sensing principle. However, unlike the photodiode powermeter, the camera is not calibrated to absolute power, and hence the following measurement was performed.

Calibrating the camera pixel values to light intensity

The output of a multimode fibre connected to the LED (as above) was measured as (424 ± 2) nW with a calibrated photodiode at 365 nm. This fibre-coupled LED output was then sent to the camera without optics, i.e. the multimode fibre illuminated the camera as a point source a few centimetre away. The distance was adjusted to be entirely within the field of view of the camera, and the output power was confirmed not to saturate any pixels.

The camera image's pixel values were summed to give 3.84×10^9 ADU/10ms (ADU: analogue-to-digital units, i.e. the digital value out of $0 \,..\, 2^{16} - 1$ reported by the camera as pixel values). Hence, a single ADU of the camera corresponds to $424\,\mathrm{nW} \cdot 10\,\mathrm{ms} / 3.84 \times 10^9\,\mathrm{ADU} = 1.1 \times 10^{-18}\,\mathrm{J\,ADU^{-1}}$.

A dark background was taken under the same conditions, giving a reading of (100 ± 6) ADU/200ms $= 0.5\,\mathrm{ADU\,ms^{-1}}$ per pixel. Using the calibration above, again per pixel, this corresponds to 0.8 nW for the given exposure, or $100 \,/\, (2^{16} - 1) = 0.15\,\%$, and is thus insignificantly small for the extinction measurements that can be carried out at higher power. The background was not observed to vary significantly even when a torch was shone on the camera, suggesting the dark noise is entirely due to electronic noise and not stray light.

Camera dynamic range

Hence, taking the above measurements, the camera's dynamic range is from

$$1200^2\mathrm{px} \cdot 100\,\mathrm{ADU\,px^{-1}} \cdot 1.1 \times 10^{-18}\,\mathrm{J\,ADU^{-1}} = 160\,\mathrm{pJ} \tag{4.2.1}$$

at the lower end (dominated by electronic noise), to

$$1200^2\mathrm{px} \cdot (2^{16} - 1)\,\mathrm{ADU\,px^{-1}} \cdot 1.1 \times 10^{-18}\,\mathrm{J\,ADU^{-1}} = 104\,\mathrm{nJ} \tag{4.2.2}$$

at the upper end where the camera's well depth is filled, i.e. pixels saturate. This is close to three orders of magnitude. In practice, this value is reached much earlier as the incoming light is not uniform in intensity, and individual pixels begin to saturate to become the limiting factor.

Timeseries from images

Based on these results, a script was written that takes a set of input image files, reads out their pixel values and sums them, creating a timeseries of light intensity.

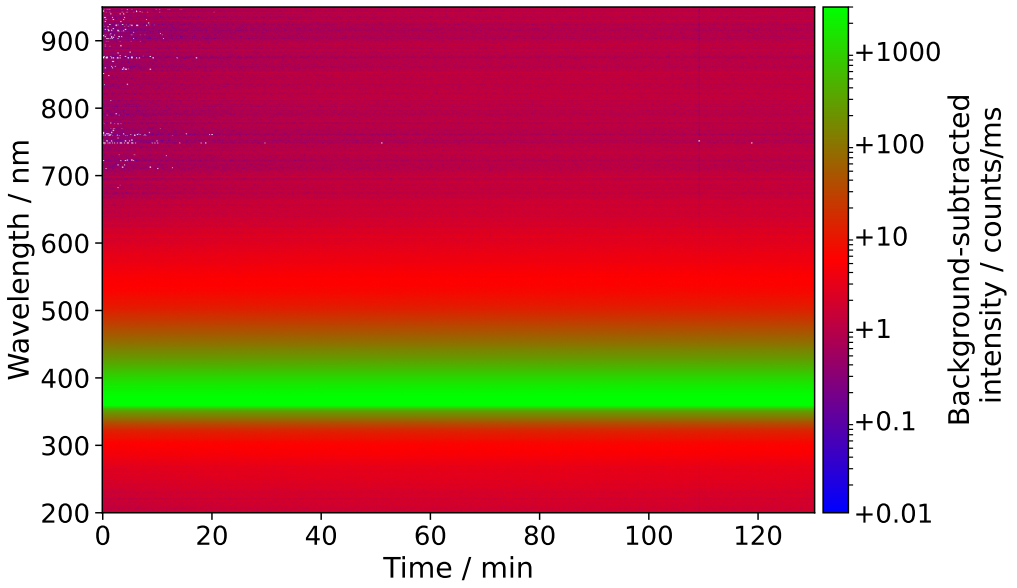

Fig. 4.2 Stability testing of the input light source. The 365 nm LED is free space coupled to a 25 µm multimode fibre (the same as is used to butt-couple to a HC-PCF), and measured with a spectrometer over two hours. Signal variation is below 1 % (see text).
(*Fig. first referenced on p. 121*)

This allowed the camera to do double duty in our experiments, acting as both the imaging needed for optical alignment, as well as providing the quantitative measurement over time. The beamsplitter of previous experiments was replaced with a mirror in this case, giving a $2\times$ increase in signal. More importantly, system complexity is reduced, with a view to making the system to more portable and compatible with existing fluorescence microscopy setups.

Characterisation of the light source

Having characterised the detection side, the light input side was studied next. Fig. 4.2 shows a spectrogram of the 365 nm LED coupled with a 25 µm multimode fibre (the same as used in the later experiments to couple into the HC-PCF), measured over two hours to characterise its spectral drift.

Drift over time

Visually, no significant drift can be observed from Fig. 4.2. To further quantify this statement, a timecourse was computed from this experiment by integrating the spectroscopic data over the wavelength range of (365 ± 15) nm, which is normalised by exposure time and spectral bandwidth. The results showed that the integrated spectrometer reading increased from (3900 ± 10) counts nm^{-1} ms^{-1} linearly to (3950 ± 10) counts nm^{-1} ms^{-1} over the course of 30 min, and then

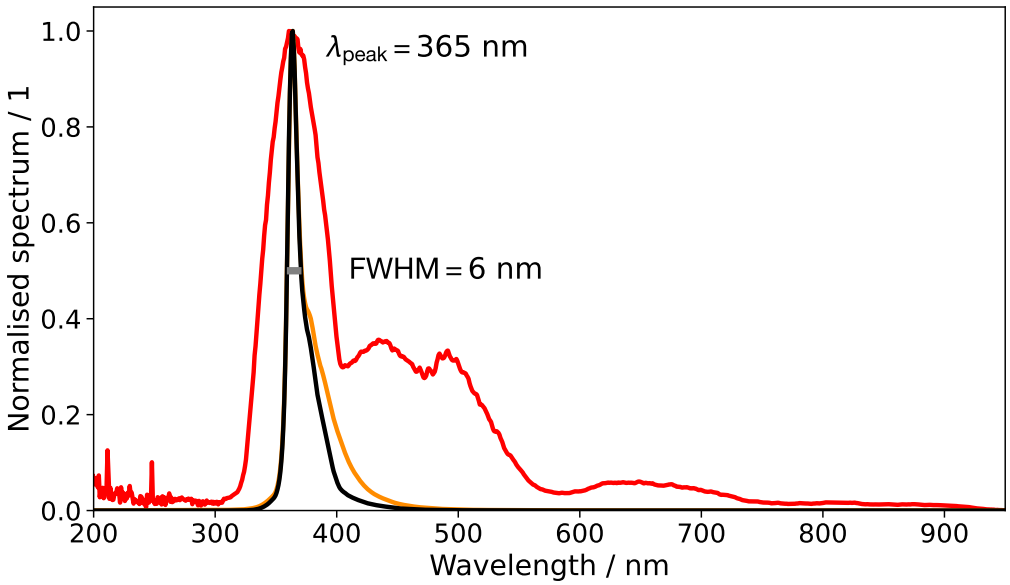

Fig. 4.3 Choice of light source optimised for HC-PCF transmission. The 365 nm LED (orange) closely matches the transmission maximum of the HC-PCF (red), and their product (black) shows that the spectral shape of the excitation light is not significantly altered by the HC-PCF transmission spectrum. *(Fig. first referenced on p. 122)*

undulated irregularly in a band of (3960 ± 20) counts nm^{-1} ms^{-1}, i.e. 0.5 % variation, over 100 min. This suggests the system is stable to better than 1 % after reaching thermal equilibrium. It cannot be established for certain whether the drift is in the output power of the LED, or in the spectrometer's accuracy over extended time, and ultimately will be a combination of both. Since the LED was already preheated prior to the readings (and, contrary to the measurement, is expected to decrease in light output with temperature), the spectrometer is likely to be the source of drift. Similar spectrometer drift has been observed previously in its dark (background) counts over similar timescales, in agreement with this hypothesis.

Spectral overlay of light source with HC-PCF transmission

In Fig. 4.3, to study the suitability of our HC-PCF for guiding the LED light, the multimode fibre coupled LED output spectrum was overlaid onto the HC-PCF transmission spectrum (shown previously in Fig. 2.17). The spectrum has its peak at 365 nm, with a FWHM of 11 nm, and is not affected significantly in its spectral shape by the HC-PCF transmission spectrum.

Summary

The above results confirm the suitability of the tested light source in terms of long-term stability (for aggregation experiments over hours to days), match between light source output and HC-PCF transmission spectrum (reduced guid-

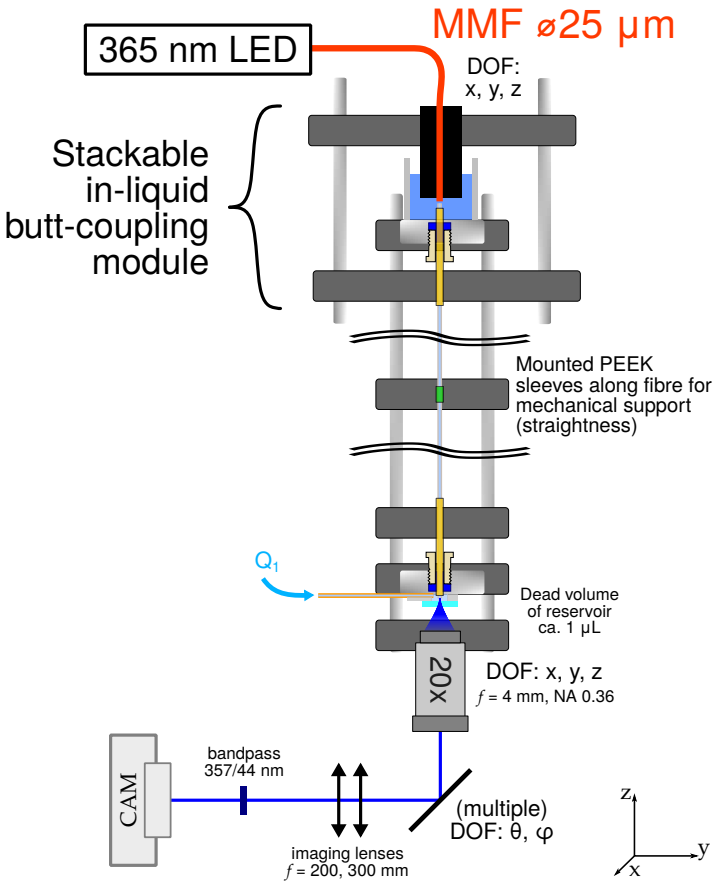

Fig. 4.4 Experimental setup shown schematically. The individual components are characterised and detailed throughout this chapter. In brief, 365 nm LED light is butt-coupled to the HC-PCF within a liquid reservoir by an add-on module stacked onto the HC-PCF mount, which keeps the fibre indexed to ease alignment after mounting, and straight to minimise bending losses. The imaging setup was simplified to use only the camera for both imaging and intensity measurements (cf. Section 4.2.1). *(Fig. first referenced on p. 123)*

ance losses which would increase background noise through stray light), and linearity (allowing modulation to take place without re-calibration). Several available light sources were tested, and the one shown here chosen as the best match to the experimental requirements.

4.2.2 Experimental setup

Fig. 4.4 describes the experimental setup schematically, and a set of photographs in Fig. 4.5 shows the different components making up the experiment. The individual elements are discussed below.

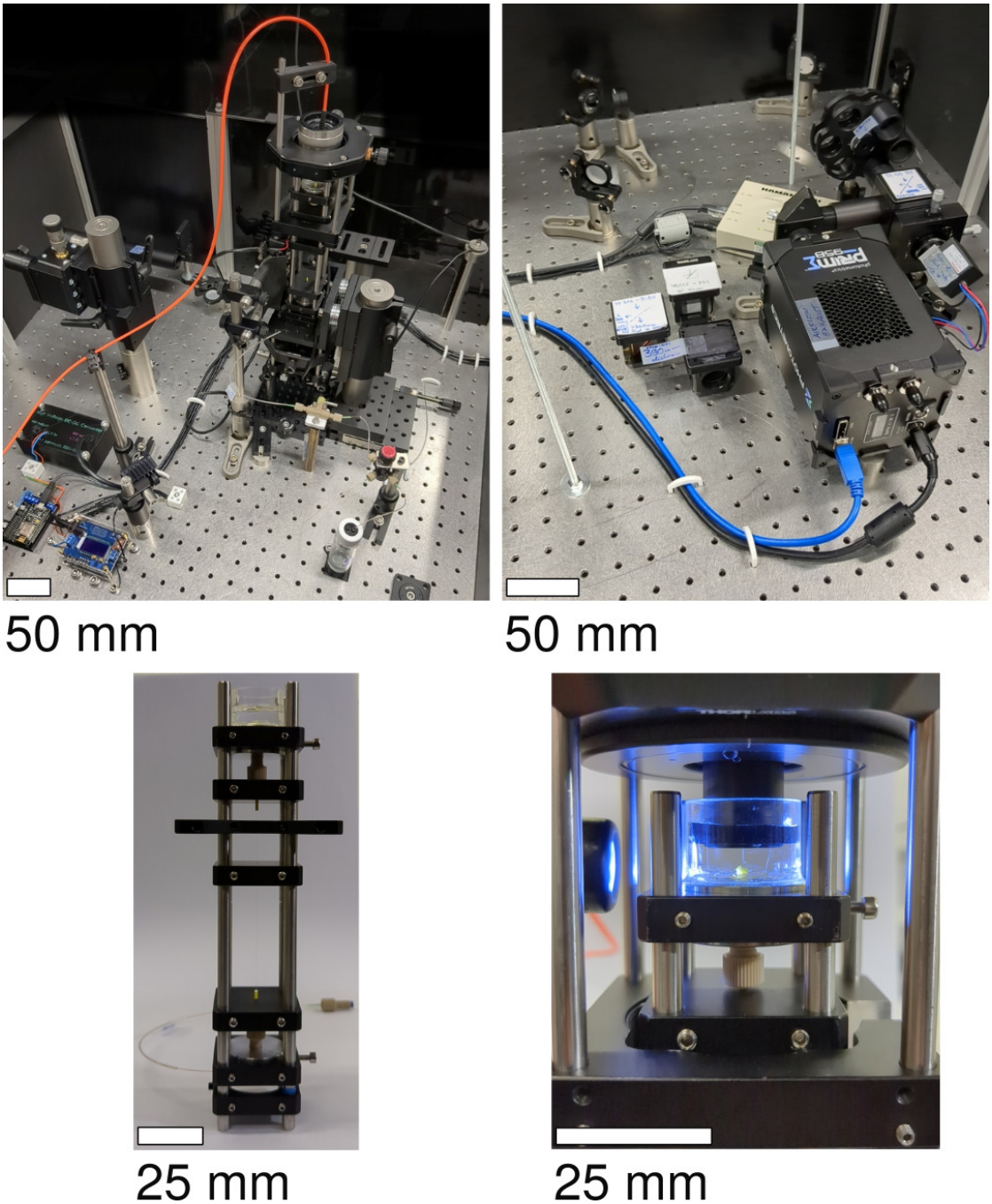

Fig. 4.5 Photographs of the optical bench and the HC-PCF insert module. **Top:** The active (left, containing the light sources) and passive (right, containing the fluorescence filtering and detection equipment) parts of the experimental setup. They are separated and connected via a small aperture to allow the detection side to remain fully enclosed throughout the experiment. **Bottom:** HC-PCF module that holds a 17 cm length of fibre (left; see schematic in Fig. 4.4), and the stackable add-on module for in-liquid butt coupling (right).

(*Fig. first referenced on p. 123*)

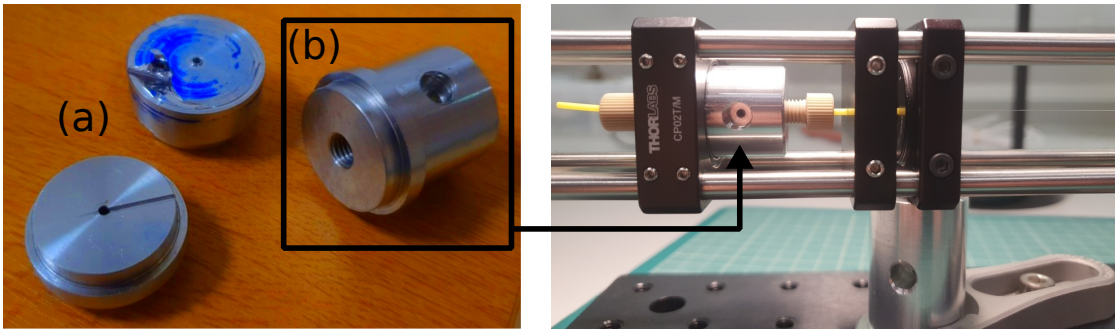

Fig. 4.6 Photo of several earlier design prototypes that preceded the final design used in the extinction experiments. (**a**) A short, circular coupling cell with a rim to allow clamping. The clamping required extensive forces to hold the cell in place as the HC-PCF is screwed into its connector, causing slippage and mechanical failure during lathe work. Hence, the final version used an orthogonal screw fitting. (**b**) T-junction in-liquid coupling cell. It was hoped that coaxial fixed incoupling MMF and HC-PCF would allow butt coupling, but resulted in insufficient stability and lack of alignment control. Hence, the final version used a micrometer stage inside a liquid reservoir to give better control and stability.

(*Fig. first referenced on p. 125*)

Optofluidic interconnect cells

The optofluidic interconnect cell went through several design cycles (Fig. 4.6). The construction drawings for this design and other designs are given in the supplementary information, Fig. S-2 and Fig. S-3.

Motivation for re-design

Other optofluidic interconnects already existed in HC-PCF research and have been successfully used for a variety of applications, including for early experiments in this dissertation. Creating a new interconnect was in no small part motivated by the learning and insight into microfluidics it would yield, for the author to practice an experimental design cycle from concept to conclusion. As part of this, new ideas could be tested, and an example of this is the vertical mounting of the HC-PCF, which is nearly always done horizontally in the literature. The motivation for this was the realisation that setting up a HC-PCF for an experiment was the limiting factor in the time required for experiments to be performed (including fibre insertion, cleaving, cleaning of facets, sealing and flushing of the microfluidic circuit). Mounting the fibre vertically addressed this in several points, as it could simply be inserted from the open reservoir on the top, significantly improving physical access to the HC-PCF during the

mounting procedure. Another motivation was the future outlook to make such a system compatible with existing microscopes as an add-on to standard commercial microscope stages, which in horizontal setups would have required periscope setups and additional optics to form additional focal planes.

Machining

The iterative construction-machining-testing cycles of the optofluidic interconnect cells helped the author gain a deeper, and often more intuitive, understanding of experimental design. In particular, it was a lesson in simplicity. The construction drawing for the final design is given in the supplementary information (Fig. S-1). It is a rotationally symmetric design that allows all manufacturing steps to take place on a lathe without re-registration, giving good concentricity. A blind hole on the side allows it to be mounted into a Thorlabs-standard cage mount system. This gives flexibility in adjusting z independently, while also giving the system rigidity that minimises movement.

Assembly

A fused silica window was glued onto the cell as described in Chapter 3. For the inflow side (bottom), a short ($\sim 10\,\mathrm{cm}$) piece of fused silica tubing inserted into a machined V-groove feeds in liquid from the side. On the outflow (top) side, a short ($\sim 2\,\mathrm{cm}$) piece of transparent acrylic pipe was glued on to form an open reservoir in which the in-liquid butt coupling can take place (see Fig. 4.5). The volume of this reservoir (several millilitre) is much larger than the HC-PCF volume, such that the concentration of this reservoir is assumed to be near zero always, even if sample solution is being flushed into it. For the longest measurements, if the total volume flushed during the experiment was in the millilitre scale, the reservoir liquid was regularly replaced and evaporated liquid topped-up. Since the reservoir is open to air, this could be done without disassembly of the experiment. This reservoir was typically filled with a dilute ($\sim 40\,\%$) solution of ethanol to decrease surface tension and reduce air bubble formation.

In-liquid continuous flow butt-coupling

Having the in-liquid butt-coupling module as a separate stackable add-on allowed for much improved experimental access and mounting of the HC-PCF, which could be slid in from the top through the series of motion-guiding PEEK sleeves. Next, after the HC-PCF has been mounted, the top reservoir is filled with liquid and illuminated with an UV torch to confirm in-focus imaging and (qualitatively) satisfactory guidance. Finally, the butt-coupling module with the orange multimode fibre is stacked on top (Fig. 4.5). It contains an xyz micrometer stage to move the multimode fibre output close to the HC-PCF with approximately $5\,\mu\mathrm{m}$ accuracy.

A useful technique for establishing the $z = 0$ contact plane between the multimode fibre and the HC-PCF is described as follows: First, the multimode fibre is lowered to within less than a millilitre of the HC-PCF by eye. Next, the multimode fibre is moved down in z towards the HC-PCF in small increments and moved slightly in xy at each step. Once the coupling of light into the HC-PCF was not seen to change with xy movement anymore, the two were in physical contact and moved in unison (for small translations). When this happened, the z axis was retracted by a small amount until the two parted again, and re-approached by half the distance. This served as reliable way of finding the ideal z position for light coupling. With only two degrees of freedom left, aligning x and y could be done reliably in less than a minute from this point.

4.2.3 Sample preparation

Gold and polystyrene nanoparticles

Different calibration and test samples were used. Of those shown in this dissertation, the gold nanoparticles solutions were prepared from Sigma-Aldrich stock, which is calibrated to an optical density of 1 cm^{-1} at 520 nm. The gold nanoparticles used in the experiments shown here were of 10 nm diameter. Cuvette UV-VIS measurements were used to find the extinction at 365 nm, which was then used to create dilutions. Polystyrene spheres from NIST (size standard nanospheres, diameter (41 ± 4) nm) were prepared in the same way. All samples were diluted in water.

Silk fibril aggregates

The silk fibril aggregates were produced with a microfluidic chip provided by Zenon Toprakcioglu, and with his training and assistance. Shown in Fig. 4.7, the process consisted of one microfluidic and one manual sample processing step.

First, silk fibroin protein solution was made to aggregate quickly in a microfluidic droplet maker. Silk and its material properties will be discussed in more detail in the aggregation experiments of the next chapter, Section 6.2.1. In the droplet maker, the aggregation occurs through the combined encapsulation of ethanol and the silk solution into water-in-oil droplets. This mixture would aggregate on an hour-to-day timescale in bulk, but does so nearly instantaneously in microfluidic droplets due to mixing and exposure to interfaces. The size is tuneable by choosing different flow rates of the aqueous phase (protein solution and ethanol) relative to the oil, resulting in different amount of protein encapsulated in each droplet. The concentrations and flow rates used were: silk fibroin

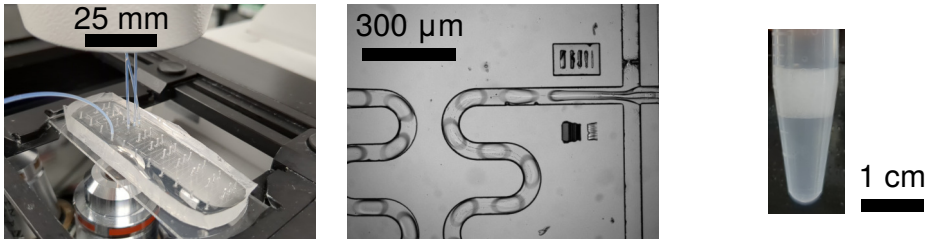

(a) setup photo (b) droplets forming (c) resulting emulsion

Fig. 4.7 Microfluidic production of nanosized silk aggregates. A silk fibroin protein solution is encapsulated into droplets (a, b) to induce aggregation, with a protocol similar to [307]. The resulting liquid (c) is then de-emulsified by repeated addition of surfactant-free oil, displacing the surfactant and leaving the aqueous protein aggregate solution. (*Fig. first referenced on p. 127*)

solution of $1\,\mathrm{g\,L^{-1}}$ at $100\,\mu\mathrm{L\,h^{-1}}$, ethanol (96 %) at the same flow rate, and FC-40 oil with surfactant at $200\,\mu\mathrm{L\,h^{-1}}$.

The output of this microfluidic chip was collected in a container, where it separates into an emulsified phase containing the droplets, and surplus oil. By repeatedly adding surfactant-free oil and extracting the oil phase, the surfactant is gradually displaced, finally leaving the protein aggregates dissolved in the aqueous phase.

SEM on aggregates

To characterise the aggregates in terms of size and morphology, SEM imaging was performed (Fig. 4.8). Just prior to SEM imaging, the silk aggregate solution were left to evaporate in air and then sputter coated with platinum to increase contrast and electrical conductivity.

The silk fibrils were seen to form fibrillar patches (networks) when imaged. The shape of these patches varied significantly, and they were typically of a few microns in extent. The thickness of individual fibrils were below the resolution limit of the SEM, with the thickest fibrils estimated at 500 nm but most much below this number.

Effect of sample preparation

We acknowledge that SEM imaging, i.e. the sample preparation, especially drying and exposure to vacuum, can affect the aggregates. It can therefore not be concluded with certainty that the samples measured in solution are of the same morphology as seen in the SEMs. The fact that imaged aggregates can differ from those in solution is fundamentally a motivation for the development of in-situ and label-free measurements. However, since quantitative ground truth to compare the HC-PCF measurements against was obtained by extinction measurements

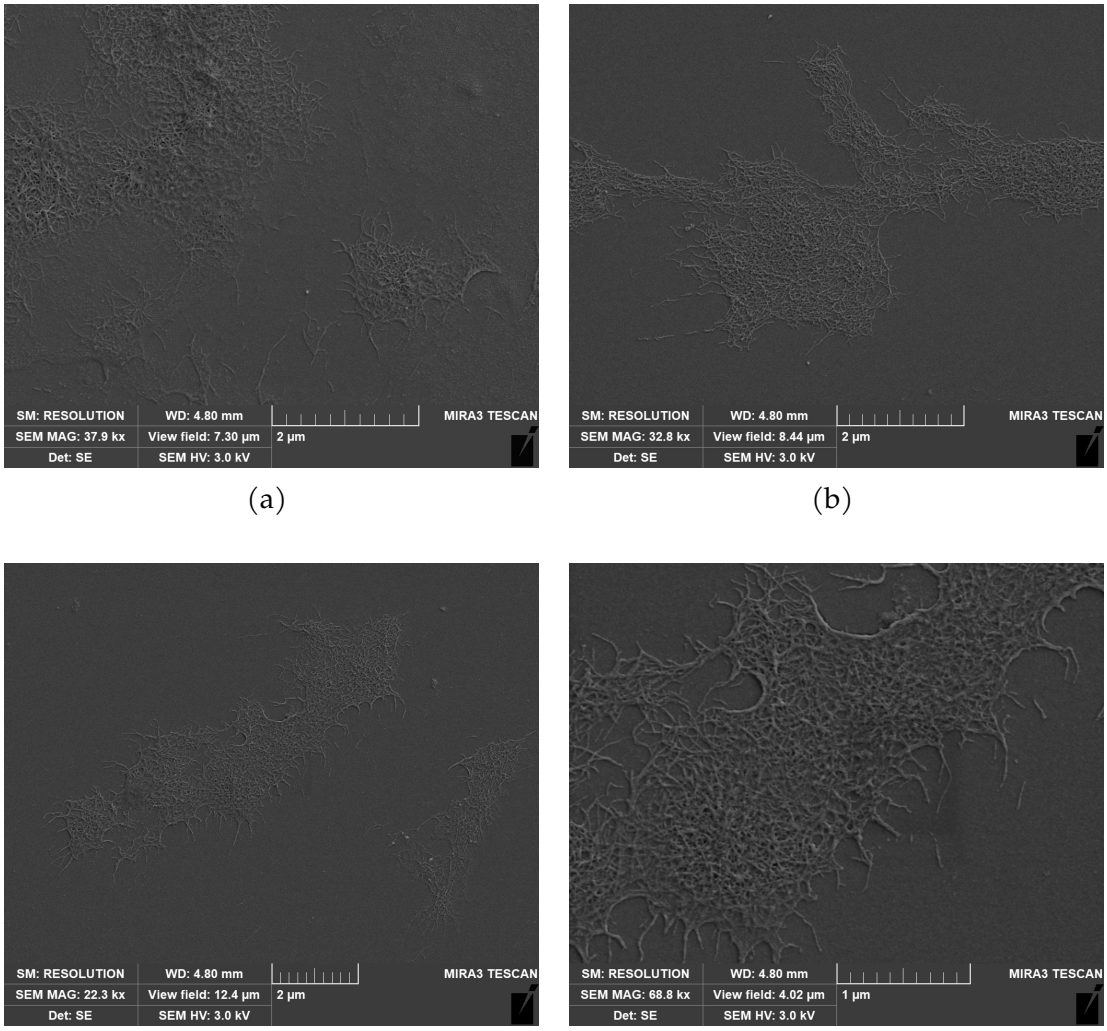

Fig. 4.8 SEM images of the silk fibril aggregates produced with the process shown in Fig. 4.7. The micrographs (**a**), (**b**), (**c**) show different fields of view, with (**d**) being a higher magnification of the area in (**c**). (*Fig. first referenced on p. 128*)

in solution in cuvettes, any possible change from SEM imaging does not carry through to the graphs shown below.

UV-VIS measurements in a cuvette were performed on the silk fibril aggregates (Fig. 4.9). The UV-VIS spectrum shows the absorbance close to 280 nm increasing strongly, attributed to tryptophan absorbance. At higher wavelengths, and specifically at our measurement wavelength of 365 nm, no peaked absorbance features are seen, indicative of non-specific scattering. The extinction at 365 nm was measured as OD 0.0104 cm^{-1} for the 2x diluted solution produced as described above. Insufficient volume was available to measure the undiluted stock

UV-VIS

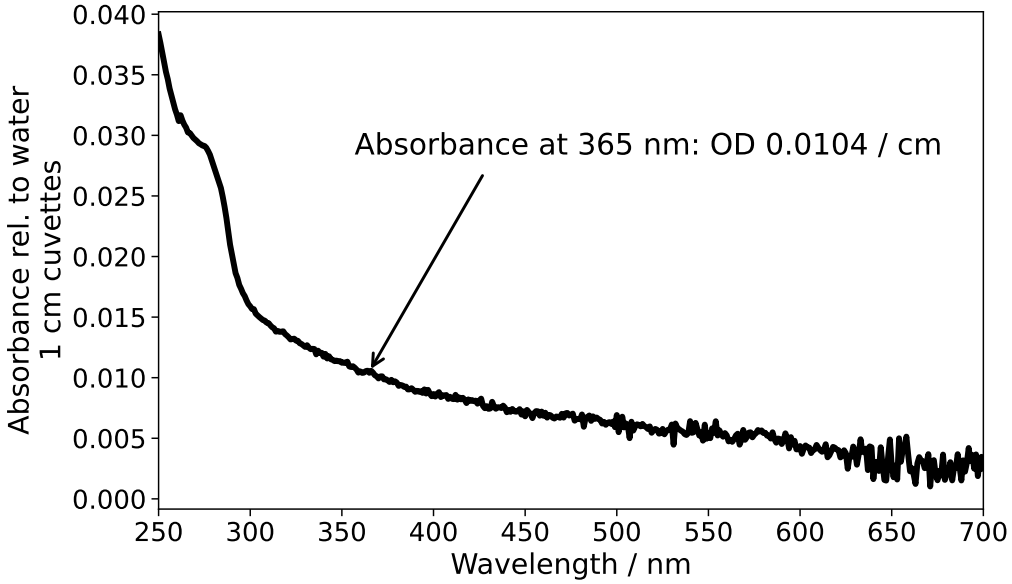

Fig. 4.9 UV-VIS absorbance spectrum of the silk aggregate solution (2x diluted stock). The extinction at 365 nm was used as the reference (ground truth) measurement to compare the HC-PCF measurements against. Further dilutions were reaching the noise floor of the UV-VIS, and their extinction was therefore calculated from the known dilution factor. (*Fig. first referenced on p. 129*)

in cuvette, and further dilutions reached the noise floor of the cuvette UV-VIS measurements. Hence, extinction was calculated from this value divided by the known dilution factor.

Characterisation of the microfluidic circuit

The microfluidic circuit was characterised with experiments such as the one shown in Fig. 4.10. Microfluidic systems have a compliance time, which is a timescale for a step change in pressure to re-establish the new equilibrium flow rate. In our system, as syringes are exchanged, the system changes from flowing → stopped flow (static) → flow of new sample solution. The new sample will then infiltrate the HC-PCF over time, which we label as the exchange time. This exchange time, i.e. the time taken to replace existing solution inside the HC-PCF, is expected to depend linearly on the flow rate (and the system dead volume fixed by the experimental design).

Compliance testing

To test this behaviour, in Fig. 4.10, several steps were taken in sequence. First, the flow rate of an already-flowing system was changed. Since this did not require manually re-connecting a syringe, the signal is seen to increase as a step

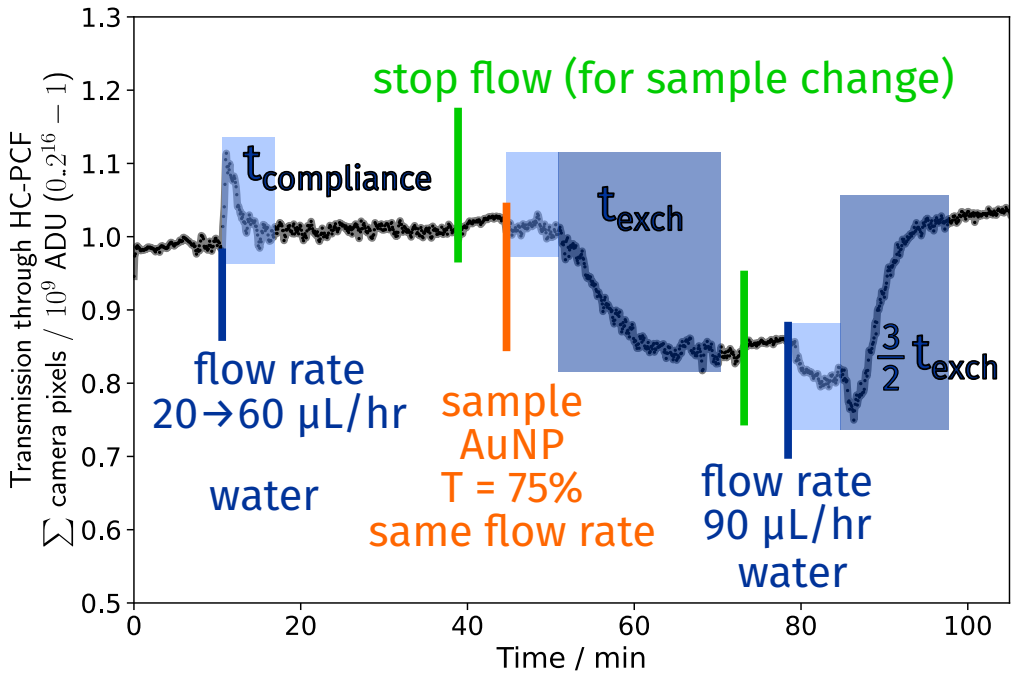

Fig. 4.10 Microfluidic compliance testing of the system. While water is already flowing, the flow rate is increased to identify the compliance time required to re-establish equilibrium. Next, syringes are exchanged to infiltrate a sample (AuNP calibrated to $T = 75\,\%$ through the HC-PCF), before changing back to water at a faster flow rate, leading to proportionally faster exchange.

(*Fig. first referenced on p. 130*)

change. While the exact mechanism is not clear, it was generally observed that transmission increased with more applied pressure. Three explanations are likely to contribute to this effect: the pressure change affecting the alignment due to movement, surfaces bulging and creating lensing, and reduced guidance losses by straightening the HC-PCF under pressure.

As the system re-establishes equilibrium at the new flow rate, the signal returns to the same baseline. Next, a change of syringe to a gold nanoparticles solution was performed. The solution was calibrated in a commercial cuvette UV-VIS to have $T = 75\,\%$ when scaled to the HC-PCF length (17 cm) at 365 nm. The transmission reaches a value of ca. 85 %, for an error of 13 %.

Next, the flow was changed back to water, but at 3 / 2 times the flow rate. This resulted in a proportionally faster exchange time, at 2 / 3 the duration, as expected.

Following the tests on different flow rates, in Fig. 4.11, four sample changes and measurements performed in succession. This tests the experimental protocol for

Reproducibility testing

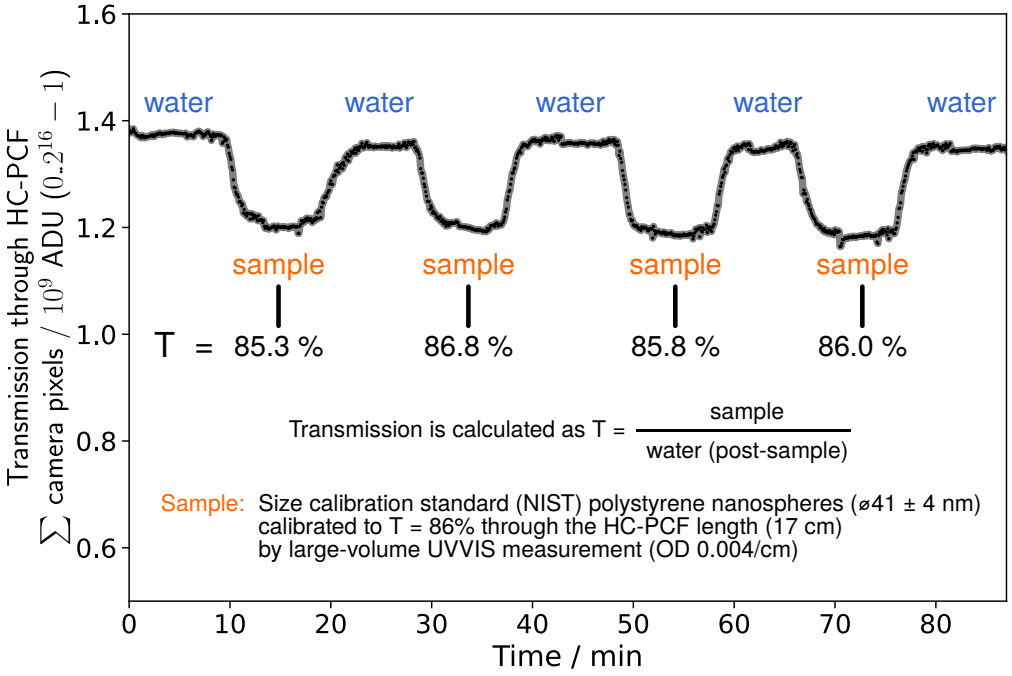

Fig. 4.11 Reproducibility testing of the system, showing the extinction measurement procedure repeated four times in sequence. The flow through the HC-PCF was briefly stopped to change the sample syringe, alternating between a polystyrene nanospheres sample (see inset) and water. The transmission ($= 1 -$ extinction) is calculated for each sample as shown. *(Fig. first referenced on p. 131)*

reproducibility. The sample used was a thousandfold diluted NIST size standard of polystyrene nanospheres (diameter (41 ± 4) nm), which was measured by cuvette UV-VIS to have an extinction of OD 0.004 cm^{-1}, or $T = 86\,\%$ over the HC-PCF length (17 cm). The flow rate in this experiment was 1050 $\mu\mathrm{L\,h}^{-1}$.

The transmission in HC-PCF was $T = 85.3\,\%, 86.8\,\%, 85.8\,\%$, and 86.0 % for the four measurements, or $T = (86.0 \pm 0.6)\,\%$, which is within the uncertainty of the UV-VIS measurement. The maximum deviation from the mean was in the second measurement, at 1 %.

This shows a good reproducibility of the measurements for the given conditions and measurement time (85 min). The water baseline did not change significantly during this time ($< 5\,\%$). More variation was seen in the time required for the signal to reach a new equilibrium after each transition between sample and water. This is attributed to the variation in manual handling of the change in syringe, already discussed before in Section 3.4.2. In addition to variations in time required to perform the procedure, re-connecting the syringes into the syringe pump lead to different initial pressures on the syringe plunger, and therefore

different starting pressures when switching the inflow valve. These points are discussed further at the end of this chapter.

Comparison to commercial spectrometer

Finally, using an IMPLEN NP80 'nanodrop' cuvette-less spectrometer, we studied how a comparable (i.e. operating on similar volume scales) commercial device performs with our samples. The device is operated by pipetting a solution onto a flat glass window, which is then sealed with a metal lid, forming a liquid volume with a defined pathlength in back-reflection of 0.67 mm. The sample requirement is one drop, ca. 2 µL. The machine then uses a broadband flash of light to take the spectroscopic reading.

The result was that all measurements fell below the detection limit of the machine, showing no significant absorbance above the noise (measured in triplicate). This agrees with the manufacturer's specifications (*link*), which state a lower limit of OD 0.02 cm^{-1}, whereas our samples measured in HC-PCF are below OD 0.01 cm^{-1} at 365 nm. Such machines are typically used to measure protein concentration via their absorption at 280 nm, where tryptophan absorbance is much higher. For measuring sample absorbance at other wavelengths, this and similar machines are not suitable, and offer no means of quantifying the intrinsic fluorescence from the absorbed light.

4.3 Results

Qualitative improvement of the experiment

Before discussing the experimental results, we note that the arguably key achievement over the experiments of the previous chapter was the ease with which a HC-PCF could be mounted, aligned, and experiments started. This improvement in experimental setup is ultimately difficult to quantify or compare objectively, but at the same time the major result of this chapter. By cutting down the time required for experimental preparation to a fraction of the time compared to how it was performed before, more experiments could be attempted. Equally, achieving stable and good mode quality (coupling to the core only in a near-fundamental mode) was more reproducible and less sensitive to movement. A typical mode of 365 nm light butt-coupled into a HC-PCF and transmitted over 17 cm of water is shown in Fig. 4.12.

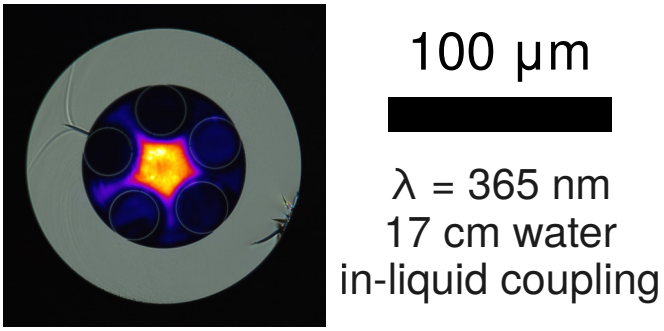

Fig. 4.12 Typical mode image of 365 nm light transmitted through 17 cm of water by in-liquid butt-coupling under continuous flow, as used during the extinction measurements. On the left side, where the inter-capillary distance is larger due to fabrication tolerance in capillary size and spacing, light can be seen leaking out from the central core. The imaged HC-PCF mode (in colour) is overlaid on a brightfield microscope image of the HC-PCF geometry.
(*Fig. first referenced on p. 133*)

4.3.1 Gold nanoparticles

Gold nanoparticles were chosen to run a complete dilution series to test the system, based on their well-characterised nature and availability. First, a single dilution of 1/200 compared to the stock concentration is measured (Fig. 4.13).

The measurement procedure was as described above in Fig. 4.11. Sample changes were performed when a new baseline was established for the previous sample, typically after 10 min. To find the transmission (or extinction as $1 - T$), a moving average (Savgol filter, window size 21, polynomial order 2) was overlaid on the data, and the points at which readings were taken are marked with green circles.

To establish a reference measurement, a tenfold dilution of the gold nanoparticle stock was measured in cuvette (i.e. 20 times more concentrated than the highest concentration in HC-PCF, which was of 200-fold dilution), and used as the base from from which all other samples were made. Based on this measurement, the stock (1x) is calculated to have an extinction of OD 1.0 cm^{-1}.[note 1] Scaling this

note 1 It is a coincidence that the stock solution, calibrated by the manufacturer to have OD 1.0 cm^{-1} at the plasmon resonance maximum (around 520 nm), also has the same OD 1.0 cm^{-1} at our wavelength of 365 nm far away from this resonance. The lack of a resonance happens to be compensated by higher scattering due to the shorter wavelength at exactly our target wavelength.

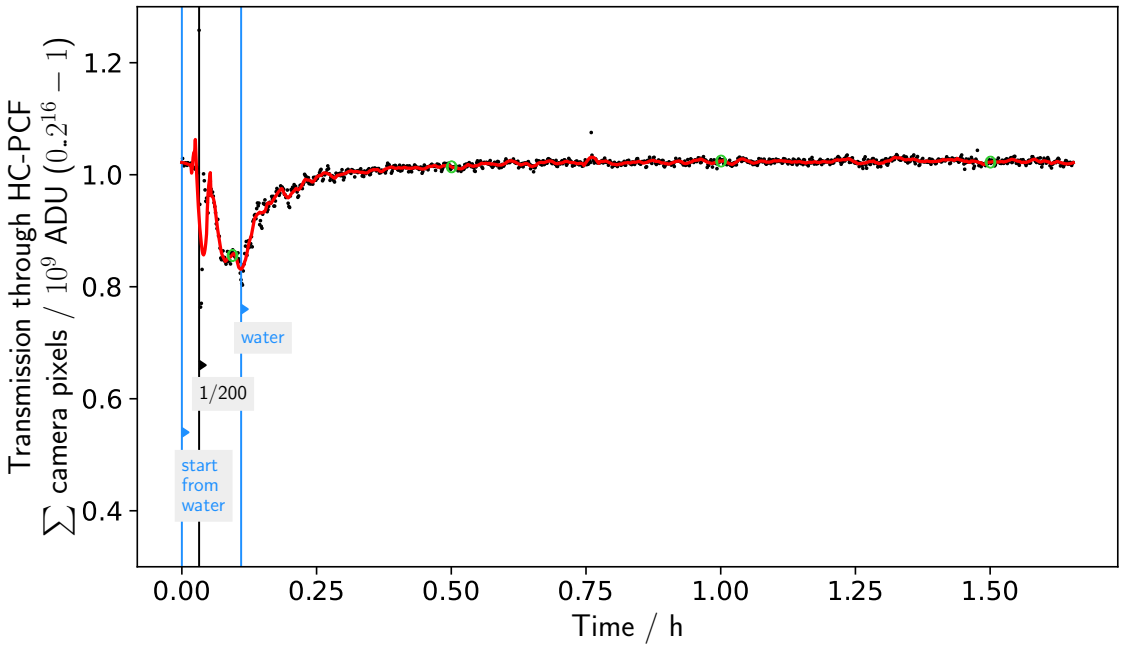

Fig. 4.13 Ultraviolet extinction measurement of a 1/200 gold nanoparticle solution in HC-PCF. The measured transmission in HC-PCF is $T = 84.4\,\%$, which is close to the value measured in cuvette and scaled to the HC-PCF length (error 3 %).

(*Fig. first referenced on p. 134*)

value to a 200-fold dilution and a 17 cm pathlength gives an expected transmission of

$$T = 10^{-1.0\,\mathrm{cm}^{-1}\cdot 17\,\mathrm{cm}\cdot(1/200\mathrm{diln.})} = 82\,\%. \tag{4.3.1}$$

For the 1/200 trace, the value measured in HC-PCF was $T = 84.4\,\%$, in close agreement with an error of 3 %. As a simple measure of baseline drift, three points as marked in the graph were compared at regular intervals, which had differences of 99.0 % and 100.2 %, respectively. This suggests a drift over one hour of less than 1 %.

Next, it was decided to run a whole dilution series as a single experiment, carried out continuously over eight hours (Fig. 4.14). Every concentration was measured in triplicate before progressing to the next concentration. (For the initial 1/200 dilution measurement, yours truly the author only did a duplicate instead of a triplicate by sheer oversight, which is why a third measurement was done separately for this concentration.)

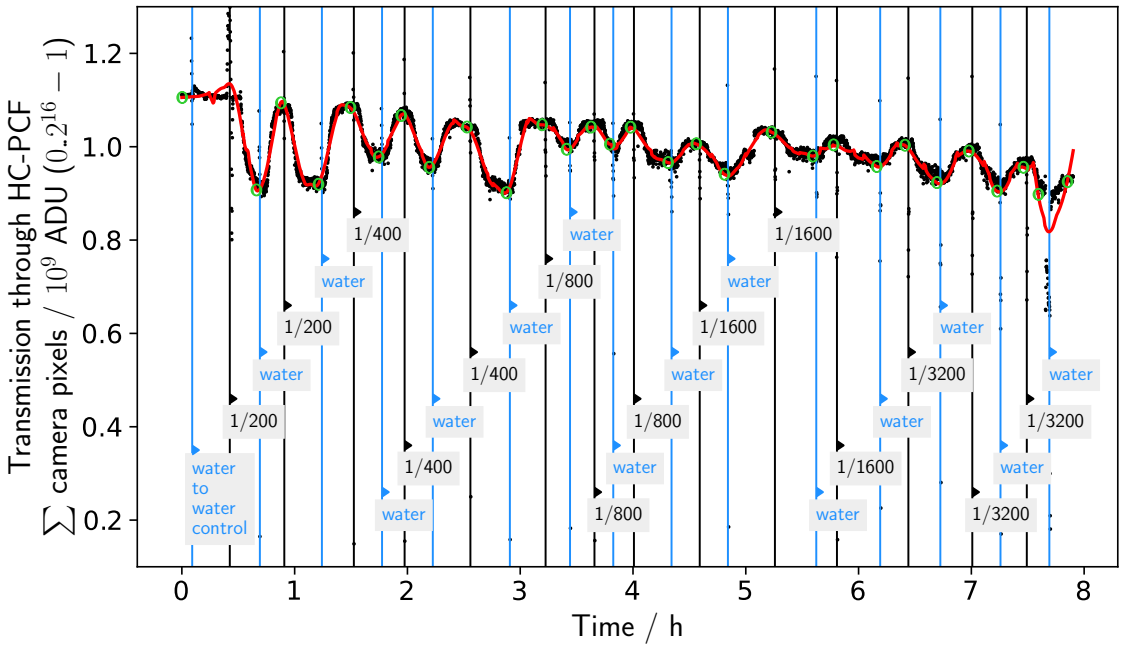

Fig. 4.14 Complete signal trace of the gold nanoparticle dilution series measured in HC-PCF. The sample syringe is changed between different dilutions (black vertical lines) and water (blue). When the signal stabilises, a reading (green) is taken based on the moving average (red) to calculate the change in transmission.

(*Fig. first referenced on p. 135*)

Following the same procedure as before, readings were taken to measure the extinction of the gold nanoparticle dilutions in the HC-PCF, which are plotted in Fig. 4.15.

The cuvette reference value was determined by measuring the extinction in a commercial cuvette UVVIS spectrometer using a stock solution that was then diluted at least twenty times further for measurements in HC-PCF. Since the cuvette measurement would have resulted in insufficient sensitivity at the lowest concentrations (highest dilutions), the horizontal axis in Fig. 4.15 extinction values are computed from this measurement divided by the known dilution factor (given on the top axis). This resulted in conservative estimates for the standard deviation in the horizontal axis, as the error is simply compounded by each dilution. Further analysis regarding the instrument's sensitivity and the comparatively low error introduced by series dilution would lead to a reduction in these error bars.

Notably, there is an apparently linear downward drift of the entire signal, and specifically the water baseline at the end of the eight hour experiment was down

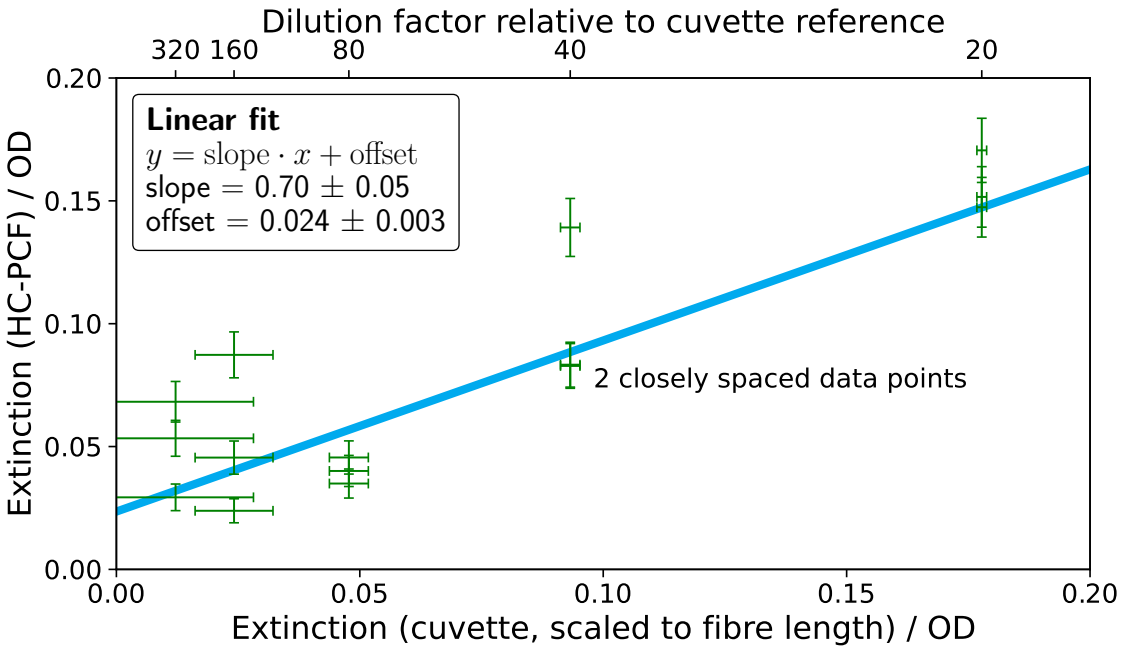

Fig. 4.15 Quantification of gold nanoparticles inside a HC-PCF using long-pathlength ultraviolet extinction measurement under continuous flow. As the flow through the HC-PCF is alternated between successive dilutions of gold nanoparticles (measured in triplicate) and water, the 365 nm light transmitted through the HC-PCF is measured. Taking the ratio between light transmitted when the sample is present and water flushed after results in the extinction, which is compared to cuvette reference values.

(*Fig. first referenced on p. 136*)

by −16 %. Since the measurement procedure was chosen to reference each sample transmission against the transmission with water flushed just after the sample, the effect of this drift on the extinction measurements is diminished. Nonetheless, to explore this drift further, a water-only run was carried out without sample changes, shown in Fig. 4.16.

Discussion

The extinction of the gold nanoparticle dilutions as measured in HC-PCF compared to the ground truth from large-volume, high-concentration cuvette measurements in Fig. 4.15 showed different behaviour for different concentrations. At the lowest concentrations (extinction less than OD 0.025 on the horizontal scale), scatter is high and adjacent concentrations could not be distinguished, indicating the limit of detection of the method. For the next higher concentration at OD 0.05, values are close to the reference value, which is also true for the value near OD 0.1, except for an outlier. Finally, the high-concentration measurements cluster within their standard errors and on average 14 % away from the ground

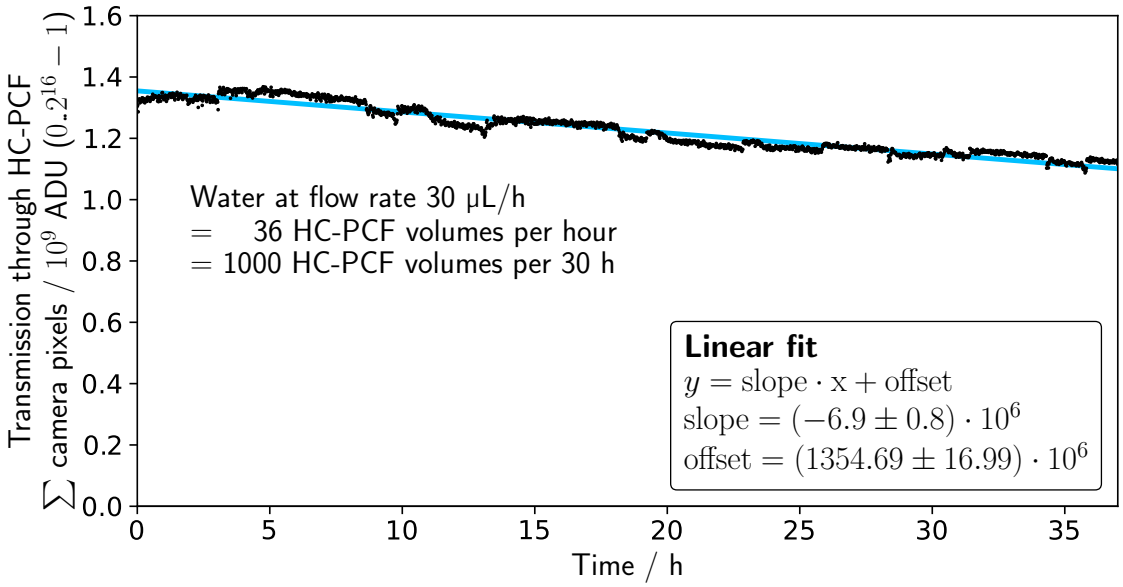

Fig. 4.16 Long-term test of the system. Water is flown through for an extended time (see inset) to study system drift. Despite the sample being only water, the signal is seen to decrease linearly at a rate of 0.5 %/h. The effect is explained as residual contamination of the inflow tubing being slowly dissolved and re-deposited inside the HC-PCF. (*Fig. first referenced on p. 137*)

truth. In terms of the linear fit, a slope of 0.70 ± 0.05 and an offset of 0.024 ± 0.003 indicate significant uncertainty and systematic error. Excluding the lowest concentration points would improve the result, but leave relatively few data points on which to perform statistically meaningful fitting, which is why this was not done. From these values, the limit of detection, by the same definition as in the previous chapter, is determined to be OD 0.11.

These results have to be seen in light of the baseline drift discussed above. In particular, the data presented later in this chapter were measured with freshly prepared tubing and cells, as well as the earlier polystyrene characterisation measurements, show a noticeably better linearity and reproducibility. This suggests contamination as the limiting factor of these experiments in particular, and not inherent to the technique. Time constraints meant the gold nanoparticle experiment could not be repeated, and the data are given as they are.

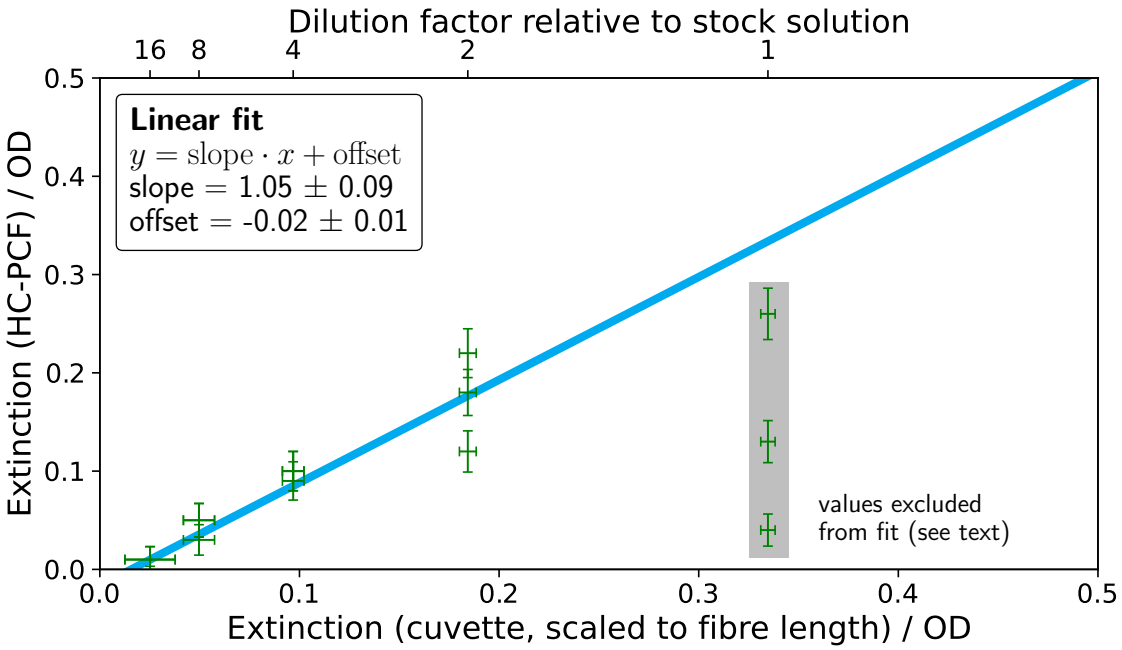

Fig. 4.17 Quantification of silk fibril aggregates inside a HC-PCF using long-pathlength ultraviolet extinction measurement under continuous flow. As the flow through the HC-PCF is alternated between successive dilutions of silk aggregates (measured in triplicate) and water, the 365 nm light transmitted through the HC-PCF is measured. Taking the ratio between light transmitted when the sample is present and water flushed after results in the extinction, which is compared to cuvette reference values.

(*Fig. first referenced on p. 139*)

4.3.2 Key experiment: Label-free quantification of silk fibril aggregates via extinction in HC-PCF under flow

Silk fibril aggregates measured via extinction in HC-PCF

The main experiment of this chapter aims to explore the use of HC-PCF in biophysics for label-free extinction measurements. Nanosized silk fibril aggregates were quantified in concentration using their extinction at a non-tryptophan wavelength at 365 nm. The measurements were performed in the same way as the gold nanoparticle detailed above. The resulting raw data are given in the supplementary information as Table SI.1, and plotted in Fig. 4.17.

General discussion

The linearity of the data was seen to be much better than the previous gold nanoparticle measurements. Discussed quantitatively below, the data points show good agreement between the newly-developed HC-PCF extinction measurement and the cuvette reference. For the triplicate above OD 0.1, the variance of the measured extinction is seen to increase, but the mean is still close to the

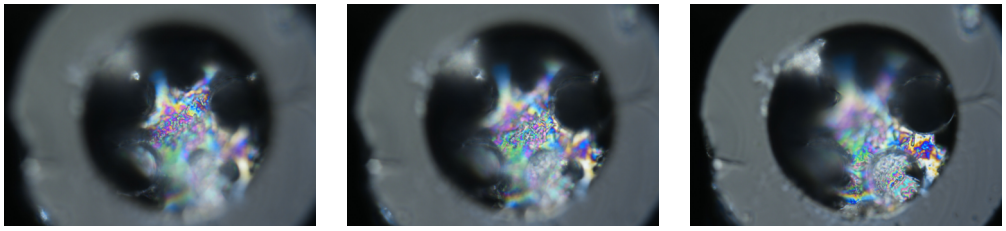

(a) (b) (c)

Fig. 4.18 Post-experiment brightfield microscopy of a HC-PCF used with silk fibrils. The three images at successive focus heights show the silk forming a three-dimensional hydrogel blocking the HC-PCF. Images are 125 µm wide horizontally. (*Fig. first referenced on p. 140*)

cuvette reference value. However, the data for the highest concentration did not follow this trend and deviate significantly by a systematic offset towards lower extinctions, despite being the highest concentrations.

Exclusion of points for fit

For these highest concentration measured (corresponding to the undiluted stock solution), poor mode quality was observed during the experiment, as well as low transmission that decreased further as the experiment progressed. At this high concentration, where transmission is expected to be around 50 %, the silk starts to form hydrogels and partial blockages leading to ill-defined transmission changes. Since extinction values in the HC-PCF were calculated as transmission ratio between sample and water flushed post-sample, if the transmission does not recover after flushing water (because the HC-PCF is clogged with silk hydrogel or aggregates), this ratio is close to unity i.e. low extinction. The raw data to illustrate this effect is given in the supplementary Fig. S-5. With the HC-PCF being occluded by these large aggregates accumulating, the high-concentration values were considered to be outliers and excluded from the fit, as indicated in the graph by a grey band.

HC-PCF post-mortem

To verify this hypothesis of hydrogels forming, a 'post-mortem' microscope inspection of a HC-PCF was performed after measuring several different high-concentration solutions of silk aggregates (Fig. 4.18). Similar hydrogels were found when inspecting other HC-PCFs which had degraded performance after used to perform many silk measurements.

As can be seen from the z-scan images, on the inflow side facet of the HC-PCF, a three dimensional gel structure has been deposited. Silk is known to form hydrogels, and this effect can be seen macroscopically with cuvettes or syringes gelling and solidifying after they have been left for hours to days with prepared the stock solution (studying silk aggregation is the focus of the next chapter).

This effect, causing partial blockages of the HC-PCF in addition to likely deposits throughout the fibre, is ascribed as the main factor in reducing the HC-PCF transmission slowly over time.

Linear fit and limit of detection

With these data points excluded, the fit gave a slope of 1.05 ± 0.09, i.e. unity to within standard deviation and an error of 8.6 %. This shows good agreement between the HC-PCF measurement and cuvette reference. The offset of -0.02 ± 0.01 indicates a small systematic error. The uncertainty in the latter value can be taken as an approximate indicator of the limit of detection, OD 0.01. This limit of detection is comparable to that of commercial UV-VIS measurements (the noise floor in Fig. 4.9 for the same sample is around OD $0.005\,\mathrm{cm}^{-1}$), despite using at least two orders of magnitude less sample and not operating in continuous flow.

4.4 Discussion and outlook

This concludes the second experimental technique introduced in this dissertation, which will be applied to additional research questions in the next two chapters. We finish the chapter by summarising its findings and learnings connected with the discussion of possible improvements.

4.4.1 Summary of findings

Through a re-design, the system improved in experimental handling and capability. Specifically, it was possible to build an in-liquid butt-coupling experiment where 365 nm light is coupled to our HC-PCF. This made possible extinction measurements to be performed at long (17 cm) pathlengths on dilute and weakly absorbing solutions (OD $< 0.01\,\mathrm{cm}^{-1}$) of gold and polystyrene nanoparticles, as well as silk fibril aggregates.

4.4.2 Possible improvements

Throughout the measurements, there was considerable variation in how reproducible a measurement was and the amount of drift present in the system over hours. Different hypotheses for the origin of this effect were explored and tested.

One suspected cause was heating of the entire setup, with the waste heat of the camera (approx. 100 W) being the major cause. As optomechanical components heat up, they can shift and cause changes in alignment, causing signal drift.

Timescales of hours would be expected for such an effect, in agreement with the data. Because the setup was entirely shielded to avoid stray light and UV exposure, it formed a closed environment that reached about 5 K above ambient. An air exhaust was added to improve the situation, but an effect on the drift was not observed. Hence, this effect was ruled out as a major cause of drift.

Residual contamination of tubing

When designing the experiments, it was previously seen in Fig. 3.11 that hysteresis between flushing different protein solutions was low. Hence, the assumption was made that the fused silica tubing used to construct the microfluidic circuits, if flushed through with many times its volume in water, would be suitably clean for new experiments. For example, if an experiment ended with a water flush, this was typically left running for several millilitres of dispensed volume after the experiment had concluded on the basis that the tubing and HC-PCF would be flushed clean. Furthermore, even if some contamination remained after flushing water, it was reasoned that any contamination still undissolved after hours of flushing was permanently adsorbed somewhere, and therefore would not be introduced into any subsequent sample. With the learnings from this chapter, it is now taken for granted that these assumptions were incorrect.

Reproducibility

After the residual contamination of tubing was identified as the most likely cause above, it became clear that there might have been cross-contamination between experiments. This would explain why some of the early characterisation measurements presented in this chapter showed much better reproducibility compared to later measurements, where many different samples (and especially protein-based samples) were studied and measured concurrently with inorganic nanoparticle samples. It is likely that the measurements with low or negligible baseline drift were performed shortly after a new piece of tubing was installed (e.g. because the experiment was changed), and those showing strong drift were done with tubing contaminated by other (esp. protein) samples.

Improvements made

Going forward, as a consequence, in the next chapter, all tubing was replaced before a new measurement was started. This is a lengthy (and somewhat costly) process, and future work should instead focus on establishing a cleaning protocol. A notable advantage of fused-silica HC-PCF is their chemical resistance (when used with equally chemically resistant optofluidic interconnects and tubing, as was the case in our experiments). This would allow aggressive solvents to be used in their cleaning, such as bleach or highly alkaline cuvette cleaning products, which are typically necessary as mechanical cleaning is not an option within microfluidic circuits.

Increasing the dynamic range

There are two values that are fundamental to the performance of an extinction measurement: sensitivity and dynamic range. Sensitivity dictates the smallest signal above noise that can still be measured, while dynamic range gives the maximum of transmitted light that can still be analysed quantitatively.

Perhaps most commonly, extinction measurements use a fixed-intensity light source and measure the light transmitted through the sample. The above two quantities are then defined primarily by the detector performance. However, to increase the dynamic range, it is also possible to modulate the light source intensity. Our system would allow for this approach, and evaluating its feasibility was the primary reason behind the measurements on LED modulation linearity (Fig. 4.1).

Closed-loop feedback measurements

To exploit the wide tunability of the light source intensity, instead of measuring transmitted light from a fixed light source intensity, the light source intensity could instead be modulated to maintain the same amount of transmitted light. Tracking the modulation signal necessary to achieve this would then be an inversely proportional measure of transmission. The advantage of this closed-loop feedback approach is that the detector can have a narrow dynamic range with a high sensitivity. Different sensors, universally, trade dynamic range vs. sensitivity (the discussion about the sensitivity of single molecule measurements in Section 1.2.1 is precisely analogous to this). Hence, with this approach, a detector with high sensitivity but narrow dynamic range could be chosen.

Last but not least, this closed-loop control further opens up the possibility for lock-in measurements and non-linear transmission measurements by modulating the input signal over time (faster than the sample would change).

5 | Capillary Action Infiltration for Minimal Sample Volume

In the previous two chapters, we have shown the potential of HC-PCF for continuous flow integration into microfluidic circuits, which can enable high-throughput applications. This chapter is a short break from this, and represents a brief excursion towards the very opposite. Relating to a point often raised by other researchers when presenting our work, there are also cases such as manual batch processes where the most desirable feature is a minimal sample volume measurement from a single drop of sample, without any need for microfluidic integration. Here, we explore adapting our work to this challenge.

5.1 Motivation 145
5.1.1 Note about availability 145
5.2 Experimental method 146
5.3 Results 148
5.4 Discussion and outlook 151

5.1 Motivation

How this chapter came about from collaborative discussions

During discussions at conferences about possible collaborations, a frequent question posed to me was the minimum sample volume required to perform a measurement from start to finish. While our measurements operate on sub-microlitre *detection* volumes, the required *sample* volumes are higher due to the continuous-flow operation. While continuous flow brings many advantages, especially for high-throughput applications and integration with other microfluidic components, for research groups that synthesise proteins in small volumes and concentrations for experimental use, this solution is not ideal. Motivated by this feedback I received, this chapter explores the passive filling of HC-PCF by capillary action to reduce the required sample volume to be close to the internal (or detection) volume, enabling ultra-low-volume measurements.

5.1.1 Note about availability

Making HC-PCF at scale

As we develop the method of this chapter, there is a practical point to note first. HC-PCF are a technology whose continuous-draw fabrication is inherently scaleable to high-volume production, as evidenced by the global telecommunication infrastructure being built on a backbone of solid-core optical fibre, which now surpasses 4×10^{12} m (over three light-hours) in total length.[308] HC-PCF is produced increasingly on an industrial scale, regularly reaching into kilometre lengths.[309] These numbers, and simulations confirming the possibility of hundred-kilometre scale fibre draws,[310] lend evidence to the view that the application presented in this chapter would be viable in principle if demand existed.

Proof-of-concept only

Despite that being the case, the actual HC-PCF used in this research is a single-spool custom draw, with its limited supply shared between all laboratory users who depend on it for their research. Hence, using a large amount of HC-PCF to demonstrate a potential use as a disposable item is undesirable and, consequently, the decision was taken to limit the number of measurement repeats to that of a proof-of-concept.

Similar work

Often labelled as 'dip sensors', the use of capillary filling is commonly found in HC-PCF applications.[213][215] However, such approaches often do not consider the ability to flush the HC-PCF, and are therefore less suitable for quantitative extinction measurements, where a solvent and fibre loss reference is needed. This is the area we want to explore with the work of this chapter.

5.2 Experimental method

Capillary forces

Any liquid–solid interface will see wetting effects that minimise surface energy, as determined by the material combination's wetting angle θ_w and surface tension γ. This causes liquids to be dragged up along the sides of any capillary they are placed in, forming a concave meniscus (given that $\theta_w > 0$, i.e. surface wetting decreases surface energy. For water–fused silica, $\theta_w \approx 25°$, dependent on surface cleaning and treatment.[311] With $\theta_w \neq 90°$, this spherical meniscus will have a radius r_m different to the capillary radius r, the ratio of which defines the wetting angle by

$$\cos\theta_w = r/r_m. \tag{5.2.1}$$

Maximum vertical rise

For a vertical rise, equilibrium height of the liquid column formed in the capillary will be reached when the pressure head due to gravity pushing down becomes equal to the capillary force pushing the liquid up. In a laboratory setting, where gravitational acceleration g and atmospheric pressure vary insignificantly with height, the only variable determining capillary liquid rise h are the liquid density ρ, wetting angle θ_w, and capillary diameter $2r$. Then, the equation known as Jurin's law gives the liquid rise as

$$h = \frac{4\gamma\cos\theta_w}{\rho g}\,\frac{1}{2r}, \tag{5.2.2}$$

and is inversely proportional to the capillary diameter. For our fibre with $r = r_{core} = 15\,\mu m$ (as the lower-bound estimate, with the cladding capillaries and interstitial spaces being even smaller), the rise is $h \approx 90\,cm$, and therefore several times longer than the fibre lengths typically used in our experiments. Furthermore, in a horizontal capillary, no force acts against the capillary flow (except friction, which as a dynamic force can only act to slow the filling), thereby offering a means of completely filling fibres of arbitrary length by capillary action alone, albeit slowly.

Timelapse of HC-PCF filling

To observe the capillary filling of HC-PCFs, a simple arrangement was constructed to record this process on a microscope, and a timelapse recording was made (Fig. 5.1).

When pipetting a drop of water onto the cleaved, empty HC-PCF facet, the water is drawn across the HC-PCF to emerge on the other end. At first, individual capillaries show a drop forming on their end facet. This agrees with the

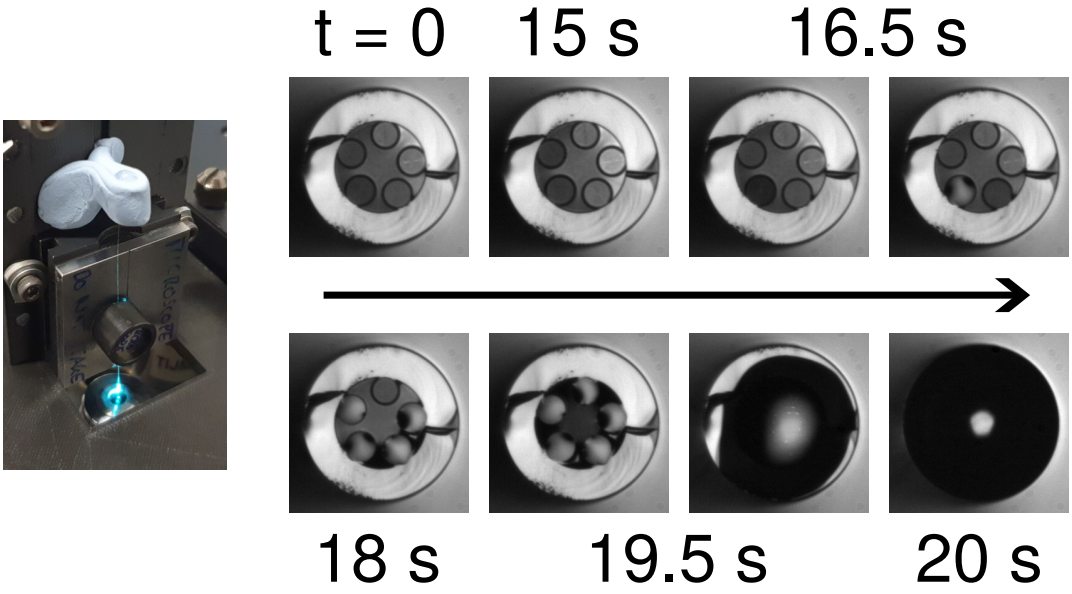

(a) Experiment (b) Resulting timelapse

Fig. 5.1 Measuring filling speed and uniformity by timelapse microscopy. A 5 cm HC-PCF segment is held ontop a brightfield microscope by a magnet clamp. The distal top facet of the fibre is held inside a piece of moulding putty, forming a small reservoir that a drop of water is pipetted into at $t = 0$. (*Fig. first referenced on p. 146*)

expectation that smaller capillaries are filled faster. The capillaries do not fill all at the same time, but do so within a few seconds, closely followed by the core and interstitial spaces being filled. Finally, a droplet encapsulating the entire HC-PCF forms, which acts as a lens. This experiment was repeated multiple times to confirm that the HC-PCF always did fill, as this would not be verifiable during the actual extinction measurements, since the HC-PCF will be mounted in a water-filled reservoir before imaging can take place. When illuminated from the side, the meniscus could be seen to move during filling as a bright spot (scattering centre) by eye. Occasionally, the HC-PCF failed to fill immediately by capillary action. In this case, a small amount of agitation helped break the surface tension and begin the filling process.

Minimal-volume extinction measurement

For the minimal-volume extinction experiment, it was found most convenient to be able to fill the HC-PCF when already installed in the setup. This would resemble the way such a setup might work in practice, with the sample to be analysed pipetted onto a glass slide and infiltrated into the HC-PCF by immersing one end into the droplet (Fig. 5.2).

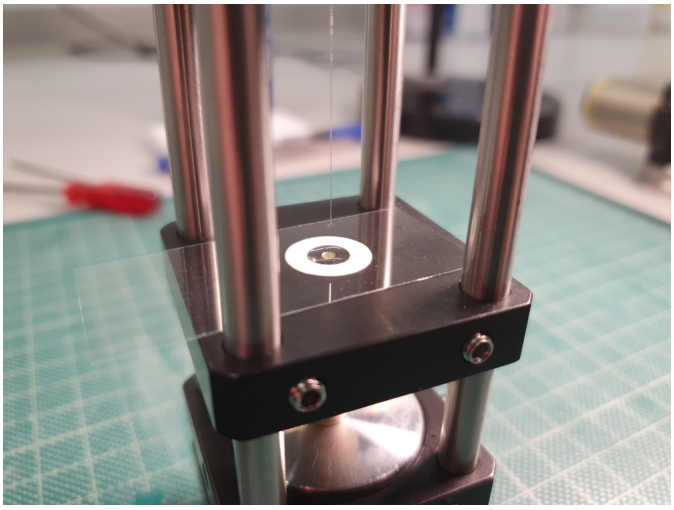

Fig. 5.2 Infiltrating the HC-PCF by capillary action. A drop of sample is pipetted onto a cover slide, with an adhesive ring preventing spillage. (*Fig. first referenced on p. 147*)

A fibre length of 17 cm was used throughout. Once the HC-PCF had been filled by capillary action with the sample solution to be analysed, it was fixed into the same measurement setup as described in Chapter 4. Before the liquid connector was fully secured, a small amount of water was pushed through to create a sheath flow around the fibre facet to remove air bubbles introduced during mounting. A low flow rate ($3\,\mu L\,min^{-1}$) was used to ensure that the pressure inside the optofluidic interconnect was kept low and no significant amount of flow would enter the HC-PCF, instead exiting through the loosened connector with much lower hydrodynamic resistance. Finally, the HC-PCF was secured and data acquisition began, again in the same way as described in the previous chapter.

Flushing water to establish a reference

After leaving the system undisturbed for a few minutes to establish a baseline (which will be the transmission through the sample solution), the HC-PCF was flushed with water, resulting in a solvent reference transmission. The two measurements are then compared against each other, yielding the desired extinction measurement as sample transmission divided by solvent transmission.

5.3 Results

Two experiment are presented. In the first, to establish a control measurement, the sample solution was simply water. In the second experiment, a 10 nm gold

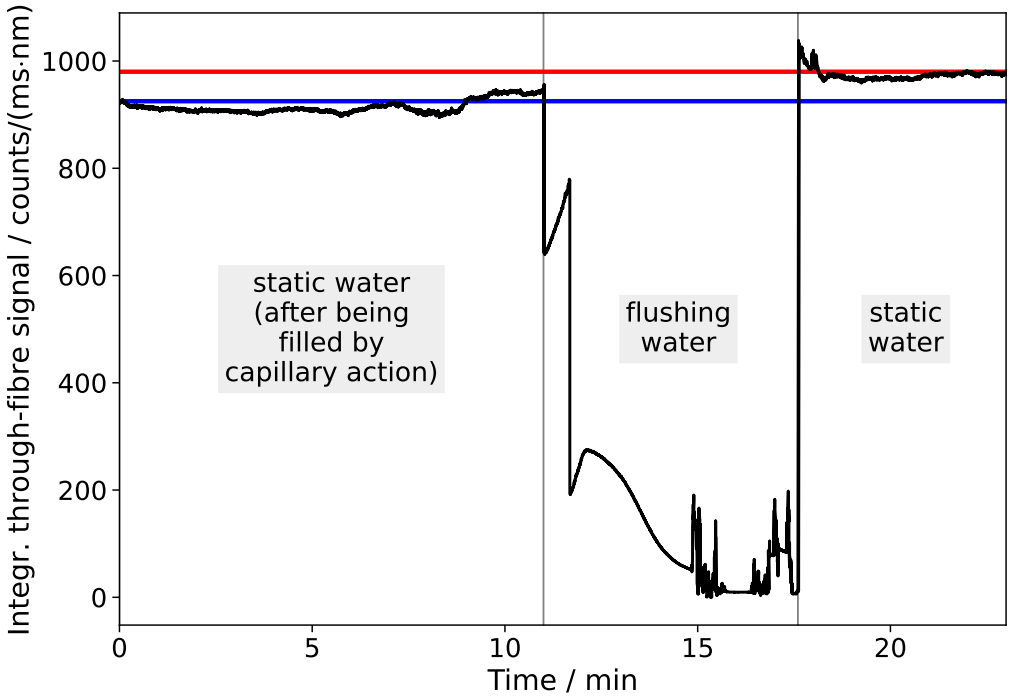

Fig. 5.3 Water–water control measurement for minimal sample volume extinction measurements through capillary filling. A small (microlitre) drop of water fills the HC-PCF by capillary action, which is then measured, flushed through with more water, and measured again to understand the baseline accuracy via this water–water control measurement. (*Fig. first referenced on p. 149*)

nanoparticle solution calibrated to $T = 25\,\%$ transmission through the length of fibre used was measured.

Water-water control

The water-to-water control measurement is shown in Fig. 5.3. After ten minutes of establishing a static baseline (blue line), fresh water was flushed through for ca. five minutes. The initial static baseline is stable to within a few percent. After water is being flushed through, the signal is seen to vary irregularly, first dropping in steps and then spiking irregularly. This action is explained as air bubbles introduced during the mounting procedure being flushed through the system. After returning to static conditions, the system quickly settles to a new baseline (red line).

Taking the ratio of these measurements gives a value of 106 %, or an error of 6 % between the water and water measurements. This number represents limit of detection of this method, with the strong limitation that this remains a single data point and should be repeated to acquire statistical confidence.

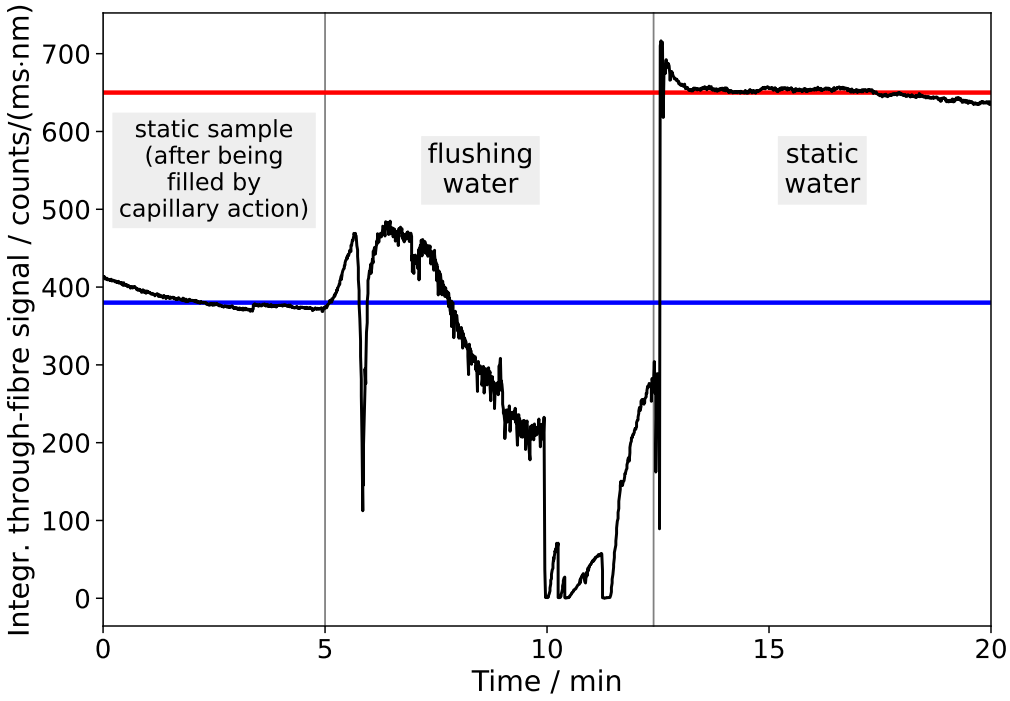

Fig. 5.4 Exchanging a sample filled by capillary action with water as the extinction reference. The sample, size standard gold nanoparticles of diameter 10 nm, are diluted to an expected transmission of $T = 50\%$ over the HC-PCF length. (*Fig. first referenced on p. 150*)

Gold nanoparticle measurement

Next, the measurement of the gold nanoparticle solution is shown in Fig. 5.4. For this measurement, the experiment was recorded with a spectrometer instead of a camera. The measurement was performed in the same way as above. The recorded signal trace shows a similarly irregular transition between sample and water as the previous water-to-water measurement, suggesting the effects are caused by trapped air in both cases.

A slow but steady fall of transmission (i.e. increase in extinction) was observed at the beginning of the measurement. This could be a residual flow into the HC-PCF, slowly exchanging the high-extinction sample with water.

The ratio of transmission between sample and water reference was 59 %. This is an error of 18 % from the calibrated value of $T = 50\,\%$. A possible explanation for the fact that the measured extinction was less than expected is that some of the gold nanoparticle solution could have been inadvertently flushed out during fibre mounting or sheath flow.

5.4 Discussion and outlook

Summary

The above was a method developed to measure minimal sample volumes in the setup presented in Chapter 4. Unlike the work shown there, aimed at high-throughput integration with microfluidics, the work of this chapter looked at the opposite end of system design, with one-off measurements for the minimal amount of sample and integration needed to perform a measurement. A given sample can be measured simply by dipping the end of the HC-PCF into it, using exactly the amount of sample required to fill the HC-PCF, and performing an extinction measurement as described in this chapter. Nonetheless, as a proof-of-concept with limited experimental runs, much work remains needed to characterise and optimise this applications.

The linear volume of the HC-PCF is 49 nL/cm, such that the volume of the 17 cm fibre is 830 nL. The fibre was filled from a drop pipetted onto a glass slide, which needs to be of a certain size to allow filling of the HC-PCF by simple dipping. Hence, a practical sample requirement would be around 2 µL. The method therefore allows measurements on minimal volumes without need for a complicated sample loading procedure. After capillary infiltration, the HC-PCF is transferred to the setup of the previous chapter where the extinction measurement is performed using the relevant solvent for reference.

Future directions

The methods of this chapter show that it is possible in principle for the low-volume measurements made possible by the HC-PCF to be carried out with similar convenience of sample loading as a commercial cuvette UVVIS measurement. The steps required after sample loading to take an extinction reading still require the operator to have expertise in HC-PCF preparation, mounting, and measurement. However, for example by designing a cartridge holder for the HC-PCF similar to how many commercial machines operate, the goal of automating many of the steps appear achievable. As described at the beginning of this chapter, the work presented here remains as a proof-of-concept.

6 | Towards Monitoring of Protein Aggregation In-Situ

In this final experimental chapter, we combine the work of the previous Chapters 3 and 4. Working towards monitoring the aggregation of a protein within a hollow-core photonic crystal fibre for over two days, we demonstrate the ability of the system to multiplex both fluorescence and extinction measurements in-situ. This allows both of these variables to be recorded over the multi-day timescales of protein aggregation from the same microfluidic circuit.

6.1 Motivation . . . 153
6.2 Experimental Method . . . 153
6.2.1 Silk fibroin protein . . . 154
6.2.2 Experimental setup . . . 156
6.2.3 Data collection . . . 162
6.3 Results . . . 164
6.3.1 Key experiment: Label-free monitoring of protein aggregation via multimodal sensing in HC-PCF under flow . . . 164
6.4 Discussion and outlook . . . 169
6.4.1 Summary of findings . . . 170
6.4.2 Possible improvements . . . 170

Contributions *This chapter corresponds to a publication currently in preparation. Zenon Toprakcioglu supplied the silk fibroin protein stock and provided advice on protein aggregation protocols. Michael Frosz supplied the HC-PCF used in this dissertation. Tijmen Euser and Tuomas Knowles supervised this work and provided guidance and advice throughout.*

6.1 Motivation

Combining different sensing principles

Protein aggregation is connected to several disease pathologies, such as the neurodegenerative Alzheimer's disease.[38][312] Key to a mechanistic understanding of protein aggregation processes is the measurements of aggregation kinetics. Among the most important in-solution measurements to characterise aggregation are fluorescence, which is affected by conformation-mediated solvent quenching, and extinction, which is the combined action of absorption and scatter. Since scattering cross-section (in the Rayleigh regime $r \ll \lambda$) scales as the sixth power of particle size, it is an indicator of size but with an overlaid absorbance contribution (such as fluorescence excitation) that complicates analysis. Similarly, fluorescence changes with aggregation, but re-absorption and spectral changes make this also a non-linear relationship. By taking measurements of different sample properties, based on different physical principles, it is possible to correlate and separate the different contributions. In this chapter, we implement both fluorescence and extinction measurements in-situ on the same protein sample (silk fibroin) in continuous flow (which eventually ceases as the aggregation progressively increases viscosity), monitoring this process over 60 h.

Work in progress

While true of science in general, and ongoing work in particular, we nonetheless want to stress the fact that the aggregation experiments in this chapter are work-in-progress. The experiments in this chapter form an application intended to leverage the individual techniques developed in this PhD. They enable an in-situ combined measurement, and this work could only be begun in the final months of the PhD as it builds on all techniques developed before it in the past chapters.

Hence, the experiments here are at an early stage. They lack repeats and thorough characterisation of individual factors, and the study of silk protein aggregation demonstrated here requires further work before biophysical conclusions could be confidently drawn from it. Still, this chapter hopes to show the possibilities opened up by combining different measurement modalities into a sensing platform based on HC-PCF, with a view towards future research.

6.2 Experimental Method

The sample used in this chapter is the same as that used before to produce the protein aggregates studied in Chapter 4. Since, in this chapter, the silk is allowed to aggregate slowly and while being monitored in HC-PCF, we give the

sample more attention here and discuss it in additional detail before describing the experimental setup. Silk was chosen as the target of protein aggregation experiments for its availability and suitable aggregation timescale (especially by induction through the addition of ethanol), while being more generally motivated as a fascinating biomaterial with a long history of use by humans.

6.2.1 Silk fibroin protein

Sample preparation

Natural silk's primary proteins are silk fibroin (80%) and sericin (20%), where the fibroin can be understood as the structural backbone and the sericin as a gummy coating.[313] The silk fibroin solution used in this dissertation was prepared by Zenon Toprakcioglu according to a published protocol.[314] In brief, to extract the silk fibroin from the natural raw silk, *Bombyx mori* silk cocoons are cut, boiled for 30 min in a dilute sodium carbonate aqueous solution, and the undissolved remnants (now mostly silk fibroin) repeatedly rinsed in water. The silk fibroin is then dissolved in lithium bromide and purified by dialysis and centrifugation. The resulting silk stock at $50\,\mathrm{g\,L^{-1}}$ can be frozen at $-80\,^{\circ}\mathrm{C}$ and was stored in aliquots at 4 to 8 °C until use. The silk solutions used in this chapter were prepared shortly before the experiment to a final protein concentration of $5\,\mathrm{g\,L^{-1}}$. Ethanol was added to induce aggregation (discussed below) to a final concentration of 40 % by a 1:1 (v/v) addition of 80 % ethanol solution to a silk fibroin solution of twice the desired concentration in water. This method was preferred over using less but more concentrated ethanol solution to minimise the evolution of heat (from the enthalpy of solvation), and reduce concentration gradients that can affect aggregation. Mixing of the silk solution was always done by repeated gentle pipetting with a large-diameter tip to keep shear forces as small as possible. Despite these measures, prepared solutions typically showed macroscopic aggregates (or other insoluble components) large enough to be visible by eye. Hence, solutions were filtered through a 450 nm syringe filter, slowly over 30 s, again in an attempt to minimise shear forces.

Silk aggregation

The silk used in the experiments of this dissertation is a naturally-derived product that has significant variation in composition and resulting aggregation behaviour. In nature, spiders form their solid webs from liquid silk. The machinery with which spiders are able to accomplish the storage of the precursors and the intricate spinning of silk – on-demand, in water-based chemistry, at high efficiency for extended periods of time with high reproducibility – are both

astonishing and complex, and tightly controlled shear forces form the primary mechanism behind it.[315]

... by shear forces

Hence, silk protein aggregation in particular is strongly affected by shear forces, as studied by rheology, and the variability of aggregation even under laboratory conditions is generally accepted.[316][317] Especially in microfluidic environments where liquids meet high pressures and narrow flow constrictions, but also by general handling and ageing, the aggregation of the silk is continuously affected and can be difficult to reproduce between experiments. Even when protocols are strictly controlled for, such as in medical applications, this remains the case. For example, a study found that all pre-filled glass syringes for the administration of therapeutic protein products had formed aggregates of many different shapes and sizes.[318]

While these effects contribute to the variability observed in silk protein aggregation, they also motivate the development of biophysical measurements where the shear forces can be tightly controlled. Made from glass with tight tolerances and supporting a wide range of flow rates and pressures, HC-PCFs could serve as such a system.

... by interfaces

Surfaces influence aggregation, in particular the different surface chemistries of plastic and glass.[319] When preparing solutions, even the careful agitation to mix solutions (which is difficult to quantify due to the often turbulent nature) plays a role in inducing aggregation.[319][320] One mechanism is the adsorption and desorption on the solid-liquid interface[321] as well as any air bubbles created during agitation, which provide air-water interfaces in addition to the liquid's meniscus if kept in partially filled containers.[318]

... by induction with ethanol

Hence, to more reliably induce and study the aggregation of silk or other proteins, it is desirable to use methods other than the ones above. In particular, such a method should be more controllable in a laboratory environment, ideally triggering a well-defined starting point for the onset of aggregation. Furthermore, when aggregation happens over long timescales (days), methods for accelerating the aggregation process become increasingly useful. For this reason, ethanol is commonly used to induce aggregation in proteins.[322] The mechanism by which ethanol induces aggregation are still being studied,[323] with the key roles being changes in protein conformation[324][325][326] (e.g. β-sheet formation) and disulfide or other bond formation.[327]

Besides ethanol, other commonly used chemicals include urea or arginine.[326] Instead of chemical induction of aggregation, temperature also strongly affects

aggregation and can be used to accelerate it, but can also affect other objects under study and is not as immediate a trigger as the addition of a chemical at a single point in time.

Aggregation kinetics

Silk, by the discussion above, therefore forms an interesting target for the study of protein aggregation. Its kinetics are most commonly studied by the addition of labels (especially Thioflavin T, ThT), which gives aggregation timescales in the range of tens of hours depending on concentration and condition, similar to what is observed below in HC-PCF.[328] At the same time, the cited study also shows the variability of the aggregation process, exploring the effect of shear forces in particular.

Label-free measurements on silk have been performed previously in the literature using the silk's intrinsic fluorescence. For example, Toprakcioglu *et al.* measured the kinetics of silk fibroin aggregation both via intrinsic fluorescence and using ThT (under static conditions).[21] This paper was already discussed in the literature review (Section 1.2.1).

Origins of fluorescence in silk

The intrinsic fluorescence of silk (fibroin) is caused primarily by its tryptophans, but their contribution and the overall fluorescence changes significantly with aggregation, which can be deconvoluted to individual spectral features.[329] In this present work, we focus on capturing the most prominent intrinsic fluorescence peak as filtered to (357 ± 22) nm, to demonstrate the general principle. Spectrally-resolved measurements therefore become an obvious target for future work, as this would allow the aggregation process to be tracked mechanistically.

6.2.2 Experimental setup

As a combined application of the techniques of previous chapters, the experimental setup is substantially the same as that of Chapter 4, with the side-excitation added to it using the material from Chapter 3. We describe differences and additions to these below. The resulting experimental setup is shown in Fig. 6.1.

Side-excitation LEDs

Only two of the LEDs from the side excitation setup were active due to size constraints, irradiating ca. 5 cm. Unlike in the approach of Chapter 3, HC-PCF access is now possible from all four sides equally, and a re-design would leverage this by positioning LEDs on different sides of the fibre. Alternatively, the mechanical supports that have been added in Chapter 4 to ensure straightness of the HC-PCF and reduce bending losses (and associated variability) could be removed or re-designed to give more side access to the HC-PCF.

Besides the addition of the 275 nm LEDs from the previous side-excitation intrinsic protein fluorescence measurements, the irradiated section was additionally enclosed with reflective foil. This helped to increase both the amount and uniformity of the LED light irradiating the HC-PCF. Furthermore, the PMT was re-introduced to the setup, this time without fibre coupling.

Temperature

Knowing that protein aggregation is affected by temperature, a temperature probe was inserted into the enclosure. An increase in temperature is expected from the LEDs (both convective waste heat and radiative). The local temperature sensor was installed into the enclosure less than a centimetre away from the HC-PCF suspended without contact to surfaces. Measurements showed that, after the system had been pre-heated (without sample present) prior to experiments, the temperature increased by (1.7 ± 0.5) K above ambient in the experiment shown in this chapter. The temperature environment of the HC-PCF then was around 26 °C, varying slowly with room temperature, which was measured by an ambient temperature sensor.

PMT for extinction measurements

The experiments in this chapter were first attempted in the same way as before, using the camera for intensity measurements. This was seen to work well for the initial stages of aggregation, but as the aggregating silk became both less intrinsically fluorescent and more absorbent, the camera began to reach its detection limit. Hence, the system was again changed to measuring the signal with the PMT while also imaging with the camera, both band-pass filtered as before. This allowed measurements to carry on to later stages of aggregation. For silk before aggregation, Fig. 6.2 shows typical images obtained.

Fluorimetry in cuvette

Fluorimetry was performed in a sealed quartz cuvette in a commercial right-angle fluorimeter over one week (Fig. 6.3). The spectrum initially has a fluorescence emission peaked close to 350 nm, characteristic of tryptophan fluorescence as expected. The narrow and comparatively weaker peak at 275 nm stems from scattered excitation light.

As the silk solution aggregates, two spectral changes occur simultaneously, with the resulting spectrum being a product of the two. One effect is the peak at 350 nm decreasing, while the other is an increase around 400 nm, growing first into a shoulder of the 350 nm peak before eventually becoming a separate peak.

The inset of the figure tracks these peaks over time. After approximately 15 h, the newly-developing visible fluorescence peak overtakes the tryptophan peak to reach a final value of around 40 % the intensity of the initial 350 nm peak.

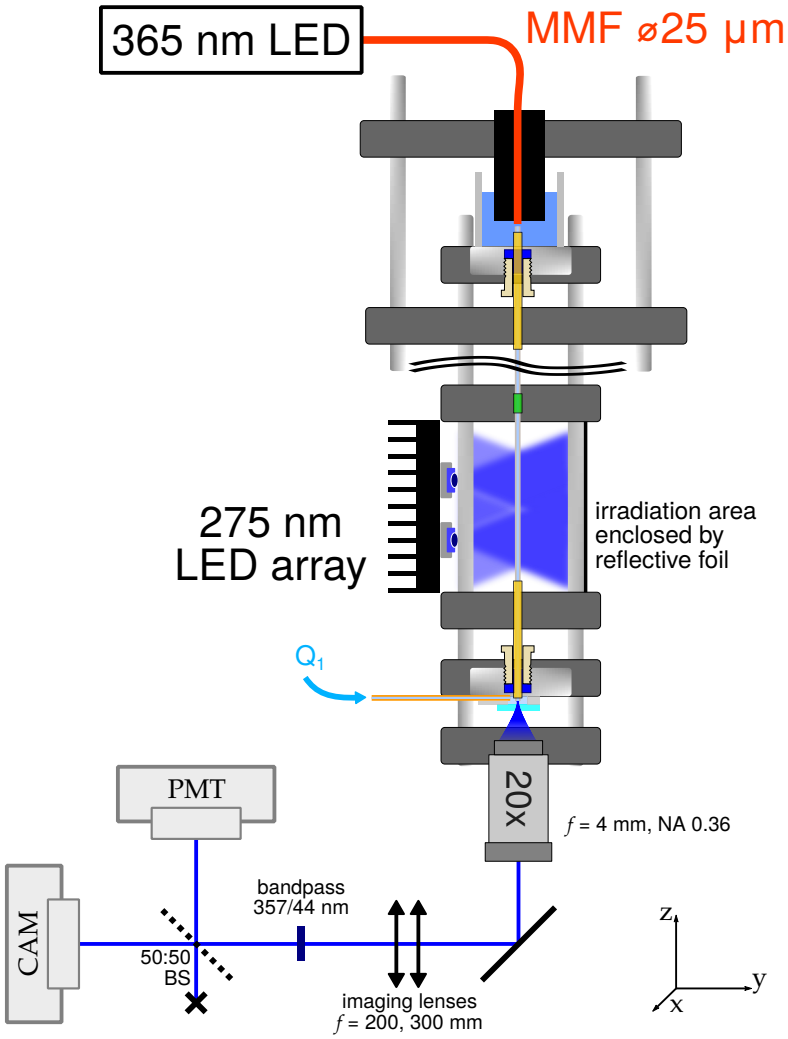

Fig. 6.1 Experimental setup showing how side-excitation is added to the extinction setup from Chapter 4. The HC-PCF, measured in transmission at 365 nm, is alternatively irradiated from the side with 275 nm to excite intrinsic protein fluorescence. The enclosed area serves to both increase uniformity and shield the deep ultraviolet light from the experimenter. (*Fig. first referenced on p. 156*)

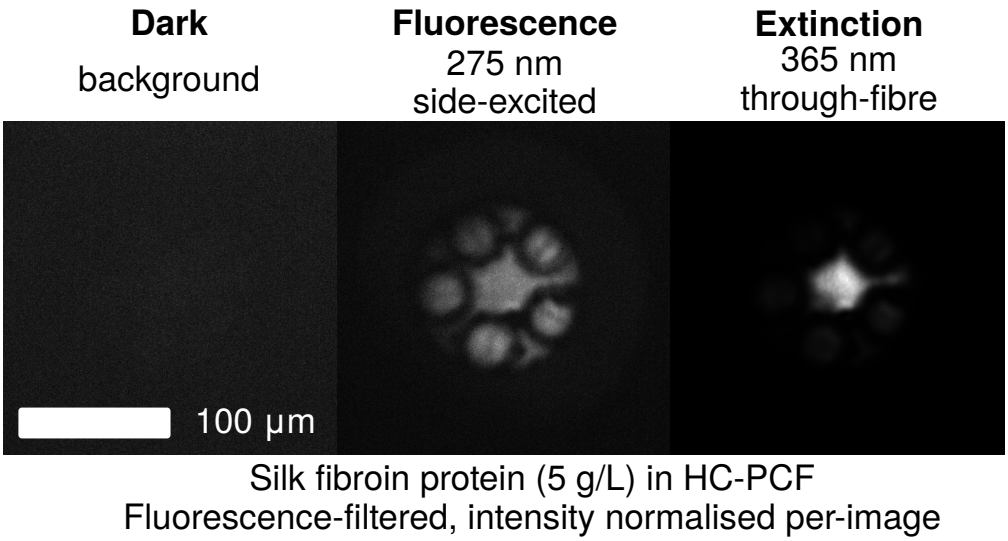

Fig. 6.2 Multiplexing extinction and fluorescence measurements in HC-PCF. By alternating between the methods developed in Chapter 3 and Chapter 4, the intrinsic fluorescence and UV extinction of silk fibroin protein can be measured in-situ and under flow. The silk in these images was fresh, non-aggregated solution.

(*Fig. first referenced on p. 157*)

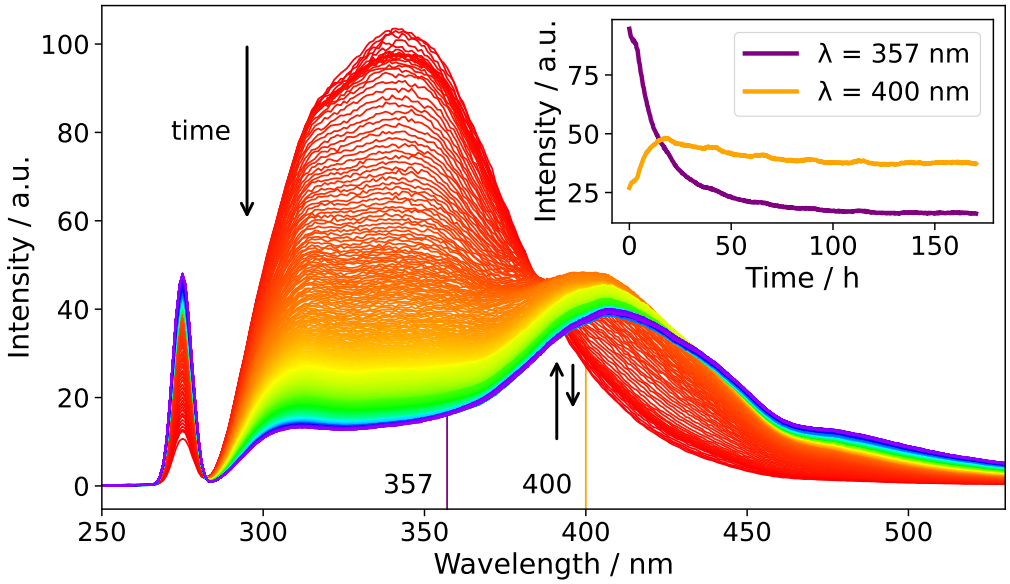

Fig. 6.3 Fluorimetry of an aggregating silk solution in cuvette. Aggregation is induced in a silk fibroin solution with ethanol ($5\,\mathrm{g\,L^{-1}}$, 40 %). **Inset:** The fluorescence at 357 nm and 400 nm is tracked over time, showing the tryptophan peak (350 nm) to decrease and a new visible fluorescence (400 nm) to develop with aggregation.

(*Fig. first referenced on p. 157*)

Meanwhile, the tryptophan fluorescence decreases continuously to a value below 20 % its initial value.

We have previously explained that tryptophan fluorescence is strongly dependent on its exposure to the solvent. Since the solvent offers non-radiative decay pathways (especially from collisional quenching) for excited tryptophans, and aggregation is expected to increase burying by increasing the volume-to-surface ratio, the tryptophan fluorescence is expected to increase with aggregation. However, the data shows the opposite trend.

Explanation of fluorescence decay with aggregation

Two factors can offer reasons for why this could be the case. First, while the solvent offers non-radiative decay pathways, the aggregated structure can do the same by coupling molecular vibrations. Second, the visible fluorescence developing through aggregation will have a fluorescence absorption close to 350 nm, serving as an inner filter to absorb any emitted tryptophan fluorescence and re-emit it at visible wavelengths.

From the given data, these effects cannot be separated, and for the purposes of method development they are considered simply as indicators of aggregation without pursuing a detailed mechanistic understanding. Further experiments measuring both absorbance and fluorescence at different wavelengths could help understand the contributions of these effects, which our HC-PCF experiments would support in principle if the PMT were replaced by a spectrometer of similar sensitivity.

UV-VIS extinction in cuvette

UV-VIS extinction measurements were performed in a UV-grade plastic cuvette (Fig. 6.4). This experiment was started with the same solution prepared for the HC-PCF experiment to run in parallel as a control. The cuvettes were covered with parafilm to avoid evaporation for these long-term measurements. The room temperature was measured to show no significant variations (below 3 K) over this time.

The qualitative trend is the same as observed in the fluorimetry experiments. A fast period of increased extinction is followed by a slow trend towards equilibrium. However, unlike the fluorimetry results, the spectrum does not develop new features. Instead, the extinction is monotonically increasing throughout aggregation, and can therefore serve as an indicator of the progression of aggregation.

The increase in extinction showed a distinct slow onset at the beginning of the measurement, then going through a fast phase, before again slowing down (while still being monotonically increasing at all times). This results in a sigmoidal curve characteristic of protein aggregation kinetics, which are dominated by a

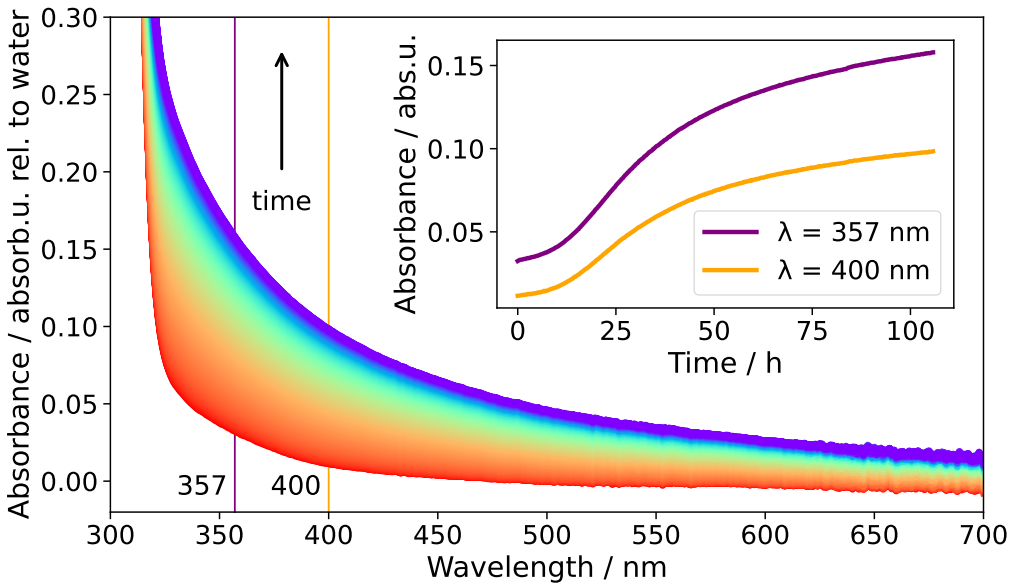

Fig. 6.4 UV-VIS extinction of an aggregating silk solution in cuvette. Aggregation is induced in a silk fibroin solution with ethanol ($5\,\mathrm{g\,L^{-1}}$, 40 %). **Inset:** The absorbance at 357 nm and 400 nm are tracked to show similar, sigmoidal increases that are characteristic of protein aggregation kinetics: a slow start, a fast transition, and again a slow trend towards equilibrium. (*Fig. first referenced on p. 160*)

nucleation phase followed by fast growth.[35] By comparison, this effect was not as pronounced in the fluorimeter measurement, although a short plateau can be seen at the beginning of the fluorimeter measurement. This suggests that the aggregation had already started to proceed to a later stage compared with the UV-VIS measurements. Since the fluorimeter measurements were performed with a different sample solution, in a different laboratory using different equipment, this variance can likely be attributed to the natural variation of silk aggregation, as discussed in Section 6.2.1.

Possibility of photobleaching

We note that in the above cuvette measurements, and also below (especially once the flow has stopped), photobleaching will form a contribution to the change in observed fluorescence, both in intensity and spectral shape. Furthermore, tryptophan is liable to photo-ionise when exposed to ultraviolet light,[330] which can lead to secondary chemical reactions that possibly affect the sample's fluorescence properties. The effect of photobleaching in the context of (tryptophan) intrinsic fluorescence has been shown in the literature, such as when inspecting medical tissue samples,[331] or giving rise to the yellow discolouration of wool when exposed to sunlight.[332][333]

While a contribution of photobleaching to the observed changes in fluorescence and absorbance is certainly present, we note that the aggregation process also results in a visible change in viscosity ultimately leading to the formation of non-flowing hydrogels, even when samples were stored in the dark. Further experiments performing dose-dependent fluorimetry (e.g. by scanning two identical samples in a fluorimeter, one at a much higher interval than the other) could quantify this effect. In flow systems, the effect is reduced by the sample being continuously replenished.

6.2.3 Data collection

Limits of long-term acquisition

Collecting measurement data continuously over 60 h posed new challenges. Most measurement equipment used did not support such long acquisition times. For example, the PMT could only collect up to $27\,\mathrm{h} = 10^5\,\mathrm{s}$ of data. It therefore had to be manually stopped, the data saved, and restarted with a new acquisition. To avoid this taking place during the night, the actual time the measurement was restarted varied with the author's schedule. When the acquisition was restarted, this introduced a short time delay where no data points were recorded, and the PMT and camera images incurred a small synchronisation error. However, since the total time of these restarts were below a minute compared to tens of hours of measurement, this effect was deemed negligible.

Data collation

Next, the data taken (over 300000 data points, now in multiple files) had to be collated. Unfortunately, the PMT software did not offer an option to timestamp the measurements with absolute time, instead recording only time since start. Hence, scripts were written that added offsets to subsequent data sets according to when they were started. As noted above, the span of time during restarts was too short to be noticeable in the plots, but we note the timestamps as 12.47, 40.24, 48.81 and 62.59 h.

Synchronisation of multiplexed data

As expected, the PMT trace showed the signal to alternate between the extinction and intrinsic fluorescence measurements. However, as recorded, these two measurements are not tagged as belonging to either the extinction or intrinsic fluorescence measurement on the PMT trace. The recorded data is simply a signal varying over time. Ideally, the PMT data would have been synchronised with the excitation light and data points saved into two separate datasets according to whether they belong to the extinction or intrinsic fluorescence measurement. However, this was not possible with the existing software, and an alternate means

had to be devised to separate unlabelled timeseries data into either fluorescence or extinction measurements. The problem becomes evident when observing the raw data (supplementary, Fig. S-6), as the signal goes through in-between states and carries noise that prevent simple thresholding.

Instead, the PMT signal was separated into the extinction and intrinsic fluorescence datasets by post processing scripts. A simple approach tried initially was to detect the edges where the PMT signal varied as a step change between the measurements. However, this was found to not be a robust enough feature to categorise the measurement data into extinction and intrinsic fluorescence due to noise, and the step changes not being aligned with the time interval between data points. Also, without success, a Hilbert transform was used to find the top and bottom envelope of the system, but the envelope tracked the signal too closely between state changes.

State machine algorithm

Finally, the following algorithm was devised and implemented. A state machine records the state the system is in, i.e. whether the signal is on the low or high level, which corresponds to extinction or intrinsic fluorescence measurements (although the categories will switch if the signals cross over). The state is switched IFF (if and only if) a significant ($>10\,\%$) change in signal occurs where the run was long enough (10 s) to not be considered noise or in-between two levels. A pseudocode implementation is given in the supplementary (Section SI.3).

This approach was found to give satisfactory results for almost the entire dataset. Nonetheless, by statistical fluctuation, the algorithm still misdetected the state at four points (out of over 300000). At these points, the algorithm was hard-coded to switch to the correct state. In particular at the cross-over points between fluorescence and extinction, the signal state (alternation between high and low levels) becomes ambiguous and this manual intervention was necessary. For completeness, these were at timestamps of 1.22, 2.97, 39.51 and 48.81 h.

Possible improvements

The above allowed the shortcomings of the measurement equipment to be overcome and measurements to be carried out. Still, to perform such long-term measurements more frequently would demand automating all measurement equipment, in the form of interfacing the equipment with APIs or reading out the signals directly from the PMT, instead of using the provided measurement software. This would be a key next step for this line of research.

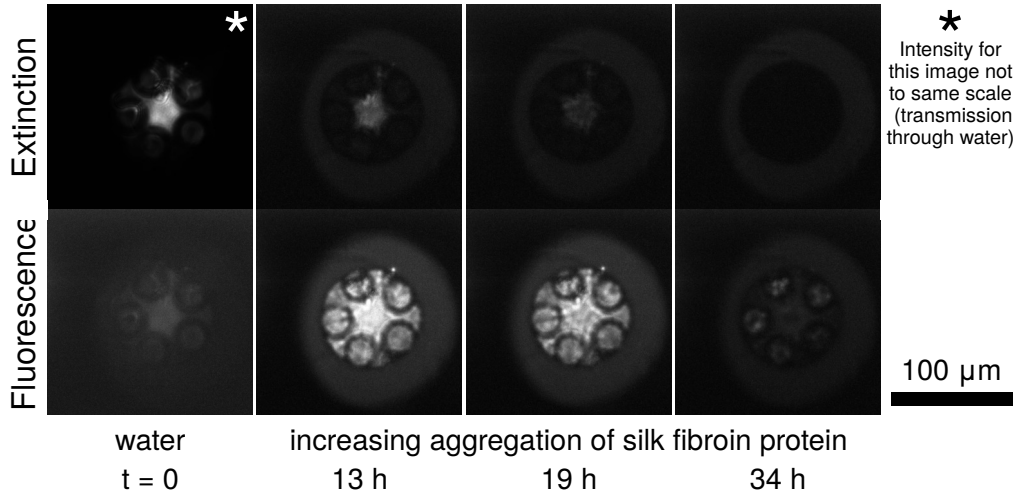

Fig. 6.5 Silk aggregating in HC-PCF. All images are normalised to the same intensity scale, except for the starred image due to much lower extinction of solvent (ethanol 40 %) compared to the protein (silk fibroin $5\,\mathrm{g\,L^{-1}}$ in ethanol 40 %). Images are bandpass-filtered to (357 ± 22) nm. In water, extinction is low and only weak background fluorescence is present. As the silk aggregates, its intrinsic fluorescence decreases while extinction increases, until the transmitted light drops below the sensitivity of the camera.
(*Fig. first referenced on p. 164*)

6.3 Results

Aggregation monitoring in HC-PCF

The aggregation of silk fibroin protein was monitored in HC-PCF by in-situ multiplexed measurements of intrinsic fluorescence and ultraviolet long-pathlength extinction. We show this through both imaging and light intensity measured by a PMT, which were both bandpass-filtered to (357 ± 22) nm.

6.3.1 Key experiment: Label-free monitoring of protein aggregation via multimodal sensing in HC-PCF under flow

Fluorescence imaging in HC-PCF

Images taken at different states of aggregation are shown in Fig. 6.5. In agreement with the cuvette fluorimetry and extinction measurements (Fig. 6.3 and Fig. 6.4, respectively), both are seen to decrease over time.

Timeseries of extinction and intrinsic fluorescence

The transmitted light intensity (as an inverse measure of extinction), and the intrinsic fluorescence, both as measured over 60 h in HC-PCF are shown in the top graph of Fig. 6.6. In the bottom graph, these two measurements are used to calculate a dimensionless ratio of fluorescence divided by transmission, proposed

exemplarily as a simple indicator of aggregation. Due to the large number of data points recorded over 60 h, the data is downsampled before plotting. The time resolution is fifteen seconds for the images, and one second of gate time for the PMT.

Description of experiment

Water (with ethanol added to 40 %, such that it matches the silk solution) was allowed to flow through the fibre for over two hours prior to starting the experiment, which also gave time for the LEDs to pre-heat the apparatus to equilibrium temperature, besides verifying correct operation of the setup. About an hour after starting the PMT recording in Fig. 6.6, the flow is changed to the silk sample, which was prepared fresh just before the switchover. Next, as the silk displaces the solvent over the course of an hour, the transmission drops abruptly by two orders of magnitude, while the fluorescence increases by nearly as much.

Next, both signals have a slow downward trend, approximately halving the intensity over the next ca. 24 h. Interestingly, the extinction measurement shows an overlaid periodic variation, apparently sinusoidal. Its amplitude is approximately 60 %, and its period of oscillation is around 6 h.

Periodic modulation of signal

No definite explanation of the origin of this modulation can be given. Since it occurs much more strongly on the transmitted through-fibre signal and not the fluorescence signal, its origin is likely related to changes in incoupling. If its cause were related to the outcoupling, such as blockages, it would affect both signals equally. Furthermore, since it was not seen in the non-aggregation experiments of the previous chapters, it is likely attributable to an effect of aggregation, rather than the measurement setup in general.

A possible cause could be changes in the hydrodynamic properties of the aggregating solution, which becomes more viscous, as well as forming small aggregates of varying sizes. The syringe pump flowing the sample was a simple feedbackless model that dispensed purely based on volume per unit time, using a stepper motor driving a set of gears at a fixed speed. As the silk aggregates, since the pump continued pumping the more viscous silk at fixed linear plunger displacement speed, there might have been variations in the force applied to the syringe. Consequently, the pressure in the system changes. Different pressures have, in all iterations of the setup built during the PhD, been seen to strongly affect HC-PCF transmission. This appears to be the most likely cause of this effect. A more advanced microfluidic flow system with active pressure control could be used to analyse these hypotheses further.

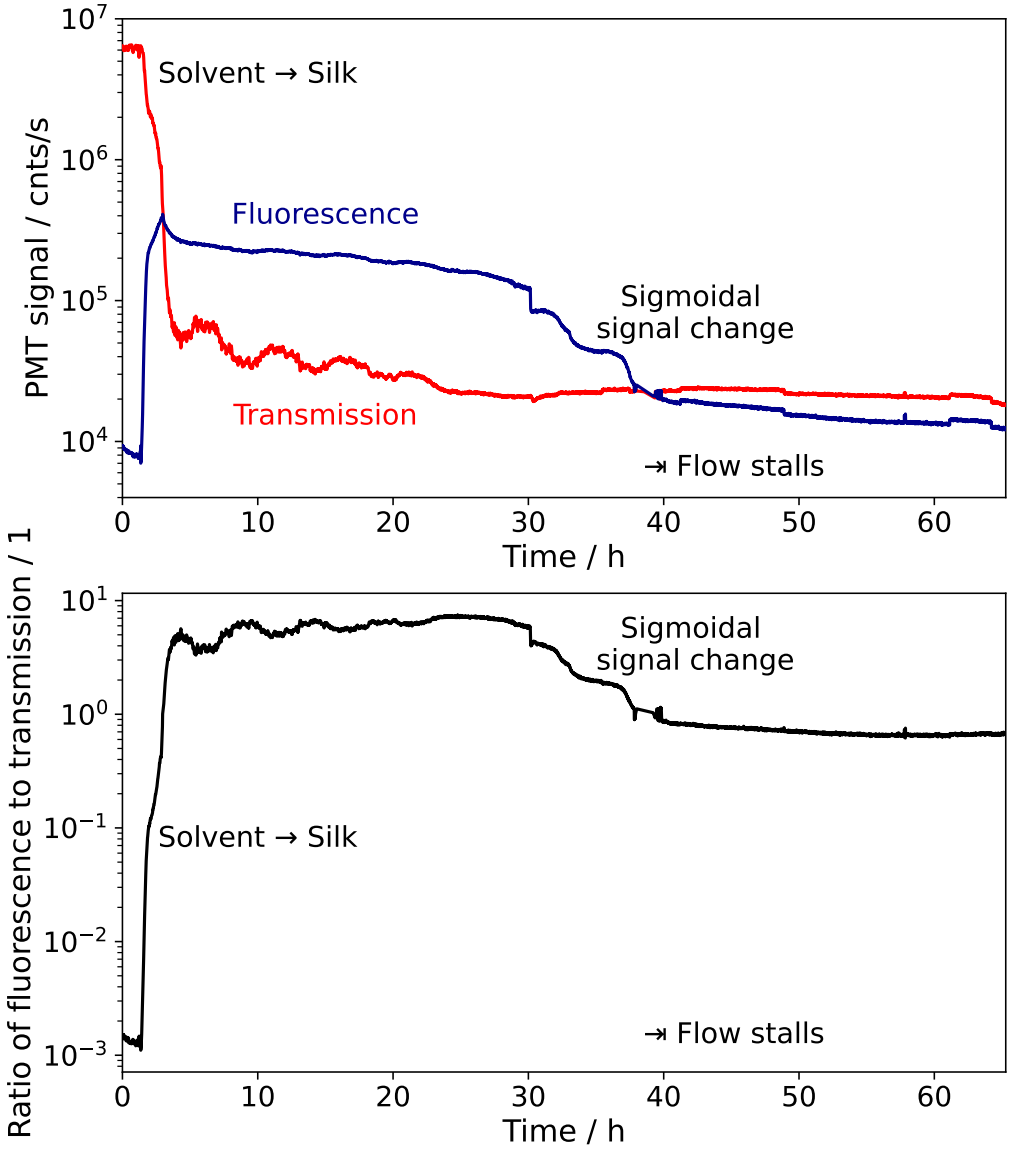

Fig. 6.6 Silk protein aggregation measured inside a HC-PCF via fluorescence and extinction. **Top:** The effect of silk aggregation on its fluorescence (blue) and extinction (transmitted light shown in red) are monitored in HC-PCF under continuous flow (30 µL/h) until the increasingly viscous solution begins to stall. **Bottom:** Taking the ratio of fluorescence to transmission (as an inverse measure of extinction), a dimensionless variable indicative of aggregation is plotted. (*Fig. first referenced on p. 164*)

Another possible cause would be an air bubble growing and shrinking in size, causing lensing effects on the in-liquid butt-coupling, in turn changing the amount of incoupled light. However, the top reservoir was filled with ethanol to reduce such effects. If a bubble had nonetheless been present near the incoupling, it would have been moved away from the HC-PCF core by the flow streaming out of it. With the flow ceasing as the pump stalls due to increasing aggregation (discussed below), this could potentially explain the periodic modulation becoming less strong as the silk aggregates.

Possible aggregation

At around the 30 h mark, an instantaneous downward step change occurs in both signals, although less strong in the (already much weaker) transmission signal. This could be an early large aggregate becoming loose and passing through the system. Next, over the course of about ten hours, the fluorescence drops by around an order of magnitude in a sigmoidal fashion (annotated in the figure). This is in agreement with the cuvette fluorimetry data of Fig. 6.3, which drops by nearly the same relative change, on a comparable timescale. It therefore appears that sigmoidal change is caused by aggregation within the HC-PCF, albeit further repeats should be performed to rule out other causes, such as aggregates passing through the fibre or photobleaching, both connected to the stalling of the flow (discussed below).

Final phase

Notably, during this time at 38 h, the fluorescence signal becomes weak enough to drop below the transmission signal, which is near-constant at this point, as described before. After this cross-over, from the 40 h mark until the end of the experiment past the 60 h mark, the fluorescence signal slowly approaches a final limit value.

Stalling of the pump

The experiments were started under continuous flow (30 µL/h), but at around 40 h, the pump stalled. The aggregation of the silk, visible in the syringe as gelling, causes blockage of the microfluidics. This means that around this time, the flow slowed down and eventually stopped, leading to static conditions. The exact time cannot be specified with good accuracy, as the stalling of the pump is a gradual process where the force applied by the pump increases until it stalls, at which point it removes pressure on the plunger (it does not retract the plunger to reverse flow). The pump is controlled by flow rate, not pressure, such that it does not compensate for increased flow resistance. That the pump would eventually stall was expected, and hence a webcam was set up to take timelapse photography of the syringe pump to monitor its behaviour throughout the experiment. The pump was seen to slow down and stop towards the 40 h mark. Besides substantially

changing the experimental conditions, both for the measurement and the actual aggregation process, this will also lead to an increase of photobleaching over time as compared to the continuous flow system.

After the experiment had been completed, the different microfluidic components were inspected. The silk in the syringe had visibly gelled (became more viscous and cloudy), but was still able to be pushed out with relative ease. The inflow tubing to the HC-PCF, however, was entirely blocked and even with manually applied pressure did not allow any flow to pass through. Bypassing this tubing and connecting the syringe directly to the HC-PCF (with the last few centimetres of tubing, which were separate) allowed liquid to be pushed through the HC-PCF, suggesting it was not entirely blocked.

The conclusions from this require further study. Given the available evidence, it appears that the inflow tubing (perhaps due to its longer length, around half a metre) blocks before the HC-PCF, such that the flow into the HC-PCF gradually slows down and then stops, but the HC-PCF itself is not blocked. A possible cause would be if aggregation happens in clumps, and when such a clump becomes loose, it accumulates inside the inflow tubing before it can reach the HC-PCF, and this process repeats until complete blockage of the inflow tubing occurs. Existing studies have given consideration to the mechanisms of protein aggregation in glass syringes for medical applications, which can serve as a starting point for further analysis.[318]

Aggregation indicator: ratio of fluorescence to transmission

To evaluate the usefulness of combining several different measurement principles into a new predictive variable, an indicator of aggregation was plotted (bottom of Fig. 6.6). In experimental science, one is driven to seek out unitless measures instead of absolute (unitful) quantities, as ratios of measurements become independent of all systematic errors or unknown effects as long as they are shared equally by both measurands. For example, since both fluorescence and transmission were measured by the same PMT at nearly the same time (seconds apart), calculating a unitless ratio of the two serves to remove any slow drift of the PMT, as long as the drift or noise is on a time scale much longer than two adjacent measurements.

Calculated as the ratio between fluorescence and transmission, the indicator of aggregation is meant to correct for the weakening of intrinsic fluorescence (tryptophan peak at 350 nm) by referencing it to the absorptivity at 365 nm. The weakening of the fluorescence is caused by self-absorption (inner filter effect)

from both higher scatter due to fibril formation (much larger than monomers), as well as absorption from the newly-developing visible fluorescence (cf. Fig. 6.3).

We want to explore the suitability of this value as a proxy for the progression of aggregation, which is possibly more robust (as a dimensionless ratio of two quantities with shared measurement equipment) than either of the two individual measurements, i.e. fluorescence or transmission.

In terms of the aggregation indicator, the experiment presents itself as follows. As the water/ethanol solvent is replaced by the silk, the indicator has a step change over three orders of magnitude. This is due to the solvent producing fluorescence only as a weak background, while being highly transmissive. When the silk is infiltrated, it is comparatively highly fluorescent but not equally less transmissive (prior to aggregation), such that the ratio increases. Next, the indicator remains near-constant on a plateau, except for the periodic modulation discussed before. As aggregation occurs, the indicator follows a sigmoidal curve down, before reaching another plateau. In this way, the indicator tracks the progress of aggregation as a dimensionless variable.

Discussion of the indicator of aggregation

The usefulness of the aggregation indicator remains to be seen as more experiments of this method are carried out. Since the transmission becomes near-constant (with noise and slow variation) after about 24 h, i.e. very little light is transmitted at all, the effect of the ratio becomes less pronounced. After this time, with the denominator near-constant, the ratio closely tracks the fluorescence, such that it could have been used on its own with only small differences.

Nonetheless, the dimensionless ratio does filter out noise and sudden jumps which occur equally in both signals, as expected. This can be seen as small spikes or drops in the fluorescence and transmission signal that are not present in the aggregation indicator. Such changes that are present equally in both signals are likely caused by alignment changes, e.g. by vibrations of the optical table, which affect all light equally irrespective of origin.

6.4 Discussion and outlook

This concludes the final experimental chapter of this dissertation. As before, we summarise the key findings and possible improvements to the studies presented.

6.4.1 Summary of findings

Summary

It was shown that the aggregation of silk fibroin protein could be monitored in HC-PCF using a multiplexed combination of the techniques developed in the previous chapters. Specifically, over 60 h, the extinction and intrinsic fluorescence of the protein was measured in HC-PCF. Hence, the work of this chapter serves to demonstrate the possibility of using HC-PCF for multi-modal biophysical measurements over the long timescales required by protein aggregation processes, and can serve as a starting point for further development.

6.4.2 Possible improvements

Due to the early stage of the experiments shown here, improvements that can be made to the setup will undoubtedly present themselves as the system is explored further. Rather than improvements per-se, further characterisation is required, in particular related to the aggregation-induced flow restrictions. Nonetheless, the experimental system offers interesting possibilities for future experiments.

Studying shear forces

As mentioned in Section 6.2.1, HC-PCFs present themselves as good candidates to study shear induced processes such as protein aggregation. Made from rigid glass (and not polymers, as in soft lithography microfluidics), they have excellent hydrodynamic compliance, i.e. closely follow changes in applied pressure with little hydrodynamic capacitance. For studying protein aggregation, it would be of interest to run the experiments of this chapter at different flow rates, inducing different amounts of shear. To differentiate the effects of shear forces induced by pressure-driven flows from the effects of pressure itself, a comparison could be made by sealing the reservoir on the top after infiltration, resulting in (nearly) static conditions but under varying pressures.

Redesign of the side-excitation layout

Unlike in the horizontal, table-mounted arrangement of Chapter 3, the HC-PCF is now mounted vertically and experimental access is unrestricted from all four sides. This could be leveraged for a redesign of the side-excitation. Placing LEDs on more than one side would allow an increase in excitation light intensity, while also making the irradiation more uniform.

A limitation to this approach is the electrical and optical power of the LEDs (convective and radiative) heating up the HC-PCF. Depending on the experiment, instead of counteracting this effect, this could be seen as beneficial. Tests in the current setup saw the temperature close to the HC-PCF increase by (1.7 ± 0.5) K above ambient, such that the temperature environment of the HC-PCF was

around 26 °C. If more LEDs were added, this could be intentionally raised further to keep the HC-PCF in the physiological temperature range around 30 to 40 °C.

Alternatively, temperature control could be added. Convective (fan-assisted) cooling is generally disfavoured due to the vibrations induced. Thermoelectric cooling is a solid-state solution to cooling (or heating) HC-PCF. Such a HC-PCF stage has been built and demonstrated by the author in a Master's project prior to the PhD, and could be adapted to this use case.

Spectroscopy

Silk, compared to the previous protein sample BSA, has a more complex fluorescence signature. A visible (400 nm) fluorescence peak appears with increased aggregation, in addition to a decreased tryptophan fluorescence peak. Our HC-PCF has a weaker but not insignificant transmission in this wavelength range of 30 % compared to its transmission peak at 350 nm (Section 2.4.3). Hence, both fluorescence peaks could be captured at the same time, and their ratio over time could be tracked. When connected with molecular dynamics simulation, the tryptophan and visible wavelength fluorescence could be correlated to changes in solvent exposure or burying of fluorophores, which ultimately would serve to parametrise models of aggregation kinetics.

7 | Conclusion and outlook

The final chapter summarises the conclusions from each previous chapter, and suggests an outlook for which findings from this PhD could be built upon in future research.

7.1 Summary of results 173
7.2 Outlook 174
7.3 Closing statement 177

7.1 Summary of results

Chapter 1

The first chapter reviewed the context of this work. The literature was reviewed, showing a large body of relevant work, with selected works discussed in more detail. It was seen that HC-PCF have been applied to biophysical applications and protein detection before, but not for the label-free analysis by intrinsic protein fluorescence or extinction, as explored in this dissertation.

Chapter 2

In chapter two, both background theory and methods were discussed. A brief introduction to HC-PCF as optofluidic waveguides was followed by microfluidic theory and methods relevant to the later experiments of this dissertation. Covering the HC-PCF used in this dissertation completed the chapter.

Chapter 3

As the main currently published experimental work resulting from this PhD, chapter three demonstrated experimentally how HC-PCF as optofluidic waveguides can be used for the label-free monitoring of proteins by their intrinsic fluorescence. A focus was put on showing that the system can operate continuously as part of a microfluidic circuit, performing measurements as a label-free protein sensor over several hours.

Chapter 4

After the intrinsic fluorescence measurements of the previous chapter were completed, chapter four turned the attention to using the HC-PCF as a waveguide for the incoupled light, instead of collecting the (isotropically) emitted fluorescence. As such, much work was devoted to designing and building a suitable optofluidic setup that allowed continuous-flow coupling of a HC-PCF into a microfluidic setup. This was achieved and demonstrated experimentally by measuring silk fibril aggregates by their UV extinction.

Chapter 5

Chapter five represented a brief excursion, exploring a question that was often posed to me by potential collaborators: Instead of continuous-flow operation, could your method be adapted for much smaller sample volumes and one-off measurements? Or, in other words: can the advantages of a HC-PCF be combined, at least partially, with the simplicity of well plate or cuvette measurements?

Albeit with few data points (to limit the use of available HC-PCF stock), our results show that it is possible to fill a HC-PCF passively and then measure the extinction of less than a microlitre of sample with a pathlength of tens of centimetre. Further development in the form of engineering an automated mounting and measurement setup could take place using this chapter's proof-of-principle as a starting point.

Chapter 6

In the final experimental chapter six, a newly-developed work in progress on studying protein aggregation in-situ inside a HC-PCF was presented. It combined in a multiplexed fashion the experimental capabilities developed in chapters three and four. The aggregation of silk fibroin protein over 60 h was monitored label-free through fluorescence and extinction. Thereby, this final piece of work demonstrates how HC-PCFs can serve as a sensing platform, where different experiments are carried out on the same specimen in-situ, opening up pathways to new kinds of multimodal analysis.

7.2 Outlook

Throughout the dissertation, possible future improvements and potentials for further development have been discussed at the end of each experimental chapter. Here, we offer thoughts on more general points and future directions.

HC-PCF for biophysics

As this work set out to do, HC-PCF have been demonstrated for biophysical measurements. The present work focussed on methods development, such that its key contributions fall into the demonstration and characterisation of HC-PCF-based techniques for the label-free measurement of biomolecules. As a more general point, the suitability of HC-PCF as glass-based optofluidic waveguides to work at ultraviolet wavelengths for biophysical analysis has been demonstrated on both protein solutions and aggregates, with a view towards monitoring the entire aggregation process in-situ. Some further avenues to continue this line of research are explored below.

Modally-resolved measurements

HC-PCFs, as optofluidic waveguides, can play to their unique strengths if their waveguiding modes are used. In the present work, coupling was either uniform (side-excitation), or optimised to be close to fundamental (through-fibre). If modes are excited in a controlled fashion, or resolved in the measurement by analysing the spatial profile of light, this opens up new kinds of experiments. The Optofluidics group is actively working on enabling such lines of research.

Exciting well-defined modes in our experiments is made more challenging by working in the ultraviolet for the same technical reasons (material absorption and background fluorescence, plus light sources and detectors) as discussed in Section 3.2.1. Furthermore, shorter wavelengths mean shorter length scales, putting more stringent requirements on the tolerances of (opto-)mechanics and vibration management.

Instead of exciting specific modes, the output light intensity distribution resolved into modes can be studied. If the proteins in the HC-PCF diffuse across the core, the coupling of scattered (extinction) or emitted (fluorescence) light to the different waveguide modes changes, and this variation in signal can be measured as a temporal and spatial component of light intensity over time. In turn, these can then be connected to the protein diffusion dynamics as per the ideas discussed in Section 2.3.2.

Time-resolved measurements

Time-resolved measurements are another promising direction to explore. While not employed in the work of this dissertation, a fast (sub-microsecond rise time) LED driver was built and tested for photochemistry experiments. It could be employed for lock-in measurements to reduce signal noise. Even this is not fast enough to probe the fluorescence lifetime of tryptophan (3 ns).[26] Other means of gating light or recording its variations faster could be used, or the finite rise time of the LED subtracted if the system remains sufficiently reproducible between measurements. However, these approaches all incur considerable system complexity.

Another way of exploring time-resolved measurements of protein fluorescence are fluorescence recovery after photobleaching (FRAP) experiments. The diffusion of proteins can be explored through FRAP by measuring the time taken for the irradiated region to become absorbent or fluorescent again. To learn about and explore these ideas, a flash as used in photography was purchased, and its acrylic windows removed. The exposed flash tube was confirmed to not only provide very intense, very short bursts of light, but also contain large amounts of deep ultraviolet light, which in normal use would be filtered out by the acrylic. Initial tests of performing FRAP in a HC-PCF were done with this setup. The challenge of this approach lies in shuttering the PMT during the flash (which would be oversaturated by even small amounts of stray flash light), and opening it again for measurements to commence immediately afterwards. Doing this in a way fast enough to reach FRAP timescales was deemed infeasible without more expensive equipment.

Electrophoresis

Further to analysing diffusion dynamics in HC-PCF, applying time-varying electric fields to the HC-PCF can induce motion of proteins via their electric charge, and the time-resolved motion can be studied to measure mobility. Using the simulations of Section 2.3.2 as a starting point, the relationship between signal variation over time and protein mobility could be quantified. An electrophoresis stage was built during the PhD to explore this idea, together with adding elec-

trophoresis into the above simulation, as well as finite element modelling of the electrophoresis within the HC-PCF.

However, before effects on a system can be studied, the system itself must first be understood thoroughly. Hence, the electrophoresis work, too, had to be postponed in favour of improving and understanding the experimental system before the effects of external stimuli could be studied as a modulation on top of any present baseline variation. This line of research could now continue with the improved experimental setups and knowledge resulting from this PhD.

Temperature control

As part of a Master's project prior to the PhD, a thermoelectric (solid-state heat pump) temperature control system for HC-PCF has been designed, built and characterised. As the research presented in this dissertation moves from methods development to new applications, more experimental control over the sample conditions becomes desirable. In particular, temperature has an effect on a wide range of physical phenomenon, including protein mobility, morphology, fluorescence and aggregation, to name only a few. The more tightly it can be controlled, the more reproducible measurements become.

Adding this temperature control to the HC-PCF experiments of this dissertation would allow further investigations to be carried out. Of particular interest would be temperature-dependent aggregation studies. Another line of research is thermal desorption spectroscopy, which was demonstrated experimentally in a non-biophysical context when the HC-PCF temperature control stage was built. The equilibrium process that causes proteins to adsorb reversibly on surfaces is temperature dependent, and by active temperature control, the amount of adsorbed protein could be controlled. Combined with the techniques for label-free concentration measurements demonstrated in this dissertation, the rate of sorption can be quantified as a function of temperature, yielding insights into protein-surface interactions and surface coverage.

280 nm through-fibre

Finally, perhaps the most promising direction to explore would be to enable through-fibre coupling of 280 nm light. This was in fact one of the initial ideas the PhD proposal was based on, but could not be attempted due to equipment failure (see Section 1.3). In the later stages of the PhD, initial trials of coupling 280 nm light through a HC-PCF were conducted using the setup of Chapter 4. For coupling light from the 275 nm LEDs through the 25 μm multimode fibre, only very weak excitation light could be obtained (below the calibrated photodiode powermeter sensitivity). The causes are primarily material absorption in the multimode fibre, and etendue mismatch between LED emission and the

multimode fibre. While this does not rule out that sufficient photon counts for the PMT to detect the light could be obtained, the HC-PCF used in this dissertation has a loss resonance at 280 nm, making it unsuitable for these experiments. Other available HC-PCFs showed guidance at 280 nm observed using the now-defunct laser, but the fibre-coupled LEDs proved too weak light source for characterising and aligning them.

Realising previous ideas experimentally

Nonetheless, with the lessons learned and experience gained from this PhD, approaching this challenge again seems feasible now – even in the absence of a bright 280 nm laser. The extinction setup of Chapter 4 requires little re-alignment after mounting different HC-PCFs, and would open up the possibility of revisiting this line of research again. Since protein absorbance at 280 nm is orders of magnitude higher than at longer wavelengths, much more dilute solutions could be measured in extinction. At the same time, co-coupling different wavelengths would allow the different contributions of tryptophan absorption and scattering to be separated. Finally, exciting the fluorescence by through-fibre coupling would allow the fluorescence to be detected from the side, instead of the excitation taking place from the side.

At the low concentrations achievable by 280 nm excitation, this then finally connects our work back to the diffusion simulations presented much earlier (Section 2.3.2). Single molecule photon emissions observed from the side could be combined, in-situ, with bulk extinction measurements that determine the concentration of the entire HC-PCF volume. In this way, the combined ability to measure both the bulk properties of the entire analyte, while simultaneously being able to perform single molecule functional studies, would open up new experimental insights into biophysical processes, label-free.

7.3 Closing statement

Thank you! :)

Thank you for reading my dissertation. Much work has been done, yet much more remains to be done, to realise fully the ideas and research contained within it. If you plan to use any of the data, findings, or concepts in this document, or otherwise think I might be able to share advice, I would be delighted to hear from you and assist as much as I can. Hence, I close by repeating once more and wholeheartedly my invitation for you to contact me and ask questions, at jan-heck.net/phd.

SI | Supplementary Information

SI.1 Construction drawings 179
SI.2 Silk aggregates measurement data 183
SI.3 State machine algorithm to separate multiplexed measurement data . . 185
SI.4 Flows from thermal volume expansion 187
SI.5 Microfluidic device fabrication protocol 189
SI.6 Other approaches to light guidance through water 190
SI.6.1 Water jets 190
SI.6.2 Mirror-coated capillaries 191
SI.6.3 Total internal reflection by coating 192
SI.7 Derivation of hydrodynamic resistance 192

SI.1 Construction drawings

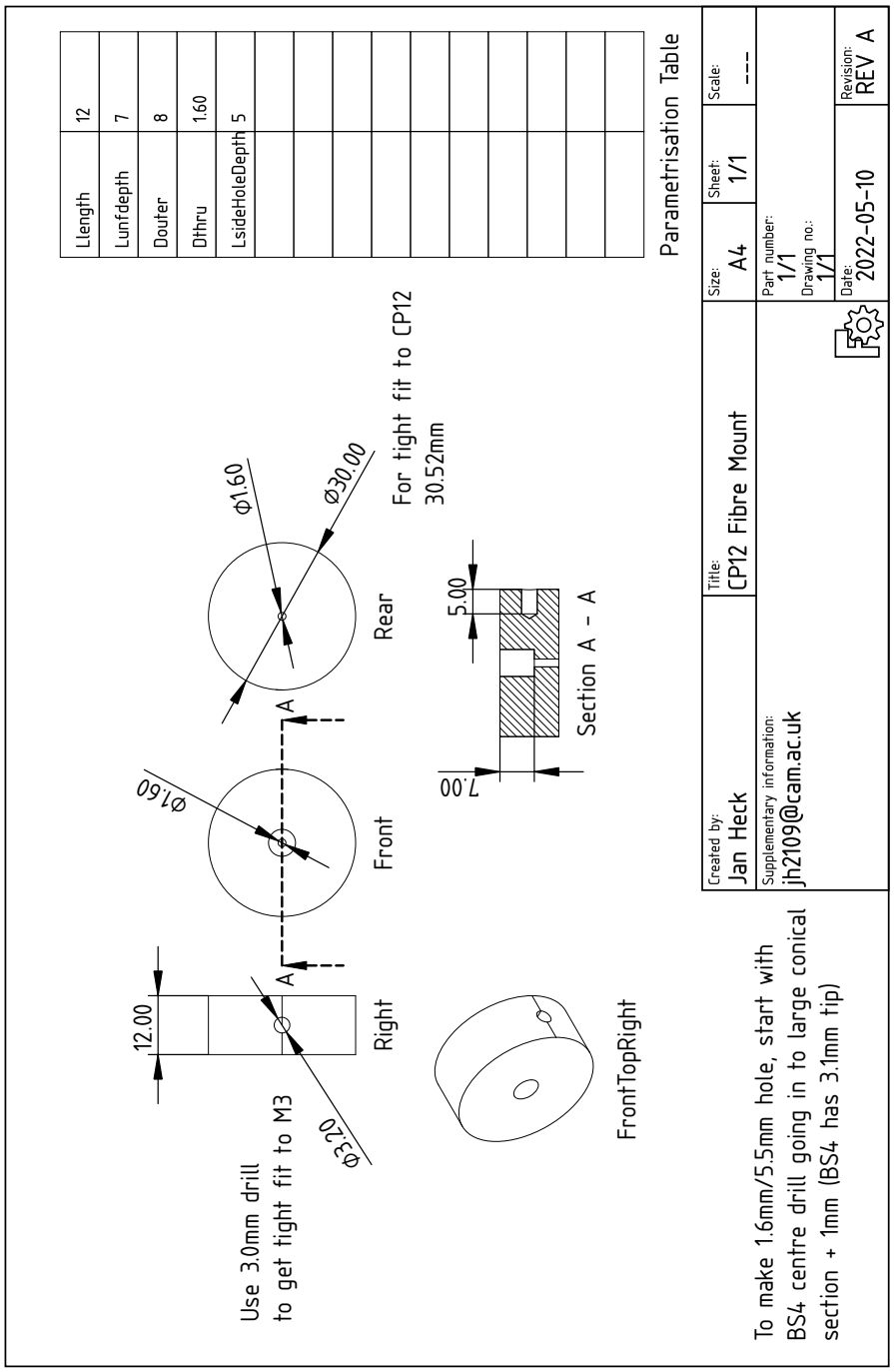




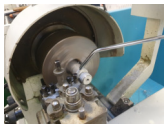
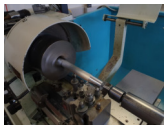


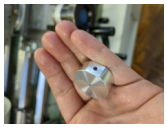

Fig. S-1 Construction drawing of the low dead volume, high compliance optofluidic interconnect, forming the final design. It was used in Chapter 4, Chapter 5, and Chapter 6. (*Fig. first referenced on p. 126*)

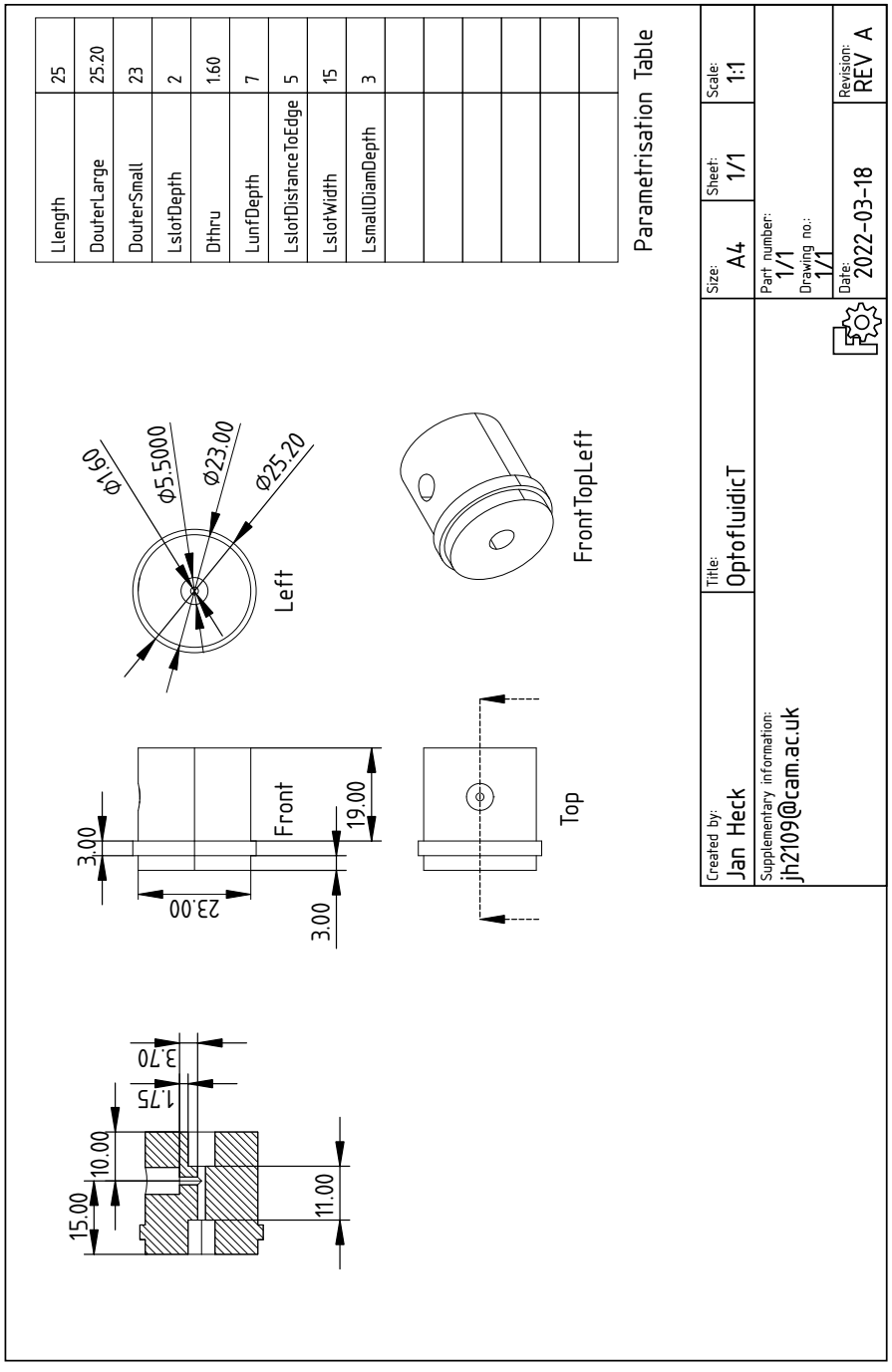

Fig. S-2 Construction drawing of the optofluidic T butt-coupling interconnect. The design was tested and subsequently rejected for lack of degrees of freedom in aligning the two fibres relative to each other. (*Fig. first referenced on p. 125*)

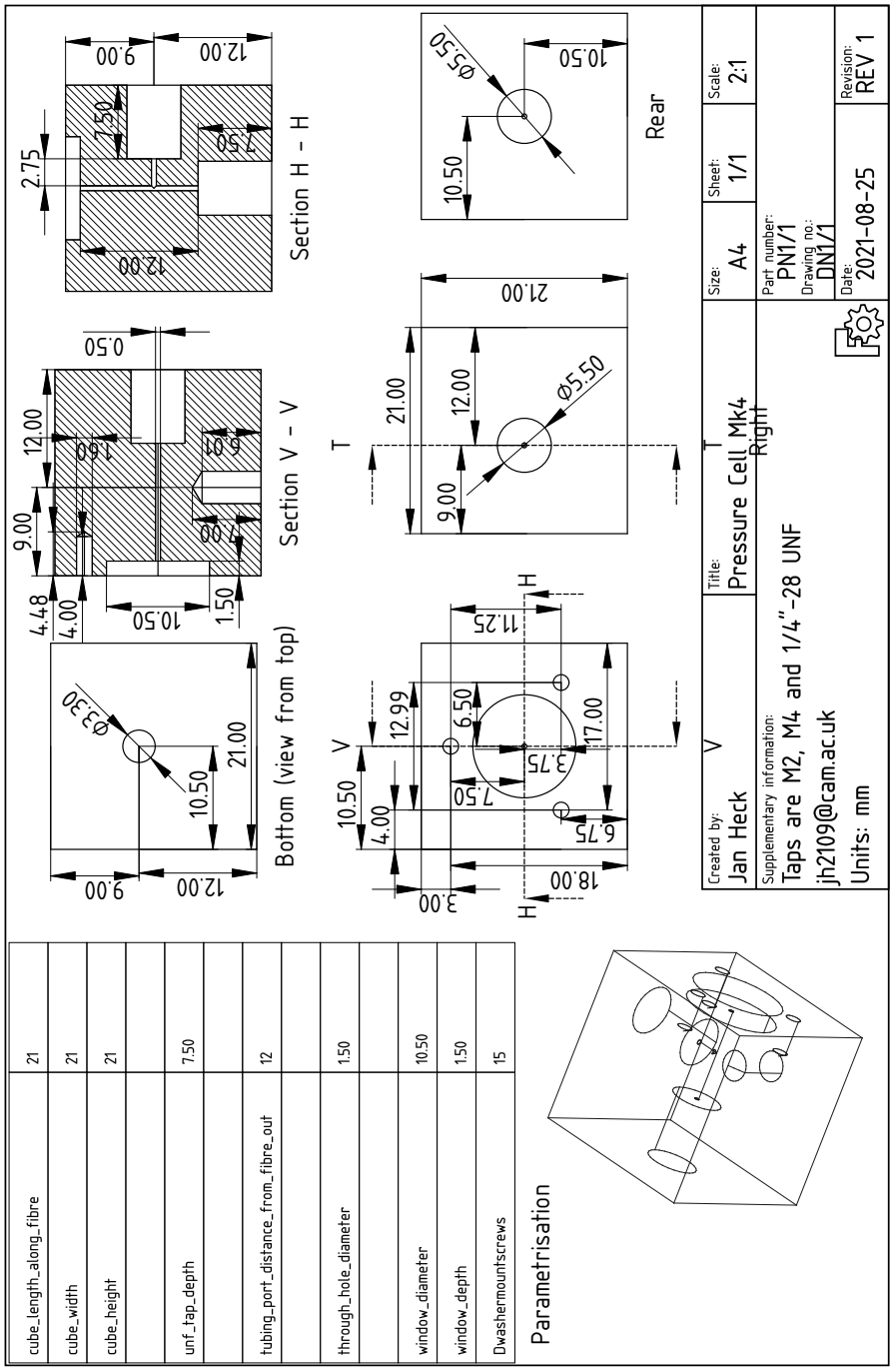

Fig. S-3 Construction drawing of an alternative version of a low dead volume optofluidic interconnect, with different design goals and the fibre intended to be held centrally by co-laminar sheath flow. It was not extensively tested due to lack of time.

(*Fig. first referenced on p. 125*)

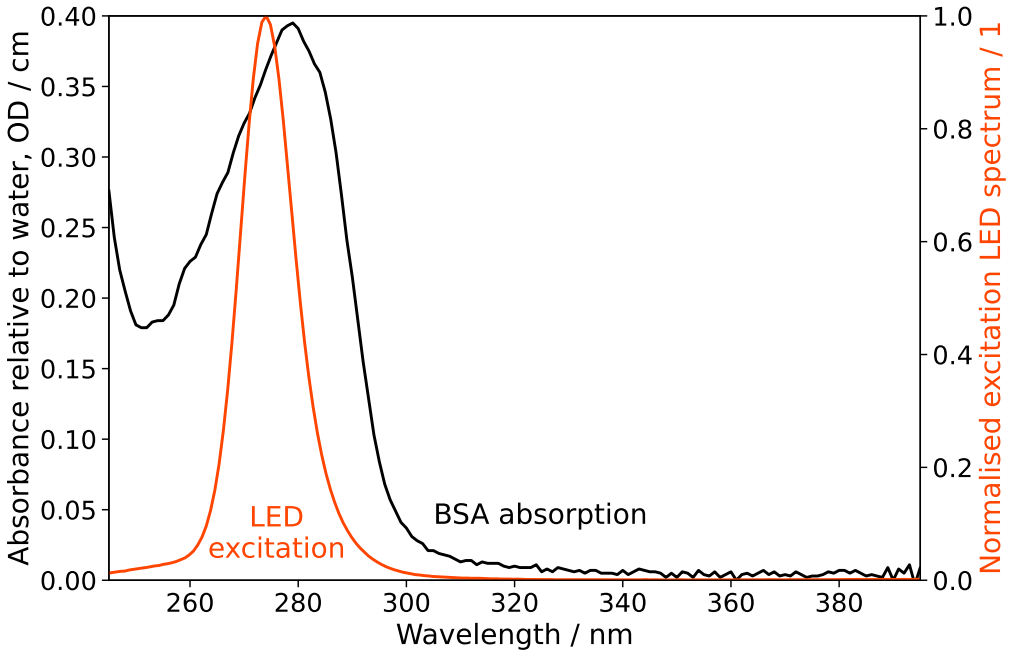

Fig. S-4 Absorption spectrum of BSA (10 µM) measured in cuvette compared to the excitation LED spectrum (normalised). While the LED excitation spectrum is centred ca. 5 nm below the absorption maximum of BSA, it is preferred over 280 nm LEDs due to its higher power (quantified in the main text). (*Fig. first referenced on p. 105*)

SI.2 Silk aggregates measurement data

Dilution	Ratio of PMT signal to water pre-sample	Ratio of PMT signal to water post-sample	Cuvette transmission scaled to HC-PCF length
1	0.81	0.96	0.66
1	0.69	0.87	0.66
1	0.85	0.74	0.66
2	0.83	0.82	0.81
2	0.72	0.88	0.81
2	0.75	0.78	0.81
4	0.92	0.90	0.90
4	0.84	0.90	0.90
4	0.86	0.91	0.90
8	0.91	0.95	0.95
8	0.92	0.97	0.95
8	0.91	0.95	0.95
16	0.98	1.01	0.97
16	0.99	0.99	0.97
16	0.96	0.99	0.97

Tbl. SI.1 Experimental data for the silk aggregates in Chapter 4. Measurements were performed as described ibid. In brief, silk aggregate solution and water are flushed alternately through the HC-PCF, and the extinction of the sample is calculated as the ratio of transmitted light when sample is present relative to when water is flushed through after. For comparison, values resulting if taking the ratio with water before sample infiltration is also shown.

(*Table first referenced on p. 184*)

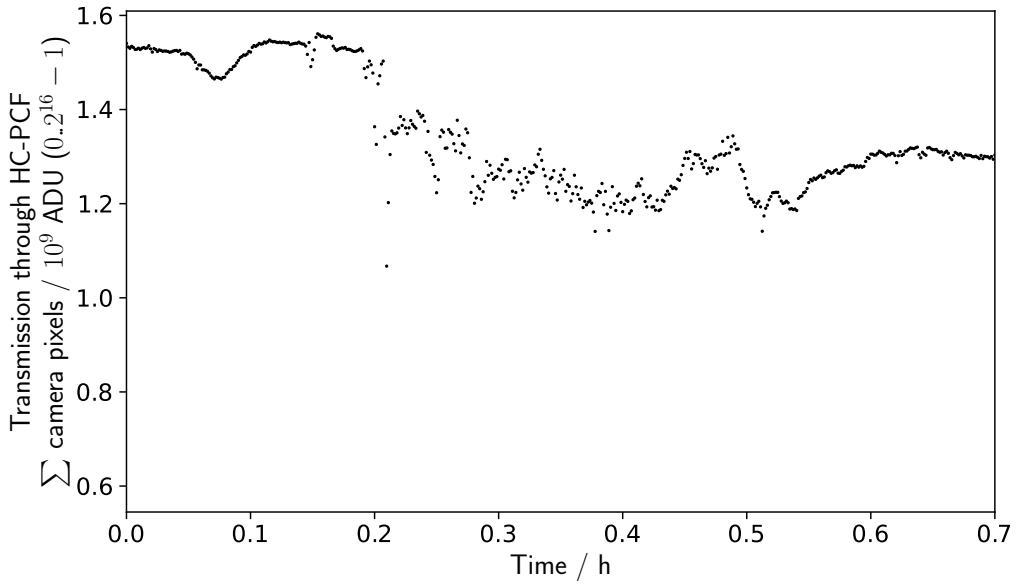

Fig. S-5 The first of the triplicate undiluted solution of silk aggregates being measured in HC-PCF (corresponding to the first line in Table SI.1). Starting from water in the beginning, the undiluted solution of silk aggregates is flown through, resulting in a decrease in transmission as expected. However, as water is flown through again afterwards, there is almost complete lack of recovery to the pre-sample water baseline, suggesting incomplete removal of sample. This was confirmed by microscopy to be due to gelled aggregates forming in the HC-PCF (Fig. 4.18) at these comparatively high concentrations, leading to exclusion of this triplicate measurement in Fig. 4.17. (*Fig. first referenced on p. 140*)

SI.3 State machine algorithm to separate multiplexed measurement data

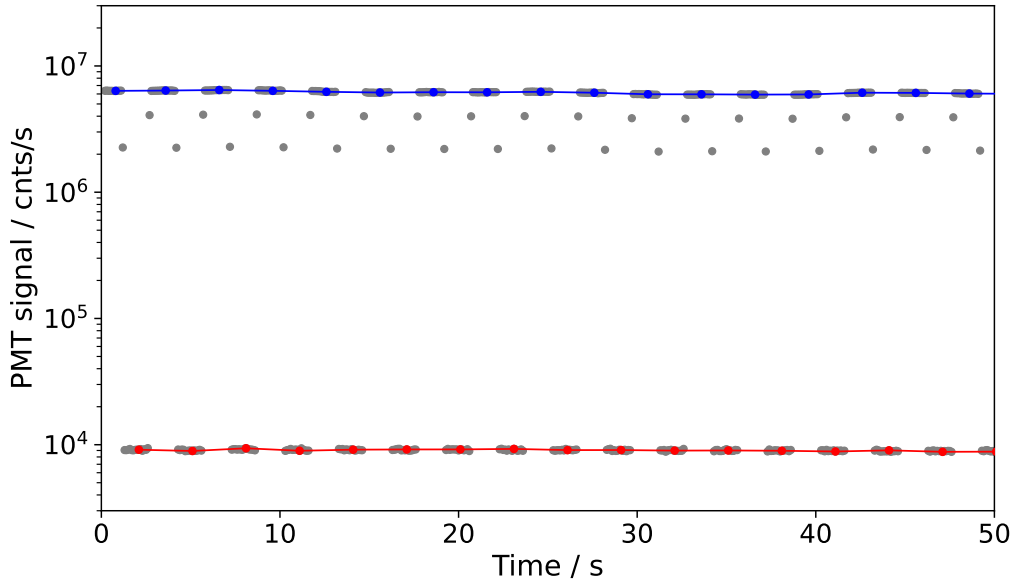

Fig. S-6 Categorising plain PMT data into different categories for multiplexed measurements. Since a single PMT signal measured both the extinction and intrinsic fluorescence emerging from the HC-PCF as a single time trace (grey dots), a method of sorting each datum into these two measurements had to be devised. The state machine algorithm identified these measurements and sorted them into extinction (blue) and fluorescence (red). (*Fig. first referenced on p. 163*)

```
# PARAMETERS
# Discard runs shorter than this as noise or as transitions between states
MIN_RUNLENGTH = 10
# Relative threshold to detect a step change between states
MAX_VARIANCE_FRACTION = 0.1

# GLOBAL VARIABLES
state = 1
k = 1
runlength = 0

# MAIN
# For all points k in the PMT data set y
```

```
while k < len(y):
  # Find the fractional change from the previous datapoint
  dy = y[k]/y[k-1]

  if |dy - 1| < MAX_VARIANCE_FRACTION:
    # Run starts or continues
    runlength += 1

  else:
    # Run stops after $runlength steps
    if runlength < MIN_RUNLENGTH:
      # Discard this run as too short (noise or in-between two states)
      runlength = 0
      k += 1
      continue

    else:
      # omit boilerplate code for saving the data together with timestamps
      saveDataIntoCategoryWithTimestamp(y, k, state)

      # toggle state
      state *= -1

  k += 1
```

SI.4 Flows from thermal volume expansion

Generally – with some few but notable exceptions, such as water below 4 °C – liquids expand in volume as they are heated. If the liquid remains confined in a fixed-volume reservoir, a temperature change will therefore induce a pressure difference to keep $N\mathrm{k_B}T = pV$ constant. This pressure difference can then drive flows.

Linear model of thermal expansion

The simplest model of this, corresponding to a first-order expansion of more complete theories, apply when the temperature change $\mathrm{d}T$ is small enough that non-linear effects are negligible. Under these assumptions, a proportionality exists between relative volume expansion $\mathrm{d}V/V$ and temperature change $\mathrm{d}T$ as

$$\frac{\mathrm{d}V}{V} = \alpha_{\mathrm{vol}}\,\mathrm{d}T. \tag{SI.4.1}$$

Assuming perfect compliance, the volume change $\mathrm{d}V$ corresponds to the flow driven through the system. With compliance in both the heated reservoir, as well as all other liquid circuitry, the driven flow will be less than this quantity. It is also important to note that thermal expansion occurs everywhere along the liquid circuitry, and is balancing pressures in equilibrium. It is therefore important to maintain stable temperatures throughout the system.

Compressibility β

The *compressibility* β of a liquid is defined as

$$\beta = -\frac{1}{V}\frac{\partial V}{\partial p}, \tag{SI.4.2}$$

where the negative sign is by convention to indicate an increase in volume upon an increase in pressure. The inverse of β is also known as the *bulk modulus*. As the volume V of the liquid is constrained by the reservoir, we can write

$$\frac{\mathrm{d}V}{\mathrm{d}p} = -\beta V. \tag{SI.4.3}$$

Numerical example

Note that this equation now considers an infinitesimal change of volume $\mathrm{d}V$ while the volume is kept constant; hence, this equation is only valid when $\mathrm{d}V \ll V$. To evaluate this assumption for our experiments, consider a reservoir of 1 mL that experiences a temperature increase of 1 K as might occur from local room temperature variations. Assume, in a first approximation, all other parts of the system to be at the same temperature (negligible $\mathrm{d}T$ compared to the reservoir).

Water has a volume expansion coefficient of $\alpha_{\text{vol, water}} = 2.14 \times 10^{-4}\,\text{K}^{-1}$, resulting in a volume expansion of $\text{d}V \approx 200\,\text{nL}$.

This is a small multiple of typical linear fibre volumes ($49\,\text{nL}\,\text{cm}^{-1}$), and of the same magnitude as the fused silica capillary that is used for the fluidic circuitry ($\text{ID} = 150\,\mu\text{m}$, with linear volume $\pi\,(\text{ID}/2)^2 \approx 180\,\text{nL}\,\text{cm}^{-1}$). Hence the effect is large enough to drive a significant flow (but three orders of magnitude less than the reservoir volume, validating the initial assumption that $\text{d}V \ll V$ underlying the calculation).

Instead of the numerical example above, by rearranging and substituting in Eq. (SI.4.1), we arrive at an expression which is independent of the reservoir volume,

$$\text{d}p = -\frac{1}{\beta}\frac{\text{d}V}{V} = -\frac{\alpha_{\text{vol}}}{\beta}\text{d}T. \tag{SI.4.4}$$

Pressure from thermal expansion

The ratio of material constants appearing in this equation gives the pressure change of a confined liquid upon a change in temperature, which is evaluated for water as

$$\frac{\text{d}p}{\text{d}T} = -\frac{\alpha_{\text{vol}}}{\beta} \approx 500\,\text{kPa}\,\text{K}^{-1}. \tag{SI.4.5}$$

This number exemplifies the immense forces that can be caused by thermal expansion of incompressible liquids in sealed containers, which are often implicated in structural failures throughout engineering.

Further considerations

It is important in all of the above to distinguish between apparent and absolute expansion of the liquid, where the former refers to relative volume changes between container and contents, which are likely to have different thermal expansion coefficients.

In the above analysis, we assumed that the reservoir was fully filled, as any trapped air would be highly compressible, thereby reducing the system's compliance, and consequently add non-linear terms to the pressure–temperature dependence. For this reason, the outgassing of water has a strong effect on the fluid dynamics of any microfluidic system, even if the air bubble itself does not obstruct any flow.

SI.5 Microfluidic device fabrication protocol

One of the most common ways to manufacture microfluidic circuits is the use of a lithographic process to pattern a photopolymer with micrometer-sized channels, known as *soft lithography*. A typical workflow protocol that was used is described below.

Lithographic fabrication of the microfluidic master wafer Onto a Si wafer, SU-8 photoresist (SU-8 3025, MicroChem[334]) is spin-coated to a desired thickness (which will become the microfluidic channel height), typically 25 µm. After a soft-bake step on a hotplate (95 °C, 5 min), the photoresist is selectively exposed to UV light (365 nm, 1000 mW, 30 s) by use of a mask to pattern the desired microfluidic circuit onto it.[335] In this negative photoresist process, the exposed parts of SU-8 will become cross-linked, while the remainder stays soluble. A post-bake step (95 °C, 15 min) is used to accelerate this conversion. The solvent propylene glycol methyl ether acetate (PGMEA) is used to wash away the soluble, unexposed SU-8. This completes the creation of the wafer template known as the 'master', which can be re-used multiple times for the device fabrication step detailed below.

Fabrication of PDMS devices from master A master wafer is placed into a Petri dish for containment. The epoxy polydimethylsiloxane (PDMS) is prepared from a 10:1 (w/w) mixture of elastomer to crosslinker (Sylgard 184[223]), stirring vigorously for three minutes. The ratio can be adjusted for different elastic properties. The PDMS is then poured onto the wafer to cover it to a height of approximately 1 cm. Being placed into a vacuum desiccator, at least 30 min are allowed for any trapped air to gas out. The device is then transferred to a 65 °C oven to cure for at least several hours, typically overnight.

Bonding of device to form microfluidic chips Once ready, the devices are cut out to the desired size using a scalpel. Care is taken to cut at a shallow angle relative to the master to avoid point contact between scalpel and master, leading to excessive forces and breakage. Biopsy punches are used to create vertical channels to the inlet structures (wells), to which tubing can be attached.

With the channel side facing up, the devices and thin (1 mm or less) glass coverslips are placed into a plasma bonder (40 % power setting, 30 s). This

forms radicals on the surfaces, which enable covalent bonding between the two materials. Within a few seconds of removing the tray from the plasma bonder, the PDMS devices are pushed channel side down onto the coverslips, ensuring even pressure over their entire surface area to ensure bonding. Failed bonding is indicated by air bubble formation. This completes the fabrication to yield the final microfluidic chip.

The Petri dish containing the master and unused sections of PDMS can now be re-used as per the fabrication steps above. Old PDMS does not need to be removed first. For aqueous samples, the device is first flushed with a hydrophobic coating agent (Aquapeel) prior to use, reducing adsorption onto the PDMS and coverslip surfaces.

SI.6 Other approaches to light guidance through water

What if we did ...

Even though practical considerations do not allow their use in our experiments, for interest, we also give brief consideration to some other novel approaches that enable waveguiding through water. By comparing and contrasting, they can offer an insight into what criteria a functional optofluidic platform must fulfil.[29]

SI.6.1 Water jets

$n_{\text{water}} > n_{\text{air}}$

While there are almost no *solid* materials of refractive index lower than that of water, a stream of water ($n = 1.33$) in air ($n = 1.00$) has a large refractive index difference of about 0.3, supporting TIR. In fact, light guided inside a stream of water streaming out of a hole near the bottom of a water-filled bucket is a common educational demonstration of TIR. Light, e.g. from a laser pointer, can be seen travelling inside the stream by being totally internally reflected multiple times.

Applications

Modern implementations using pressurised, vertical jets have been used for fluorescence collection under UV excitation, using a solid-core fibre in the stream for fluorescence collection.[336] Fluorescence and Raman spectroscopy are often limited by the fluorescence background that glass or polymer materials introduce, which water jets can avoid.[337] While water-based liquid jets are the most common version, since all liquids have a refractive index higher than air, any solvent can be used in principle.

Drawbacks

Despite being conceptually simple, there are drawbacks to the use of water-in-air jet waveguides. They do not offer the engineering flexibility and integration potential that silica fibres or microfluidic chips offer and, even in a laboratory setting, the use of pumps and reservoirs makes clean sample exchange without cross-contamination difficult, and components are prone to biofouling. Most importantly, the formation of stable water streams requires flow rates of the order of $\mathrm{mL\,min^{-1}}$, and corresponding large amounts of sample that are not compatible with microfluidic experiments. Possible applications are expected in power-efficient disinfection[338] and high-power laser delivery for machining,[339] where the constantly-replenished water jet is more resilient against material offshoot and debris than solid glass materials, while also serving as the machining coolant.

SI.6.2 Mirror-coated capillaries

Can't we just use mirrored walls?

In Section 2.1.2, we saw how anti-reflective coatings can be used to reduce transmission losses in an otherwise lossy waveguide. Considering this solution, one might be tempted to suggest an ever simpler one. By coating the inside of a capillary with some highly reflective coating, a cylindrical mirror can be formed. A motivation to this approach is that common mirrors are made by evaporating metals onto glass substrates, and hence such a process can rely on existing technology (e.g. chemical vapour deposition), and is not entirely infeasible. However, in practice, achieving a coating smoothness on the size scale of λ is not possible all throughout the capillary, and the light scatters off of any imperfections. Each scattering event after a mean free path of $\Lambda \sim \lambda$ decreases the light intensity to a fraction R. The ensuing exponential decreases the intensity to a fraction $R^{-d/\Lambda}$ after a distance d. Since d is macroscopic and $d/\Lambda \sim 10^6$, high losses are unavoidable even for the most reflective (for a given wavelength) metal coatings, with $R > 99\%$.[340] Hence, a mirror-coated channel does not transmit light efficiently. Nonetheless, for very large core sizes (e.g. 0.75 mm diameter for infrared laser delivery[31]), these approaches can be a good engineering tradeoff.

The very opposite

In fact, what we described as a potential waveguide turns out to be the basis for how high-power optical beam blocks are made. A large number of flat metal blades are arranged in parallel with a small (sub-mm) separation between them. Any light entering the beam block in-between two blades will reflect and scatter back and forth repeatedly, quickly attenuating away as described above. Unlike a simple shutter, this does not deposit the beam's energy onto a single spot, which

allows high-power beams to be blocked. Furthermore, almost all reflections are away from the source (glancing incidence), preventing stray light from escaping the beam block.

SI.6.3 Total internal reflection by coating

PTFE-coated capillary waveguides

While silica is of higher refractive index than water, there exists only a limited set of solids that have lower refractive index than water.[341] Specialised amorphous formulations of PTFE polymer (2,2-bistrifluoromethyl-4,5-difluoro-1,3,-dioxole) have refractive indices in the range $n = 1.31 \ldots 1.29$, slightly below water at $n = 1.33$.[222] This allows for TIR-based optofluidic waveguides to be constructed, such as by coating the inside of a glass capillary with molten PTFE polymer. [342] Drawbacks of such approaches are their large diameters (250 µm) required for coating, leading to multimode-guidance; high material costs[342]; and low numerical aperture due to the small refractive index contrast: by Eq. (2.1.2),

$$\theta_{\text{crit}} = \arcsin\left(\frac{n_{\text{outer}}}{n_{\text{inner}}}\right) = 1.36, \tag{SI.6.1}$$

or a numerical aperture of $\text{NA} = n_{\text{core}} \cdot \sin(\frac{\pi}{2} - \theta_{\text{crit}}) = 0.28$.

SI.7 Derivation of hydrodynamic resistance

Dimensional analysis is a powerful technique[343][344] to find the functional dependence between a complete set of physical variables that are known to be dependent on each other (and only on each other).

Ansatz

Consider what physical quantities are expected to contribute to the hydrodynamic resistance along a straight channel. We will build a functional relationship between the hydrodynamic resistance R_{hyd} and its dependent variables until we can use dimensional analysis to complete the relation.

Hydrodynamic resistance is the fluidic equivalent of Ohm's law[300]. In a fluid flow, potential energy from a pressure differential Δp is dissipated between inlet and outlet to drive a flow of volumetric flow rate Q. Then, the channel is said to present a hydrodynamic resistance of

$$R_{\text{hyd}} := \frac{\Delta p}{Q}. \tag{SI.7.1}$$

From mechanics, frictional damping terms are proportional to velocity. Assuming a purely axial flow, this leads to the relation

Frictional damping $\propto v$

$$\mathrm{d}R_{\mathrm{hyd}} \;\propto\; \eta v(r,\theta)\,\mathrm{d}r\mathrm{d}\theta\mathrm{d}z, \tag{SI.7.2}$$

which gives the contribution of each infinitesimal cross-section $\mathrm{d}z$ along the channel. Assuming translational invariance (i.e. a straight channel of invariant cross-section), and if friction is a linear (local) phenomenon not affected by other parts of the channel, the cross-sectional fluid velocity field $v(r,\theta)$ must have no z dependence. Then, each unit length of the channel contributes equally, and integrating over z leads to

$$\mathrm{d}R_{\mathrm{hyd}} \;\propto\; \eta v(r,\theta)\,\mathrm{d}r\mathrm{d}\theta \cdot L. \tag{SI.7.3}$$

For an incompressible flow, the flow rate Q along the channel must be constant. However, this does not imply the fluid velocity $v(r,\theta)$ being a constant. Instead, since $Q = \textsc{const.}$, the fluid velocity $v(r,\theta)$ inside the channel must be distributed over its cross-sectional area A, such that Q is the normalisation of $v(r,\theta)$ in the form

Incompressibility

$$Q = \int_{\{r\}}\int_{\{\theta\}} v(r,\theta)\,\mathrm{d}A. \tag{SI.7.4}$$

It follows that a larger area $A = \int_{\{r\}}\int_{\{\theta\}}\mathrm{d}A$ must result in a smaller integrated flow speed $\int_{\{r\}}\int_{\{\theta\}} v(r,\theta)\mathrm{d}r\mathrm{d}\theta$. However, these statements and the normalisation condition above apply to the integrated cross-section; the form of $v(r,\theta)$ remains unknown and would need to be found by solving the Navier-Stokes equations (Eq. (2.2.3)) under the above constraints, combined with boundary conditions (e.g. no-slip boundary condition $v(r,\theta) = 0$ at the channel walls).

Finding $v(r,\theta)$ is possible only for geometrical shapes where symmetry allows the problem to be simplified sufficiently to yield an analytical solution. More complicated shapes are generally solved by numerical methods. However, at this point, dimensional analysis allows us to find the functional dependence of R_{hyd} on the variables introduced so far. What remains unknown is the dimensionless factor between the solution from dimensional analysis, and that of a full analytic

Solution for simple geometries

or numerical solution. We refer to this discrepancy as the geometrical correction factor α, as it will be determined by the form of $v(r, \theta)$, and write

$$\alpha = \frac{R_{\text{hyd}}}{R_{\text{hyd}}^{\text{dim}}}, \tag{SI.7.5}$$

where $R_{\text{hyd}}^{\text{dim}}$ is the result from dimensional analysis.

Dimensional analysis

Now, considering that we argued that $R_{\text{hyd}} \propto \eta L/A$, we find that the factor of proportionality required to satisfy this equation using dimensional analysis. Denoting the dimension of a quantity by $[\square]$,

$$[R_{\text{hyd}}] \stackrel{!}{=} [\alpha\, \eta\, \frac{L}{A^2}] \tag{SI.7.6}$$

$$\left(\frac{\text{mass}}{\text{length} \cdot \text{time}}\right) = 1 \cdot \left(\frac{\text{mass}}{\text{length} \cdot \text{time}}\right)^a \cdot (\text{length})^b \cdot \left(\text{length}^{-4}\right)^c \tag{SI.7.7}$$

Solving for the minimal coefficients a, b, c yields the proportionality for hydrodynamic radius, i.e. the result from dimensional analysis,

$$R_{\text{hyd}}^{\text{dim}} = \eta L A^{-2}. \tag{SI.7.8}$$

Cylindrical channel

We also note that for some simple shapes, R_{hyd} can be found analytically. For example, a cylindrical capillary has

$$R_{\text{hyd},\bigcirc} = \frac{8}{\pi} \eta L r^{-4}, \tag{SI.7.9}$$

in agreement with our result up to a small numerical factor. In general, any other arbitrary shape can be treated numerically, e.g. using finite element modelling (FEM). However, for building an intuition, analytical solutions are of higher value.

Compactness C

For shapes that are more complex, a useful indicative measure of hydrodynamic resistance is a dimensionless ratio known as *compactness*, defined as[345]

$$C = \frac{(\text{channel circumference})^2}{\text{channel area}}. \tag{SI.7.10}$$

For example, the compactness of a square is $C_\square = 16$, and that of a circle $C_\bigcirc = 4\pi$. In general, shapes can have non-constant compactnesses, e.g. $C_\square = 4(a+b)^2/(ab)$

for a rectangle. Higher compactness correlates with higher hydrodynamic resistance, with circles being the most compact and of the lowest hydrodynamic resistance.

Perturbation theory

Even more complicated shapes can still be treated analytically by use of perturbation theory if they are similar enough to shapes for which R_{hyd} is already known. Where this is possible, a geometrical correction factor α can be assigned to the new shape relative to a base measure[345], such that $\alpha = R_{\mathrm{hyd}}/(\eta L/A^2)$. In other words, α is the dimensionless correction factor between the hydrodynamic resistance $\bar{R}_{\mathrm{hyd}} = (\eta L/A^2)$ found independent of any geometry (which can be done with dimensional analysis), and the perturbed shape of interest. A series expansion of α in terms of C and the perturbation parameters then allows the hydrodynamic resistance to be found.

Deriving the hydrodynamic resistance via a harmonically perturbed circle

A particular shape for which α can be found is a *harmonically perturbed circle*.[345] We define this shape in polar (r, θ) coordinates by the equations (adapted from [345])

$$r = \bar{r}\,(1 + \delta_r \sin(k\theta)) \tag{SI.7.11}$$

$$\theta \in [0,\ 2\pi[, \tag{SI.7.12}$$

where $\bar{r}$ is the mean radius (equal to that of the unperturbed circle), k is the number of perturbations along the circle, and δ_r is the relative perturbation amplitude, such that $(1 \pm \delta_r)\,\bar{r}$ are the maximal radii.

In Fig. S-7, we overlay a harmonically perturbed circle on top of our fibre geometry, showing that the perturbed circle is nearly congruent with the hollow region between the capillaries, except for small regions that will not contribute significantly due to their high surface-to-volume ratio. For simplicity, we will refer to this region as the *core* for this microfluidic analysis, in contrast to the flow through the five outer capillaries. Note that in other sections of this report, the term 'core' is reserved to the central inscribed circle.

We are now in a position to approximate the hydrodynamic resistance of our whole fibre without resorting to numerical simulation. The full fibre geometry is assembled as a set of parallel liquid interconnects, i.e. the harmonically perturbed circle and a set of five identical cylindrical capillaries.

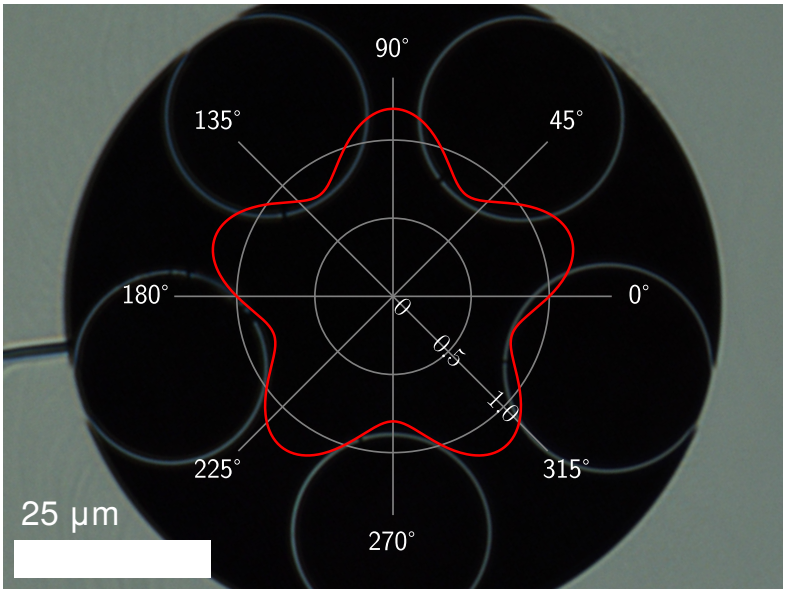

Fig. S-7 A harmonically perturbed circle overlaid on our fibre channel geometry. The overlay is defined by the Eq. (SI.7.11), with parameters $k = 5$ and $\delta_r = 0.2$. The free parameter $\bar{r}$ was scaled for best fit to the fibre geometry. (*Fig. first referenced on p. 195*)

Following the analysis of [345] adapted to our particular geometry, we find a compactness of

$$C = 4\pi + 2\pi(k^2 - 1)\delta_r^2 \approx 13.5, \tag{SI.7.13}$$

and a geometrical correction factor

$$\alpha = \frac{8}{1+k}\, C - 8\pi \frac{3-k}{1+k} + \mathcal{O}(\delta_r^4) \approx 19. \tag{SI.7.14}$$

Hence, for the perturbed circle,

$$R_{\text{hyd, core}} = \alpha\, R_{\text{hyd}}^{\text{dim}} = \alpha\, \frac{\eta L}{A^2}, \tag{SI.7.15}$$

from which we find the hydrodynamic resistance per unit length as

$$R_{\text{hyd, core}}/L = \frac{\alpha\eta}{\bar{r}^4\pi^2}. \tag{SI.7.16}$$

For our HC-PCF with $C = 19, \bar{r} = 30\,\mu\text{m}$ and filled with water, this evaluates to

$$R_{\text{hyd, core}}/L = 0.4\,\text{Pa}/(\text{cm}\cdot\text{nL/min}). \tag{SI.7.17}$$

Flow in both core and capillaries

However, the five capillaries offer additional flow paths to the fluid, thus the flow rate through the core is less than this number. We will treat the capillaries as circles with a radius of 25 µm (Fig. 2.4). The analytical result for the flow resistance of a circular channel yields

$$\frac{R_{\text{hyd},\bigcirc}}{L} = \frac{8\eta}{\pi r^4} \approx 1.1\,\text{Pa}/(\text{cm}\cdot\text{nL/min}). \tag{SI.7.18}$$

There are five capillaries in parallel, so that their combined flow resistances add as $1/R = \sum 1/R_i$ to

$$\frac{R_{\text{hyd, capillaries}}}{L} \approx 0.22\,\text{Pa}/(\text{cm}\cdot\text{nL/min}). \tag{SI.7.19}$$

Core bypass ratio

Comparing the five capillaries and the core, we find the core–capillary flow rate ratio of

$$\frac{Q_{\text{core}}}{Q_{\text{capillaries}}} = \frac{R_{\text{hyd, capillaries}}}{R_{\text{hyd, core}}} \approx 0.55, \tag{SI.7.20}$$

which could be termed the bypass ratio if sensing happens predominantly in the core, meaning that for every volume of fluid traversing the core, $1/0.55 = 1.8$ traverse the capillaries instead.

Comparison to back-of-the-envelope calculation

Finally, we openly admit that for the HC-PCF used in these experiments, which closely approximates individual circles in its geometry, the above derivation is not far from being a rounding error on the back-of-the-envelope approximation that would have been found by simply treating it as a circle (using $R_{\text{hyd},\bigcirc} = 8\eta L \,/\, \pi r^4$). However, the above remains as a demonstration of the power of perturbation theory, and could quickly be adapted to other HC-PCF geometries where more microstructure exists.

Resulting experimental intuition

As expected from the r^{-4} scaling of hydrodynamic resistance, the combined flow resistance of the five capillaries and the core is only 65 % higher than the core alone, despite the capillaries contributing 3.5 times as much cross-sectional area (and hence linear volume).

To illustrate this number from an experimental perspective, consider how atmospheric pressure drops with increasing altitude by approximately 11.3 Pa/m. If the fibre ends differ in elevation by about 60 mm, gravity would drive a flow of 1 nL/(min · cm). In practice, this would require the outflow facet to be free of

back pressures, in particular from surface tensions by droplets that form. Surface tension is the reason a filled fibre is not seen to leak when held vertically.

Similarly, another first comparison for this figure is the observation that a drop of liquid left the fibre every few seconds when applying pressure with a syringe. Neglecting the flow resistance of all other tubing in the first instance (since tubing diameter/fibre channel diameter ≈ 5), a typical manually-applied force $mg = 0.5\,\mathrm{kg} \cdot g$ pushing on a small glass syringe (plunger diameter $d = 1\,\mathrm{cm}$) would result in a flow rate of

$$Q = \left(\frac{Q_{\text{total}}}{L}\right) \cdot L \cdot \frac{mg}{\pi\left(\frac{d}{2}\right)^2} \approx 4\,\mu\mathrm{L\,min^{-1}} \tag{SI.7.21}$$

through a 10 cm piece of fibre. The droplets were about 1 mm in diameter, such that they each have a volume of $\frac{4}{3}\pi r^3 \approx 0.5\,\mu\mathrm{L}$. Hence, $Q \approx 8$ drops per minute or one drop every 8 s, confirming the observation.

Ref | References

[1] Jan R Heck, Ermanno Miele, Ralf Mouthaan, Michael H Frosz, Tuomas P J Knowles and Tijmen G Euser. 'Label-Free Monitoring of Proteins in Optofluidic Hollow-Core Photonic Crystal Fibres'. In: *Methods and Applications in Fluorescence* 10.4 (1st Oct. 2022), p. 045008. ISSN: 2050-6120. DOI: 10.1088/2050-6120/ac9113 Citations on pp. **18, 70, 95, 99, 108**.

[2] Jan R. Heck, Ermanno Miele, Ralf Mouthaan, Michael Frosz, Tuomas Knowles and Tijmen Euser. 'Label-Free Detection of Proteins with Optofluidic Hollow-Core Photonic Crystal Fibre Sensors'. In: *SPIE Future Sensing Technologies 2023*. SPIE Future Sensing Technologies. Ed. by Osamu Matoba, Christopher R. Valenta and Joseph A. Shaw. Yokohama, Japan: SPIE, 22nd May 2023, p. 12. ISBN: 978-1-5106-5722-9. DOI: 10.1117/12.2643905 Citations on pp. **18, 19**.

[3] Vasileios Tsoutsouras, Orestis Kaparounakis, Chatura Samarakoon, Bilgesu Bilgin, James Meech, Jan Heck and Phillip Stanley-Marbell. 'The Laplace Microarchitecture for Tracking Data Uncertainty'. In: *IEEE Micro* 42.4 (1st July 2022), pp. 78–86. ISSN: 0272-1732, 1937-4143. DOI: 10.1109/MM.2022.3166067 Citation on p. **18**.

[4] Robert Hooke. *Micrographia, or Some Physiological Descriptions of Minute Bodies Made by Magnifying Glasses, with Observations and Inquiries Thereupon. By R. Hooke.* Printed by Jo. Martyn, and Ja. Allestry, printers to the Royal Society, 1665. URL: http://explore.bl.uk/BLVU1:LSCOP-ALL:BLL01001727682 Citation on p. **22**.

[5] Galilei Galileo. *Sidereus nuncius* (*'The Starry Messenger'*). Cambridge University Library: Apud Thomam Baglionum, 1610. URL: https://cudl.lib.cam.ac.uk/view/PR-ADAMS-00005-00061-00001/5 Citation on p. **22**.

[6] Charles Tanford and Jacqueline Reynolds. *Nature's Robots: A History of Proteins*. 1st ed. New York, NY Oxford: Oxford Univ. Press, 2001. 304 pp. ISBN: 978-0-19-860694-9 Citation on p. **22**.

[7] Aleksej Vitalevič Finkelštejn and Oleg Borisovič Pticyn. *Protein Physics: A Course of Lecture*. Second, updated, and extended edition. Amsterdam Boston: Elsevier/Academic Press, 2016. ISBN: 978-0-12-809676-5 Citation on p. **22**.

[8] Pradip K. Ghosh. *Introduction to Protein Mass Spectrometry*. London: Academic Press, 2016. 298 pp. ISBN: 978-0-12-805123-8
Citation on p. **22**.

[9] Marko Haramija. 'Challenges in Separations of Proteins and Small Biomolecules and the Role of Modern Mass Spectroscopy Tools for Solving Them, as Well as Bypassing Them, in Structural Analytical Studies of Complex Biomolecular Mixtures'. In: *Separations* 5.1 (5th Feb. 2018), p. 11. ISSN: 2297-8739. DOI: 10.3390/separations5010011 Citation on p. **22**.

[10] Alexander Wlodawer, Zbigniew Dauter and Mariusz Jaskolski, eds. *Protein Crystallography: Methods and Protocols*. Vol. 1607. Methods in Molecular Biology. New York, NY: Springer New York, 2017. ISBN: 978-1-4939-6998-2. DOI: 10.1007/978-1-4939-7000-1 Citation on p. **22**.

[11] Jan Drenth and Jeroen Mesters. *Principles of Protein X-Ray Crystallography*. 3rd ed. New York: Springer, 2007. 332 pp. ISBN: 978-0-387-33334-2
Citation on p. **22**.

[12] Richard N. Day and Michael W. Davidson, eds. *The Fluorescent Protein Revolution*. Series in Cellular and Clinical Imaging. Boca Raton: CRC Press, Taylor & Francis Group, 2014. 333 pp. ISBN: 978-1-4398-7508-7
Citations on pp. **22, 23**.

[13] 'Protein Fluorescence'. In: *Principles of Fluorescence Spectroscopy*. Ed. by Joseph R. Lakowicz. Boston, MA: Springer US, 2006, pp. 529–575. ISBN: 978-0-387-46312-4. DOI: 10.1007/978-0-387-46312-4_16
Citations on pp. **22, 35, 38, 40**.

[14] Kevin Francis Sullivan, ed. *Fluorescent Proteins*. 2nd ed. Methods in Cell Biology v. 85. Amsterdam ; Boston : San Diego, CA: Elsevier ; Academic Press, 2010. 592 pp. ISBN: 978-0-12-372558-5 Citation on p. **22**.

[15] William E. Arter, Aviad Levin, Georg Krainer and Tuomas P. J. Knowles. 'Microfluidic Approaches for the Analysis of Protein – Protein Interactions in Solution'. In: *Biophysical Reviews* (8th Apr. 2020). ISSN: 1867-2450, 1867-2469. DOI: 10.1007/s12551-020-00679-4
Citation on p. **22**.

[16] Jérôme Charmet, Paolo Arosio and Tuomas P.J. Knowles. 'Microfluidics for Protein Biophysics'. In: *Journal of Molecular Biology* 430.5 (Mar. 2018),

pp. 565–580. ISSN: 00222836. DOI: 10.1016/j.jmb.2017.12.015
Citation on p. **22**.

[17] Huaying Zhao, Patrick H. Brown and Peter Schuck. 'On the Distribution of Protein Refractive Index Increments'. In: *Biophysical Journal* 100.9 (May 2011), pp. 2309–2317. ISSN: 00063495. DOI: 10.1016/j.bpj.2011.03.004
Citations on pp. **22, 50**.

[18] Christopher P. Toseland. 'Fluorescent Labeling and Modification of Proteins'. In: *Journal of Chemical Biology* 6.3 (July 2013), pp. 85–95. ISSN: 1864-6158, 1864-6166. DOI: 10.1007/s12154-013-0094-5
Citations on pp. **23, 35**.

[19] Osamu Shimomura. 'Discovery of Green Fluorescent Protein (GFP) (Nobel Lecture)'. In: *Angewandte Chemie International Edition* 48.31 (20th July 2009), pp. 5590–5602. ISSN: 14337851, 15213773. DOI: 10.1002/anie.200902240
Citation on p. **23**.

[20] Kadi-Liis Saar, Emma V. Yates, Thomas Müller, Séverine Saunier, Christopher M. Dobson and Tuomas P.J. Knowles. 'Automated Ex Situ Assays of Amyloid Formation on a Microfluidic Platform'. In: *Biophysical Journal* 110.3 (Feb. 2016), pp. 555–560. ISSN: 00063495. DOI: 10.1016/j.bpj.2015.11.3523
Citations on pp. **23, 27**.

[21] Zenon Toprakcioglu, Pavankumar Challa, Catherine Xu and Tuomas P. J. Knowles. 'Label-Free Analysis of Protein Aggregation and Phase Behavior'. In: *ACS Nano* 13.12 (24th Dec. 2019), pp. 13940–13948. ISSN: 1936-0851, 1936-086X. DOI: 10.1021/acsnano.9b05552
Citations on pp. **23, 39, 156**.

[22] Emma V. Yates, Thomas Müller, Luke Rajah, Erwin J. De Genst, Paolo Arosio, Sara Linse, Michele Vendruscolo, Christopher M. Dobson and Tuomas P. J. Knowles. 'Latent Analysis of Unmodified Biomolecules and Their Complexes in Solution with Attomole Detection Sensitivity'. In: *Nature Chemistry* 7.10 (Oct. 2015), pp. 802–809. ISSN: 1755-4330, 1755-4349. DOI: 10.1038/nchem.2344
Citation on p. **23**.

[23] Kai Wu, Wuxuepeng Sun, Dechang Li, Jiajie Diao and Peng Xiu. 'Inhibition of Amyloid Nucleation by Steric Hindrance'. In: *J. Phys. Chem. B* (2022)
Citations on pp. **23, 26**.

[24] Minna Groenning. 'Binding Mode of Thioflavin T and Other Molecular Probes in the Context of Amyloid Fibrils—Current Status'. In: *Journal of Chemical Biology* 3.1 (Mar. 2010), pp. 1–18. ISSN: 1864-6158, 1864-6166. DOI: 10.1007/s12154-009-0027-5 Citations on pp. **23, 26**.

[25] Harish Chander, Abha Chauhan and Ved Chauhan. 'Binding of Proteases to Fibrillar Amyloid- β Protein and Its Inhibition by Congo Red'. In: *Journal of Alzheimer's Disease* 12.3 (1st Nov. 2007), pp. 261–269. DOI: 10.3233/JAD-2007-12308 Citations on pp. **23, 27**.

[26] Amar Ghisaidoobe and Sang Chung. 'Intrinsic Tryptophan Fluorescence in the Detection and Analysis of Proteins: A Focus on Förster Resonance Energy Transfer Techniques'. In: *International Journal of Molecular Sciences* 15.12 (5th Dec. 2014), pp. 22518–22538. ISSN: 1422-0067. DOI: 10.3390/ijms151222518 Citations on pp. **23, 36–38, 42, 175**.

[27] Henryk Szmacinski, Krishanu Ray and Joseph R. Lakowicz. 'Metal-Enhanced Fluorescence of Tryptophan Residues in Proteins: Application toward Label-Free Bioassays'. In: *Analytical Biochemistry* 385.2 (Feb. 2009), pp. 358–364. ISSN: 00032697. DOI: 10.1016/j.ab.2008.11.025 Citations on pp. **23, 41**.

[28] Aaron Ho-Pui Ho, Donghyun Kim and Michael G. Somekh, eds. *Handbook of Photonics for Biomedical Engineering*. Springer Reference. Dordrecht: Springer Netherlands, 2017. ISBN: 978-94-007-5052-4. DOI: 10.1007/978-94-007-5052-4 Citation on p. **25**.

[29] Xudong Fan and Ian M. White. 'Optofluidic Microsystems for Chemical and Biological Analysis'. In: *Nature Photonics* 5.10 (Oct. 2011), pp. 591–597. ISSN: 1749-4885, 1749-4893. DOI: 10.1038/nphoton.2011.206 Citations on pp. **25, 190**.

[30] Clemens F. Kaminski and Gabriele S. Kaminski Schierle. 'Probing Amyloid Protein Aggregation with Optical Superresolution Methods: From the Test Tube to Models of Disease'. In: *Neurophotonics* 3.4 (29th June 2016), p. 041807. ISSN: 2329-423X. DOI: 10.1117/1.NPh.3.4.041807 Citations on pp. **25, 40**.

[31] Trenton M. Peters-Clarke, Kevin L. Schauer, Nicholas M. Riley, Jean M. Lodge, Michael S. Westphall and Joshua J. Coon. 'Optical Fiber-Enabled Photoactivation of Peptides and Proteins'. In: *Analytical Chemistry* 92.18

(15th Sept. 2020), pp. 12363–12370. ISSN: 0003-2700, 1520-6882. DOI: 10.1021/acs.analchem.0c02087 Citations on pp. **26, 191**.

[32] Wei Wang and Christopher J. Roberts. 'Protein Aggregation – Mechanisms, Detection, and Control'. In: *International Journal of Pharmaceutics* 550.1-2 (Oct. 2018), pp. 251–268. ISSN: 03785173. DOI: 10.1016/j.ijpharm.2018.08.043 Citation on p. **26**.

[33] Tuomas P. J. Knowles, Michele Vendruscolo and Christopher M. Dobson. 'The Physical Basis of Protein Misfolding Disorders'. In: *Physics Today* 68.3 (Mar. 2015), pp. 36–41. ISSN: 0031-9228, 1945-0699. DOI: 10.1063/PT.3.2719 Citations on pp. **26, 28, 52**.

[34] Fabrizio Chiti and Christopher M. Dobson. 'Protein Misfolding, Amyloid Formation, and Human Disease: A Summary of Progress Over the Last Decade'. In: *Annual Review of Biochemistry* 86.1 (20th June 2017), pp. 27–68. ISSN: 0066-4154, 1545-4509. DOI: 10.1146/annurev-biochem-061516-045115 Citations on pp. **26, 28**.

[35] Georg Meisl, Julius B Kirkegaard, Paolo Arosio, Thomas C T Michaels, Michele Vendruscolo, Christopher M Dobson, Sara Linse and Tuomas P J Knowles. 'Molecular Mechanisms of Protein Aggregation from Global Fitting of Kinetic Models'. In: *Nature Protocols* 11.2 (Feb. 2016), pp. 252–272. ISSN: 1754-2189, 1750-2799. DOI: 10.1038/nprot.2016.010 Citations on pp. **26, 28, 161**.

[36] Anna I. Sulatskaya, Andrey V. Lavysh, Alexander A. Maskevich, Irina M. Kuznetsova and Konstantin K. Turoverov. 'Thioflavin T Fluoresces as Excimer in Highly Concentrated Aqueous Solutions and as Monomer Being Incorporated in Amyloid Fibrils'. In: *Scientific Reports* 7.1 (19th May 2017), p. 2146. ISSN: 2045-2322. DOI: 10.1038/s41598-017-02237-7 Citation on p. **27**.

[37] Matthew Biancalana and Shohei Koide. 'Molecular Mechanism of Thioflavin-T Binding to Amyloid Fibrils'. In: *Biochimica et Biophysica Acta (BBA) - Proteins and Proteomics* 1804.7 (July 2010), pp. 1405–1412. ISSN: 15709639. DOI: 10.1016/j.bbapap.2010.04.001 Citation on p. **27**.

[38] Tuomas P. J. Knowles, Michele Vendruscolo and Christopher M. Dobson. 'The Amyloid State and Its Association with Protein Misfolding Diseases'. In: *Nature Reviews Molecular Cell Biology* 15.6 (June 2014), pp. 384–396.

ISSN: 1471-0072, 1471-0080. DOI: 10.1038/nrm3810

Citations on pp. **28, 52, 153**.

[39] Christopher M Dobson. 'Principles of Protein Folding, Misfolding and Aggregation'. In: *Seminars in Cell & Developmental Biology* 15.1 (Feb. 2004), pp. 3–16. ISSN: 10849521. DOI: 10.1016/j.semcdb.2003.12.008

Citations on pp. **28, 52**.

[40] Dominic M. Walsh, Dean M. Hartley, Yoko Kusumoto, Youcef Fezoui, Margaret M. Condron, Aleksey Lomakin, George B. Benedek, Dennis J. Selkoe and David B. Teplow. 'Amyloid β-Protein Fibrillogenesis'. In: *Journal of Biological Chemistry* 274.36 (Sept. 1999), pp. 25945–25952. ISSN: 00219258. DOI: 10.1074/jbc.274.36.25945 Citation on p. **28**.

[41] Georg Meisl, Tuomas PJ Knowles and David Klenerman. 'The Molecular Processes Underpinning Prion-like Spreading and Seed Amplification in Protein Aggregation'. In: *Current Opinion in Neurobiology* 61 (Apr. 2020), pp. 58–64. ISSN: 09594388. DOI: 10.1016/j.conb.2020.01.010

Citation on p. **28**.

[42] Einar M. Sigurdsson, Miguel Calero and María Gasset, eds. *Amyloid Proteins*. 3rd ed. Methods in Molecular Biology 1779. New York, NY: Springer New York, 2018. 542 pp. ISBN: 978-1-4939-7815-1. DOI: 10.1007/978-1-4939-7816-8 Citation on p. **28**.

[43] Alexander J. Dear, Georg Meisl, Thomas C. T. Michaels, Manuela R. Zimmermann, Sara Linse and Tuomas P. J. Knowles. 'The Catalytic Nature of Protein Aggregation'. In: *The Journal of Chemical Physics* 152.4 (31st Jan. 2020), p. 045101. ISSN: 0021-9606, 1089-7690. DOI: 10.1063/1.5133635

Citation on p. **28**.

[44] Fiona T S Chan, Gabriele S Kaminski Schierle, Janet R Kumita, Carlos W Bertoncini, Christopher M Dobson and Clemens F Kaminski. 'Protein Amyloids Develop an Intrinsic Fluorescence Signature during Aggregation'. In: (2017), p. 14

Citations on pp. **28, 40**.

[45] Shi-Jie Chen et al. 'Protein Folds vs. Protein Folding: Differing Questions, Different Challenges'. In: *Proceedings of the National Academy of Sciences* 120.1 (3rd Jan. 2023), e2214423119. ISSN: 0027-8424, 1091-6490. DOI: 10.1073/pnas.2214423119 Citation on p. **28**.

[46] Zygmunt Gryczynski and Ignacy Gryczynski. *Practical Fluorescence Spectroscopy*. Boca Raton: CRC Press, 2020. ISBN: 978-1-4398-2169-5
Citation on p. **29**.

[47] Gareth O. S. Williams, Tijmen G. Euser, Jochen Arlt, Philip St.J. Russell and Anita C. Jones. 'Taking Two-Photon Excitation to Exceptional Path-Lengths in Photonic Crystal Fiber'. In: *ACS Photonics* 1.9 (17th Sept. 2014), pp. 790–793. ISSN: 2330-4022, 2330-4022. DOI: 10.1021/ph5002236
Citations on pp. **29, 42, 43**.

[48] Matthias Schmidt, Ana M. Cubillas, Nicola Taccardi, Tijmen G. Euser, Till Cremer, Florian Maier, Hans-Peter Steinrück, Philip St. J. Russell, Peter Wasserscheid and Bastian J. M. Etzold. 'Chemical and (Photo)-Catalytical Transformations in Photonic Crystal Fibers'. In: *ChemCatChem* 5.3 (Mar. 2013), pp. 641–650. ISSN: 18673880. DOI: 10.1002/cctc.201200676
Citations on pp. **29, 42**.

[49] Gareth O. S. Williams, Tijmen G. Euser, Philip St. J. Russell, Alexander J. MacRobert and Anita C. Jones. 'Highly Sensitive Luminescence Detection of Photosensitized Singlet Oxygen within Photonic Crystal Fibers'. In: *ChemPhotoChem* 2.7 (July 2018), pp. 616–621. ISSN: 23670932. DOI: 10.1002/cptc.201800028
Citations on pp. **29, 42**.

[50] Stephan Smolka, Michael Barth and Oliver Benson. 'Highly Efficient Fluorescence Sensing with Hollow Core Photonic Crystal Fibers'. In: *Optics Express* 15.20 (2007), p. 12783. ISSN: 1094-4087. DOI: 10.1364/OE.15.012783
Citations on pp. **29, 42**.

[51] Gareth O S Williams, Tijmen G Euser, Philip St J Russell and Anita C Jones. 'Spectrofluorimetry with Attomole Sensitivity in Photonic Crystal Fibres'. In: *Methods and Applications in Fluorescence* 1.1 (28th Jan. 2013), p. 015003. ISSN: 2050-6120. DOI: 10.1088/2050-6120/1/1/015003
Citations on pp. **29, 43**.

[52] Xiao Xia Han, Rebeca S. Rodriguez, Christy L. Haynes, Yukihiro Ozaki and Bing Zhao. 'Surface-Enhanced Raman Spectroscopy'. In: *Nature Reviews Methods Primers* 1.1 (6th Jan. 2022), p. 87. ISSN: 2662-8449. DOI: 10.1038/s43586-021-00083-6
Citation on p. **30**.

[53] Steven E. J. Bell, Gaëlle Charron, Emiliano Cortés, Janina Kneipp, Marc Lamy Chapelle, Judith Langer, Marek Procházka, Vi Tran and Sebastian Schlücker. 'Towards Reliable and Quantitative Surface - Enhanced Raman Scattering (SERS): From Key Parameters to Good Analytical Practice'. In: *Angewandte Chemie International Edition* 59.14 (27th Mar. 2020), pp. 5454–5462. ISSN: 1433-7851, 1521-3773. DOI: 10.1002/anie.201908154 Citation on p. **30**.

[54] Ralph A. Tripp, Richard A. Dluhy and Yiping Zhao. 'Novel Nanostructures for SERS Biosensing'. In: *Nano Today* 3.3-4 (June 2008), pp. 31–37. ISSN: 17480132. DOI: 10.1016/S1748-0132(08)70042-2 Citation on p. **30**.

[55] Cristina L. Zavaleta, Bryan R. Smith, Ian Walton, William Doering, Glenn Davis, Borzoyeh Shojaei, Michael J. Natan and Sanjiv S. Gambhir. 'Multiplexed Imaging of Surface Enhanced Raman Scattering Nanotags in Living Mice Using Noninvasive Raman Spectroscopy'. In: *Proceedings of the National Academy of Sciences* 106.32 (11th Aug. 2009), pp. 13511–13516. ISSN: 0027-8424, 1091-6490. DOI: 10.1073/pnas.0813327106 Citation on p. **30**.

[56] Huiqiao Liu, Xia Gao, Chen Xu and Dingbin Liu. 'SERS Tags for Biomedical Detection and Bioimaging'. In: *Theranostics* 12.4 (2022), pp. 1870–1903. ISSN: 1838-7640. DOI: 10.7150/thno.66859 Citation on p. **30**.

[57] Ermanno Miele, Wesley M. Dose, Ilya Manyakin, Michael H. Frosz, Zachary Ruff, Michael F. L. De Volder, Clare P. Grey, Jeremy J. Baumberg and Tijmen G. Euser. 'Hollow-Core Optical Fibre Sensors for Operando Raman Spectroscopy Investigation of Li-ion Battery Liquid Electrolytes'. In: *Nature Communications* 13.1 (Dec. 2022), p. 1651. ISSN: 2041-1723. DOI: 10.1038/s41467-022-29330-4 Citations on pp. **30, 43**.

[58] Di Yan, Jürgen Popp, Mathias W. Pletz and Torsten Frosch. 'Highly Sensitive Broadband Raman Sensing of Antibiotics in Step-Index Hollow-Core Photonic Crystal Fibers'. In: *ACS Photonics* 4.1 (18th Jan. 2017), pp. 138–145. ISSN: 2330-4022, 2330-4022. DOI: 10.1021/acsphotonics.6b00688 Citation on p. **30**.

[59] Zhiwen Xia, Xin Zhang, Jingyuan Yao, Zihao Liu, Yulong Jin, Huabing Yin, Pu Wang and Xiu-Hong Wang. 'Giant Enhancement of Raman Scattering by a Hollow-Core Microstructured Optical Fiber Allows Single Exosome Probing'. In: *ACS Sensors* 8.4 (28th Apr. 2023), pp. 1799–1809. ISSN: 2379-

3694, 2379-3694. DOI: 10.1021/acssensors.3c00131
Citation on p. **31**.

[60] Bijan Ranjbar and Pooria Gill. 'Circular Dichroism Techniques: Biomolecular and Nanostructural Analyses- A Review'. In: *Chemical Biology & Drug Design* 74.2 (Aug. 2009), pp. 101–120. ISSN: 17470277, 17470285. DOI: 10.1111/j.1747-0285.2009.00847.x Citation on p. **31**.

[61] Steven S. Andrews and James Tretton. 'Physical Principles of Circular Dichroism'. In: *Journal of Chemical Education* 97.12 (8th Dec. 2020), pp. 4370–4376. ISSN: 0021-9584, 1938-1328. DOI: 10.1021/acs.jchemed.0c01061
Citation on p. **31**.

[62] G. Snatzke. 'Circular Dichroism and Optical Rotatory Dispersion— Principles and Application to the Investigation of the Stereochemistry of Natural Products'. In: *Angewandte Chemie International Edition in English* 7.1 (Jan. 1968), pp. 14–25. ISSN: 0570-0833, 1521-3773. DOI: 10.1002/anie.196800141 Citation on p. **31**.

[63] Lee Whitmore, Benjamin Woollett, Andrew John Miles, D. P. Klose, Robert W. Janes and B. A. Wallace. 'PCDDB: The Protein Circular Dichroism Data Bank, a Repository for Circular Dichroism Spectral and Metadata'. In: *Nucleic Acids Research* 39 (suppl_1 1st Jan. 2011), pp. D480–D486. ISSN: 0305-1048, 1362-4962. DOI: 10.1093/nar/gkq1026 Citation on p. **31**.

[64] Timothy A Keiderling. 'Protein and Peptide Secondary Structure and Conformational Determination with Vibrational Circular Dichroism'. In: *Current Opinion in Chemical Biology* 6.5 (Oct. 2002), pp. 682–688. ISSN: 13675931. DOI: 10.1016/S1367-5931(02)00369-1 Citation on p. **31**.

[65] Robert E. Synovec and Edward S. Yeung. 'Fluorescence Detected Circular Dichroism as a Detection Principle in High-Performance Liquid Chromatography'. In: *Journal of Chromatography A* 368 (Jan. 1986), pp. 85–93. ISSN: 00219673. DOI: 10.1016/S0021-9673(00)91049-5 Citation on p. **31**.

[66] Tatsuo Nehira, Kaoru Ishihara, Koichi Matsuo, Shunsuke Izumi, Takeshi Yamazaki and Atsuhiko Ishida. 'A Sensitive Method Based on Fluorescence-Detected Circular Dichroism for Protein Local Structure Analysis'. In: *Analytical Biochemistry* 430.2 (Nov. 2012), pp. 179–184. ISSN: 00032697. DOI: 10.1016/j.ab.2012.08.020 Citation on p. **31**.

[67] Florian Schorn, Arabella Essert, Yu Zhong, Sahib Abdullayev, Kathrin Castiglione, Marco Haumann and Nicolas Y. Joly. 'Measurement of Minute Liquid Volumes of Chiral Molecules Using In-Fiber Polarimetry'. In: *Analytical Chemistry* 95.6 (14th Feb. 2023), pp. 3204–3209. ISSN: 0003-2700, 1520-6882. DOI: 10.1021/acs.analchem.2c03347 Citation on p. **31**.

[68] P. Roth, Y. Chen, M. C. Günendi, R. Beravat, N. N. Edavalath, M. H. Frosz, G. Ahmed, G. K. L. Wong and P. St J. Russell. *Strong Circular Dichroism in Twisted Single-Ring Hollow-Core Photonic Crystal Fiber*. 30th July 2018. arXiv: 1807.11209 [physics]. URL: http://arxiv.org/abs/1807.11209. preprint Citation on p. **31**.

[69] G. K. L. Wong, X. M. Xi, M. H. Frosz and P. St.J. Russell. 'Enhanced Optical Activity and Circular Dichroism in Twisted Photonic Crystal Fiber'. In: *Optics Letters* 40.20 (15th Oct. 2015), p. 4639. ISSN: 0146-9592, 1539-4794. DOI: 10.1364/OL.40.004639 Citation on p. **31**.

[70] A Taranta. 'Exceptional Polarization Purity in Antiresonant Hollow-Core Optical Fibres'. In: *Nature Photonics* 14 (2020), p. 9 Citation on p. **31**.

[71] Vladimir M. Gun'ko, Alla V. Klyueva, Yuri N. Levchuk and Roman Leboda. 'Photon Correlation Spectroscopy Investigations of Proteins'. In: *Advances in Colloid and Interface Science* 105.1-3 (Sept. 2003), pp. 201–328. ISSN: 00018686. DOI: 10.1016/S0001-8686(03)00091-5 Citation on p. **31**.

[72] Bernard Lorber, Frédéric Fischer, Marc Bailly, Hervé Roy and Daniel Kern. 'Protein Analysis by Dynamic Light Scattering: Methods and Techniques for Students'. In: *Biochemistry and Molecular Biology Education* 40.6 (Nov. 2012), pp. 372–382. ISSN: 14708175. DOI: 10.1002/bmb.20644 Citation on p. **31**.

[73] Jörg Stetefeld, Sean A. McKenna and Trushar R. Patel. 'Dynamic Light Scattering: A Practical Guide and Applications in Biomedical Sciences'. In: *Biophysical Reviews* 8.4 (Dec. 2016), pp. 409–427. ISSN: 1867-2450, 1867-2469. DOI: 10.1007/s12551-016-0218-6 Citation on p. **31**.

[74] Petru Ghenuche, Hervé Rigneault and Jérôme Wenger. 'Hollow-Core Photonic Crystal Fiber Probe for Remote Fluorescence Sensing with Single Molecule Sensitivity'. In: *Optics Express* 20.27 (17th Dec. 2012), p. 28379. ISSN: 1094-4087. DOI: 10.1364/OE.20.028379 Citations on pp. **32, 43**.

[75] Jaime Ortega-Arroyo and Philipp Kukura. 'Interferometric Scattering Microscopy (iSCAT): New Frontiers in Ultrafast and Ultrasensitive Optical Microscopy'. In: *Physical Chemistry Chemical Physics* 14.45 (2012), p. 15625. ISSN: 1463-9076, 1463-9084. DOI: 10.1039/c2cp41013c Citation on p. **32**.

[76] J. Ortega Arroyo, J. Andrecka, K. M. Spillane, N. Billington, Y. Takagi, J. R. Sellers and P. Kukura. 'Label-Free, All-Optical Detection, Imaging, and Tracking of a Single Protein'. In: *Nano Letters* 14.4 (9th Apr. 2014), pp. 2065–2070. ISSN: 1530-6984, 1530-6992. DOI: 10.1021/nl500234t Citation on p. **32**.

[77] S. T. Jepsen, T. M. Jørgensen, W. Zong, T. Trydal, S. R. Kristensen and H. S. Sørensen. 'Evaluation of Back Scatter Interferometry, a Method for Detecting Protein Binding in Solution'. In: *The Analyst* 140.3 (2015), pp. 895–901. ISSN: 0003-2654, 1364-5528. DOI: 10.1039/C4AN01129E Citation on p. **32**.

[78] Marek Piliarik and Vahid Sandoghdar. 'Direct Optical Sensing of Single Unlabelled Proteins and Super-Resolution Imaging of Their Binding Sites'. In: *Nature Communications* 5.1 (Dec. 2014), p. 4495. ISSN: 2041-1723. DOI: 10.1038/ncomms5495 Citation on p. **32**.

[79] Nikolas Hundt. 'Label-Free, Mass-Sensitive Single-Molecule Imaging Using Interferometric Scattering Microscopy'. In: *Essays in Biochemistry* 65.1 (16th Apr. 2021). Ed. by Dominika Gruszka, pp. 81–91. ISSN: 0071-1365, 1744-1358. DOI: 10.1042/EBC20200023 Citation on p. **32**.

[80] Gavin Young et al. 'Quantitative Mass Imaging of Single Biological Macromolecules'. In: *Science* 360.6387 (27th Apr. 2018), pp. 423–427. ISSN: 0036-8075, 1095-9203. DOI: 10.1126/science.aar5839 Citations on pp. **33, 102**.

[81] Zhanling Wang, Kelly Swinney and Darryl J. Bornhop. 'Attomole Sensitivity for Unlabeled Proteins and Polypeptides with On-Chip Capillary Electrophoresis and Universal Detection by Interferometric Backscatter'. In: *ELECTROPHORESIS* 24.5 (Mar. 2003), pp. 865–873. ISSN: 01730835, 15222683. DOI: 10.1002/elps.200390109 Citation on p. **33**.

[82] Stanley D Chandradoss, Anna C Haagsma, Young Kwang Lee, Jae-Ho Hwang, Jwa-Min Nam and Chirlmin Joo. 'Surface Passivation for Single-molecule Protein Studies'. In: *Journal of Visualized Experiments* (2014), p. 8
Citation on p. **34**.

[83] R. Baxter, A. Jones and H. Baxter. 'Quantification of Protein Contamination on Surfaces'. In: *2012 Abstracts IEEE International Conference on Plasma Science*. 2012 IEEE 39th International Conference on Plasma Sciences (ICOPS). Edinburgh: IEEE, July 2012, 2P-176-2P–176. ISBN: 978-1-4577-2129-8. DOI: 10.1109/PLASMA.2012.6383563
Citation on p. **34**.

[84] Tongcang Li and Mark G. Raizen. 'Brownian Motion at Short Time Scales: Brownian Motion at Short Time Scales'. In: *Annalen der Physik* 525.4 (Apr. 2013), pp. 281–295. ISSN: 00033804. DOI: 10.1002/andp.201200232
Citation on p. **34**.

[85] Alexander P Demchenko. 'Photobleaching of Organic Fluorophores: Quantitative Characterization, Mechanisms, Protection'. In: *Methods and Applications in Fluorescence* 8.2 (20th Feb. 2020), p. 022001. ISSN: 2050-6120. DOI: 10.1088/2050-6120/ab7365 Citation on p. **34**.

[86] Carlo Bradac. 'Nanoscale Optical Trapping: A Review'. In: *Advanced Optical Materials* 6.12 (June 2018), p. 1800005. ISSN: 21951071. DOI: 10.1002/adom.201800005 Citations on pp. **34, 45, 47**.

[87] A Ashkin and J. Dziedzic. 'Optical Trapping and Manipulation of Viruses and Bacteria'. In: *Science* 235.4795 (20th Mar. 1987), pp. 1517–1520. ISSN: 0036-8075, 1095-9203. DOI: 10.1126/science.3547653
Citations on pp. **34, 46**.

[88] Ahmed A. Al Balushi, Abhay Kotnala, Skyler Wheaton, Ryan M. Gelfand, Yashaswini Rajashekara and Reuven Gordon. 'Label-Free Free-Solution Nanoaperture Optical Tweezers for Single Molecule Protein Studies'. In: *The Analyst* 140.14 (2015), pp. 4760–4778. ISSN: 0003-2654, 1364-5528. DOI: 10.1039/C4AN02213K Citations on pp. **34, 47**.

[89] Yuanjie Pang and Reuven Gordon. 'Optical Trapping of a Single Protein'. In: *Nano Letters* 12.1 (11th Jan. 2012), pp. 402–406. ISSN: 1530-6984, 1530-6992. DOI: 10.1021/nl203719v
Citation on p. **34**.

[90] Junyi Jiao, Aleksander A. Rebane, Lu Ma and Yongli Zhang. 'Single-Molecule Protein Folding Experiments Using High-Precision Optical Tweezers'. In: *Optical Tweezers*. Ed. by Arne Gennerich. Vol. 1486. New York, NY: Springer New York, 2017, pp. 357–390. ISBN: 978-1-4939-6421-5. DOI: 10.1007/978-1-4939-6421-5_14 Citation on p. **34**.

[91] Anders E. Wallin, Heikki Ojala, Gabija Ziedaite and Edward Hæggström. 'Dual-Trap Optical Tweezers with Real-Time Force Clamp Control'. In: *Review of Scientific Instruments* 82.8 (Aug. 2011), p. 083102. ISSN: 0034-6748, 1089-7623. DOI: 10.1063/1.3615309 Citation on p. **34**.

[92] Avinash Kumar and John Bechhoefer. 'Nanoscale Virtual Potentials Using Optical Tweezers'. In: *Applied Physics Letters* 113.18 (29th Oct. 2018), p. 183702. ISSN: 0003-6951, 1077-3118. DOI: 10.1063/1.5055580 Citation on p. **34**.

[93] Jiang Zhe, Ashish Jagtiani, Prashanta Dutta, Jun Hu and Joan Carletta. 'A Micromachined High Throughput Coulter Counter for Bioparticle Detection and Counting'. In: *Journal of Micromechanics and Microengineering* 17.2 (1st Feb. 2007), pp. 304–313. ISSN: 0960-1317, 1361-6439. DOI: 10.1088/0960-1317/17/2/017 Citation on p. **34**.

[94] O. A. Saleh and L. L. Sohn. 'Quantitative Sensing of Nanoscale Colloids Using a Microchip Coulter Counter'. In: *Review of Scientific Instruments* 72.12 (1st Dec. 2001), pp. 4449–4451. ISSN: 0034-6748, 1089-7623. DOI: 10.1063/1.1419224 Citation on p. **34**.

[95] Ulrich F. Keyser, Bernard N. Koeleman, Stijn van Dorp, Diego Krapf, Ralph M. M. Smeets, Serge G. Lemay, Nynke H. Dekker and Cees Dekker. 'Direct Force Measurements on DNA in a Solid-State Nanopore'. In: *Nature Physics* 2.7 (July 2006), pp. 473–477. ISSN: 1745-2473, 1745-2481. DOI: 10.1038/nphys344 Citation on p. **35**.

[96] Filip Bošković and Ulrich F. Keyser. 'Toward Single-Molecule Proteomics'. In: *Science* 374.6574 (17th Dec. 2021), pp. 1443–1444. ISSN: 0036-8075, 1095-9203. DOI: 10.1126/science.abn0001 Citation on p. **35**.

[97] Kaikai Chen, Adnan Choudhary, Sarah E. Sandler, Christopher Maffeo, Caterina Ducati, Aleksei Aksimentiev and Ulrich F. Keyser. 'Super - Resolution Detection of DNA Nanostructures Using a Nanopore'. In:

Advanced Materials 35.12 (Mar. 2023), p. 2207434. ISSN: 0935-9648, 1521-4095. DOI: 10.1002/adma.202207434

Citation on p. **35**.

[98] Bernard Valeur. 'Molecular Fluorescence'. In: *Digital Encyclopedia of Applied Physics*. Ed. by Wiley-VCH Verlag GmbH & Co. KGaA. Weinheim, Germany: Wiley-VCH Verlag GmbH & Co. KGaA, 15th Dec. 2009, pp. 477–531. ISBN: 978-3-527-60043-4. DOI: 10.1002/3527600434.eap684

Citation on p. **35**.

[99] Nils G. Walter, ed. *Fluorescence Based Approaches*. 1. ed. Single Molecule Tools ed. by Nils G. Walter ; Pt. A. Amsterdam: Elsevier, Acad. Press, 2010. 476 pp. ISBN: 978-0-12-374954-3 Citation on p. **35**.

[100] Dongqing Li, ed. *Encyclopedia of Microfluidics and Nanofluidics*. New York, NY: Springer New York, 2015. ISBN: 978-1-4614-5491-5. DOI: 10.1007/978-1-4614-5491-5 Citation on p. **35**.

[101] Sigma-Aldrich. *Datasheet for Sigma Aldrich's 41698 Atto 488 NHS Ester*. Sigma-Aldrich, Merck KGaA, Darmstadt, Germany, 2018 Citation on p. **37**.

[102] Veerle Lemmens, Keerthana Ramanathan and Jelle Hendrix. 'Fluorescence Microscopy Data for Quantitative Mobility and Interaction Analysis of Proteins in Living Cells'. In: *Data in Brief* 29 (Apr. 2020), p. 105348. ISSN: 23523409. DOI: 10.1016/j.dib.2020.105348 Citation on p. **38**.

[103] Benjamien Moeyaert and Peter Dedecker. 'A Comprehensive Dataset of Image Sequences Covering 20 Fluorescent Protein Labels and 12 Imaging Conditions for Use in Super-Resolution Imaging'. In: *Data in Brief* 29 (Apr. 2020), p. 105273. ISSN: 23523409. DOI: 10.1016/j.dib.2020.105273

Citation on p. **38**.

[104] Mikhail Drobizhev, Nikolay S Makarov, Shane E Tillo, Thomas E Hughes and Aleksander Rebane. 'Two-Photon Absorption Properties of Fluorescent Proteins'. In: *Nature Methods* 8.5 (May 2011), pp. 393–399. ISSN: 1548-7091, 1548-7105. DOI: 10.1038/nmeth.1596 Citation on p. **38**.

[105] Shama Sograte-Idrissi, Nazar Oleksiievets, Sebastian Isbaner, Mariana Eggert-Martinez, Jörg Enderlein, Roman Tsukanov and Felipe Opazo. 'Nanobody Detection of Standard Fluorescent Proteins Enables Multi-Target DNA-PAINT with High Resolution and Minimal Displacement

Errors'. In: *Cells* 8.1 (14th Jan. 2019), p. 48. ISSN: 2073-4409. DOI: 10.3390/cells8010048 Citation on p. **38**.

[106] Mike Filius, Tao Ju Cui, Adithya N. Ananth, Margreet W. Docter, Jorrit W. Hegge, John van der Oost and Chirlmin Joo. 'High-Speed Super-Resolution Imaging Using Protein-Assisted DNA-PAINT'. In: *Nano Letters* 20.4 (8th Apr. 2020), pp. 2264–2270. ISSN: 1530-6984, 1530-6992. DOI: 10.1021/acs.nanolett.9b04277 Citation on p. **38**.

[107] Joseph R Lakowicz. *Topics in Fluorescence Spectroscopy*. New York: Plenum Press, 1991. ISBN: 0-306-47102-7 Citation on p. **38**.

[108] Yoshiko Moriyama, Daisuke Ohta, Kazuaki Hachiya, Yasuhiro Mitsui and Kunio Takeda. 'Fluorescence Behavior of Tryptophan Residues of Bovine and Human Serum Albumins in Ionic Surfactant Solutions: A Comparative Study of the Two and One Tryptophan(s) of Bovine and Human Albumins'. In: *Journal of Protein Chemistry* 15.3 (Apr. 1996), pp. 265–272. ISSN: 0277-8033, 1573-4943. DOI: 10.1007/BF01887115 Citations on pp. **38, 42**.

[109] James T. Vivian and Patrik R. Callis. 'Mechanisms of Tryptophan Fluorescence Shifts in Proteins'. In: *Biophysical Journal* 80.5 (May 2001), pp. 2093–2109. ISSN: 00063495. DOI: 10.1016/S0006-3495(01)76183-8 Citations on pp. **38, 41**.

[110] E. A. Burstein, N. S. Vedenkina and M. N. Ivkova. 'Fluorescence and the Location of Tryptophan Residues in Protein Molecules'. In: *Photochemistry and Photobiology* 18.4 (Oct. 1973), pp. 263–279. ISSN: 0031-8655, 1751-1097. DOI: 10.1111/j.1751-1097.1973.tb06422.x Citations on pp. **38, 40, 41**.

[111] Pavan Kumar Challa, Quentin Peter, Maya A. Wright, Yuewen Zhang, Kadi L. Saar, Jacqueline A. Carozza, Justin L. P. Benesch and Tuomas P. J. Knowles. 'Real-Time Intrinsic Fluorescence Visualization and Sizing of Proteins and Protein Complexes in Microfluidic Devices'. In: *Analytical Chemistry* 90.6 (20th Mar. 2018), pp. 3849–3855. ISSN: 0003-2700, 1520-6882. DOI: 10.1021/acs.analchem.7b04523 Citation on p. **39**.

[112] Kadi L. Saar, Quentin Peter, Thomas Müller, Pavan K. Challa, Therese W. Herling and Tuomas P. J. Knowles. 'Rapid Two-Dimensional Characterisation of Proteins in Solution'. In: *Microsystems & Nanoengineering* 5.1 (Dec. 2019), p. 33. ISSN: 2055-7434. DOI: 10.1038/s41378-019-0072-3 Citation on p. **40**.

[113] Philipp Schulze, Martin Ludwig, Frank Kohler and Detlev Belder. 'Deep UV Laser-Induced Fluorescence Detection of Unlabeled Drugs and Proteins in Microchip Electrophoresis'. In: *Analytical Chemistry* 77.5 (Mar. 2005), pp. 1325–1329. ISSN: 0003-2700, 1520-6882. DOI: 10.1021/ac048596m
Citation on p. **40**.

[114] Dorothea Pinotsi, Alexander K. Buell, Christopher M. Dobson, Gabriele S. Kaminski Schierle and Clemens F. Kaminski. 'A Label-Free, Quantitative Assay of Amyloid Fibril Growth Based on Intrinsic Fluorescence'. In: *ChemBioChem* 14.7 (10th May 2013), pp. 846–850. ISSN: 14394227. DOI: 10.1002/cbic.201300103 Citation on p. **40**.

[115] Yvette Mattley. 'Quantifying Protein Concentration Using UV Absorbance Measured by the Ocean HDX Spectrometer'. In: (), p. 4 Citation on p. **40**.

[116] Arne Meyer, Christian Betzel and Marc Pusey. 'Latest Methods of Fluorescence-Based Protein Crystal Identification'. In: *Acta Crystallographica Section F Structural Biology Communications* 71.2 (1st Feb. 2015), pp. 121–131. ISSN: 2053-230X. DOI: 10.1107/S2053230X15000114 Citation on p. **40**.

[117] Krishanu Ray, Henryk Szmacinski and Joseph R. Lakowicz. 'Enhanced Fluorescence of Proteins and Label-Free Bioassays Using Aluminum Nanostructures'. In: *Analytical Chemistry* 81.15 (Aug. 2009), pp. 6049–6054. ISSN: 0003-2700, 1520-6882. DOI: 10.1021/ac900263k
Citations on pp. **41, 42**.

[118] Atsushi Ono, Masakazu Kikawada, Rentaro Akimoto, Wataru Inami and Yoshimasa Kawata. 'Fluorescence Enhancement with Deep-Ultraviolet Surface Plasmon Excitation'. In: *Optics Express* 21.15 (29th July 2013), p. 17447. ISSN: 1094-4087. DOI: 10.1364/OE.21.017447 Citation on p. **41**.

[119] Ignacy Gryczynski, Joanna Malicka, Zygmunt Gryczynski, Kazimierz Nowaczyk and Joseph R. Lakowicz. 'Ultraviolet Surface Plasmon-Coupled Emission Using Thin Aluminum Films'. In: *Analytical Chemistry* 76.14 (1st July 2004), pp. 4076–4081. ISSN: 0003-2700, 1520-6882. DOI: 10.1021/ac040004c Citation on p. **41**.

[120] Matías Möller and Ana Denicola. 'Protein Tryptophan Accessibility Studied by Fluorescence Quenching'. In: *Biochemistry and Molecular Biology Education* 30.3 (May 2002), pp. 175–178. ISSN: 14708175, 15393429. DOI: 10.1002/bmb.2002.494030030035 Citation on p. **41**.

[121] T. Truong, R. Bersohn, P. Brumer, C.K. Luk and T. Tao. 'Effect of pH on the Phosphorescence of Tryptophan, Tyrosine, and Proteins'. In: *Journal of Biological Chemistry* 242.12 (June 1967), pp. 2979–2985. ISSN: 00219258. DOI: 10.1016/S0021-9258(18)99601-8 Citation on p. **41**.

[122] S Akbar, K Sreeramulu and Hari C Sharma. 'Tryptophan Fluorescence Quenching as a Binding Assay to Monitor Protein Conformation Changes in the Membrane of Intact Mitochondria'. In: *J Bioenerg Biomembr* (2015), p. 7 Citation on p. **41**.

[123] J. R. Albani. 'Origin of Tryptophan Fluorescence Lifetimes Part 1: Fluorescence Lifetimes Origin of Tryptophan Free in Solution'. In: *Journal of Fluorescence* 24.1 (Jan. 2014), pp. 93–104. ISSN: 1053-0509, 1573-4994. DOI: 10.1007/s10895-013-1277-8 Citation on p. **41**.

[124] J. R. Albani. 'Origin of Tryptophan Fluorescence Lifetimes. Part 2: Fluorescence Lifetimes Origin of Tryptophan in Proteins'. In: *Journal of Fluorescence* 24.1 (Jan. 2014), pp. 105–117. ISSN: 1053-0509, 1573-4994. DOI: 10.1007/s10895-013-1274-y Citation on p. **41**.

[125] Frank W. Putnam. *The Plasma Proteins: Structure, Function, and Genetic Control*. 2d. ed. New York: Academic Press, 1975. 1 p. ISBN: 978-0-12-568401-9

Citations on pp. **42, 81, 102**.

[126] Oliver A. Schmidt, Tijmen G. Euser and Philip St.J. Russell. 'Mode-Based Microparticle Conveyor Belt in Air-Filled Hollow-Core Photonic Crystal Fiber'. In: *Optics Express* 21.24 (2nd Dec. 2013), p. 29383. ISSN: 1094-4087. DOI: 10.1364/OE.21.029383 Citations on pp. **43, 46**.

[127] Andrei Ruskuc, Philipp Koehler, Marius A. Weber, Ana Andres-Arroyo, Michael H. Frosz, Philip St.J. Russell and Tijmen G. Euser. 'Excitation of Higher-Order Modes in Optofluidic Photonic Crystal Fiber'. In: *Optics Express* 26.23 (12th Nov. 2018), p. 30245. ISSN: 1094-4087. DOI: 10.1364/OE.26.030245 Citation on p. **43**.

[128] Ruth J. McQuitty, Sarah Unterkofler, Tijmen G. Euser, Philip St.J. Russell and Peter J. Sadler. 'Rapid Screening of Photoactivatable Metallodrugs: Photonic Crystal Fibre Microflow Reactor Coupled to ESI Mass Spectrometry'. In: *RSC Advances* 7.59 (2017), pp. 37340–37348. ISSN: 2046-2069. DOI: 10.1039/C7RA06735F Citation on p. **43**.

[129] S. Unterkofler, R. J. McQuitty, T. G. Euser, N. J. Farrer, P. J. Sadler and P. St.J. Russell. 'Microfluidic Integration of Photonic Crystal Fibers for Online Photochemical Reaction Analysis'. In: *Optics Letters* 37.11 (1st June 2012), p. 1952. ISSN: 0146-9592, 1539-4794. DOI: 10.1364/OL.37.001952
Citation on p. **43**.

[130] Ana M. Cubillas, Sarah Unterkofler, Tijmen G. Euser, Bastian J. M. Etzold, Anita C. Jones, Peter J. Sadler, Peter Wasserscheid and Philip St.J. Russell. 'Photonic Crystal Fibres for Chemical Sensing and Photochemistry'. In: *Chemical Society Reviews* 42.22 (2013), p. 8629. ISSN: 0306-0012, 1460-4744. DOI: 10.1039/c3cs60128e Citations on pp. **43, 62, 63, 67, 72**.

[131] Maksim Skorobogatiy and Jianke Yang. *Fundamentals of Photonic Crystal Guiding*. Cambridge: Cambridge University Press, 2008. ISBN: 978-0-511-57522-8. DOI: 10.1017/CBO9780511575228
Citations on pp. **43, 60**.

[132] Frédéric Zolla, ed. *Foundations of Photonic Crystal Fibres*. London : Singapore ; Hackensack, N.J: Imperial college Press : Distributed by World Scientific, 2005. 343 pp. ISBN: 978-1-86094-507-6 Citations on pp. **43, 60, 61**.

[133] F. Poli, A. Cucinotta and Stefano Selleri. *Photonic Crystal Fibers: Properties and Applications*. Springer Series in Materials Science 102. Dordrecht: Springer, 2007. 233 pp. ISBN: 978-1-4020-6325-1 Citation on p. **43**.

[134] Liyang Shao, Zhengyong Liu, Jie Hu, Dinusha Gunawardena and Hwa-Yaw Tam. 'Optofluidics in Microstructured Optical Fibers'. In: *Micromachines* 9.4 (24th Mar. 2018), p. 145. ISSN: 2072-666X. DOI: 10.3390/mi9040145 Citation on p. **43**.

[135] Gareth Owen Scott Williams. 'Photochemical Kinetics and Fluorescence Spectroscopy in Photonic Crystal Fibres'. The University of Edinburgh, 2013 Citation on p. **43**.

[136] Jocelyn Ssu-Yin Chen. 'Nanochemistry and Sensing in Photonic Crystal Fibers'. PhD thesis. Naturwissenschaftliche Fakultät der Friedrich-Alexander-Universität Erlangen-Nürnberg, 2010. 149 pp.
Citation on p. **43**.

[137] Philipp Koehler. 'Optofluidic Microreactors for Advanced Photocatalysis'. PhD thesis. University of Cambridge, 26th Sept. 2019. 199 pp.
Citation on p. **43**.

[138] Sebastian Wolf, Timea Frosch, Juergen Popp, Mathias W. Pletz and Torsten Frosch. 'Highly Sensitive Detection of the Antibiotic Ciprofloxacin by Means of Fiber Enhanced Raman Spectroscopy'. In: *Molecules* 24.24 (10th Dec. 2019), p. 4512. ISSN: 1420-3049. DOI: 10.3390/molecules24244512 Citation on p. **43**.

[139] Stanislav O. Konorov, Christopher J. Addison, H. Georg Schulze, Robin F. B. Turner and Michael W. Blades. 'Hollow-Core Photonic Crystal Fiber-Optic Probes for Raman Spectroscopy'. In: *Optics Letters* 31.12 (15th June 2006), p. 1911. ISSN: 0146-9592, 1539-4794. DOI: 10.1364/OL.31.001911 Citation on p. **43**.

[140] Di Yan, Jürgen Popp and Torsten Frosch. 'Analysis of Fiber-Enhanced Raman Gas Sensing Based on Raman Chemical Imaging'. In: *Analytical Chemistry* 89.22 (21st Nov. 2017), pp. 12269–12275. ISSN: 0003-2700, 1520-6882. DOI: 10.1021/acs.analchem.7b03209 Citation on p. **43**.

[141] A. Kudlinski, A. Cassez, O. Vanvincq, D. Septier, A. Pastre, R. Habert, K. Baudelle, M. Douay, V. Mytskaniuk, V. Tsvirkun, H. Rigneault and G. Bouwmans. 'Double Clad Tubular Anti-Resonant Hollow Core Fiber for Nonlinear Microendoscopy'. In: *Optics Express* 28.10 (11th May 2020), p. 15062. ISSN: 1094-4087. DOI: 10.1364/OE.389084 Citation on p. **43**.

[142] Wei Jin, Yingchun Cao, Fan Yang and Hoi Lut Ho. 'Ultra-Sensitive All-Fibre Photothermal Spectroscopy with Large Dynamic Range'. In: *Nature Communications* 6.1 (Nov. 2015), p. 6767. ISSN: 2041-1723. DOI: 10.1038/ncomms7767 Citation on p. **43**.

[143] Matías Calcerrada, Carmen García-Ruiz and Miguel González-Herráez. 'Chemical and Biochemical Sensing Applications of Microstructured Optical Fiber-Based Systems: Chemical and Biochemical Sensing Applications . . .' In: *Laser & Photonics Reviews* 9.6 (Nov. 2015), pp. 604–627. ISSN: 18638880. DOI: 10.1002/lpor.201500045 Citation on p. **43**.

[144] Sarah Unterkofler. 'Optofluidic Photonic Crystal Fibres for Biomedical Research in Fibra'. PhD thesis. Dissertation im Fachbereich Physik der Friedrich-Alexander-Universität Erlangen-Nürnberg, 2013. 154 pp. Citations on pp. **43, 46, 60, 67, 72, 80**.

[145] Valerii Ter-Mikirtychev. *Fundamentals of Fiber Lasers and Fiber Amplifiers*. Vol. 181. Springer Series in Optical Sciences. Cham: Springer International Publishing, 2014. ISBN: 978-3-319-02337-3. DOI: 10.1007/978-3-319-02338-0 Citation on p. **43**.

[146] Adrian Love. *Hollow Core Optical Fibre Based Gas Discharge Laser Systems*. Springer Theses. Cham: Springer International Publishing, 2018. ISBN: 978-3-319-93969-8. DOI: 10.1007/978-3-319-93970-4 Citation on p. **43**.

[147] Ronny Förster, Stefan Weidlich, Mona Nissen, Torsten Wieduwilt, Jens Kobelke, Aaron M. Goldfain, Timothy K. Chiang, Rees F. Garmann, Vinothan N. Manoharan, Yoav Lahini and Markus A. Schmidt. 'Tracking and Analyzing the Brownian Motion of Nano-objects Inside Hollow Core Fibers'. In: *ACS Sensors* 5.3 (27th Mar. 2020), pp. 879–886. ISSN: 2379-3694, 2379-3694. DOI: 10.1021/acssensors.0c00339

Citations on pp. **43, 44, 244**.

[148] Jonathan Knight. 'Photonic Crystal and Microstructured Fibers: Making Fibers Better by Leaving Bits Out'. In: *Optical Fiber Communication Conference/National Fiber Optic Engineers Conference 2011*. Optical Fiber Communication Conference. Los Angeles, California: OSA, 2011, OTuJ4. ISBN: 978-1-55752-906-0. DOI: 10.1364/OFC.2011.OTuJ4

Citations on pp. **44, 62**.

[149] Sanli Faez, Yoav Lahini, Stefan Weidlich, Rees F. Garmann, Katrin Wondraczek, Matthias Zeisberger, Markus A. Schmidt, Michel Orrit and Vinothan N. Manoharan. 'Fast, Label-Free Tracking of Single Viruses and Weakly Scattering Nanoparticles in a Nanofluidic Optical Fiber'. In: *ACS Nano* 9.12 (22nd Dec. 2015), pp. 12349–12357. ISSN: 1936-0851, 1936-086X. DOI: 10.1021/acsnano.5b05646 Citation on p. **44**.

[150] Angela Leung, P. Mohana Shankar and Raj Mutharasan. 'A Review of Fiber-Optic Biosensors'. In: *Sensors and Actuators B: Chemical* 125.2 (Aug. 2007), pp. 688–703. ISSN: 09254005. DOI: 10.1016/j.snb.2007.03.010

Citation on p. **44**.

[151] Sanli Faez, Pierre Türschmann, Harald R. Haakh, Stephan Götzinger and Vahid Sandoghdar. 'Coherent Interaction of Light and Single Molecules in a Dielectric Nanoguide'. In: *Physical Review Letters* 113.21 (18th Nov. 2014), p. 213601. ISSN: 0031-9007, 1079-7114. DOI: 10.1103/PhysRevLett.113.213601 Citation on p. **44**.

[152] Torsten Wieduwilt, Ronny Förster, Mona Nissen, Jens Kobelke and Markus A. Schmidt. 'Characterization of Diffusing Sub-10 Nm Nano-Objects Using Single Anti-Resonant Element Optical Fibers'. In: *Nature Communications* 14.1 (5th June 2023), p. 3247. ISSN: 2041-1723. DOI: 10.1038/s41467-023-39021-3 Citation on p. **44**.

[153] Vidhu S. Tiwari, Altaf Khetani, Majid Naji and Hanan Anis. 'Study of Surface Enhanced Raman Scattering (SERS) within Hollow Core Photonic Crystal Fiber'. In: *2009 IEEE Sensors*. 2009 IEEE Sensors. Christchurch, New Zealand: IEEE, Oct. 2009, pp. 367–370. ISBN: 978-1-4244-4548-6. DOI: 10.1109/ICSENS.2009.5398238 Citation on p. **45**.

[154] Altaf Khetani, Ali Momenpour, Emilio I. Alarcon and Hanan Anis. 'Hollow Core Photonic Crystal Fiber for Monitoring Leukemia Cells Using Surface Enhanced Raman Scattering (SERS)'. In: *Biomedical Optics Express* 6.11 (1st Nov. 2015), p. 4599. ISSN: 2156-7085, 2156-7085. DOI: 10.1364/BOE.6.004599 Citation on p. **45**.

[155] 'Diagnostic Sensing of Specific Proteins in Breast Cancer Cells Using Hollow-Core Photonic Crystal Fiber'. In: E. Y. K. Ng, U. Rajendra Acharya, Rangaraj M. Rangayyan and Jasjit S. Suri. *Multimodality Breast Imaging: Diagnosis and Treatment*. Society of Photo-Optical Instrumentation Engineers, 2013. ISBN: 978-0-8194-9294-4. DOI: 10.1117/3.1000499.ch17 Citation on p. **45**.

[156] Saraswathi Padmanabhan, Vengalathunadakal K. Shinoj, Vadakke M. Murukeshan and Parasuraman Padmanabhan. 'Highly Sensitive Optical Detection of Specific Protein in Breast Cancer Cells Using Microstructured Fiber in Extremely Low Sample Volume'. In: *Journal of Biomedical Optics* 15.1 (2010), p. 017005. ISSN: 10833668. DOI: 10.1117/1.3302810 Citations on pp. **45, 53**.

[157] David G. Grier. 'A Revolution in Optical Manipulation'. In: *Nature* 424.6950 (Aug. 2003), pp. 810–816. ISSN: 0028-0836, 1476-4687. DOI: 10.1038/nature01935 Citation on p. **45**.

[158] Philip H. Jones, Onofrio M. Maragò and Giovanni Volpe. *Optical Tweezers: Principles and Applications*. Cambridge: Cambridge University Press, 2015. 547 pp. ISBN: 978-1-107-05116-4 Citation on p. **45**.

[159] V. Garcés-Chávez, D. McGloin, H. Melville, W. Sibbett and K. Dholakia. 'Simultaneous Micromanipulation in Multiple Planes Using a Self-Reconstructing Light Beam'. In: *Nature* 419.6903 (Sept. 2002), pp. 145–147. ISSN: 0028-0836, 1476-4687. DOI: 10.1038/nature01007 Citation on p. **45**.

[160] Dhawal Choudhary, Alessandro Mossa, Milind Jadhav and Ciro Cecconi. 'Bio-Molecular Applications of Recent Developments in Optical Tweezers'. In: *Biomolecules* 9.1 (11th Jan. 2019), p. 23. ISSN: 2218-273X. DOI: 10.3390/biom9010023 Citation on p. **45**.

[161] Jochen Guck, Revathi Ananthakrishnan, Hamid Mahmood, Tess J. Moon, C. Casey Cunningham and Josef Käs. 'The Optical Stretcher: A Novel Laser Tool to Micromanipulate Cells'. In: *Biophysical Journal* 81.2 (Aug. 2001), pp. 767–784. ISSN: 00063495. DOI: 10.1016/S0006-3495(01)75740-2 Citations on pp. **45, 47**.

[162] Zhanshi Yao, Ching Chi Kwan and Andrew W. Poon. 'An Optofluidic "Tweeze-and-Drag" Cell Stretcher in a Microfluidic Channel'. In: *Lab on a Chip* 20.3 (2020), pp. 601–613. ISSN: 1473-0197, 1473-0189. DOI: 10.1039/C9LC01026B Citation on p. **45**.

[163] Totaro. Imasaka, Yuji. Kawabata, Takashi. Kaneta and Yasunori. Ishidzu. 'Optical Chromatography'. In: *Analytical Chemistry* 67.11 (1st June 1995), pp. 1763–1765. ISSN: 0003-2700. DOI: 10.1021/ac00107a003 Citation on p. **46**.

[164] Takashi Kaneta, Yasunori Ishidzu, Naoki Mishima and Totaro Imasaka. 'Theory of Optical Chromatography'. In: *Analytical Chemistry* 69.14 (July 1997), pp. 2701–2710. ISSN: 0003-2700, 1520-6882. DOI: 10.1021/ac970079z Citation on p. **46**.

[165] Alex V. Terray, Sean J. Hart, Katherine L. Kuhn and Jonathan Arnold. 'Optical Chromatography in a PDMS Microfluidic Environment'. In: Optical Science and Technology, the SPIE 49th Annual Meeting. Ed. by Kishan Dholakia and Gabriel C. Spalding. Denver, CO, 18th Oct. 2004, p. 695. DOI: 10.1117/12.557890 Citation on p. **46**.

[166] P. C. Ashok, R. F. Marchington, M. Mazilu, T. F. Krauss and K. Dholakia. 'Towards Integrated Optical Chromatography Using Photonic Crystal Fiber'. In: SPIE NanoScience + Engineering. Ed. by Kishan Dholakia and Gabriel C. Spalding. San Diego, CA, 20th Aug. 2009, 74000R. DOI: 10.1117/12.825933 Citation on p. **46**.

[167] P. C. Ashok, R. F. Marchington, P. Mthunzi, T. F. Krauss and K. Dholakia. 'Optical Chromatography Using a Photonic Crystal Fiber with On-Chip Fluorescence Excitation'. In: *Optics Express* 18.6 (15th Mar. 2010), p. 6396. ISSN: 1094-4087. DOI: 10.1364/OE.18.006396 Citation on p. **46**.

[168] Jun Makihara, Takashi Kaneta and Totaro Imasaka. 'Optical Chromatography Size Determination by Eluting Particles'. In: (1999), p. 7 Citation on p. **46**.

[169] Sean J. Hart, Alex Terray, Jonathan Arnold and Tomasz A. Leski. 'Sample Concentration Using Optical Chromatography'. In: *Optics Express* 15.5 (5th Mar. 2007), p. 2724. ISSN: 1094-4087. DOI: 10.1364/OE.15.002724 Citation on p. **46**.

[170] Alex Terray, Joseph D. Taylor and Sean J. Hart. 'Cascade Optical Chromatography for Sample Fractionation'. In: *Biomicrofluidics* 3.4 (Dec. 2009), p. 044106. ISSN: 1932-1058. DOI: 10.1063/1.3262415 Citation on p. **46**.

[171] A. Terray, C. G. Hebert and S. J. Hart. 'Optical Chromatographic Sample Separation of Hydrodynamically Focused Mixtures'. In: *Biomicrofluidics* 8.6 (Nov. 2014), p. 064102. ISSN: 1932-1058. DOI: 10.1063/1.4901824 Citation on p. **46**.

[172] Yuzhi Shi, Sha Xiong, Lip Ket Chin, Jingbo Zhang, Wee Ser, Jiuhui Wu, Tianning Chen, Zhenchuan Yang, Yilong Hao, Bo Liedberg, Peng Huat Yap, Din Ping Tsai, Cheng-Wei Qiu and Ai Qun Liu. 'Nanometer-Precision Linear Sorting with Synchronized Optofluidic Dual Barriers'. In: *Science Advances* 4.1 (Jan. 2018), eaao0773. ISSN: 2375-2548. DOI: 10.1126/sciadv.aao0773 Citation on p. **46**.

[173] Yuzhi Shi, Sha Xiong, Lip Ket Chin, Jingbo Zhang, Wee Ser, Jiuhui Wu, Tianning Chen, Zhenchuan Yang, Yilong Hao, Bo Liedberg, Peng Huat Yap, Din Ping Tsai, Cheng-Wei Qiu and Ai Qun Liu. 'Nanometer-Precision Linear Sorting with Synchronized Optofluidic Dual Barriers. Supplementary'. In: *Science Advances* 4.1 (Jan. 2018), eaao0773. ISSN: 2375-2548. DOI: 10.1126/sciadv.aao0773 Citation on p. **46**.

[174] Sarah Unterkofler, Martin K. Garbos, Tijmen G. Euser and Philip St. J. Russell. 'Long-Distance Laser Propulsion and Deformation-Monitoring of Cells in Optofluidic Photonic Crystal Fiber'. In: *Journal of Biophotonics* 6.9 (Sept. 2013), pp. 743–752. ISSN: 1864063X. DOI: 10.1002/jbio.201200180 Citation on p. **46**.

[175] Michael J. Renn, Robert Pastel and Heather J. Lewandowski. 'Laser Guidance and Trapping of Mesoscale Particles in Hollow-Core Optical Fibers'. In: *Physical Review Letters* 82.7 (15th Feb. 1999), pp. 1574–1577. ISSN: 0031-9007, 1079-7114. DOI: 10.1103/PhysRevLett.82.1574
Citation on p. **46**.

[176] F. Benabid, J. C. Knight and P. St. J. Russell. 'Particle Levitation and Guidance in Hollow-Core Photonic Crystal Fiber'. In: *Optics Express* 10.21 (21st Oct. 2002), p. 1195. ISSN: 1094-4087. DOI: 10.1364/OE.10.001195
Citation on p. **46**.

[177] T. G. Euser, M. K. Garbos, J. S. Y. Chen and P. St.J. Russell. 'Precise Balancing of Viscous and Radiation Forces on a Particle in Liquid-Filled Photonic Bandgap Fiber'. In: *Optics Letters* 34.23 (1st Dec. 2009), p. 3674. ISSN: 0146-9592, 1539-4794. DOI: 10.1364/OL.34.003674 Citation on p. **47**.

[178] Oliver Otto, Philipp Rosendahl, Alexander Mietke, Stefan Golfier, Christoph Herold, Daniel Klaue, Salvatore Girardo, Stefano Pagliara, Andrew Ekpenyong, Angela Jacobi, Manja Wobus, Nicole Töpfner, Ulrich F Keyser, Jörg Mansfeld, Elisabeth Fischer-Friedrich and Jochen Guck. 'Real-Time Deformability Cytometry: On-the-Fly Cell Mechanical Phenotyping'. In: *Nature Methods* 12.3 (Mar. 2015), pp. 199–202. ISSN: 1548-7091, 1548-7105. DOI: 10.1038/nmeth.3281 Citation on p. **47**.

[179] Ahmad Ahsan Nawaz, Marta Urbanska, Maik Herbig, Martin Nötzel, Martin Kräter, Philipp Rosendahl, Christoph Herold, Nicole Toepfner, Markéta Kubánková, Ruchi Goswami, Shada Abuhattum, Felix Reichel, Paul Müller, Anna Taubenberger, Salvatore Girardo, Angela Jacobi and Jochen Guck. 'Intelligent Image-Based Deformation-Assisted Cell Sorting with Molecular Specificity'. In: *Nature Methods* 17.6 (June 2020), pp. 595–599. ISSN: 1548-7091, 1548-7105. DOI: 10.1038/s41592-020-0831-y
Citation on p. **47**.

[180] Philipp Rosendahl, Katarzyna Plak, Angela Jacobi, Martin Kraeter, Nicole Toepfner, Oliver Otto, Christoph Herold, Maria Winzi, Maik Herbig, Yan Ge, Salvatore Girardo, Katrin Wagner, Buzz Baum and Jochen Guck. 'Real-Time Fluorescence and Deformability Cytometry'. In: *Nature Methods* 15.5 (May 2018), pp. 355–358. ISSN: 1548-7091, 1548-7105. DOI: 10.1038/nmeth.4639 Citation on p. **47**.

[181] M. K. Garbos, T. G. Euser and P. St. J. Russell. 'Optofluidic Immobility of Particles Trapped in Liquid-Filled Hollow-Core Photonic Crystal Fiber'. In: *Optics Express* 19.20 (Sept. 2011), pp. 19643–19652. DOI: 10.1364/OE.19.019643 Citation on p. **47**.

[182] Martin Garbos. 'LASER-Propulsion of Microparticles in Liquid-Filled Hollow-Core Photonic-Crystal Fibers. Going against the Flow'. PhD thesis. Naturwissenschaftliche Fakultät der Friedrich-Alexander-Universität Erlangen-Nürnberg, 2011. 121 pp.
Citation on p. **47**.

[183] Oliver Alexander Schmidt. 'Dynamics of Optically Trapped Microparticles in Hollow-Core Photonic Crystal Fibers'. PhD thesis. Naturwissenschaftliche Fakultät der Friedrich-Alexander-Universität Erlangen-Nürnberg, 2014. 144 pp. Citation on p. **47**.

[184] Richard Zeltner. 'Optical Trapping in Liquid-Filled Hollow-Core Photonic Crystal Fibers. Optische Fallen in Flüssigkeitsgefüllten Photonischen Hohlkernfasern'. PhD thesis. Naturwissenschaftliche Fakultät der Friedrich-Alexander-Universität Erlangen-Nürnberg, Sept. 2018. 113 pp.
Citations on pp. **47, 62**.

[185] D. S. Bykov, O. A. Schmidt, T. G. Euser and P. St. J. Russell. 'Flying Particle Sensors in Hollow-Core Photonic Crystal Fibre'. In: *Nature Photonics* 9.7 (July 2015), pp. 461–465. ISSN: 1749-4885, 1749-4893. DOI: 10.1038/nphoton.2015.94 Citation on p. **47**.

[186] O. A. Schmidt, M. K. Garbos, T. G. Euser and P. St. J. Russell. 'Reconfigurable Optothermal Microparticle Trap in Air-Filled Hollow-Core Photonic Crystal Fiber'. In: *Physical Review Letters* 109.2 (9th July 2012), p. 024502. ISSN: 0031-9007, 1079-7114. DOI: 10.1103/PhysRevLett.109.024502
Citation on p. **47**.

[187] Mona Nissen, Brenda Doherty, Jonas Hamperl, Jens Kobelke, Karina Weber, Thomas Henkel and Markus Schmidt. 'UV Absorption Spectroscopy in Water-Filled Antiresonant Hollow Core Fibers for Pharmaceutical Detection'. In: *Sensors* 18.2 (6th Feb. 2018), p. 478. ISSN: 1424-8220. DOI: 10.3390/s18020478 Citations on pp. **47, 48**.

[188] Jiawen Li, Heike Ebendorff-Heidepriem, Brant C. Gibson, Andrew D. Greentree, Mark R. Hutchinson, Peipei Jia, Roman Kostecki, Guozhen Liu, Antony Orth, Martin Ploschner, Erik P. Schartner, Stephen C. Warren-Smith, Kaixin Zhang, Georgios Tsiminis and Ewa M. Goldys. 'Perspective: Biomedical Sensing and Imaging with Optical Fibers—Innovation through Convergence of Science Disciplines'. In: *APL Photonics* 3.10 (Oct. 2018), p. 100902. ISSN: 2378-0967. DOI: 10.1063/1.5040861

Citation on p. **49**.

[189] Arif E. Cetin and Seda Nur Topkaya. 'Photonic Crystal and Plasmonic Nanohole Based Label-Free Biodetection'. In: *Biosensors and Bioelectronics* 132 (May 2019), pp. 196–202. ISSN: 09565663. DOI: 10.1016/j.bios.2019.02.047 Citations on pp. **49, 50**.

[190] Yonghao Liu, Weidong Zhou and Yuze Sun. 'Optical Refractive Index Sensing Based on High-Q Bound States in the Continuum in Free-Space Coupled Photonic Crystal Slabs'. In: *Sensors* 17.8 (11th Aug. 2017), p. 1861. ISSN: 1424-8220. DOI: 10.3390/s17081861 Citation on p. **49**.

[191] Stefan A. Maier. *Plasmonics: Fundamentals and Applications*. New York: Springer, 2007. 223 pp. ISBN: 978-0-387-33150-8 Citations on pp. **49, 50**.

[192] Thomas L. McMeekin, Merton L. Groves and Norbert J. Hipp. 'Refractive Indices of Amino Acids, Proteins, and Related Substances'. In: *Amino Acids and Serum Proteins*. Ed. by Jacob A. Stekol. Vol. 44. Washington, D.C.: American Chemical Society, Jan. 1964, pp. 54–66. ISBN: 978-0-8412-0045-6. DOI: 10.1021/ba-1964-0044.ch004 Citation on p. **49**.

[193] T. Cole, A. Kathman, S. Koszelak and A. Mcpherson. 'Determination of Local Refractive Index for Protein and Virus Crystals in Solution by Mach-Zehnder Interferometry'. In: *Analytical Biochemistry* 231.1 (1st Oct. 1995), pp. 92–98. ISSN: 0003-2697. DOI: 10.1006/abio.1995.1507

Citation on p. **49**.

[194] M.C. Estevez, M. Alvarez and L.M. Lechuga. 'Integrated Optical Devices for Lab-on-a-Chip Biosensing Applications'. In: *Laser & Photonics Reviews* 6.4 (16th July 2012), pp. 463–487. ISSN: 18638880. DOI: 10.1002/lpor.201100025 Citation on p. **50**.

[195] Da-Shin Wang and Shih-Kang Fan. 'Microfluidic Surface Plasmon Resonance Sensors: From Principles to Point-of-Care Applications'. In: *Sensors* 16.8 (27th July 2016), p. 1175. ISSN: 1424-8220. DOI: 10.3390/s16081175 Citation on p. **50**.

[196] Jeffrey N. Anker, W. Paige Hall, Olga Lyandres, Nilam C. Shah, Jing Zhao and Richard P. Van Duyne. 'Biosensing with Plasmonic Nanosensors'. In: *Nature Materials* 7.6 (June 2008), pp. 442–453. ISSN: 1476-1122, 1476-4660. DOI: 10.1038/nmat2162 Citation on p. **50**.

[197] Heinz Raether. *Surface Plasmons: On Smooth and Rough Surfaces and on Gratings*. Springer Tracts in Modern Physics 111. Berlin: Springer, 1988. 136 pp. ISBN: 978-3-540-17363-2 Citation on p. **50**.

[198] Patrick Uebel. 'Metal Filled Optical Fibers. Photonics and Plasmonics at the Nanoscale'. Naturwissenschaftliche Fakultät der Friedrich-Alexander-Universität Erlangen-Nürnberg, 16th July 2013 Citation on p. **50**.

[199] Mohammad Al Mahfuz, Md. Anwar Hossain, Emranul Haque, Nguyen Hoang Hai, Yoshinori Namihira and Feroz Ahmed. 'A Bimetallic-Coated, Low Propagation Loss, Photonic Crystal Fiber Based Plasmonic Refractive Index Sensor'. In: *Sensors* 19.17 (1st Sept. 2019), p. 3794. ISSN: 1424-8220. DOI: 10.3390/s19173794 Citation on p. **50**.

[200] Oleksiy Krupin, Hamoudi Asiri, Chen Wang, R. Niall Tait and Pierre Berini. 'Biosensing Using Straight Long-Range Surface Plasmon Waveguides'. In: *Optics Express* 21.1 (14th Jan. 2013), p. 698. ISSN: 1094-4087. DOI: 10.1364/OE.21.000698 Citation on p. **50**.

[201] Zhengyong Li, Changrui Liao, Danni Chen, Jun Song, Wei Jin, Gang-Ding Peng, Feng Zhu, Ying Wang, Jun He and Yiping Wang. 'Label-Free Detection of Bovine Serum Albumin Based on an in-Fiber Mach-Zehnder Interferometric Biosensor'. In: *Optics Express* 25.15 (24th July 2017), p. 17105. ISSN: 1094-4087. DOI: 10.1364/OE.25.017105 Citation on p. **50**.

[202] Matteo Barozzi, Alex Manicardi, Armando Vannucci, Alessandro Candiani, Michele Sozzi, Maria Konstantaki, Stavros Pissadakis, Roberto Corradini, Stefano Selleri and Annamaria Cucinotta. 'Optical Fiber Sensors for Label-Free DNA Detection'. In: *Journal of Lightwave Technology* 35.16

(15th Aug. 2017), pp. 3461–3472. ISSN: 0733-8724, 1558-2213. DOI: 10.1109/JLT.2016.2607024 Citation on p. **51**.

[203] Timur Ermatov, Julia S. Skibina, Valery V. Tuchin and Dmitry A. Gorin. 'Functionalized Microstructured Optical Fibers: Materials, Methods, Applications'. In: *Materials* 13.4 (19th Feb. 2020), p. 921. ISSN: 1996-1944. DOI: 10.3390/ma13040921 Citation on p. **51**.

[204] Sergey A. Pidenko, Natalia A. Burmistrova, Pavel S. Pidenko, Andrey A. Shuvalov, Anastasiya A. Chibrova, Yulia S. Skibina and Irina Y. Goryacheva. 'Controlled Chemical Modification of the Internal Surface of Photonic Crystal Fibers for Application as Biosensitive Elements'. In: *Optical Materials* 60 (Oct. 2016), pp. 283–289. ISSN: 09253467. DOI: 10.1016/j.optmat.2016.07.046 Citation on p. **51**.

[205] Lars Rindorf, Jesper B. Jensen, Martin Dufva, Lars Hagsholm Pedersen, Poul Erik Høiby and Ole Bang. 'Photonic Crystal Fiber Long-Period Gratings for Biochemical Sensing'. In: *Optics Express* 14.18 (2006), p. 8224. ISSN: 1094-4087. DOI: 10.1364/OE.14.008224 Citation on p. **51**.

[206] Fabio Giovanardi, Annamaria Cucinotta, Andrea Rozzi, Roberto Corradini, Fetah Benabid, Lorenzo Rosa and Luca Vincetti. 'Hollow Core Inhibited Coupling Fibers for Biological Optical Sensing'. In: *Journal of Lightwave Technology* 37.11 (1st June 2019), pp. 2598–2604. ISSN: 0733-8724, 1558-2213. DOI: 10.1109/JLT.2019.2892077 Citation on p. **51**.

[207] F. Giovanardi, A. Cucinotta and Luca Vincetti. 'Inhibited Coupling Guiding Hollow Fibers for Label-Free DNA Detection'. In: *Optics Express* 25.21 (16th Oct. 2017), p. 26215. ISSN: 1094-4087. DOI: 10.1364/OE.25.026215 Citation on p. **51**.

[208] Timur Ermatov, Marina Novoselova, Julia Skibina, Andrey Machnev, Dmitry Gorin and Roman E. Noskov. 'Ultrasmooth, Biocompatible, and Removable Nanocoating for Hollow-Core Microstructured Optical Fibers'. In: *Optics Letters* 46.19 (1st Oct. 2021), p. 4828. ISSN: 0146-9592, 1539-4794. DOI: 10.1364/OL.436220 Citation on p. **52**.

[209] Pavel S. Pidenko, Dmitry V. Martynov, Anastasia A. Zanishevskaya and Natalia A. Burmistrova. 'The pH of Protein Solutions Effect on Microstructured Optical Fibers Transmission Spectrum'. In: *Proceedings of the Saratov Fall Meeting 2018: Optical and Nano-Technologies for Biology and*

Medicine. Ed. by Valery V. Tuchin and Elina A. Genina. Saratov, Russian Federation: SPIE, 3rd June 2019, p. 80. ISBN: 978-1-5106-2820-5. DOI: 10.1117/12.2523348 Citation on p. **52**.

[210] Priya R. Banerjee and Ashok A. Deniz. 'Shedding Light on Protein Folding Landscapes by Single-Molecule Fluorescence'. In: *Chem. Soc. Rev.* 43.4 (2014), pp. 1172–1188. ISSN: 0306-0012, 1460-4744. DOI: 10.1039/C3CS60311C Citation on p. **52**.

[211] Tanya M. Monro, Stephen Warren-Smith, Erik P. Schartner, Alexandre François, Sabrina Heng, Heike Ebendorff-Heidepriem and Shahraam Afshar. 'Sensing with Suspended-Core Optical Fibers'. In: *Optical Fiber Technology* 16.6 (Dec. 2010), pp. 343–356. ISSN: 10685200. DOI: 10.1016/j.yofte.2010.09.010 Citation on p. **53**.

[212] Yinlan Ruan, Tze Cheung Foo, Stephen Warren-Smith, Peter Hoffmann, Heike Ebendorff-Heidepriem and Tanya M Monro. 'Antibody Immobilization within Glass Microstructured Fibers: A Route to Sensitive and Selective Biosensors'. In: (2008) Citation on p. **53**.

[213] Erik P. Schartner, Heike Ebendorff-Heidepriem, Stephen C. Warren-Smith, Richard T. White and Tanya M. Monro. 'Driving down the Detection Limit in Microstructured Fiber - Based Chemical Dip Sensors'. In: *Sensors* 11.3 (4th Mar. 2011), pp. 2961–2971. ISSN: 1424-8220. DOI: 10.3390/s110302961 Citations on pp. **53, 145**.

[214] Yanyu Xiong, Skye Shepherd, Joseph Tibbs, Amanda Bacon, Weinan Liu, Lucas D. Akin, Takhmina Ayupova, Seemesh Bhaskar and Brian T. Cunningham. 'Photonic Crystal Enhanced Fluorescence: A Review on Design Strategies and Applications'. In: *Micromachines* 14.3 (17th Mar. 2023), p. 668. ISSN: 2072-666X. DOI: 10.3390/mi14030668 Citation on p. **53**.

[215] Yinlan Ruan, Erik P Schartner, Heike Ebendorff-Heidepriem, Peter Hoffmann and Tanya M Monro. 'Detection of Quantum-Dot Labeled Proteins Using Soft Glass Microstructured Optical Fibers'. In: (2007) Citations on pp. **53, 145**.

[216] Jens Meissner, Albert Prause, Bhuvnesh Bharti and Gerhard H. Findenegg. 'Characterization of Protein Adsorption onto Silica Nanoparticles: Influence of pH and Ionic Strength'. In: *Colloid and Polymer Science* 293.11 (Nov. 2015), pp. 3381–3391. ISSN: 0303-402X, 1435-1536. DOI: 10.1007/s00396-015-3754-x Citation on p. **54**.

[217] F. Vollmer, D. Braun, A. Libchaber, M. Khoshsima, I. Teraoka and S. Arnold. 'Protein Detection by Optical Shift of a Resonant Microcavity'. In: *Applied Physics Letters* 80.21 (27th May 2002), pp. 4057–4059. ISSN: 0003-6951, 1077-3118. DOI: 10.1063/1.1482797
Citation on p. **55**.

[218] Sean E. Lehman, Imali A. Mudunkotuwa, Vicki H. Grassian and Sarah C. Larsen. 'Nano – Bio Interactions of Porous and Nonporous Silica Nanoparticles of Varied Surface Chemistry: A Structural, Kinetic, and Thermodynamic Study of Protein Adsorption from RPMI Culture Medium'. In: *Langmuir* 32.3 (26th Jan. 2016), pp. 731–742. ISSN: 0743-7463, 1520-5827. DOI: 10.1021/acs.langmuir.5b03997 Citation on p. **55**.

[219] Herbert Venghaus and Norbert Grote, eds. *Fibre Optic Communication: Key Devices*. Vol. 161. Springer Series in Optical Sciences. Cham: Springer International Publishing, 2017. ISBN: 978-3-319-42365-4. DOI: 10.1007/978-3-319-42367-8 Citation on p. **58**.

[220] Francis Graham-Smith, Terry A. King and Dan Wilkins. *Optics and Photonics: An Introduction*. 2nd ed. Chichester, England ; Hoboken, NJ: J. Wiley, 2007. 506 pp. ISBN: 978-0-470-01783-8 Citations on pp. **58, 73**.

[221] Jörg Haus. *Optical Sensors: Basics and Applications*. 1st ed. Wiley, 27th Jan. 2010. ISBN: 978-3-527-40860-3. DOI: 10.1002/9783527629435
Citation on p. **58**.

[222] Tim Dallas and Purnendu K. Dasgupta. 'Light at the End of the Tunnel: Recent Analytical Applications of Liquid-Core Waveguides'. In: *TrAC Trends in Analytical Chemistry* 23.5 (May 2004), pp. 385–392. ISSN: 01659936. DOI: 10.1016/S0165-9936(04)00522-9 Citations on pp. **59, 192**.

[223] The Dow Chemical Company. *Technical Data Sheet for SYLGARD 184 Silicone Elastomer*. 2017 Citations on pp. **59, 189**.

[224] J. David Musgraves, Juejun Hu and Laurent Calvez, eds. *Springer Handbook of Glass*. Springer Handbooks. Cham: Springer International Publishing, 2019. ISBN: 978-3-319-93728-1. DOI: 10.1007/978-3-319-93728-1
Citation on p. **59**.

[225] David J. Griffiths. *Introduction to Electrodynamics*. Fourth edition. Cambridge, United Kingdom ; New York, NY: Cambridge University Press, 2018. ISBN: 978-1-108-42041-9 Citation on p. **60**.

[226] Torsten Fließbach. *Elektrodynamik*. 6. Aufl. Lehrbuch zur Theoretischen Physik 2. Berlin: Springer Spektrum, 2012. 375 pp. ISBN: 978-3-8274-3036-6
Citation on p. **60**.

[227] Chengli Wei, R. Joseph Weiblen, Curtis R. Menyuk and Jonathan Hu. 'Negative Curvature Fibers'. In: *Advances in Optics and Photonics* 9.3 (30th Sept. 2017), p. 504. ISSN: 1943-8206. DOI: 10.1364/AOP.9.000504
Citations on pp. **60, 71**.

[228] J. C. Knight, T. A. Birks, P. St. J. Russell and J. P. de Sandro. 'Properties of Photonic Crystal Fiber and the Effective Index Model'. In: *Journal of the Optical Society of America A* 15.3 (1st Mar. 1998), p. 748. ISSN: 1084-7529, 1520-8532. DOI: 10.1364/JOSAA.15.000748 Citation on p. **60**.

[229] Michael Bass, Virendra N. Mahajan and Optical Society of America, eds. *Handbook of Optics*. 3rd ed. New York: McGraw-Hill, 2010. 1 p. ISBN: 978-0-07-149889-0 978-0-07-163598-1 978-0-07-163604-9 978-0-07-149892-0 978-0-07-163606-3 978-0-07-163313-0
Citations on pp. **60, 61**.

[230] María L. Calvo and Vasudevan Lakshminarayanan, eds. *Optical Waveguides: From Theory to Applied Technologies*. Optical Science and Engineering 120. Boca Raton, FL: CRC Press, 2007. 401 pp. ISBN: 978-1-57444-698-2
Citation on p. **60**.

[231] Katsunari Okamoto. *Fundamentals of Optical Waveguides*. 2nd ed. Amsterdam and Boston: Elsevier, 2006. 561 pp. ISBN: 978-0-12-525096-2
Citation on p. **60**.

[232] Allan W. Snyder and J. D. Love. *Optical Waveguide Theory*. Science Paperbacks 190. London and New York: Chapman and Hall, 1983. 734 pp. ISBN: 978-0-412-09950-2 Citation on p. **60**.

[233] E. A. J. Marcatili and R. A. Schmeltzer. 'Hollow Metallic and Dielectric Waveguides for Long Distance Optical Transmission and Lasers'. In: *Bell System Technical Journal* 43.4 (July 1964), pp. 1783–1809. ISSN: 00058580. DOI: 10.1002/j.1538-7305.1964.tb04108.x Citations on pp. **60, 62**.

[234] Fei Yu. 'Hollow Core Negative Curvature Fibres'. University of Bath, 1st Nov. 2013. 140 pp. Citations on pp. **60, 61**.

[235] Boris T Kuhlmey. 'Theoretical and Numerical Investigation of the Physics of Microstructured Optical Fibres'. Department of Theoretical Physics at the University of Sydney, Australia, and Université de Droit, d'Économie et des Sciences d'Aix-Marseille, France, June 2004. 204 pp.
Citation on p. **60**.

[236] Eli Yablonovitch. 'Inhibited Spontaneous Emission in Solid-State Physics and Electronics'. In: *Physical Review Letters* 58.20 (18th May 1987), pp. 2059–2062. ISSN: 0031-9007. DOI: 10.1103/PhysRevLett.58.2059
Citation on p. **62**.

[237] Sajeev John. 'Strong Localization of Photons in Certain Disordered Dielectric Superlattices'. In: *Physical Review Letters* 58.23 (8th June 1987), pp. 2486–2489. ISSN: 0031-9007. DOI: 10.1103/PhysRevLett.58.2486
Citation on p. **62**.

[238] F. Benabid, P. J. Roberts, F. Couny and P. S. Light. 'Light and Gas Confinement in Hollow-Core Photonic Crystal Fibre Based Photonic Microcells'. In: *Journal of the European Optical Society: Rapid Publications* 4 (21st Jan. 2009), p. 09004. ISSN: 1990-2573. DOI: 10.2971/jeos.2009.09004
Citation on p. **63**.

[239] Eli Yablonovitch. 'Photonic Crystals: Semiconductors of Light'. In: *Scientific American* 285.6 (Dec. 2001), pp. 46–51, 54–55. ISSN: 1946-7087
Citation on p. **64**.

[240] Jean Pol Vigneron and Priscilla Simonis. 'Natural Photonic Crystals'. In: *Physica B: Condensed Matter* 407.20 (Oct. 2012), pp. 4032–4036. ISSN: 09214526. DOI: 10.1016/j.physb.2011.12.130 Citation on p. **64**.

[241] J. V. Sanders. 'Colour of Precious Opal'. In: *Nature* 204.4964 (Dec. 1964), pp. 1151–1153. ISSN: 0028-0836, 1476-4687. DOI: 10.1038/2041151a0
Citation on p. **64**.

[242] Yuanjin Zhao, Luoran Shang, Yao Cheng and Zhongze Gu. 'Spherical Colloidal Photonic Crystals'. In: *Accounts of Chemical Research* 47.12 (16th Dec. 2014), pp. 3632–3642. ISSN: 0001-4842, 1520-4898. DOI: 10.1021/ar500317s
Citations on pp. **64, 244**.

[243] Tural Khudiyev, Tamer Dogan and Mehmet Bayindir. 'Biomimicry of Multifunctional Nanostructures in the Neck Feathers of Mallard (Anas

Platyrhynchos L.) Drakes'. In: *Scientific Reports* 4.1 (May 2015), p. 4718. ISSN: 2045-2322. DOI: 10.1038/srep04718 Citation on p. **64**.

[244] J. Zi, X. Yu, Y. Li, X. Hu, C. Xu, X. Wang, X. Liu and R. Fu. 'Coloration Strategies in Peacock Feathers'. In: *Proceedings of the National Academy of Sciences* 100.22 (28th Oct. 2003), pp. 12576–12578. ISSN: 0027-8424, 1091-6490. DOI: 10.1073/pnas.2133313100

Citation on p. **64**.

[245] Doekele G. Stavenga, Jan Tinbergen, Hein L. Leertouwer and Bodo D. Wilts. 'Kingfisher Feathers – Colouration by Pigments, Spongy Nanostructures and Thin Films'. In: *Journal of Experimental Biology* 214.23 (1st Dec. 2011), pp. 3960–3967. ISSN: 1477-9145, 0022-0949. DOI: 10.1242/jeb.062620 Citation on p. **64**.

[246] D.M. Atkin, T.J. Shepherd, T.A. Birks, P.St.J. Russell and P.J. Roberts. 'Full 2-D Photonic Bandgaps in Silica/Air Structures'. In: *Electronics Letters* 31.22 (26th Oct. 1995), pp. 1941–1943. ISSN: 0013-5194, 1350-911X. DOI: 10.1049/el:19951306 Citation on p. **62**.

[247] Jes Broeng, Dmitri Mogilevstev, Stig E. Barkou and Anders Bjarklev. 'Photonic Crystal Fibers: A New Class of Optical Waveguides'. In: *Optical Fiber Technology* 5.3 (July 1999), pp. 305–330. ISSN: 10685200. DOI: 10.1006/ofte.1998.0279 Citation on p. **62**.

[248] J. C. Knight, T. A. Birks, P. St. J. Russell and D. M. Atkin. 'All-Silica Single-Mode Optical Fiber with Photonic Crystal Cladding'. In: *Optics Letters* 21.19 (1st Oct. 1996), p. 1547. ISSN: 0146-9592, 1539-4794. DOI: 10.1364/OL.21.001547 Citations on pp. **62, 73**.

[249] R. F. Cregan, B. J. Mangan, J. C. Knight, T. A. Birks, P. St. J. Russell, P. J. Roberts and D. C. Allan. 'Single-Mode Photonic Band Gap Guidance of Light in Air'. In: *Science, New Series* 285.5433 (1999), pp. 1537–1539. JSTOR: 2898107. URL: http://www.jstor.org/stable/2898107 Citation on p. **63**.

[250] T.G. Euser. 'Ultrafast Optical Switching of Photonic Crystals'. PhD thesis. Enschede: Complex Photonic Systems Group, Faculty of Science and Technology and MESA+ Research Institute for Nanotechnology, University of Twente, 2nd Mar. 2007. 168 pp. URL: http://ieeexplore.ieee.org/document/4629083/ Citation on p. **63**.

[251] P.J Harding. 'Photonic Crystals Modified by Optically Resonant Systems'. PhD thesis. 2008. ISBN: 9789036526838 Citation on p. **63**.

[252] Philip St. J. Russell, Timothy A. Birks and F. Dominic Lloyd-Lucas. 'Photonic Bloch Waves and Photonic Band Gaps'. In: *Confined Electrons and Photons*. Ed. by Elias Burstein and Claude Weisbuch. Vol. 340. Boston, MA: Springer US, 1995, pp. 585–633. ISBN: 978-1-4615-1963-8. DOI: 10.1007/978-1-4615-1963-8_19 Citation on p. **63**.

[253] H. A. Macleod. *Thin-Film Optical Filters*. 4th ed. Series in Optics and Optoelectronics. Boca Raton, FL: CRC Press/Taylor & Francis, 2010. 782 pp. ISBN: 978-1-4200-7302-7 Citation on p. **65**.

[254] P. Hariharan. *Basics of Interferometry*. 2nd ed. Amsterdam ; Boston: Elsevier Academic Press, 2007. 226 pp. ISBN: 978-0-12-373589-8 Citation on p. **65**.

[255] N. M. Litchinitser, A. K. Abeeluck, C. Headley and B. J. Eggleton. 'Antiresonant Reflecting Photonic Crystal Optical Waveguides'. In: *Optics Letters* 27.18 (15th Sept. 2002), p. 1592. ISSN: 0146-9592, 1539-4794. DOI: 10.1364/OL.27.001592 Citation on p. **65**.

[256] Christos Markos, John C. Travers, Amir Abdolvand, Benjamin J. Eggleton and Ole Bang. 'Hybrid Photonic-Crystal Fiber'. In: *Reviews of Modern Physics* 89.4 (27th Nov. 2017), p. 045003. ISSN: 0034-6861, 1539-0756. DOI: 10.1103/RevModPhys.89.045003 Citation on p. **67**.

[257] G J Pearce, G S Wiederhecker, C G Poulton, S Burger and P St J Russell. 'Models for Guidance in Kagome-Structured Hollow-Core Photonic Crystal Fibres'. In: (2007), p. 6

Citation on p. **67**.

[258] Ramin Beravat. 'Twisted Photonic Crystal Fibers - Verdrillte Photonische Kristalfasern'. Naturwissenschaftliche Fakultät der Friedrich-Alexander-Universität Erlangen-Nürnberg, Nov. 2018

Citations on pp. **67, 72**.

[259] Sébastien Février, Benoît Beaudou and Pierre Viale. 'Understanding Origin of Loss in Large Pitch Hollow-Core Photonic Crystal Fibers and Their Design Simplification'. In: *Optics Express* 18.5 (1st Mar. 2010), p. 5142. ISSN: 1094-4087. DOI: 10.1364/OE.18.005142 Citation on p. **67**.

[260] Arumugam Ramachandran, Padmanaban Ramesh Babu and Krishnamoorthy Senthilnathan. 'Designing a Dual Steering Wheel Microstructured Blood Components Sensor in Terahertz Wave Band'. In: *Optical Engineering* 59.04 (17th Apr. 2020), p. 1. ISSN: 0091-3286. DOI: 10.1117/1.OE.59.4.047104 Citation on p. **67**.

[261] Mikhail N. Polyanskiy. *Refractiveindex.Info: A Compilation of Data Sources for Refractive Indices*. URL: https://refractiveindex.info Citations on pp. **67, 69, 98**.

[262] Ralf Mouthaan, Peter J. Christopher, Jonathan Pinnell, Michael Frosz, George Gordon, Timothy D. Wilkinson and Tijmen G. Euser. 'Efficient Excitation of High-Purity Modes in Arbitrary Waveguide Geometries'. In: *Journal of Lightwave Technology* 40.4 (15th Feb. 2022), pp. 1150–1160. ISSN: 0733-8724, 1558-2213. DOI: 10.1109/JLT.2021.3124469 Citations on pp. **68, 70**.

[263] F. Benabid. 'Stimulated Raman Scattering in Hydrogen-Filled Hollow-Core Photonic Crystal Fiber'. In: *Science* 298.5592 (11th Oct. 2002), pp. 399–402. ISSN: 00368075, 10959203. DOI: 10.1126/science.1076408 Citation on p. **71**.

[264] M. A. Duguay, Y. Kokubun, T. L. Koch and Loren Pfeiffer. 'Antiresonant Reflecting Optical Waveguides in SiO_2 - Si Multilayer Structures'. In: *Applied Physics Letters* 49.1 (7th July 1986), pp. 13–15. ISSN: 0003-6951, 1077-3118. DOI: 10.1063/1.97085 Citation on p. **72**.

[265] D. Yin, H. Schmidt, J. P. Barber and A. R. Hawkins. 'Integrated ARROW Waveguides with Hollow Cores'. In: *Optics Express* 12.12 (2004), p. 2710. ISSN: 1094-4087. DOI: 10.1364/OPEX.12.002710 Citation on p. **72**.

[266] Andrey D. Pryamikov, Alexander S. Biriukov, Alexey F. Kosolapov, Victor G. Plotnichenko, Sergei L. Semjonov and Evgeny M. Dianov. 'Demonstration of a Waveguide Regime for a Silica Hollow - Core Microstructured Optical Fiber with a Negative Curvature of the Core Boundary in the Spectral Region > 35 M m'. In: *Optics Express* 19.2 (17th Jan. 2011), p. 1441. ISSN: 1094-4087. DOI: 10.1364/OE.19.001441 Citation on p. **72**.

[267] Wei Ding and Yingying Wang. 'Semi-Analytical Model for Hollow-Core Anti-Resonant Fibers'. In: *Frontiers in Physics* 3 (27th Mar. 2015). ISSN: 2296-424X. DOI: 10.3389/fphy.2015.00016 Citation on p. **72**.

[268] Jonathan C Knight. 'Anti-Resonant Hollow Core Fibers'. In: *Optical Fiber Communication Conference (OFC) 2019*. Optical Fiber Communication Conference. San Diego, California: OSA, 2019, Th3E.4. ISBN: 978-1-943580-53-8. DOI: 10.1364/OFC.2019.Th3E.4

Citation on p. **72**.

[269] Philip St.J. Russell. 'Photonic-Crystal Fibers'. In: *Journal of Lightwave Technology* 24.12 (Dec. 2006), pp. 4729–4749. ISSN: 0733-8724. DOI: 10.1109/JLT.2006.885258 Citations on pp. **72, 73**.

[270] Pochi Yeh, Amnon Yariv and Emanuel Marom. 'Theory of Bragg Fiber'. In: *Journal of the Optical Society of America* 68.9 (Sept. 1978), pp. 1196–1201. DOI: 10.1364/JOSA.68.001196 Citation on p. **73**.

[271] Guillaume Vienne, Yong Xu, Christian Jakobsen, Hans-Jürgen Deyerl, Jesper B. Jensen, Thorkild Sørensen, Theis P. Hansen, Yanyi Huang, Matthew Terrel, Reginald K. Lee, Niels A. Mortensen, Jes Broeng, Harald Simonsen, Anders Bjarklev and Amnon Yariv. 'Ultra-Large Bandwidth Hollow-Core Guiding in All-Silica Bragg Fibers with Nano-Supports'. In: *Optics Express* 12.15 (2004), p. 3500. ISSN: 1094-4087. DOI: 10.1364/OPEX.12.003500

Citation on p. **73**.

[272] Jeremy Flannery, Golam Bappi, Vineeth Bhaskara, Omar Alshehri and Michal Bajcsy. 'Implementing Bragg Mirrors in a Hollow-Core Photonic-Crystal Fiber'. In: *Optical Materials Express* 7.4 (1st Apr. 2017), p. 1198. ISSN: 2159-3930. DOI: 10.1364/OME.7.001198 Citation on p. **73**.

[273] Alexander Argyros, Ian M. Bassett, Martijn A. van Eijkelenborg and Maryanne C. J. Large. 'Analysis of Ring-Structured Bragg Fibres for Single TE Mode Guidance'. In: *Optics Express* 12.12 (14th June 2004), p. 2688. ISSN: 1094-4087. DOI: 10.1364/OPEX.12.002688 Citation on p. **73**.

[274] Yong Soo Lee, Chung Ghiu Lee and Soeun Kim. 'Annular Core Photonic Quasi-Crystal Fiber with Wideband Nearly Zero Ultra-Flat Dispersion, Low Confinement Loss and High Nonlinearity'. In: *Optik* 157 (Mar. 2018), pp. 141–147. ISSN: 00304026. DOI: 10.1016/j.ijleo.2017.10.166

Citation on p. **73**.

[275] Kyunghwan Oh. 'Hollow Annular Core Fibres'. In: *Workshop on Specialty Optical Fibers and Their Applications* (2015), p. 1 Citation on p. **73**.

[276] Davide Passaro, Matteo Foroni, Federica Poli, Annamaria Cucinotta, Stefano Selleri, Jesper Laegsgaard and Anders Overgaard Bjarklev. 'All-Silica Hollow-Core Microstructured Bragg Fibers for Biosensor Application'. In: *IEEE Sensors Journal* 8.7 (July 2008), pp. 1280–1286. ISSN: 1530-437X. DOI: 10.1109/JSEN.2008.926969

Citation on p. **73**.

[277] Liang Shang and Kunjie Zheng. 'Design of Hollow Core Bragg Fibers for a Compact Fluorescence Sensing Scheme'. In: *IEEE Photonics Journal* 9.2 (Apr. 2017), pp. 1–15. ISSN: 1943-0655. DOI: 10.1109/JPHOT.2017.2677582

Citation on p. **73**.

[278] Petr Solarik, Zdenek Burian and Ivan Kasik. 'Dielectric Annular Core Optical Fiber for Chemical Trace Analysis'. In: SPIE Proceedings. Ed. by Pavel Tománek, Miroslav Hrabovský, Miroslav Miler and Dagmar Senderákova. 3rd Mar. 2006, pp. 618015-618015–5. DOI: 10.1117/12.675692 Citation on p. **73**.

[279] Yu Wang, Guofeng Yan, Zhenggang Lian, Chunzhou Wu and Sailing He. 'Liquid-Level Sensing Based on a Hollow Core Bragg Fiber'. In: *Optics Express* 26.17 (20th Aug. 2018), p. 21656. ISSN: 1094-4087. DOI: 10.1364/OE.26.021656 Citation on p. **73**.

[280] Subhasis Chaudhuri, Justin R. Sparks, Rongrui He and John V. Badding. 'Hollow Core Silicon-Silica Bragg Fiber'. In: *CLEO: 2015*. CLEO: Science and Innovations. San Jose, California: OSA, 2015, STu1N.5. ISBN: 978-1-55752-968-8. DOI: 10.1364/CLEO_SI.2015.STu1N.5

Citation on p. **73**.

[281] Turan Erdogan. 'Fiber Grating Spectra'. In: *Journal of Lightwave Technology* 15.8 (Aug. 1997), pp. 1277–1294. ISSN: 07338724. DOI: 10.1109/50.618322

Citation on p. **73**.

[282] Pietro Ferraro and Giuseppe De Natale. 'On the Possible Use of Optical Fiber Bragg Gratings as Strain Sensors for Geodynamical Monitoring'. In: *Optics and Lasers in Engineering* 37.2-3 (Feb. 2002), pp. 115–130. ISSN: 01438166. DOI: 10.1016/S0143-8166(01)00141-5 Citation on p. **73**.

[283] Francesco Poletti, Marco N. Petrovich and David J. Richardson. 'Hollow-Core Photonic Bandgap Fibers: Technology and Applications'. In: *Nanophotonics* 2.5-6 (16th Dec. 2013), pp. 315–340. ISSN: 2192-8614, 2192-

8606. DOI: 10.1515/nanoph-2013-0042

Citations on pp. **73, 74**.

[284] Roland Wengenmayr. 'Regenbogen in der Glasfaser'. In: *MaxPlanck Forschung. Das Wissenschaftsmagazin der Max-Planck-Gesellschaft* (Heft 2 2017). URL: https://www.mpg.de/10952090/MPF_2017_2 Citation on p. **74**.

[285] P. Russell. 'Photonic Crystal Fibers'. In: *Science* 299.5605 (17th Jan. 2003), pp. 358–362. ISSN: 00368075, 10959203. DOI: 10.1126/science.1079280 Citation on p. **73**.

[286] Giovanni Luzi, Philipp Epple, Michael Scharrer, Ken Fujimoto, Cornelia Rauh and Antonio Delgado. 'Influence of Surface Tension and Inner Pressure on the Process of Fibre Drawing'. In: *Journal of Lightwave Technology* 28.13 (July 2010), pp. 1882–1888. ISSN: 0733-8724, 1558-2213. DOI: 10.1109/JLT.2010.2049251 Citation on p. **73**.

[287] P. J. Roberts, F. Couny, H. Sabert, B. J. Mangan, D. P. Williams, L. Farr, M. W. Mason, A. Tomlinson, T. A Birks, J. C. Knight and P. St. J. Russell. 'Ultimate Low Loss of Hollow-Core Photonic Crystal Fibres'. In: *Optics Express* 13.1 (2005), p. 236. ISSN: 1094-4087. DOI: 10.1364/OPEX.13.000236 Citation on p. **74**.

[288] Kiarash Zamani Aghaie, Michel J. F. Digonnet and Shanhui Fan. 'Modeling Loss and Backscattering in a Photonic-Bandgap Fiber Using Strong Perturbation'. In: SPIE OPTO. Ed. by Ali Adibi, Shawn-Yu Lin and Axel Scherer. San Francisco, California, USA, 21st Feb. 2013, 86320K. DOI: 10.1117/12.2006446 Citation on p. **74**.

[289] Eric Numkam Fokoua, Francesco Poletti and David J Richardson. 'Analysis of Light Scattering from Surface Roughness in Hollow-Core Photonic Bandgap Fibers'. In: (2012), p. 12 Citation on p. **74**.

[290] Minh-Chau Phan-Huy, J.-M. Moison, J.A. Levenson, S. Richard, G. Melin, M. Douay and Y. Quiquempois. 'Surface Roughness and Light Scattering in a Small Effective Area Microstructured Fiber'. In: *Journal of Lightwave Technology* 27.11 (June 2009), pp. 1597–1604. ISSN: 0733-8724. DOI: 10.1109/JLT.2009.2020608 Citation on p. **74**.

[291] Hanna Izabela Stawska and Maciej Andrzej Popenda. 'A Dual Hollow Core Antiresonant Optical Fiber Coupler Based on a Highly Birefringent

Structure-Numerical Design and Analysis'. In: *Fibers* 7.12 (7th Dec. 2019), p. 109. ISSN: 2079-6439. DOI: 10.3390/fib7120109 Citation on p. **75**.

[292] Shou-fei Gao, Ying-ying Wang, Wei Ding, Dong-liang Jiang, Shuai Gu, Xin Zhang and Pu Wang. 'Hollow-Core Conjoined-Tube Negative-Curvature Fibre with Ultralow Loss'. In: *Nature Communications* 9.1 (Dec. 2018), p. 2828. ISSN: 2041-1723. DOI: 10.1038/s41467-018-05225-1

Citations on pp. **75, 92**.

[293] Helmut Vogel and Christian Gerthsen. *Physik Ein Lehrbuch zum Gebrauch neben Vorlesungen*. 17. Auflage. Berlin, Heidelberg: Springer, 1993. ISBN: 978-3-662-09301-6. URL: http://www.springerlink.com/content/978-3-642-87839-8 Citation on p. **76**.

[294] G. K. Batchelor. *An Introduction to Fluid Dynamics*. 1. Cambridge mathematical ed., 14. print. Cambridge Mathematical Library. Cambridge: Cambridge Univ. Press, 2010. 615 pp. ISBN: 978-0-521-66396-0

Citations on pp. **76, 77**.

[295] Christopher I. Trombley and Maria L. Ekiel-Jeżewska. 'Basic Concepts of Stokes Flows'. In: *Flowing Matter*. Ed. by Federico Toschi and Marcello Sega. Cham: Springer International Publishing, 2019, pp. 35–50. ISBN: 978-3-030-23369-3. DOI: 10.1007/978-3-030-23370-9_2

Citations on pp. **76, 77**.

[296] C. Kleinstreuer. *Microfluidics and Nanofluidics: Theory and Selected Applications*. Hoboken: John Wiley & Sons, 2014. 436 pp. ISBN: 978-0-470-61903-2

Citation on p. **77**.

[297] Bruce Roy Munson, T. H. Okiishi, Wade W. Huebsch and Alric P. Rothmayer. *Fundamentals of Fluid Mechanics*. 7th edition. Hoboken, NJ: John Wiley & Sons, Inc, 2013. 747 pp. ISBN: 978-1-118-39971-2 Citation on p. **77**.

[298] Wolfgang Demtröder. *Experimentalphysik 1. Mechanik und Wärme*. 8th ed. Springer-Lehrbuch. Berlin, Heidelberg: Springer Berlin Heidelberg, 2018. ISBN: 978-3-662-54847-9. DOI: 10.1007/978-3-662-54847-9

Citation on p. **78**.

[299] Henrik Bruus. *Theoretical Microfluidics*. Oxford Master Series in Physics 18. Oxford ; New York: Oxford University Press, 2008. 346 pp. ISBN: 978-0-19-923509-4

Citation on p. **78**.

[300] Kwang W. Oh, Kangsun Lee, Byungwook Ahn and Edward P. Furlani. 'Design of Pressure-Driven Microfluidic Networks Using Electric Circuit Analogy'. In: *Lab Chip* 12.3 (2012), pp. 515–545. ISSN: 1473-0197, 1473-0189. DOI: 10.1039/C2LC20799K Citations on pp. **80, 192**.

[301] Rohit Karnik. 'Microfluidic Mixing'. In: *Encyclopedia of Microfluidics and Nanofluidics*. Ed. by Dongqing Li. Boston, MA: Springer US, 2008, pp. 1177–1186. ISBN: 978-0-387-48998-8. DOI: 10.1007/978-0-387-48998-8_939 Citation on p. **80**.

[302] Richard P. Feynman, Robert B. Leighton and Matthew L. Sands. 'Ch. 41. The Brownian Movement'. In: *The Feynman Lectures on Physics*. New millennium ed. Vol. 1. 3 vols. New York: Basic Books, 2011. ISBN: 978-0-465-02414-8 Citation on p. **81**.

[303] Victor M. Rosenoer, Murray Oratz and Marcus Adolphus Rothschild, eds. *Albumin Structure, Function and Uses*. 1st ed. Oxford ; New York: Pergamon Press, 1977. 397 pp. ISBN: 978-0-08-019603-9 Citation on p. **102**.

[304] Phil G. Squire, Peter. Moser and Chester T. O'Konski. 'Hydrodynamic Properties of Bovine Serum Albumin Monomer and Dimer'. In: *Biochemistry* 7.12 (Dec. 1968), pp. 4261–4272. ISSN: 0006-2960, 1520-4995. DOI: 10.1021/bi00852a018 Citation on p. **102**.

[305] A.K. Wright and M.R. Thompson. 'Hydrodynamic Structure of Bovine Serum Albumin Determined by Transient Electric Birefringence'. In: *Biophysical Journal* 15.2 (Feb. 1975), pp. 137–141. ISSN: 00063495. DOI: 10.1016/S0006-3495(75)85797-3 Citation on p. **102**.

[306] Valeria Levi and F.Luis González Flecha. 'Reversible Fast-Dimerization of Bovine Serum Albumin Detected by Fluorescence Resonance Energy Transfer'. In: *Biochimica et Biophysica Acta (BBA) - Proteins and Proteomics* 1599.1-2 (Sept. 2002), pp. 141–148. ISSN: 15709639. DOI: 10.1016/S1570-9639(02)00414-4 Citation on p. **102**.

[307] Zenon Toprakcioglu and Tuomas P. J. Knowles. 'Shear-Mediated Sol-Gel Transition of Regenerated Silk Allows the Formation of Janus-like Microgels'. In: *Scientific Reports* 11.1 (23rd Mar. 2021), p. 6673. ISSN: 2045-2322. DOI: 10.1038/s41598-021-85199-1 Citation on p. **128**.

[308] Mitch Jacoby. 'A Way Forward for Optical Fibers'. In: *C&EN Global Enterprise* 98.10 (16th Mar. 2020), pp. 28–33. DOI: 10.1021/cen-09810-cover
Citation on p. **145**.

[309] Y. Chen, Z. Liu, S.R. Sandoghchi, G. Jasion, T. D. Bradley, E. Numkam, J. R. Hayes, N. V. Wheeler, D. R. Gray, B. J. Mangan, R. Slavík, F. Poletti, M. N. Petrovich and D. J. Richardson. 'Demonstration of an 11km Hollow Core Photonic Bandgap Fiber for Broadband Low-latency Data Transmission'. In: *Optical Fiber Communication Conference Post Deadline Papers*. Optical Fiber Communication Conference. Los Angeles, California: OSA, 2015, Th5A.1. ISBN: 978-1-55752-940-4. DOI: 10.1364/OFC.2015.Th5A.1
Citation on p. **145**.

[310] Gregory T. Jasion, Eric Numkam Fokoua, John S. Shrimpton, David J. Richardson and Francesco Poletti. 'Studying the Limits of Production Rate and Yield for the Volume Manufacturing of Hollow Core Photonic Band Gap Fibers'. In: *Optics Express* 23.25 (14th Dec. 2015), p. 32179. ISSN: 1094-4087. DOI: 10.1364/OE.23.032179 Citation on p. **145**.

[311] M.W. Ogden and H.M. McNair. 'Characterization of Fused-Silica Capillary Tubing by Contact Angle Measurements'. In: *Journal of Chromatography A* 354 (Jan. 1986), pp. 7–18. ISSN: 00219673. DOI: 10.1016/S0021-9673(01)87006-0 Citation on p. **146**.

[312] Suman De, Daniel R. Whiten, Francesco S. Ruggeri, Craig Hughes, Margarida Rodrigues, Dimitrios I. Sideris, Christopher G. Taylor, Francesco A. Aprile, Serge Muyldermans, Tuomas P. J. Knowles, Michele Vendruscolo, Clare Bryant, Kaj Blennow, Ingmar Skoog, Silke Kern, Henrik Zetterberg and David Klenerman. 'Soluble Aggregates Present in Cerebrospinal Fluid Change in Size and Mechanism of Toxicity during Alzheimer' s Disease Progression'. In: *Acta Neuropathologica Communications* 7.1 (Dec. 2019), p. 120. ISSN: 2051-5960. DOI: 10.1186/s40478-019-0777-4
Citation on p. **153**.

[313] M N Padamwar and A P Pawar. 'Silk Sericin and Its Applications: A Review'. In: *Journal of Scientific & Industrial Research* 63 (2004), pp. 323–329 Citation on p. **154**.

[314] Danielle N Rockwood, Rucsanda C Preda, Tuna Yücel, Xiaoqin Wang, Michael L Lovett and David L Kaplan. 'Materials Fabrication from Bombyx Mori Silk Fibroin'. In: *Nature Protocols* 6.10 (Oct. 2011), pp. 1612–1631.

ISSN: 1754-2189, 1750-2799. DOI: 10.1038/nprot.2011.379
Citation on p. **154**.

[315] X. Hu, K. Vasanthavada, K. Kohler, S. McNary, A. M. F. Moore and C. A. Vierra. 'Molecular Mechanisms of Spider Silk'. In: *Cellular and Molecular Life Sciences* 63.17 (Sept. 2006), pp. 1986–1999. ISSN: 1420-682X, 1420-9071. DOI: 10.1007/s00018-006-6090-y Citation on p. **155**.

[316] Maxime Boulet-Audet, Ann E. Terry, Fritz Vollrath and Chris Holland. 'Silk Protein Aggregation Kinetics Revealed by Rheo-IR'. In: *Acta Biomaterialia* 10.2 (Feb. 2014), pp. 776–784. ISSN: 17427061. DOI: 10.1016/j.actbio.2013.10.032 Citation on p. **155**.

[317] Innocent B. Bekard, Peter Asimakis, Joseph Bertolini and Dave E. Dunstan. 'The Effects of Shear Flow on Protein Structure and Function'. In: *Biopolymers* (2011), n/a–n/a. ISSN: 00063525. DOI: 10.1002/bip.21646
Citation on p. **155**.

[318] Alana Gerhardt, Nicole R. Mcgraw, Daniel K. Schwartz, Jared S. Bee, John F. Carpenter and Theodore W. Randolph. 'Protein Aggregation and Particle Formation in Prefilled Glass Syringes'. In: *Journal of Pharmaceutical Sciences* 103.6 (June 2014), pp. 1601–1612. ISSN: 00223549. DOI: 10.1002/jps.23973 Citations on pp. **155, 168**.

[319] Birgit Mueller-Chorus, Erica Tullo, Vinod Vilivalam and Lloyd Waxman. 'Effect of Agitation on Protein Aggregation in Vials Made from Glass or Plastics'. In: *Single-Use Technologies II: Bridging Polymer Science to Biotechnology Applications*. 5th July 2017
Citation on p. **155**.

[320] Marion Schvartz, Florent Saudrais, Stéphanie Devineau, Jean-Christophe Aude, Stéphane Chédin, Céline Henry, Aarón Millán-Oropeza, Thomas Perrault, Laura Pieri, Serge Pin, Yves Boulard, Guillaume Brotons and Jean-Philippe Renault. 'A Proteome Scale Study Reveals How Plastic Surfaces and Agitation Promote Protein Aggregation'. In: *Scientific Reports* 13.1 (21st Jan. 2023), p. 1227. ISSN: 2045-2322. DOI: 10.1038/s41598-023-28412-7 Citation on p. **155**.

[321] Tatiana Perevozchikova, Hirsh Nanda, Douglas P. Nesta and Christopher J. Roberts. 'Protein Adsorption, Desorption, and Aggregation Mediated by Solid-Liquid Interfaces'. In: *Journal of Pharmaceutical Sciences* 104.6 (June

2015), pp. 1946–1959. ISSN: 00223549. DOI: 10.1002/jps.24429
Citation on p. **155**.

[322] Joëlle A. J. Housmans, Guiqin Wu, Joost Schymkowitz and Frederic Rousseau. 'A Guide to Studying Protein Aggregation'. In: *The FEBS Journal* 290.3 (Feb. 2023), pp. 554–583. ISSN: 1742-464X, 1742-4658. DOI: 10.1111/febs.16312 Citation on p. **155**.

[323] Hanns-Christian Mahler, Wolfgang Friess, Ulla Grauschopf and Sylvia Kiese. 'Protein Aggregation: Pathways, Induction Factors and Analysis'. In: *Journal of Pharmaceutical Sciences* 98.9 (Sept. 2009), pp. 2909–2934. ISSN: 00223549. DOI: 10.1002/jps.21566 Citation on p. **155**.

[324] C.V. Morr and S.H.C. Lin. 'Preparation and Properties of an Alcohol-Precipitated Whey Protein Concentrate'. In: *Journal of Dairy Science* 53.9 (Sept. 1970), pp. 1162–1170. ISSN: 00220302. DOI: 10.3168/jds.S0022-0302(70)86362-7 Citation on p. **155**.

[325] Surinder M. Singh, Javier Cabello-Villegas, Regina L. Hutchings and Krishna M. G. Mallela. 'Role of Partial Protein Unfolding in Alcohol-Induced Protein Aggregation'. In: *Proteins: Structure, Function, and Bioinformatics* (1st July 2010), n/a–n/a. ISSN: 08873585, 10970134. DOI: 10.1002/prot.22778 Citation on p. **155**.

[326] Ishrat Jahan and Shahid M. Nayeem. 'Effect of Urea, Arginine, and Ethanol Concentration on Aggregation of $_{179}$CVNITV$_{184}$ Fragment of Sheep Prion Protein'. In: *ACS Omega* 3.9 (30th Sept. 2018), pp. 11727–11741. ISSN: 2470-1343, 2470-1343. DOI: 10.1021/acsomega.8b00875
Citation on p. **155**.

[327] Yangyang Feng, Xiaoli Ma, Baohua Kong, Qian Chen and Qian Liu. 'Ethanol Induced Changes in Structural, Morphological, and Functional Properties of Whey Proteins Isolates: Influence of Ethanol Concentration'. In: *Food Hydrocolloids* 111 (Feb. 2021), p. 106379. ISSN: 0268005X. DOI: 10.1016/j.foodhyd.2020.106379 Citation on p. **155**.

[328] Ayaka Kamada, Zenon Toprakcioglu and Tuomas P. J. Knowles. 'Kinetic Analysis Reveals the Role of Secondary Nucleation in Regenerated Silk Fibroin Self-Assembly'. In: *Biomacromolecules* 24.4 (10th Apr. 2023), pp. 1709–1716. ISSN: 1525-7797, 1526-4602. DOI: 10.1021/acs.biomac.2c01479 Citation on p. **156**.

[329] Irene Georgakoudi, Irene Tsai, Cherry Greiner, Cheryl Wong, Jordy DeFelice and David Kaplan. 'Intrinsic Fluorescence Changes Associated with the Conformational State of Silk Fibroin in Biomaterial Matrices'. In: *Optics Express* 15.3 (2007), p. 1043. ISSN: 1094-4087. DOI: 10.1364/OE.15.001043 Citation on p. **156**.

[330] David Creed. 'The Photophysics and Photochemistry of the Near-Uv Absorbing Amino Acids-I. Tryptophan and Its Simple Derivatives'. In: *Photochemistry and Photobiology* 39.4 (2nd Jan. 2008), pp. 537–562. ISSN: 00318655, 17511097. DOI: 10.1111/j.1751-1097.1984.tb03890.x Citation on p. **161**.

[331] Anna Gakamsky, Rory R. Duncan, Nicola M. Howarth, Baljean Dhillon, Kim K. Buttenschön, Daniel J. Daly and Dmitry Gakamsky. 'Tryptophan and Non-Tryptophan Fluorescence of the Eye Lens Proteins Provides Diagnostics of Cataract at the Molecular Level'. In: *Scientific Reports* 7.1 (10th Jan. 2017), p. 40375. ISSN: 2045-2322. DOI: 10.1038/srep40375 Citation on p. **161**.

[332] Jolon M. Dyer, Scott D. Bringans and Warren G. Bryson. 'Determination of Photo-oxidation Products Within Photoyellowed Bleached Wool Proteins'. In: *Photochemistry and Photobiology* 82.2 (2006), p. 551. ISSN: 0031-8655. DOI: 10.1562/2005-08-29-RA-663 Citation on p. **161**.

[333] J. M. Dyer, S. D. Bringans and W. G. Bryson. 'Characterisation of Photo-Oxidation Products within Photoyellowed Wool Proteins: Tryptophan and Tyrosine Derived Chromophores'. In: *Photochemical & Photobiological Sciences* 5.7 (July 2006), pp. 698–706. ISSN: 1474-905X, 1474-9092. DOI: 10.1039/b603030k Citation on p. **161**.

[334] Kayaku MicroChem. *Technical Data Sheet SU-8-3000*. Sept. 2019. URL: https://kayakuam.com/wp-content/uploads/2019/09/SU-8-3000-Data-Sheet.pdf Citation on p. **189**.

[335] Pavan K. Challa, Tadas Kartanas, Jérôme Charmet and Tuomas P. J. Knowles. 'Microfluidic Devices Fabricated Using Fast Wafer-Scale LED-lithography Patterning'. In: *Biomicrofluidics* 11.1 (Jan. 2017), p. 014113. ISSN: 1932-1058. DOI: 10.1063/1.4976690 Citation on p. **189**.

[336] Gianluca Persichetti, Genni Testa and Romeo Bernini. 'High Sensitivity UV Fluorescence Spectroscopy Based on an Optofluidic Jet Waveguide'. In: *Optics Express* 21.20 (7th Oct. 2013), p. 24219. ISSN: 1094-4087. DOI: 10.1364/OE.21.024219 Citation on p. **190**.

[337] Gianluca Persichetti, Genni Testa and Romeo Bernini. 'Optofluidic Jet Waveguide Enhanced Raman Spectroscopy'. In: *Sensors and Actuators B: Chemical* 207 (Feb. 2015), pp. 732–739. ISSN: 09254005. DOI: 10.1016/j.snb.2014.10.060 Citation on p. **190**.

[338] Takahiro Matsumoto, Rika Kikojima, Tomomi Fukuoka, Ichiro Tatsuno and Tadao Hasegawa. 'Total Internal Reflection of Deep-Ultraviolet Light in a Water Waveguide and Its Application to Water Disinfection Technologies'. In: *Water* 11.2 (8th Feb. 2019), p. 294. ISSN: 2073-4441. DOI: 10.3390/w11020294 Citation on p. **191**.

[339] Frank Wagner, Ochélio Sibailly, Nandor Vágó, Rafal Romanowicz and Bernold Richerzhagen. 'The Laser Microjet® Technology – 10 Years of Development'. In: *International Congress on Applications of Lasers & Electro-Optics*. ICALEO® 2003: 22nd International Congress on Laser Materials Processing and Laser Microfabrication. Jacksonville, Florida, USA: Laser Institute of America, 2003, p. M401. ISBN: 978-0-912035-75-8. DOI: 10.2351/1.5060119 Citation on p. **191**.

[340] Philip Russell. 'Photonic Crystal Fiber: Finding the Holey Grail'. In: *Optics and Photonics News* 18.7 (1st July 2007), p. 26. ISSN: 1047-6938, 1541-3721. DOI: 10.1364/OPN.18.7.000026 Citation on p. **191**.

[341] Aaron R. Hawkins and Holger Schmidt. 'Optofluidic Waveguides: II. Fabrication and Structures'. In: *Microfluidics and Nanofluidics* 4.1-2 (Jan. 2008), pp. 17–32. ISSN: 1613-4982, 1613-4990. DOI: 10.1007/s10404-007-0194-z Citation on p. **192**.

[342] R. Altkorn, I. Koev, R. P. Van Duyne and M. Litorja. 'Low-Loss Liquid-Core Optical Fiber for Low-Refractive-Index Liquids: Fabrication, Characterization, and Application in Raman Spectroscopy'. In: *Applied Optics* 36.34 (1st Dec. 1997), p. 8992. ISSN: 0003-6935, 1539-4522. DOI: 10.1364/AO.36.008992 Citation on p. **192**.

[343] Jens Højgaard Jensen. 'Introducing Fluid Dynamics Using Dimensional Analysis'. In: *American Journal of Physics* 81.9 (Sept. 2013), pp. 688–694. ISSN: 0002-9505, 1943-2909. DOI: 10.1119/1.4813064 Citation on p. **192**.

[344] Sanjoy Mahajan. *Street-Fighting Mathematics: The Art of Educated Guessing and Opportunistic Problem Solving*. Cambridge, Massachusetts: MIT Press, 2010. 134 pp. ISBN: 978-0-262-51429-3 Citation on p. **192**.

[345] Niels Asger Mortensen, Fridolin Okkels and Henrik Bruus. 'Reexamination of Hagen-Poiseuille Flow: Shape Dependence of the Hydraulic Resistance in Microchannels'. In: *Physical Review E* 71.5 (5th May 2005), p. 057301. ISSN: 1539-3755, 1550-2376. DOI: 10.1103/PhysRevE.71.057301 Citations on pp. **194–196**.

„Hier konnte niemand sonst Einlaß erhalten, denn dieser Eingang war nur für dich bestimmt. Ich gehe jetzt und schließe ihn.“ – Franz Kafka, *Der Prozeß*, 1925

The End.